IONOSPHERIC RESPONSE TO EARTHQUAKES AND SCHUMANN RESONANCES

A THESIS

Submitted in partial fulfilment of the requirements for the award of the degree of

DOCTOR OF PHILOSOPHY

in

EARTH SCIENCES

by

RAMESH CHAND

DEPARTMENT OF EARTH SCIENCES
INDIAN INSTITUTE OF TECHNOLOGY ROORKEE
ROORKEE - 247 667 (INDIA)

JULY, 2009

INDIAN INSTITUTE OF TECHNOLOGY ROORKEE
ROORKEE

CANDIDATE'S DECLARATION

I hereby certify that the work which is being presented in the thesis entitled **IONOSPHERIC RESPONSE TO EARTHQUAKES AND SCHUMANN RESONANCES** in partial fulfilment of the requirements for the award of the Degree of Doctor of Philosophy and submitted in the Department of Earth Sciences of the Indian Institute of Technology Roorkee, Roorkee is an authentic record of my own work carried out during a period from January, 2004 to July, 2009 under the supervision of Dr. M. Israil, Professor, Department of Earth Sciences and Dr. Jagdish Rai, Professor, Department of Physics, Indian Institute of Technology Roorkee, Roorkee.

The matter presented in the thesis has not been submitted by me for the award of any other degree of this or any other Institute.

Rchand

(RAMESH CHAND)

This is to certify that the above statement made by the candidate is correct to the best of our knowledge.

(Jagdish Rai)
Supervisor

(M. Israil)
Supervisor

Date: 22-07-09

The Ph.D. Viva-Voice Examination of **Mr. RAMESH CHAND**, Research Scholar, has been held on 07.11.2009

Signature of Supervisors

Signature of External Examiner

ABSTRACT

The region extended from 60 km to about 1000 km altitude above the earth's surface containing free electrons, ions and neutral atoms/molecules of atmospheric gases is known as ionosphere. It is formed mainly by the ionization of neutral gas atoms/molecules present in the upper atmosphere by exposure to solar radiation. The degree of ionization changes with height leads to the formation of several distinct ionization peaks identified as D, E, F1, F2 layers. Ionospheric weather play very important role in sustaining our life, which largely dependent on present day technological systems. Understanding, monitoring and forecasting the changes in the ionosphere weather are crucial for communication, navigation, exploration of the near earth space and even exploration of electrical structure of deeper part of earth's interior.

Variability of the ionospheric weather, and it's response to the phenomena occurring above and below it, can be studied by monitoring it's electrons and ions temperature, density and ion compositions. Many experimental and theoretical studies were devoted for monitoring and predicting ionospheric weather in the form of electron and ion temperature, density and ion compositions. The data used for these studies were either procured by ground based probes or by satellite observations. Some examples of dedicated satellites for these studies are: SROSS-C2 satellite recorded ionospheric temperature and density data in Indian region from 1995-2000 using RPA payload. DEMETER satellite was used to detect anomalous variations of electromagnetic waves, particle fluxes or thermal plasma parameters related to seismic activity.

Numerous workers have used the data generated by these satellites for ionospheric characterization. SROSS-C2 data were used for electron, ion temperature and density variations in Indian region (Bhuyan et al., 2003; Sharma et al., 2004; Sharma et al., 2005). The study reveals that the ionospheric parameter (temperature and density) varies as a response to the anomalous phenomena occurring above and below it. Many other studies were also dedicated to investigate the ionospheric irregularities due to atmospheric gravity waves,

thunderstorms, hurricanes, tornadoes, seismological and volcanic events. Some of these events are responsible for generating observable variations in ionospheric parameters (Ahmamedov, 1993; Taranenko et al., 1993; Depuev and Zelenova, 1996; Molchanov and Hayakawa, 1998; Molchanov et al., 1998; Ondoh, 1998, 2000; Kazimirovsky et al., 2003; Pulinets et al., 1994, 2000, 2003; Liu et al., 2000, 2004; Parrot, 1994, 1995, Parrot et al., 2006; Hayakawa et al., 1996a, b, 2006; Sharma et al., 2004, 2005, 2006; Rishbeth, 2006).

Gokhberg, et al., 1994; Parrot 1995; Pulinets 1998a, b and Parrot et al., 2006 have discussed the generation and propagation of seismo-electric field from epicentral zone into the ionosphere. The emission and propagation of electromagnetic radiations in a wide frequency band, covering ULF, ELF and VLF from epicenter zone of earthquake were also reported (Parrot, 1995; Koshevaya et al., 1997; Shalimov and Gokhberg, 1998; Hayakawa et al., 1996a, b, 2000; Kushwah et al., 2005).

Low frequency EM (micro pulsation) field generated as a results of complex interaction of solar wind and magnetosphere are modified by ionosphere before reaching to the earth surface, where it is used as a source in Magnetotelluric (MT) method to delineated electrical structure of the earth interior (Kaufman and Keller, 1981). High frequency (>1Hz) EM field excited by thunderstorm\lightening discharge propagates globally in waveguide mode in the cavity formed by the earth and ionosphere as conducting boundaries. Schumann (1952) has used simplest vacuum model confined with two concentric perfectly conducting spheres (earth and ionosphere) and obtained first five Schumann resonance (SR) frequencies: 10.6, 18.4, 26.0, 35.5 and 41.1 Hz. However it was found that these were not in agreement with the observed SR frequency. Madden and Thomson, 1965, observed SR frequencies: 7.8, 14.1, 20.3, 26.3 and 32.5 Hz using finite conductivity of ionosphere which are in reasonable agreement with the observed frequencies.

Amplitude and frequency characteristics of SR depend on the characteristics of their source, location of observation point with respect to source and ionospheric electron density\conductivity. For a local region assuming the

average constant source distribution, SR frequency variations can be used to determine average conductivity profile of ionosphere and vice versa (Tran & Polk, 1979a, b; Sentman, 1983). It was investigated that attenuation characteristics, frequency shift and diurnal variations are different for different field components (Sentman 1987, 1989; Bliokh et al., 1980; Nickolaenko, 1997; Roldugin et al., 2004a). SR in magnetic field components was also studied by Fullekrug (1995). Penetration of electric and magnetic field components of the SR into the ionosphere was numerically investigated by Grimalsky et al., (2005) for possible daytime and nighttime variation of conductivity in the ionospheric D- and E- layers. Hayakawa et al., (2008) showed the short term spectral modification, associated with the Moshiri (Japan) earthquake, in the SR frequency band of 2.5- 40 Hz.

The study of the Schumann resonance frequency variation has become an important tool for ionospheric characterization in terms of electron density variations and monitoring sudden disturbance in the ionosphere during solar proton events (Roldugin, et al., 2001; Roldugin, et al., 2003). Precise measurements of the SR frequencies with high spectral resolution were carried out from the audiomagnetotelluric and magnetotelluric data (Beamish and Tzanis, 1986; Melnikov, et al., 2004; Tulunay et al., 2008).

Present work is devoted to study the following points related to the ionospheric response to the earthquakes and Schumann resonances:

(a) Ionospheric temperature and density responses to earthquakes using SROSS-C2 satellite data for Indian region.

(b) Characterization of SR frequencies using MT data acquired from Himalayan region and its application in determination of electron density variation in lower ionospheric region.

(c) Acquired MT data were also used to delineate electrical structure of earth crust along a selected profile in Himalayan region which is added as an appendix in the thesis.

The entire work is presented systematically in the form of following five chapters.

A brief description of ionospheric weather and its variability has been presented in **Chapter-I**. The descriptions of the solar phenomena, thunderstorms, lightning/sprites and their electromagnetic fields generated due the phenomena occurring above and below it have also been given.

Chapter-II, The studies on the diurnal, seasonal variations of the ionospheric electron and ion temperatures and their ratio (Te/Ti) using SROSS-C2 satellite data in ionospheric F2 region during the period from 1995 to 1999 is presented. The ionospheric electron temperature shows the 'morning overshoot' to about 3 to 5 times of average electron temperature and 1.5 to 2 times of average ion temperature during the sunrise hours. The temperature ratio Te/Ti, was almost unity during the nighttime and shows variations during the daytime in all seasons.

The ionospheric temperature response to earthquakes has been studied. 14 earthquake events were analysed in 6 years (January 1995 to December 2000) data recorded by SROSS-C2 satellite and found that 13 events out of 14 show increase in average electron temperature during earthquake days by an amount approximately 1.1 to 1.5 times of the normal days while 14 events out of 15 show the increase in ion temperature during earthquake days by amount 1.1 to 1.3 of the normal days. Electron and ion temperature data were analyzed in such a way that the diurnal, seasonal, latitudinal, longitudinal, altitudinal, solar flare, thunderstorm and magnetic storm variations are not masked with the earthquake anomalies. The seismogenic vertical electric field and associated electromagnetic radiation from epicentral zones reaches up to ionospheric height, induces joule heating, might be responsible for the ionospheric temperature perturbation.

Chapter-III, we have analyzed the ion density response to the earthquake for H^+, He^+, NO^+, $NO2^+$ ions in the ionospheric F2 region. 12 earthquake events were analysis for the ion density anomalies in ionospheric F2 region for which satellite data matches with the epicenter location. Out of these, 10 events show decrease in ion density during earthquake days over normal days while only 2 events show increase during earthquake days than normal days. The observed density variation is generally consistent with the corresponding temperature anomalies. Care has been taken to remove the masking of other effects in the

earthquake anomalies. We therefore conclude that the ion density anomalies are related to earthquake events and in reasonable agreement with the temperature anomalies.

Chapter-IV discusses the Schumann resonance (SR) frequency variation using Magnetotelluric (MT) data recorded in one of the world toughest and generally inaccessible Himalayan terrain. Spectral analysis of MT time series data at frequency resolution of 0.03 Hz has been performed using Fast Fourier transform (FFT) algorithm. Spectral stabilization in Schumann resonance mode has been achieved by averaging over thirty two individual power spectral magnitude. Average amplitude and frequency variation in the Schumann resonance are presented.

It has been observed that pair of same polarization components, shows a similar variation in SR frequencies. However, different frequency variations were observed for different polarizations: north-south (N-S) and east-west (E-W) magnetic field components.

SR frequency variation obtained in the recorded data was used to estimate electron density in lower ionosphere. For this purpose we have reformulated Roldugin et al., (2003) analytic expression for SR frequencies in a two-layer wave guide model. We believe, however, their corresponding formula is incorrect and proposed the slightly modified alternative expression relating SR frequency with the electron density in the lower ionosphere. We have then estimated the electron density in lower ionosphere from SR frequencies. The estimated electron density has b een compared with the values derived from the International Reference ionosphere (IRI) model.

Magnetotelluric (MT) data recorded in Himalayan region were also used to determine electrical structure of the upper crust to a depth of about 6 km along the selected profile. Based on the regional geology, possible geological interpretation of the Geoelectrical model is presented. The MT studies have been kept in the appendix of the present thesis.

Summary and conclusion is presented in **chapter V** along with the recommendations for future work.

LIST OF PUBLICATIONS

A. **Paper in Referred Journals**

1. D. K. Sharma, M. Israil, **Ramesh Chand**, Jagdish Rai, P. Subrahmanyam and S. C. Garg, Signature of seismic activities in the F2 region ionospheric electron temperature, Journal of Atmospheric and Solar-Terrestrial Physics 68, 691-696 (2006).

2. D. K. Sharma, **R. Chand**, J. Rai and M. Israil, Effect of seismic activities on ion temperature in the F2 region of the ionosphere, Atmosfera 19 (1), 1-7 (2006).

3. D. K. Sharma, **Ramesh Chand**, M. Israil and Jagdish Rai, Variation of electron and ion temperatures ratio over the Indian region during the period 1995-1999 as measured by SROSS-C2 satellite, Journal of Atmospheric and Solar-Terrestrial Physics 67, 1443-1147 (2005).

4. **Ramesh Chand**, M. Israil and Jagdish Rai, Schumann resonance frequency variations observed in Magnetotelluric data recorded from Garhwal Himalayan region India, Annales Geophysical 27, 3497-3507 (2009).
5. **Ramesh Chand**, M. Israil, D. K. Sharma and Jagdish Rai, Ionospheric temperature perturbation related to seismic activities using satellite data (Submitted in Advances in Space Research).

6. **Ramesh Chand**, M. Israil, D. K. Sharma and Jagdish Rai, Ionospheric density response to the earthquake using satellite data (Submitted in Journal of Atmospheric and Solar-Terrestrial Physics).

B. **In conference proceedings**

1. J. Rai, **R. Chand**, S. Kamakhi and M. Israil, Schumann resonances in earth - ionospherte cavity, XXIX General Assembly of the International Union of Radio Science, Chicago, Illinois, USA, 324, 2008.

2. J. Rai, **R. Chand**, D. K. Sharma, S. Kamakhi and M. Israil, Studies on ionospheric perturbation due to seismic activity using Indian SROSS C2 satellite data, XXIX General Assembly of the International Union of Radio Science, Chicago, Illinois, USA, 243, 2008.

3. **R. Chand**, M. Israil, D. K. Sharma and J. Rai, Effect of seismic activities in the F2 region ionospheric electron and ion temperature, IUGG XXIV General Assembly, International Association of seismology and Physics of the Earth's interior Perugia, Itlay, 293, 2007.

4. D. K. Sharma, **R. Chand**, M. Israil and J. Rai, Signature of seismic activities in the F2 region ionosphere, International workshop on

electromagnetic studies related to earthquakes and volcanoes, R.B.S. College, Agra, India, 74, 2006.

5. D. K. Sharma, **R. Chand**, M. Israil and J. Rai, Study of the ionospheric temperatures with the help of Satellite, National Symposium on Atmospheric & Environmental Sciences: New Dimensions (in Hindi), NPL, New Delhi, 3/1, 2006.

6. **R. Chand**, D. K. Sharma, M. Israil and J. Rai, Ionospheric response to seismic activity using the satellite data, XIV National Space Science Symposium, Andhra University, Visakhapatnam, 120, 2006.

ACKNOWLEDGEMENTS

It is my great pleasure and privilege to express my deep sense of gratitude and profound indebtedness to my respected supervisors Prof. M. Israil, Department of Earth Sciences and Prof. Jagdish Rai, Department of Physics, Indian Institute of Technology, Roorkee, for their incessant invaluable guidance, inspiring encouragement and kind cooperation throughout this work. The work could not have been completed without their helpful counsel and constant cooperation. The fruitful discussions and pertinent suggestions not only strengthened my skills in research but also helped me a more confident personality.

During this research, the department has had two heads; Prof. R. P. Gupta, Prof. V. N. Singh and most fortunately they encouraged me by extending every sort of help as and when sought for.

The author is especially thankful to Prof. Sri Niwas, Prof. P. K. Gupta Department of Earth Sciences for their invaluable help and advice from time to time as when needed.

I would like to make a special note of thank to all faculty members of the Department of Earth Sciences for their co-operation. Thanks are also to Dr. Bhism Singh, Scientist, National Institute of Hydrology for their constant encouragement during my research work. The author is also thankful to Prof. S. C. Sharma, Department of Mechanical Engineering and Dr. P. K. Sharma, Department of Civil Engineering for their invaluable help from time to time as when needed. The author also acknowledge his deep sense of gratitude to *Late Prof. P. Weidelt*, Institute of Geophysics and Meterology,TU Braunschweig, Germany, *Prof. B. Tezkan,* Institute for Geophysics, Gottingen, Germany, whose critical and timely suggestions proved to be helpful.

I am highly obliged and wish to express my sincere thanks to the technical staff of the Department of Earth Sciences, especially to *Mr. Nayar, Mr. Rakesh, Mr. V. K. Saini, Mr. S. K. Sharma,* who have helped him in all possible ways during the official work.

The financial support from Council of Scientific and Industrial Research (CSIR) and Ministry of Human Resources and Development (MHRD), New Delhi to complete the present investigations is highly acknowledged.

I express my sincere thanks to Dr. D. K. Sharma to provide all necessary help, guidance and encouragement at every moment. Without his help the work done in thesis is not possible. The help provided by Mr. Krishna Kumar (Krish) during write up of the thesis is especially acknowledged.

I express my special thanks to my lovely friends, who helped lighten the burden, especially to *Dr. D. K. Tyagi, Dr. Anurag Gaur, Dr. Manoj Kumar, Vishal, Subhash, Yogesh, Kuldeep rana, Vijay (Mota bhai), Dr. Pundeer, Dr. Neer, Dr. Tiwari, Deepak (Tinnu), Nagesh, Nigmanand ojha, Dr. Parminder, Dr. Ajay Kumar, Dr. Amrish, Dr. Sandeep, Dr. Nitin, Dr. Sapan, Dr. Aman Pal, Dr. Nirpendra, P. K. R. Gautam, Ritesh, Pankaj, Nitil, Anuj, Yogendra, Rahul, Uday Prabhat, Vimlesh, Kuldeep, Deepsikha, Dr. Ritu Sharma, Radhey, R. B. S. yadav, Rajiv Rana, Ankit, Raghu, Yashpal, Sonu Dhiman, Dikku, Anil Boyal, Rajiv, Najim, Varun* who always motivated and encourage me at every moment and keep me always cheerful and happy. I enjoyed a lot with their company especially during tea times, short trips at Haridwar and made my stay really memorable in I.I.T. Roorkee. I can't forget the company of my dear friend Raj Kumar chauhan, Gulab, Vikash, Pramod, Perminder.

The ever enthusiastic help of my family members specially my beloved elder brother Shri S. P. Dhiman & N. K. Dhiman, who were distant to me but were always by his side whenever the need so arrived and accompany for me to work peacefully during the study period. I am in dearth of proper words to express my abounding feelings and affection for my Lovely Jiju S. P. Dhiman & my Sister Sunita Dhiman. I am also thankful to my lovely and cute nephews and nieces Manju, Meenu, Sonia, Saurabh, Himanshu, Rinjhun, Happy, and shakshi, who encouraged me to do more work. I also wishes to register thank to my sister in law Sadhna dhiman & Pravesh Dhiman , who made her surrounding vivacious enough to ensconce perfectly.

Finally I express my heartfelt gratitude to my highly respectable and adorable father, Mr. Bishamber Singh and mother, Mrs. Bala Devi for their unconditional love, encouragement and blessings. Words can never express my feelings for them. They have been a guiding force all his life and I tried to measure up to their expectations. The author humbly dedicates this work to them.

At last thanks to the almighty god who has given the author spiritual support and courage to carry out this work.

I.I.T. Roorkee (Ramesh Chand)

July, 2009

CONTENTS

LIST OF FIGURES

LIST OF TABLES

CHAPTER 1

INTRODUCTION

The ionosphere is a very important part of the earth's atmosphere because our society depends on the technological systems many of which can be affected by the ionospheric phenomena. The understanding, monitoring and forecasting changes in the ionosphere are of crucial importance to communication, navigation and the exploration of the near earth space. Thus the study of the ionosphere and it's interaction with the processes below and above it becomes significant in the present day scenario.

The ionosphere serves us as an effective mirror for reflecting shortwave radio signals. Radio communication is not possible without ionosphere. It is primarily responsible for generating magnetotelluric current sources on the earth. The weather disturbances like thunderstorms change the ion-electron production rate and hence change the ionospheric temperature and density. The thunderstorms are the main source of lightning and sprites. Lightning sprites are luminous giant flashes of light above thundercloud in the altitude range from about 10-90 km. The solar radiations can provide several information concerning the earth's crust structure and act as a source of magnetotelluric currents which is used for the purpose of geophysical exploration. The ELF radiation generated during lightning has been used for the study of radio propagation at Schumann resonance frequencies. Further, the solar activity such as solar flares, coronal mass ejection, solar wind, sudden ionospheric disturbances, solar proton events, geomagnetic disturbances etc. also play significant role in changing the ionospheric temperature and ion density. It has also b een examined that the electromagnetic radiations emitted during the seismic activity affect the ionosphere. T he upper ionosphere can be studied with the help of sa tellites, balloons or high flying aircraft. The long range communication capabilities like ship-to-shore communication, trans-oceanic aircraft links, military communication and surveillance systems can be provided with the help of ionosphere through out the world.

1.1 CHARACTERISTICS OF LOWER ATMOSPHERE AND IONOSPHERE

The earth's atmosphere is a cloud of gas and suspended solid particles lying from earth's surface to many thousands of kilometers (km), being up to such a large distance always held by the Earth's gravitational pull. It is usually divided into a large number of regions such as lower atmosphere, middle atmosphere and upper atmosphere, where different physical or chemical processes take place.

Due to the reaction of ions with neutral molecules and attached to water molecules always present in the atmosphere, cluster ions are formed. The cluster ions are relatively stable. Most of the ions of molecular size are called small ions. Large ions are formed after the attachment of small ions with aerosol particles. Small ions are in higher concentration than large ions in the atmosphere apart from for the polluted region. The concentration of small ions is the result of the balance between production and destruction of ions for a given time and place, during steady state condition.

There are positive and negative ions in the lower and middle atmosphere but considerable amount of free electron in the upper atmosphere due to the absorption of short wavelength of solar radiation by atmospheric molecules and atoms. This process is known as photoionization. Thus creation of electrons and ions by this process make atmosphere a good conductor, forming a region called ionosphere. There may be excess of positive or negative charges in the region of ionosphere but in comparison to total charge of each polarity excess is little fraction of it such that the ionosphere can be regarded as neutral. The upper boundary of the ionosphere is known as magnetopause. The charged particles are geomagnetically trapped in the earth's magnetic field lines in the inner part of the ionosphere, forming radiation belts around the earth.

1.1.1 The Earth's Lower Atmosphere

The troposphere is the lowest layer from the Earth's surface up to 10 km containing the neutral atmosphere. The height range of upper limit of troposphere is from 7-18 km depending upon time of year and latitude. The troposphere is the region of strong vertical mixing and heat exchange with the surface of earth. The

molecular Oxygen (O_2) and molecular Nitrogen (N_2) are the predominant gases in this region. All the weather phenomena and our normal day-to-day activities occur in this lower region and it contains 99% of water vapor and 90% of the Earth's atmosphere. The stratosphere extends from about 10 to roughly 50 Km. The temperature increases with height in this layer. The molecular Oxygen (O_2) is dissociated into Oxygen atom at the wavelength below 240 nm of incoming solar radiation in the stratosphere. Then Oxygen atom may combine with an Oxygen molecule (O_2), to form Ozone (O_3). The Ozone gas attains maximum density at an altitude of about 25 km. At high altitude the air becomes rarefied. In stratospheric layer, temperature increases progressively due to the absorption of ultra- violet radiation by Ozone molecules.

The region lying from about 50-80 km above the Earth's surface contains neutral atmosphere and is known as the mesosphere. The composition of the lower and the middle atmosphere is remarkably constant up to 70 km, comprising about 78% Nitrogen, 20% Oxygen and the remainder small quantities of Argon, Carbon Dioxide, water vapour, traces of Helium, Neon, Krypton, Xenon, Methane, and Hydrogen.

The thermosphere extends from 80 km to just about 500 km. There is sharp temperature increase in this region due to the absorption of ultra-violet radiation from sun.

1.1.2 Ionosphere

The region extended from 60-70 km to about 1000 km altitude above the earth's surface having free electrons and ions in large number is known as ionosphere. The ionosphere is formed mainly by the ionization of neutral gas atoms/molecules present in the upper atmosphere by exposure to solar radiation. In the higher region of the atmosphere, above about 80 km, molecular and atomic constituents are ionized by solar ultraviolet radiation and, at high latitudes, by energetic electrons of solar and magnetospheric origin. The free thermal electrons produced by high-energy photoelectron collision with neutral atoms, form more than 90% of the flux in the ionosphere. The ionosphere has the properties of a

plasma state. The collision dominates. Though there is the presence of strong magnetic field, high rate of collision defines the properties of plasma. Because of collision, a particle moving under the influence of magnetic field changes it's trajectory randomly and hence the magnetic field is not able to play any role.

1.1.3 Formation of Ionospheric Layers

The range of solar radiation spectrum is from radio frequencies through infrared radiation and visible light to X-rays. The ultraviolet and shorter wavelengths of solar radiation are considered to be ionizing source. During a collision, photons are able to dislodge an electron from the neutral atom or molecule.

When the solar radiation is incident on a gas atom or molecule, a part of this radiation is absorbed by the atoms which result in the production of a free electron and a positively charged ion pairs (Figure 1.1). Solar wind and Cosmic rays also play a role in this process but in comparison to Sun's radiation their effect is very small. In the Earth's outer atmosphere solar radiation is strong but ionization is very small due to low density. Figure 1.2 shows the ionospheric height structure and the main source of ionization for every layer of the ionosphere. Ionization increases with decreasing altitude as more gas atoms are present at low altitude. An opposite recombination process take place at the same instant at which a moving free electron is captured by a nearby positive ion. The recombination process accelerates at lower altitude because the ions and gas molecules are closer together. The degree of ionization is determined by balance between ionization and recombination at any given time. In the further lower altitude there are more opportunity for the absorption of photon energy from the solar radiation because number of gas atom and molecules increase with decreasing altitude. However, the intensity of solar radiation becomes smaller at such lower altitude because at higher altitude a significant part of it was absorbed. A point reaches where greater gas density, lower radiation and greater recombination rates balance out and the decrease of ionization starts with decreasing altitude. Thus the changes in atmospheric composition with height lead

to changes in ion production rate which causes the formation of several distinct ionization peaks known as D, E, F1, F2 layers.

The D layer is the region from about 65-90 km above the earth's surface. In this layer nitric oxide (NO) is ionized giving out Lyman alpha radiation at a wavelength of 121.5 nanometer (nm). In the condition of active sun with 50 or more sunspot numbers, the air (N_2, O_2) is ionized by hard X-rays with the wavelength less than 1 nm. The ionization is also produced by cosmic rays during night times. The net ionization effect is very less in D-layer due to high recombination rate. In this region collision frequency between electrons and neutral particles is around 10 million collisions per second during day time. D layer is mostly responsible for the absorption of HF radio waves, particularly at 10 MHz and below and smaller absorption at the higher frequencies. The absorption is highest during mid day and small in the night. After the sunset, D layer is greatly absent.

The middle layer extended from 90-120 km above the surface of earth is known as E layer. In E layer molecular oxygen (O_2) is ionized with soft X-ray (1-10 nm) and far ultraviolet solar radiation. Radio waves covering frequencies less than about 10 MHz can only be reflected from this layer. The frequencies above 10 MHz suffer partial absorption in this layer.

The top layer of the ionosphere extending from 120 km to about 1000 km above the earth's surface is recognized as F layer. In this layer extreme ultraviolet solar radiation (10-100 nm) is the ionization source for the present atomic oxygen. Only one layer exist in F region in the night time while during day time it splits into two layers, labeled as F1 and F2 (Figure 1.3).

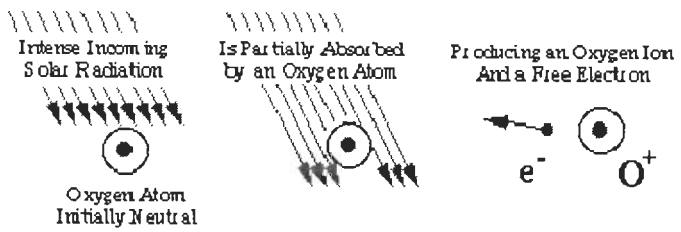

Figure 1.1 Production of electron and ion due to solar radiation.

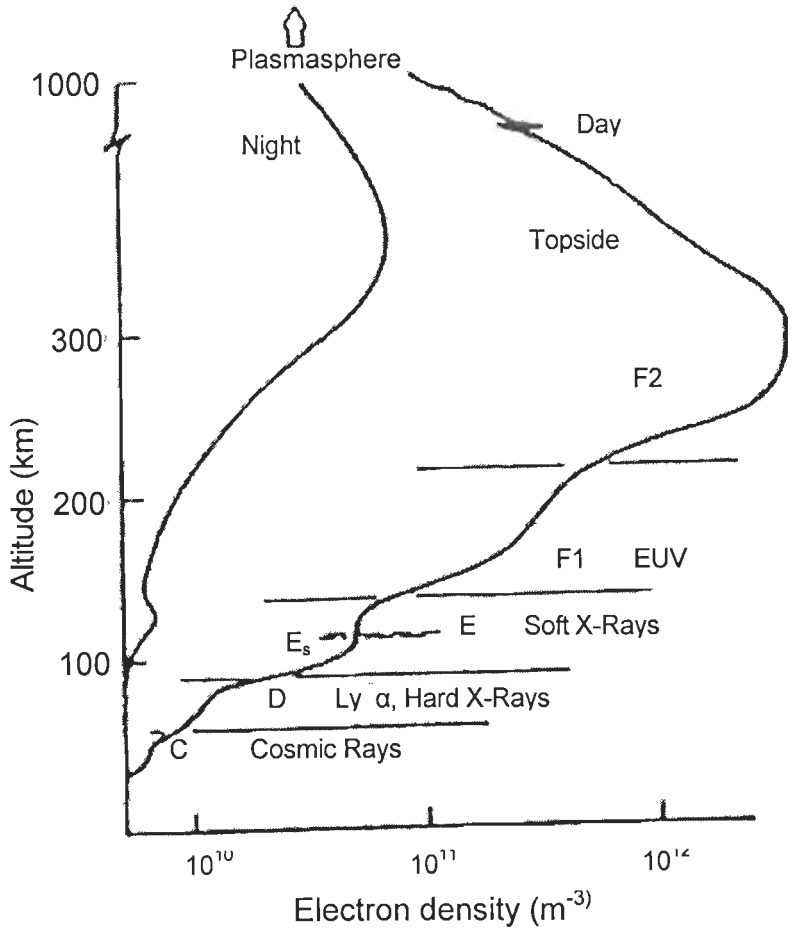

Figure 1.2 **Ionosphere structure on a summer day and night in middle latitude and the main ionization region (after Davies, 1990).**

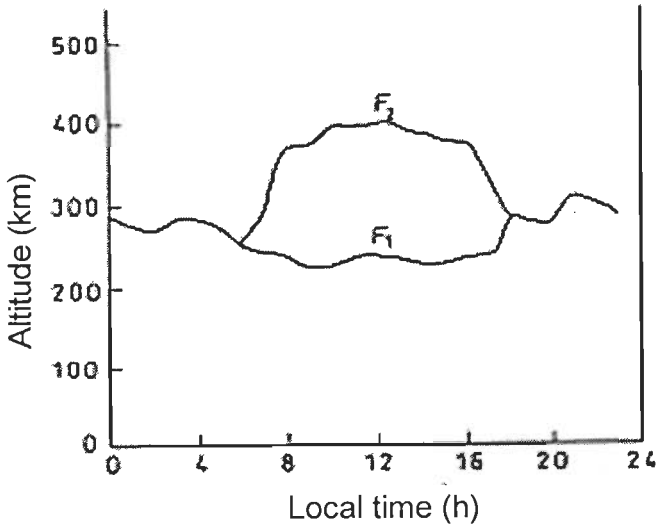

Figure 1.3 **The day time splitting of F region into F1 and F2 at Canberra (Mitra, 1992).**

1.1.4 Ionospheric Temperature Profile

Solar ultraviolet radiation and X-rays are the main source of heating the ionosphere. Earthquakes, volcanic eruptions, lightning/sprites and thunderstorms also contribute to the ionospheric heating. The high energy photoelectrons are created in the process of photo-ionization. The collision of these photoelectrons with neutral atoms and molecules increases their internal energy. Depending upon the solar activity the ionospheric temperature ranges from 500 ^{0}K to as much as 2000 ^{0}K as shown in Figure (1.4). The temperature profile is variable with space and time.

1.1.5 Ionospheric Density Profile

In the upper atmosphere both neutral and ion composition depend to a large extent upon direct perturbation of the region by solar corpuscles. The mean free path of particles increases rapidly on increasing the height. In the upper ionosphere the free electrons created by Sun's ionizing radiation has much longer life time than produced from various sources at lower levels. The ionospheric electron density varies significantly with latitude, altitude, solar activity, time of day and other local factors. The diurnal variation in solar radiation causes the primary variation of electron density. Most of the free electrons in the atmosphere are located above 60 km. A vertical profile of total particle density along with free electron density is shown (Figure 1.5).

The concentration of free electrons increases monotonically with height from very small values at less than 60 km to a maximum value at about 300 km. Due to collisions between electrons and neutral particles, strong absorption of radio waves occur in D layer. Most of the electrons in the D and E regions recombine with positive ions during night. So the absorption of radio waves is reduced due to virtual disappearance of D layer. Electron density also varies with the events which occur in sun that modify the X-rays, reaching the ionosphere. Ionospheric density and structure varies with geographic location, season, time of day, sunspot number etc. As electron density increases in D region during day side of the earth with strong solar flares accompanied by X-ray burst. During the

day time charged particle number density varies from 10^2 to 10^4 cm^{-3} in D layer while at night time this layer disappears because of recombination process. Positive and negative ions of NO, O and O_2 are the dominant constituents. The electron number density is of the order of 10^5 cm^{-3} during day time while it is approximately 10^4 cm^{-3} during night times in E layer. O_2^+ and NO^+ are the main ions in E layer. The main ionized components in F layer are N_2, O, and a lesser extent O_2. The maximum electron number density in F1 layer in the altitude range of 170-250 km is around 10^5 cm^{-3}. The F1 region also disappears due to recombination process during night times. The electron number density varies from 10^5-10^6 cm^{-3} in F2 layer. The maximum electron number density is at about 300 km in the F2 layer. In the F region O^+ is the dominant positive ion.

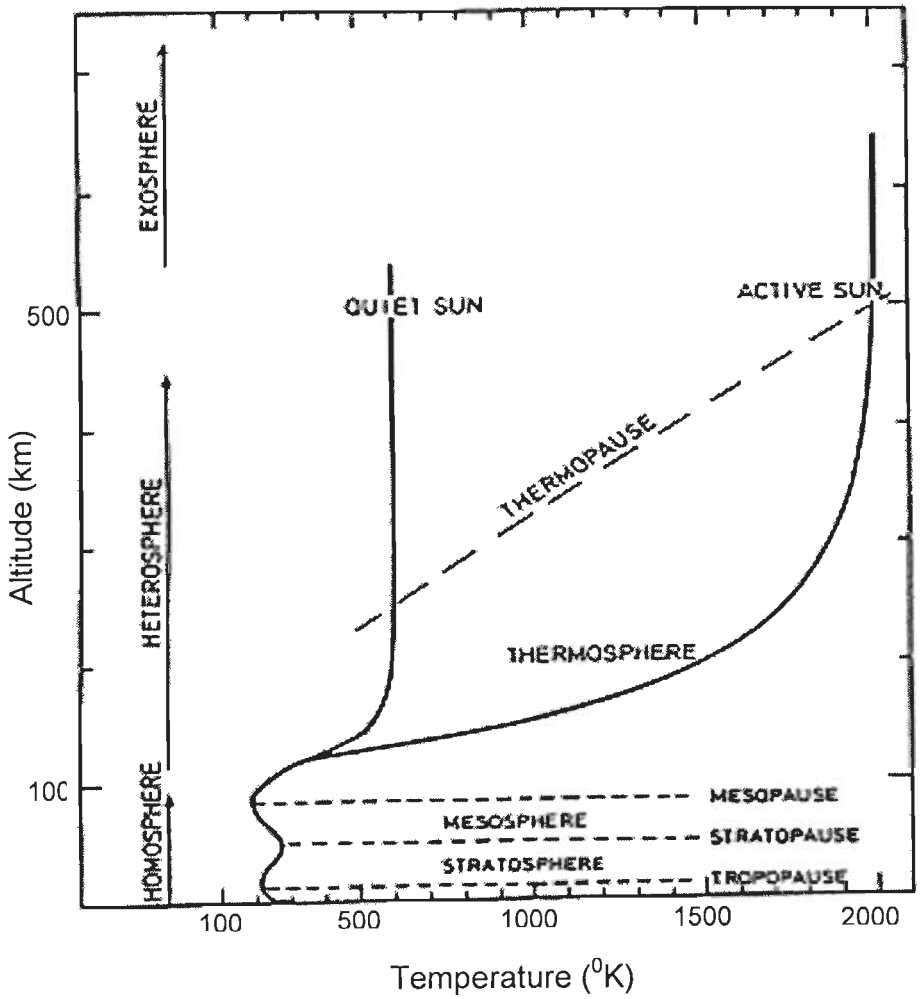

Figure 1.4 Vertical temperature distributions in the earth's atmosphere with emphasis on the thermosphere (Banks and Kockarts, 1973).

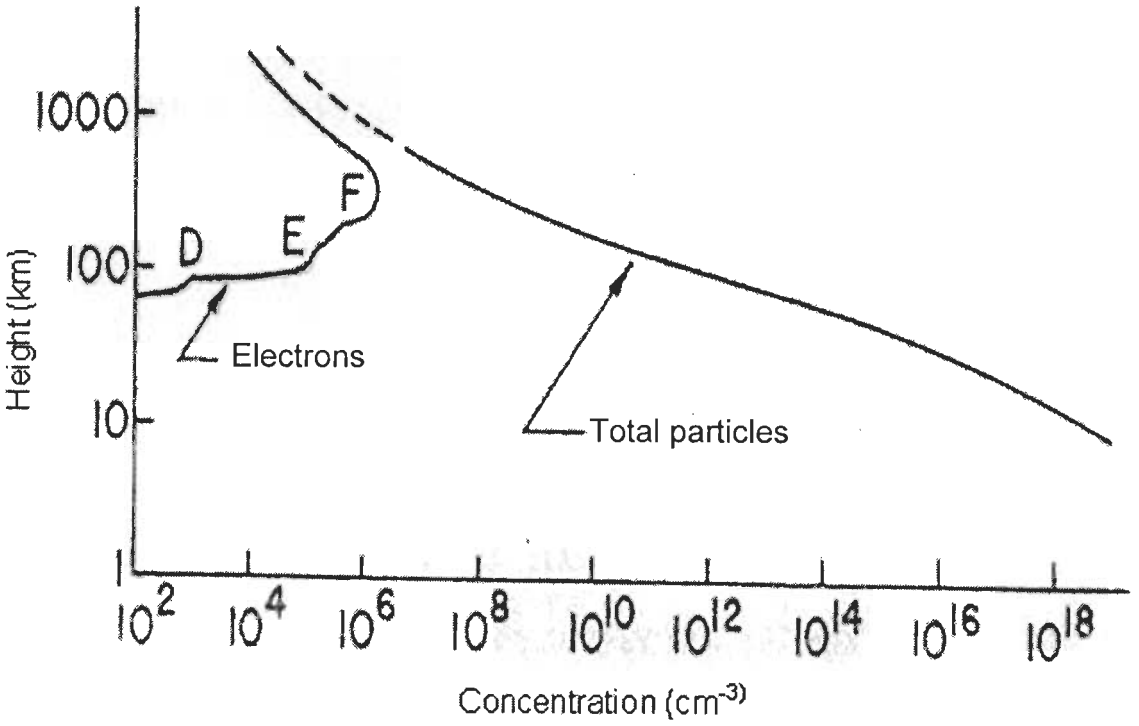

Figure 1.5 Total particle density and number density of electrons as a function of height (after Fleagle, R. G., and Businger, J. A., 1963).

1.1.6 Ion Sources in the Atmosphere

Ions are created by different sources in the earth's atmosphere. The main sources of ionization in the lower atmosphere are radiation created by the decay of radioactive substances in the soil as uranium and thorium, and gas radon in the air and the cosmic rays. Free electron and positive ions are created as the result of ionization of molecules. The radioactive emanation from the earth's crust and airborne radioactive substances are the dominate sources of ionization from earth's surface to about 3 km altitude. Galactic cosmic rays (GCR) and solar cosmic rays (SCR) are the main sources of ionization below around 65 km while electromagnetic radiation from the sun is the major source of ionization above around 65 km.

1.1.7 Cosmic Rays as Sources of Ion Generation

The cosmic rays are the charged particles from the space either of galactic (GCR) or solar (SCR) origin. Primary cosmic ray particles arriving from outer space consist mainly of protons (99%). The rate of ionization illustrates large variation with time wherever the ionization source is solar cosmic rays due to varying solar activity. The intensity of galactic cosmic ray is almost distributed isotropically in the earth's vicinity (Herman and Goldberg, 1978) and is modulated over a solar cycle (Rosenberg and Lanzerotti, 1979). In the lower atmosphere, galactic cosmic ray activity varies by about a factor of 2 between the equator and pole (Hays and Roble, 1979). GCR penetrates deep into the earth's atmosphere due to their high energy range from tens of MeV to hundreds of GeV. The solar flare and coronal hole enhance the SCR (Munro and Withbroe, 1972).

1.2 IRREGULARITIES IN THE IONOSPHERE

Ionospheric irregularities are the most actual and complex phenomena in modern ionospheric physics. It is impossible to determine the main cause of these effects. Earthquake also generates irregularities in the ionospheric parameters. Largest temporal scale of ionospheric variability is connected with solar activity. Sudden ionospheric disturbance, solar proton event, solar wind, geomagnetic storm, solar flare, earthquake are among the phenomena that create irregularities in the ionosphere.

1.2.1 Sudden Ionospheric Disturbance

When a solar flare is observed suddenly on the sun, accompanied by an increase in ultraviolet and X-radiation, it increases ionization in the ionosphere at the same time. Electron content in D or lower E region increases during sudden ionospheric disturbances. These released electrons increase absorption rapidly, causing a High Frequency (3-30 MHz) radio blackout. Very Low Frequency (3-30 kHz) signals are reflected by the D layer instead of the E layer, where the absorption of the waves is enlarged by the increased density. It is associated with abnormal occurrences on the sun. It's effects are most noticeable in the D region,

and takes about 20 to 90 minutes in the recovery to the normal stage. This phenomenon is noticed only in sunlit hemisphere.

1.2.2 Ionospheric Precursors of Earthquake

The study of ionospheric response prior to earthquake is a tough task. Some ionospheric precursors related to earthquakes are temperature, density, some optical phenomena, critical frequency, electromagnetic and plasma phenomena. Air glow emissions are caused by the atmospheric species excited directly or indirectly by the sun's electromagnetic radiation. The emission layer of atomic oxygen 557.7 nm (green line) is situated at an altitude of about 85-100 km that corresponds to the ionospheric E layer. And the emission line at 630.0 nm (red line) is situated at an altitude of 200-300 km, related to the ionospheric F layer. The night time data of earthquake period can be used for the study related to air glow because this emission is mainly confined to night time. The heating of ionospheric F region was also attributed to the seismic activity.

Mukherjee (1999) studied the earthquake signatures in the emission of atomic oxygen at 557.7 nm and at 630.0 nm. He concluded that several days before an earthquake the anomalous intensity enhancement in 557.7 nm took place compared to the background emission. Two days before the earthquake the increase in sporadic E layer occurred. However, at 630.0 nm the intensity decreased one day before the earthquake. But the ionospheric plasma temperature in height range from 200-300 km was found to increase by 350 ^{0}K. He suggested that the gravity waves are generated due to seismic-gravity oscillations just before the earthquake, which increases in amplitude due to upward propagation and can cause the increase in emission intensity of 557.7 nm lines.

1.3 THUNDERSTORMS/LIGHTNING INDUCED ELECTROMAGNETIC FIELDS

The main sources of lightning discharges are different atmospheric processes like volcanic eruptions, dust storms, snowstorms, and thunderclouds. However, thundercloud is the most common source of lightning. The atmospheric pressure decreases with altitude constantly. An air parcel expands and cools

adiabatically on rising upwards. The atmosphere becomes unstable when the atmospheric lapse rate exceeds the adiabatic lapse rate. On rising further the air parcel gets buoyancy. The moist content condenses into drops and ice crystals, releasing latent heat which provides further buoyancy to the air parcel. A cloud is a suspension of very small water droplets or snow crystals in a region of atmospheric air.

The occurrence of thunderstorms is high in tropics and temperate zones but rare in polar regions. The solar heating and convection are maximum in mid afternoon over the earth surface, therefore the frequency of thunderstorms is maximum at these times. However, they can occur at any time during day and night. The thunderstorms and lightning are more active over the earth surface than over the oceans. Thunderclouds do not often produce lightning until they grow to a height of about 3 km whereas average thunderstorms are of the order of 10 km in altitude.

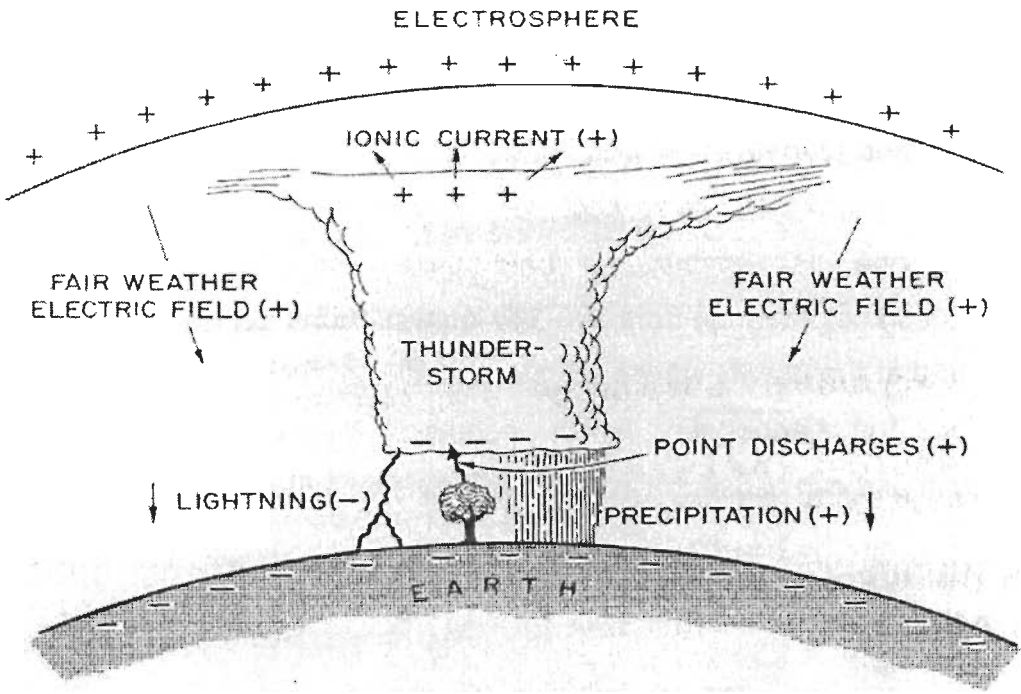

Figure 1.6 Schematic of the global electrical circuit. The positive and negative signs in parentheses indicate the signs of the charges transported in the direction of the arrows.

An electric dipole is main charge structure of the thundercloud. The upper part of the thundercloud carries a net positive charge, while the lower part carries a net negative charge and a small pocket of positive charge (Simpson and Scrase, 1937; Pathak et al., 1980). The diameter of the charged regions of the dipole is of the order of a few km. Agarwal et al. (1995) reported that average value of electric field over Indian subcontinent at ground surface is about 110 Vm^{-1}. A Schematic of the complete global electrical circuit is shown in Figure 1.6.

1.3.1 Types of Lightning Discharge

The lightning is generally defined as a high current electric discharge. The luminous channel of lightning discharge has the lengths of the order of a few km. If the discharge takes place between positive and negative charge centers of the cloud, it is known as the intracloud (IC) discharge and in case of discharge between lower charge center of the cloud and the ground, it is termed as cloud to ground (CG) discharge. The IC discharges are the most frequent in nature, mainly in the tropical regions. The phenomena of ground discharges is well studied (Wang, 1963; Mackerras, 1968; Rai, 1974; Krehbiel et al., 1979, Hazarika et al., 1987, Soriano et al., 2005; Baba and Rakov, 2008; Rakov and Uman, 1990).

1.3.1.1 Cloud to Ground Lightning Discharge

In the lightning between cloud and ground, the C-G discharge consists of one or more intermitted partial discharges, whose time duration is of the order of 0.2 sec and is called a flash. A flash consists of several components with duration tenths of a millisecond known as stroke. The stroke per flash varies from cloud to cloud distance and with geographical location of the cloud. In tropical region, there are three or four strokes per flash (Rai and Varshneya, 1982) but it can be as high as 32 strokes per flash at high latitudes (Uman, 1969). The successive strokes are found separated from each other on the average of 40 msec.

A cloud to ground lightning begins with a faintly luminous predischarge, the leader process, which create a negatively charged and ionized path between cloud and ground for the return stroke. The leader discharge preceding the first return

stroke in a flash is called stepped leader due to it's travel downward in steps. The length of each step lies on the average of about 50 m and a time pause between steps is in the order of 50 μs. The average velocity of stepped leader during its trip to the ground is 2 x 10^5 m/sec. During stepped leader process a few coulomb (about 5 to 10 C) charge is transferred along the channel and an average current of about 100 A flows through it.

The stepped leader channel moving down ward carries the potential to the ground. When the stepped leader reaches very close to ground at an altitude of about 10 to 20 meter, the air between it's tip and the ground breaks up. A highly luminous fast moving discharge is initiated towards cloud by this breakdown which is known as return stroke. The velocity of return stroke varies from one third to one tenth of the speed of light (Weidman and Krider, 1980; Idone and Orville, 1982). It takes about 100 μs to reach the top of the channel. A high current (of the order of around 30 kA) flows through the channel during return stroke and the temperature of the channel is around 4000 ^{0}K. The return stroke leaves behind an ionized medium between cloud and ground. After a time pause of about 40 ms of return stroke, the cloud develops sufficient potential to initiate another discharge. The new predischarge now propagates downward continuously (without stepping) and initiates further a new fast moving highly luminous discharge moving upward known as subsequent return stroke. The predischarge preceding the subsequent return stroke is known as dart leader. A complete picture of the cloud to ground lightning is given in Figure 1.7.

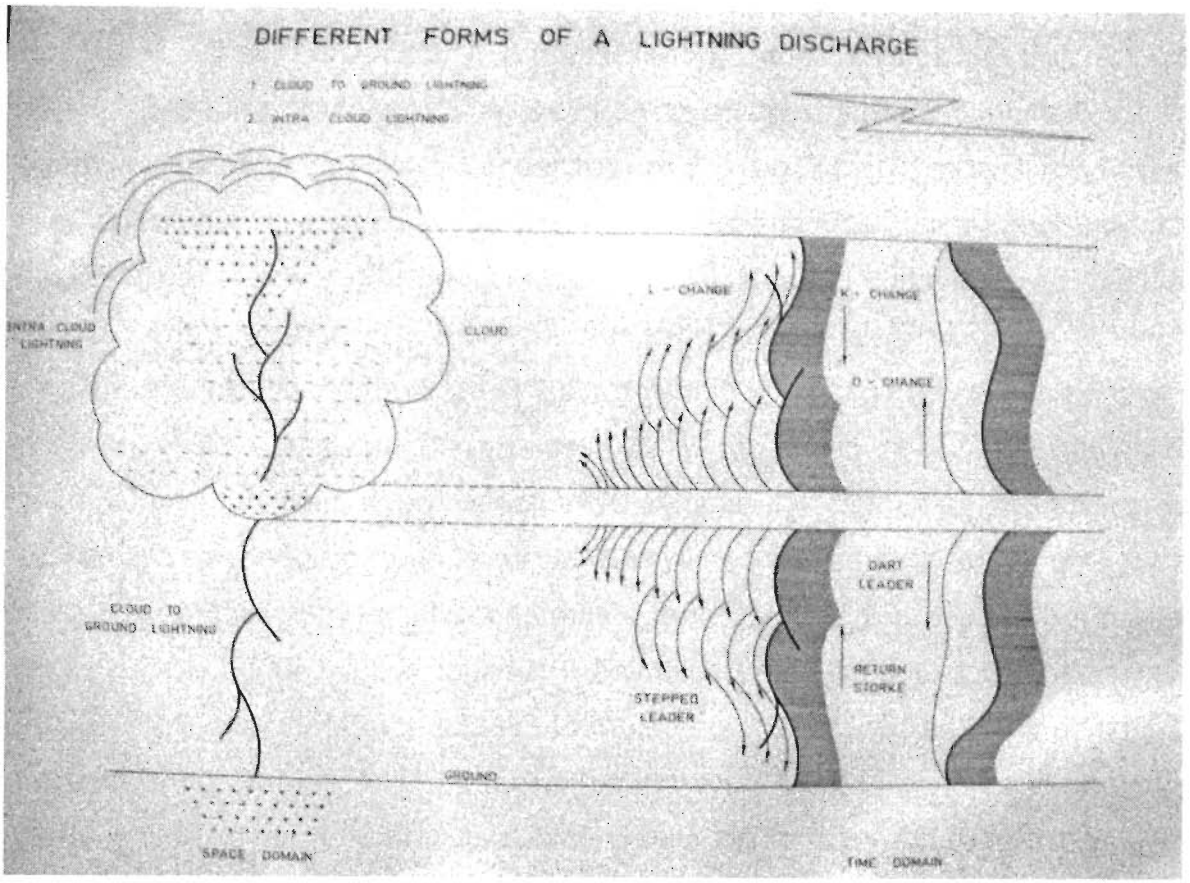

Figure 1.7 Different forms of lightning discharge

1.3.1.2 Cloud to Ionosphere Lightning Discharge

A phenomena known as cloud to ionosphere lightning (lightning sprites or sprites) has been observed recently. Lightning sprites are luminous giant flashes of light above thundercloud in the altitude range from 10-90 km. These are coincident with intracloud or cloud-to-ground lightning discharges (Fishman et al., 1994; Bell et al., 1995; Otsuyama et al., 1999 etc.). The colour of these sprites is red, therefore known as red sprite. The study of sprites by aircrafts shows the heating effect in D region, influences on electric field and conductivity structure in the stratosphere and mesosphere. There is brightest region in the altitude range from 65-75 km, but above this a faint red glow structure extending to around 90 km (Bell et al., 1995; Otsuyama et al., 1999)., Blue tendril-like filamentary structures frequently extend down to as low as 40 km below the bright red region. Sprites generally occur in clusters of two, three or more (Wescott et al., 1995).

1.3.1.3 Intracloud Lightning Discharge

The cloud discharges take place more frequently than ground discharge. Intracloud lightning discharge occurs between the two main opposite charge centre. A huge amount of current flow in intracloud discharge. A cloud discharge is initiated by a negative streamer moving upward from the lower N region to the upper P region or by a positive streamer moving downwards from the upper P region to the lower N region. Kumar (1995) found that similar cloud to ground lightning, intracloud discharge is initiated by an upward moving stepped predischarge (L-changes). L change is followed by a highly luminous main discharge (K- discharge) propagating downwards from the upper positive charge centre to the base of the cloud. After some time, another predischarge moves in the same flash without stepping known as D-change. The D-change starts another K-change from the positive charge centre of the cloud. In many cases, the return stroke after entering into cloud becomes horizontal. Thus the horizontal lightning takes place near the base of the cloud. Pathak et al. (1980) have shown that K-change is strong source of Ultra High Frequency (UHF) whereas the horizontal lightning is a strong source of Very Low Frequency (VLF) emission.

1.3.2 Characteristics of Lightning Induced Electromagnetic Fields

The lightning discharge is a wide band transmitter of electromagnetic (EM) waves. The EM radiation generated by lightning discharge propagates in all directions. The lightning radiation ranges from low radio frequencies of a few hertz to gigahertz and from the optical to the X-ray regions of the spectrum. A lot of study has been done experimentally as well as theoretically in different frequency ranges of EM radiation from lightning viz. ELF, VLF and UHF (Dennis and Pierce, 1964; Rai et al., 1972, 74; Weidman et al., 1981; Rai and Varshneya, 1982; Rinnert et al., 1985; Uman, 1985; Barr, 1987; Gomes, et al., 2004; Hayakawa et al., 2008). However, most of the experimental studies are related to ELF and VLF regions because signal strength is sufficiently large in these frequencies range. Several acoustic, electrical, and optical measurements by different workers (Uman, 1969; Hill, 1979; etc.) have found that most of the energy of a lightning

stroke is dissipated in producing thunder (about 80-90%) whereas only 0.04% of the lightning energy is utilized in generating electromagnetic radiations. The rest of the energy is used in the dissociation, ionization, excitation and kinetic heating for the atmospheric particles. The ELF and VLF radiations can provide several information concerning the earth crust structure and acts as a source of magnetotelluric method for the purpose of geophysical exploration.

The prevailing source of atmospherics in the VLF range is return stroke. The horizontal lightning and K-changes also emit the EM radiations in this frequency rage (Rao, 1967). The emission of the ELF component in atmospherics is known to occur due to lateral corona current flowing laterally between the leader channel and return stroke (Rao, 1967). Rai et al. (1972) and Rai (1978) observed bremsstrahlung due to acceleration or deceleration of an electron in its hyperbolic orbit around the ion or atom due to coulomb field interaction in the lightning channel. They also showed that stepped leaders, K- changes and dart leaders being partially ionized channels are the strongest sources of UHF radiation and radiation from fully ionized return strokes are negligibly small in this region.

The emissions of VLF radiation from lightning have been studied by many workers (Divya and Rai, 1985; Cooray, 1992; Jacobson et al., 2000; and others). Divya and Rai (1985) considered the earth to be finitely conducting. They obtained both horizontal and vertical component of VLF electric field components. They also measured the electrical conductivity of the ground by measuring horizontal and vertical field components of atmospherics.

1.3.3 Application of Lightning Induced Electromagnetic Fields

Since lightning induced EM radiation propagates to large distances in earth-ionosphere cavity, the propagation characteristics of these waves like attenuation, group delay time between two frequencies etc are used for determining the location of thunderstorm activity. Divya and Rai (1986) from their experimental observations found that the ratio of parallel to perpendicular electric field components of lightning depends only upon the ground conductivity. Therefore ground conductivity information can be acquired on measuring these electric field

components that is useful for ground water detection and geophysical exploration.

The studies of whistlers have been found more suitable in predicting the electron number density, temperature variation, plasma drift velocity and wave particle interaction in the upper atmosphere (Carpenter et al., 1972; Hayakawa and Ohtsu, 1973; Thomson and Dowden, 1977; Hayakawa et al., 1981). In the study of photographic and spectroscopic, visible radiation is utilized (Boys, 1929; Uman and Orville, 1965; Orville et al., 1978; Guo and Krider, 1982) while radiation in the ELF and VLF regions can be used as a dominant source in understanding the propagation characteristics of these waves. The ELF and VLF radiation can be used for the study of long range communication, navigation systems, and the characteristics of the waveguide between earth and ionosphere.

1.3.4 Propagation in the Earth-Ionosphere Cavity

The cavity between earth and ionospheric lower boundaries acts as a parallel plate waveguide for very low frequencies. The lightning flash excites a number of quasi linear waveguide modes that propagates between the earth ionosphere waveguide. The VLF waves propagate in the lower boundary of ionosphere and the earth. These modes can be excited with either the transverse magnetic (TM) or transverse electric (TE) fields to the direction of propagation. Poor excitation was found in TE modes due to ground acting as an electrical conductor (Pappert and Bickel, 1970). For large distance propagation of VLF waves in the earth ionosphere waveguide TM modes are generally more important in spherics studies.

The ELF and VLF waves propagate to large distances before the field decays below the noise level. The propagation characteristics of these waves are influenced by finite conductivity of the earth and ionosphere (Wait, 1970). The propagation characteristics are mainly affected by the ionosphere because properties of earth surface do not change significantly with time. The height of ionospheric lower boundary is 70 km during day time, and it reaches to 90 km during night time. The electron density increases due to solar flare in D-layers

within time interval of 5-10 minutes. The flares last for about 1 hour prior to restoring normal conditions (Whitten and Poppoff, 1971).

In whistler mode propagation, EM waves (VLF radiation) penetrate the ionosphere and propagate essentially along the geomagnetic field lines. Davis and Rosa (1969) have shown that collisions in the lower ionosphere are essential for the electromagnetic wave generated in the ionosphere to couple to whistler mode. Some of EM energy is transmitted through ionosphere and propagate in whistler mode produced by lightning discharges.

1.3.5 The Propagation of ELF Waves and the Schumann Resonances

Schumann (1952) predicted extremely low frequency (ELF) resonance in the earth-ionospheric waveguide. The resonance occurs between the electromagnetic wave generated by lightening and thunderstorm, traveling along ground surface and the lower ionosphere. Schumann resonance (SR) is a set of spectral peaks in the extremely low frequency (ELF) region of the earth's electromagnetic field spectrum. SR is global electromagnetic resonance phenomena excited by lightning discharges. Assuming the perfectly conducting earth and ionospheric boundaries, different mode resonance frequencies are 10.6, 18.4, 26.0, 35.5 and 41.1 Hz. But ionosphere is not perfectly conducting medium and energy losses due to its finite conductivity reduces the resonance frequencies to 7.8, 14.1, 20.3, 26.3 and 32.5 Hz (Madden and Thomson, 1965). Schumann resonance frequency variations can be used to determine average conductivity profile of the ionosphere (Tran and Polk, 1979a, b) and also for tracking global lightning activity. Schumann resonance is possibly suitable as a sensitive thermometer for global temperature changes. Tulunay et al. (2008) suggested that the characteristics of SR may be important in aerospace and marine applications, atmospheric studies, as precursors in earthquake prediction etc. For example, for the communication between the submarines and the aircraft, the ELF band is employed due to their longer wavelengths. Penetration of electric and magnetic field components of the Schumann resonances into the ionosphere was numerically investigated by Grimalsky et al. (2005). Fullekrug and Smith (1997)

found that the mean seasonal variations of continental lightning in mid- and tropical latitudes are related to surface temperature variations in moderate- and tropical rain forest climates. Hayakawa et al. (2008a) found very anomalous effects in the Schumann resonance associated with two large earthquakes. Anomalous Schumann resonance signals appeared from about one week to a few days before the main shock.

1.3.6 Earthquake Induced Electromagnetic Fields

The emission and propagation of electromagnetic radiations in a wide frequency band, covering ULF, ELF and VLF from epicenter in earthquake region were reported by several workers (Gokhberg et al., 1982, 1984; Parrot, 1994, 1995; Hayakawa et al., 1996 a, b, 2000; Koshevaya et al., 1997; Shalimov and Gokhberg, 1998; Kushwah et al., 2005). These waves may create localized joule heating in the ionosphere. DC-ULF electromagnetic signals have a precursory time from few days to several weeks (Hayakawa, et al., 2000), whereas this time is much shorter (from a few hours to several hours) for VLF to VHF signals (Gokhberg et al., 1982; Eftaxis et al., 2001). The ULF waves from earthquakes have been observed in the ionosphere and Magnetosphere through satellite observations and designated as precursors of earthquake (Parrot, 1994). ULF emission can penetrate the crust and propagate through the ionosphere and Magnetosphere (Molchanov et al., 1995). The generation mechanism of low frequency electromagnetic emission during earthquake is related to fracturing process (Molchanov and Hayakawa, 1995; Freund et al., 2006). Hayakawa et al. (1996b) has reported the pioneer work on the emission of VLF subionospheric signal as precursory signatures of the effect of the Kobe earthquake. Recently a decent review of electromagnetic phenomena associated with earthquake was also presented by Hayakawa (2004).

1.4 SOME PHENOMENA AFFECTING THE EM PROPAGATION

1.4.1 Solar Wind

The hot solar corona is the source of the solar wind. The sun's gravity cannot hold on to it due to high temperature of corona so that coronal gas flows out in significant amount. This result in a steady stream flow of solar material recognized as the 'Solar Wind'. The solar wind is an irregular stream of ionized particles emanating outward from the sun with velocities of the order of about 400 km/s. It is always directed away from the sun with changing speed and carries charged particles through it. All the light and heavy particles move with equal velocity. Since the solar wind is highly conductive plasma, the solar magnetic field is frozen in it and magnetic field lines are dragged by the solar plasma flow. The magnetic field of earth is compressed in the sunward direction and stretched out in the anti-solar direction, creating a long magnetotail. This interaction creates the magnetosphere as a complex magnetic cavity around earth (Russell, 1972; Kivelson and Russell, 1995).

The solar wind interacts with the geomagnetic field lines and gives rise to micro-pulsations, geomagnetic storms and cause many other phenomena. The micro-pulsations penetrate into the earth's crust and generate magnetotelluric currents. The resistivity distribution with depth can be determined on measuring electric and magnetic field components on the earth's surface with the help of the magnetotelluric current. This tool is known as the magnetotelluric method of geoexploration. The enhanced flux of high-energy particles emanating from the sun in the solar wind gives rise to Auroras. The disturbances transmitted by solar wind generally require several days to reach on earth.

1.4.2 Solar Flares

Flares are intense bursts of radiation and high energy particles emanating from the sun's atmosphere within the active region. Carrington (1860) observed that a flare occurs when magnetic energy built up in the solar atmosphere is suddenly released. On releasing this energy, a large number of particles (electrons, protons and heavy nuclei) are heated and accelerated in the solar

atmosphere (Anastasiadis, 1999; Kudryashev and Avakyan, 2000). The released energy during solar flare is used in intense heating, particle acceleration and in mass flows (Priest, 1992).

The flare is generally invisible under ordinary conditions. The brightness of the flare region is increased nearly tenfold in Hα light. A large flare expands over a hundred million to a billion square miles of the disk within minutes. Intense flares have bright filaments structure of the order of 10^4-10^5 km in size while small flares have bright circular patches. Flares are classified according to its X-ray emission in the band 1-8 Å in emission classes B (with peak < 10^{-6} Wm^{-2}), C (peak between 10^{-6} and 10^{-5} Wm^{-2}), M (with peak between 10^{-5} and 10^{-4} Wm^{-2}) and X (with peak > 10^{-4} Wm^{-2}). The electromagnetic spectrum from flares extend from gamma rays and X-rays through visible light out to the kilometric radio waves. The enhanced X-ray and extreme ultraviolet (EUV) solar radiations during a flare enhance ionospheric ionization, effecting radio-propagation and telecommunication systems (Svestka, 1976; Sturrock, 1980).

Solar flare last from a few minutes to few hours (Herman and Goldberg, 1978). Relativistic electrons and protons with high energy (10-200 MeV) are emitted from active spot group along with solar flares and polar cap absorption is produced in the polar cap region of the earth's atmosphere (Reid and Collins, 1959). The effect of solar flare occurrence on potential gradient, air-earth current density and thundercloud activity has been studied by many workers (Cobb, 1967; Reiter, 1972; Yan and Zhang, 1992). Holzworth and Mozer (1979) found that the electric field and air-earth current density started to increase shortly after the flare. A typical flare lasts on the order of an hour. The magnetic energy of 10^{29} to 10^{33} ergs is released by means of magnetic reconnection during solar flare (Anastasiadis, 1999). The biggest flare ever recorded in X-rays measurements by GOES is classified as X28 type flare. The effects of solar flares on the ionospheric F region are also manifested as a sudden increase of Total Electron Content by Afraimovich, et al. (2002).

1.4.3 Geomagnetic Disturbances

A geomagnetic storm is temporary intense disturbance of the earth's magnetosphere. Geomagnetic storms are most important phenomenon related to high-energy particles and solar wind. They produce large and global disturbances in the ionosphere, but they affect also the neutral atmosphere, including the troposphere and middle atmosphere (Lastovicka 1996, 1997). A large amount of energy is deposited into thermosphere during such disturbances at high latitudes. This leads to the increase of neutral gas temperature *T* and variations of the neutral composition. The electron concentration in the high-latitude ionosphere decreases by these factors. In the ionospheric *F2* region, geomagnetic storm changes neutral atmospheric composition. Such a neutral atmospheric effect becomes less important at lower heights due to shorter electron lifetime. A large increase of energetic particle precipitation increases the electron density in lower ionosphere, mainly at night. Some effects of enhanced particle precipitation have been found in the neutral lower thermosphere and mesosphere; but these effects weaken with decreasing altitude. Geomagnetic storms and fluctuations in the ionosphere can be particularly damaging to satellite as well as ground based systems. The increased ionospheric current during such events can induce voltages up to or the ground that are large enough to cause transformer failures and blackouts. The entire Hydro-Qubec power system collapsed leaving millions of people without electricity for many hours (Schunk and Sojka, 1996).

The intensity of magnetic storm varies with time and geographical location. Increase in geomagnetic field called the initial phase, results in the increase of mid-latitude horizontal component of the geomagnetic field at the surface of the Earth. The initial phase can last from a few hours to a day. During main phase horizontal magnetic field generally decreases but some storms proceed directly into the main phase without initial phase. The main phase normally lasts less than one day and can be as short as an hour. At last a recovery phase occurs when the depressed northward geomagnetic field component returns to normal levels. Recovery is typically complete in one to two days, but can take longer time. The relation between measured air-earth current and geomagnetic activity during

relatively disturbed years in 1960 was reported by Cobb (1967). Park (1976) and Roble and Hays (1979) found that magnetosphere generator can produce + 20% perturbation in ground electric field and air-earth current over the quiet geomagnetic period and larger variations can take place during geomagnetic storm and substorms. Park (1976) found that the global thundercloud activity starts to increase around 3 days after the passage of solar magnetic sector boundary (MSB). Reiter (1977) observed air-earth current density and electric field to be maximum, 1-2 days after the passage of MSB. Magnetic storm events begin suddenly at about the same time all over the world.

CHAPTER 2

SEISMOGENIC TEMPERATURE ANOMALIES IN THE IONOSPHERE

2.1 INTRODUCTION

The electron and ion temperatures in the ionosphere are mainly governed by the phenomena occurring above and below it. Solar flares, magnetospheric perturbation and geomagnetic storm play a major role in generating temperature anomalies in the ionosphere, while below the ionosphere lightning, earthquakes and volcanic events are responsible for ionospheric temperature perturbations. Many workers have studied the ionospheric anomalies due to these phenomena (Parks et al., 1981; McCarthy and Parks, 1985; Inan et al., 1991; Kleusberg, 1992; Akmamedov, 1993; T aranenko et al., 1993; Parrot, 1994, 1995; Depuev and Zelenova, 1996; Molchanov and Hayakawa, 1998; Molchanov et al., 1998; Ondoh, 1998, 2000; Eack et al., 2000; Pulinets et al., 1994, 1998a, b, 2003; Kazimirovsky et al., 2003; Liu et al., 2000, 2001, 2004; Tsai and Liu 2004; Hayakawa et al., 1996a, b, 2006; Sharma et al., 2004a, 2004b, 2005, 2006; Rishbeth, 2006; Muto et el., 2008; Velinov and Tonev, 2008; Saroso et al., 2009; Yiyan et al., 2009). An extensive review of the effect on the ionosphere due to phenomena occurring below it is given by Kazimirovsky et al. (2003). The diurnal, season, latitude, longitude, altitude and the solar cycle variations also affect the ionospheric parameters. The effect of solar flares, thunderstorms and lighting/sprites on the ion temperature has been studied using the data recorded by RPA payload aboard the Indian SROSS-C2 satellite over Indian region has been studied by Sharma et al. (2004a, b). The diurnal, seasonal and latitudinal variations of the ionospheric temperatures of the topside F region over Indian region during solar minimum year 1995-96 have also been studied by Sharma et al. (2005).

The ionospheric temperature variations have been studied broadly using ground-based and *in situ* observations (Farley et al., 1967; Evans, 1973; Oyama and Hirao, 1975; Oyama et al., 1985; Su et al., 1995; Watanabe et al., 1995;

Bhuyan and Kakoty, 2000; Singh and Patel, 2001) and through theoretical calculations (Dalgarno et al., 1963; Geisler and Bowhill, 1965; Banks and Nagy, 1970; Bailey et al., 1975).

The spatial and temporal variation of the electron temperature at equatorial anomaly latitudes has been studied by Su et al. (1996) at around 600 km altitude using the Hinotori satellite data. Oyama et al. (1996a) have studied the electron temperature (Te) by downward plasma drift in the equatorial topside ionosphere and observed that the electron temperature increases rapidly during early morning period, known as morning overshoot phenomena. Oyama et al. (1996b) observed electron temperature enhancement in the morning period (between 5:00 to 8:00 LT) on studying the local time, seasonal and longitude variations of the electron temperature at a height of about 600 km in the low latitude region. The peak value reaches about 5000 ^{0}K for the high solar activity.

Schunk and Sojka (1982) studied the ionospheric temperature anomalies theoretically. Their studies were conducted for low and middle latitudes. The ion temperature was found to be higher in summer than winter during solar maximum year. Due to ion thermal conduction, the ion temperature profile becomes isothermal at high altitudes. Electron temperature is considerably greater than the ion temperature at all altitudes.

Many optical phenomena like blue jets, blue starters, elves red sprites, and related phenomena above an active thunderstorm also play an important role in the variation of ionospheric parameters (Sentman and Wescott, 1993; Taranenko et al., 1993; Lyons, 1994; Inan et al., 1996; Wescott et al., 1996).

Molchanov and Hayakawa (1998) analyzed 10 major earthquake related electromagnetic signals. They found that the ionospheric effect was a transient oscillation with a 5 to 10 day period, which is initiated a few days before a large earthquake and decays over a few days to weeks after it. The ionospheric anomalies due to the seismic activity appearing before few hours to a few days to the earthquake have been studied by several workers (Koshevaya et al., 1997; Zaslavski et al., 1998; Silina et al., 2001; Liu et al., 2000, 2004; Pulinets, 1998a, 2004; Pulinets et al., 2003 etc.). Mukherjee (1999) found that the ionospheric

plasma temperature was found to increase by 350 ^{0}K in height range from 200-300 km during the earthquake.

Shalimov and Gokhberg (1998) reported local enhancement of temperature in the ionospheric F region at a height of 270 km during earthquakes. They suggested that both temperature and intensity disturbance have reached their peak value just before the earthquake. Gokhberg, et al., 1994; Parrot, 1994; Molchanov et al., 1995; Parrot 1995; Pulinets 1998a an d Parrot et al., 2006 observed the penetration of seismo electric fields into the ionosphere using satellite data for detecting ionospheric anomalies.

Sorokin et al. (2001) presented an electrodynamical model of ionospheric precursors to earthquakes. This model explains some electromagnetic and plasma phenomena related to earthquakes by amplification of DC electric fields in the ionosphere over a seismic region. Possible connection of atmospheric electric field with seismic activity and mechanism of penetration of this field into the ionosphere were studied by Pulinets et al. (1994) and Pulinet (1998b).

Gokhberg, et al., 1994; Parrot 1995; Pulinets 1998a and Parrot et al., 2006 observed the penetration of seismic electric fields into the ionosphere using satellite data for detecting ionospheric anomalies. Pulinets (1998b) showed that the seismogenic vertical electric field from the epicenter zone penetrates into the ionosphere and creates irregularities. The temporal and spatial variations in the ionospheric parameters as precursors before the strong earthquake have been studied by Pulinets and Legen'ka (2003). Chmyrev et al. (1989) found that the magnetic field disturbances have values of 0.2-0.5 nT/Hz$^{1/2}$ at altitudes of 800-900 km and frequency about 8 Hz for the moderate earthquake (M = 3.5-5.0) and suggested that these disturbances propagate through the ionospheric plasma as Alfven waves.

2.2 ELECTRON TO ION TEMPERATURE RATIO

To study the electron and ion temperature anomalies in the ionosphere, it is first necessary to define normal ionospheric electron and ion temperature and their relative sensitivity. For this purpose we have first worked out normal behavior of

electron to ion temperature ratio in Indian region using SROSS-C2 satellite data recorded by RPA payload during 1995-1999.

Electron and ion temperature data are used to determine electron to ion temperature ratio for three different seasons; summer (May, June, July and August), winter (November, December, January and February) and equinoxes (March, April, September and October) during the low solar radio flux (F10.7 < 50) from 1995 to 1997 and higher solar radio flux (F10.7 > 50) which includes data from 1998 to 1999. The results are discussed in the following section.

The diurnal variations of electron and ion temperatures are shown in Figure 2.1(a-c) and Figure 2.2(a-c) respectively for summer, winter and equinox seasons during the period from 1995 to 1997 (F10.7 < 50). Statistics of the data are displayed in the form of histogram and standard deviation with each. Similarly, the diurnal variations of electron and ion temperatures for these three different seasons during the period from 1998 to 1999 (F10.7 > 50) are also shown in Figure 2.3(a-c) and Figure 2.4(a-c) respectively.

Hourly variation of the electron and ion temperature indicates morning overshoot and a secondary enhancement in the evening hours. It has been observed that the electron temperatures rise sharply during the sunrise hours (5:00 to 7:00 LT) for all seasons during low solar radio flux. In summer, the average electron temperature during sunrise hours rises to over 3550 ^{0}K (Figure 2.1a) from the night time average electron temperature of approximately 750 ^{0}K. The enhancement for average electron temperature during sunrise hours is approximately 5 times to the night time average electron temperature. Similar enhancements have also been observed during the winter and equinoxes seasons during sunrise. In the winter, the average electron temperature during sunrise rises to over 3400 ^{0}K (Figure 2.1b) from the night time average temperature of 800 ^{0}K. During equinoxes the average electron temperature at sunrise rises to over 3900 ^{0}K (Figure 2.1c) from the night time average temperature of 800 ^{0}K.

The ion temperature enhancements during the sunrise hours (5:00 to 7:00 LT) have also been observed for all seasons during solar minimum years over the

Indian region (Figure 2.2). However, the enhancement peak magnitudes are smaller than the corresponding electron temperature peaks. In the summer, the average ion temperature at sunrise increases to approximately 1300 ^{0}K (Figure 2.2a) from the night time average temperature of 650 ^{0}K. Whereas in the winter, it increases to over 1850 ^{0}K (Figure 2.2b) from the night time average ion temperature of 700 ^{0}K and in the equinoxes, over 1500 ^{0}K from the night time average temperature of 650 ^{0}K (Figure 2.2c). Temperature variation displayed in the Figures (2.1 & 2.2) indicates the lower magnitudes and relatively broader peaks for the ion in comparison to the corresponding variation for electron indicate low sensitivity of ions to the response of solar flux.

In a similar study conducted by Chao et al. (2003), pre-sunrise ion temperature enhancement in the low and mid latitude ionosphere at 600 km was reported. The spatial and temporal variations of the electron temperature at equatorial anomaly latitudes have also been studied by Su et al. (1996) using the Hinotori satellite at an altitude of about 600 km. They have observed a similar morning rise in electron temperature. Thus, the results obtained from SROSS-C2 satellite data are consistent with those measured from the other satellite data too (Su et al., 1996).

To study the relative sensitivity of electron and ion temperatures we have calculated electron and ion temperature ratio for the period from January 1995 to December 1997 (F10.7 < 50) and from January 1998 to December 1999 (F10.7 > 50). Estimated electron and ion temperature ratio (Te/Ti) for the above period are shown in Figures 2.5 (a-c) and 2.6 (a-c) for summer, winter and equinox seasons for low solar radio flux and high solar radio flux respectively. The Figures 2.5 and 2.6 show that the electron and ion temperature ratio are approximately one for all seasons. During sunrise hours, the electron and ion temperature ratio is reaching 3.3 in summer season whereas it is 2 and 2.5 in winter and equinox, respectively (Figure 2.5). For rest of the day hours the ratio is approximately 1.5 and remains constant. The electron and ion temperature ratio for the period from 1998-99 (F10.7 > 50) shows higher values (Figures 2.6b & 2.6c) in comparison to the period from 1995-97 (low solar radio flux) in winter and equinoxes respectively.

However, in summer the ratio is slightly less than 3 (Figure 2.6a). The analysis indicates that the electron and ion temperature ratio (Te/Ti), generally changes with the solar flux and retains peak during morning temperature overshoot. This also indicates the higher sensitivity of electron temperature to the solar flux.

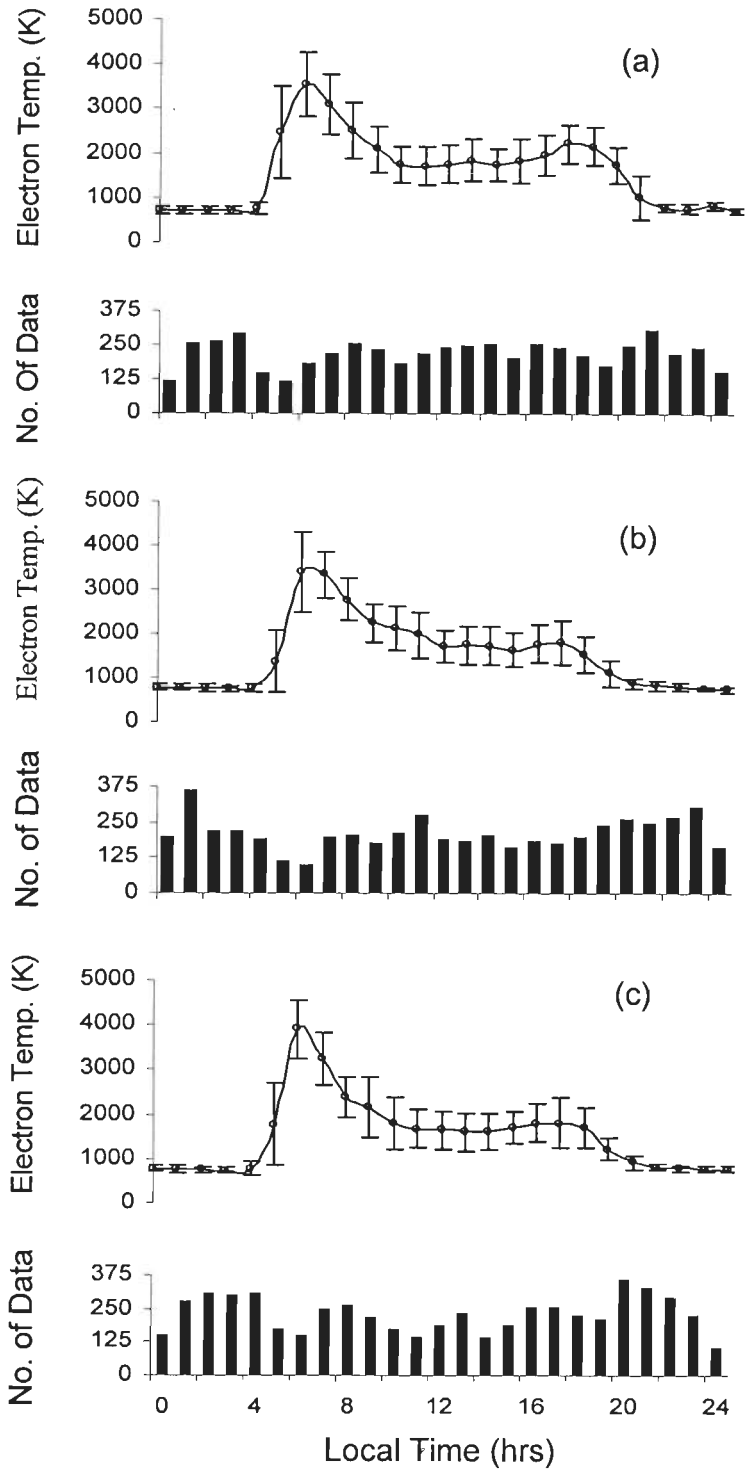

Figure 2.1: Diurnal variation of electron temperature for different seasons: (a) summer, (b) winter and (c) equinoxes recorded by SROSS-C2 at ~500 km for solar minimum period.

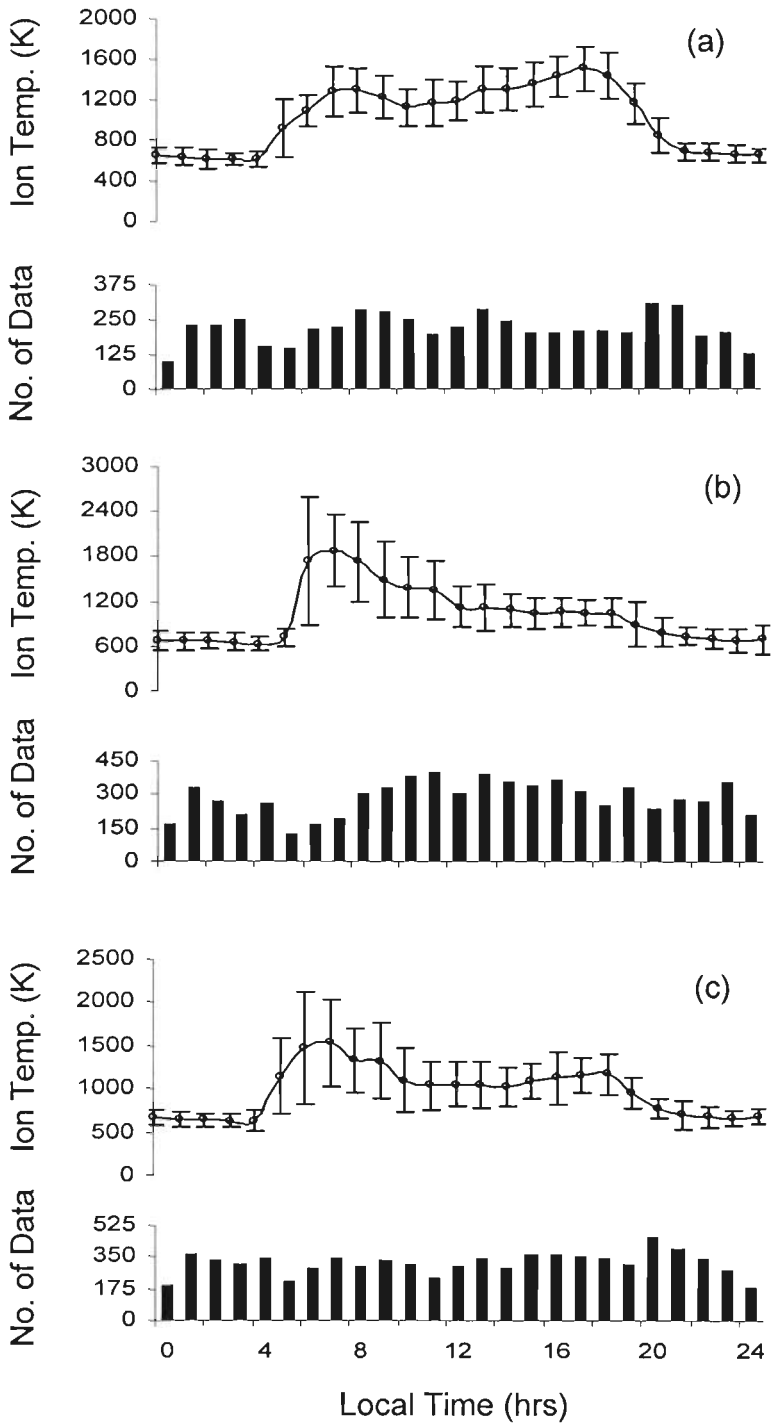

Figure 2.2: Diurnal variation of ion temperature for different seasons: (a) summer, (b) winter and (c) equinoxes recorded by SROSS-C2 at ~500 km for solar minimum period.

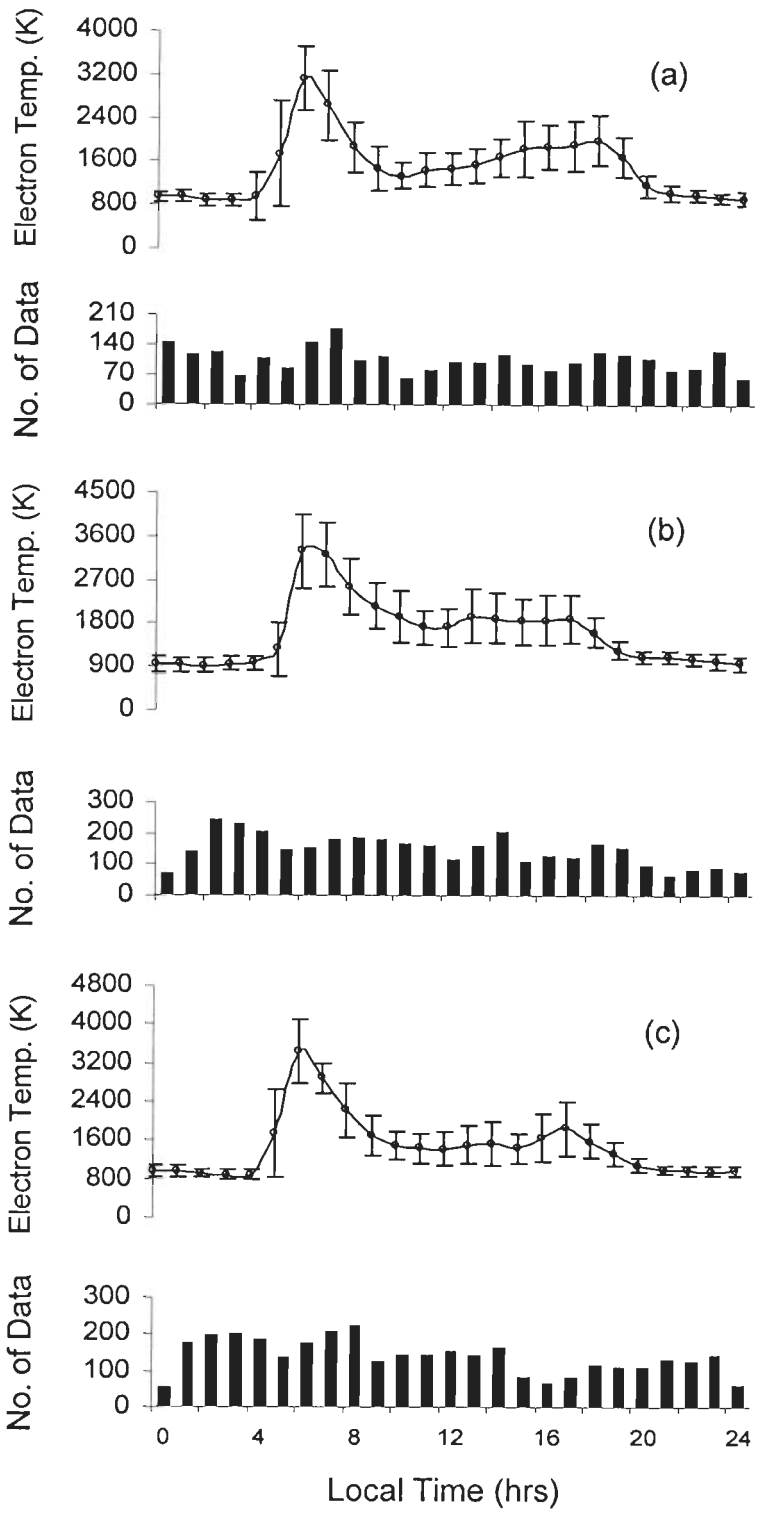

Figure 2.3: Diurnal variation of electron temperature for different seasons: (a) summer, (b) winter and (c) equinoxes recorded by SROSS-C2 at ~500 km for the period 1998- 1999.

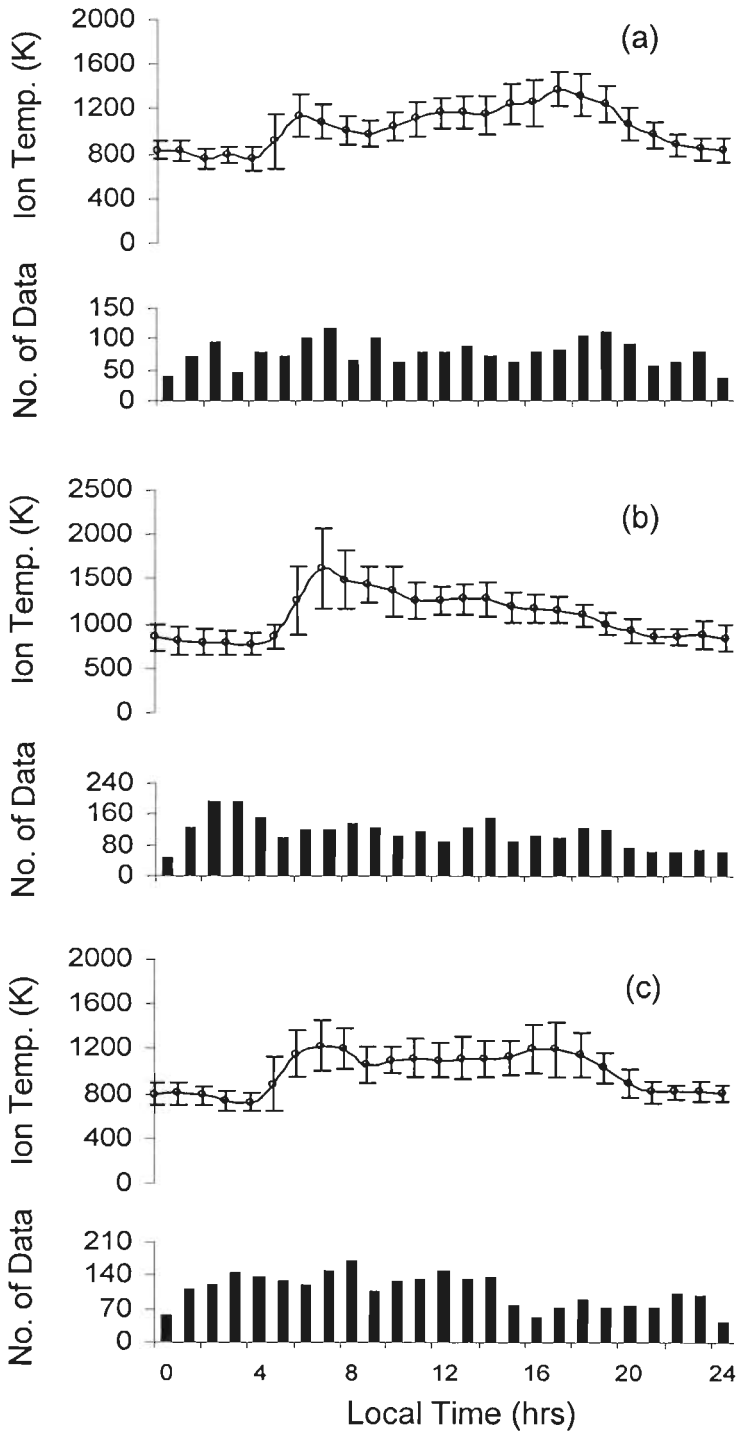

Figure 2.4: Diurnal variation of ion temperature for different seasons: (a) summer, (b) winter and (c) equinoxes recorded by SROSS-C2 at ~500 km for the period 1998- 1999.

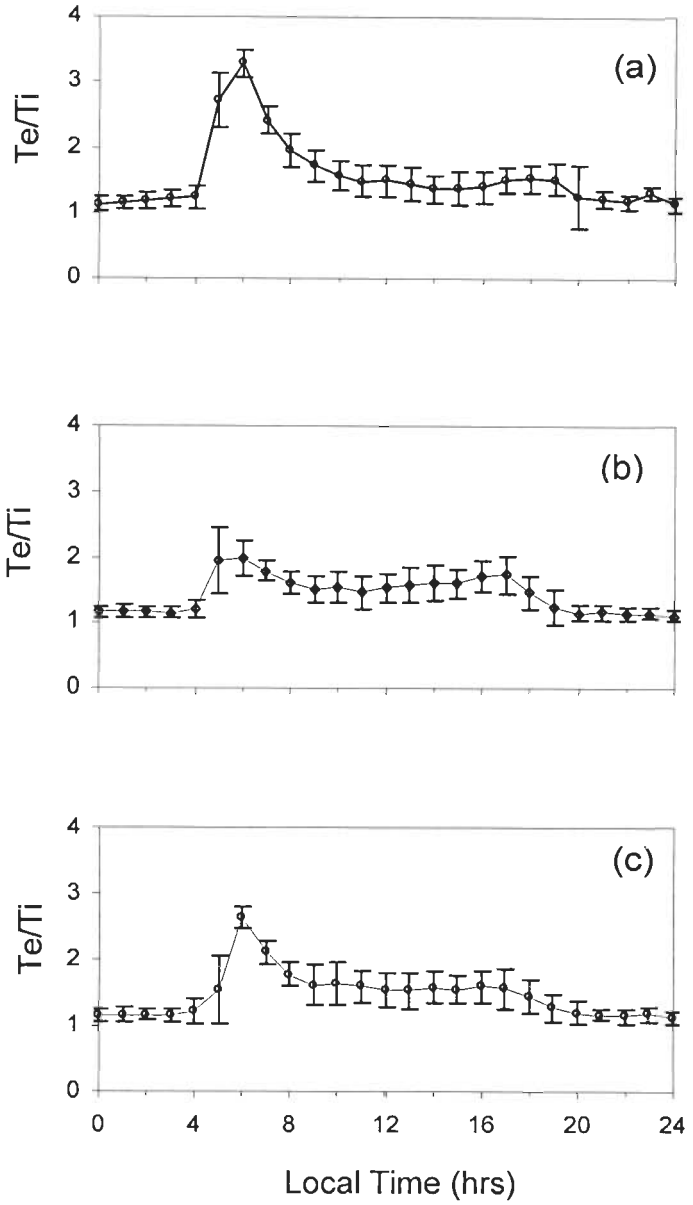

Figure 2.5: Diurnal variation of electron and ion temperatures ratio (Te/Ti) for different seasons: (a) summer, (b) winter and (c) equinoxes recorded by SROSS-C2 at ~500 km for the period 1995- 1997.

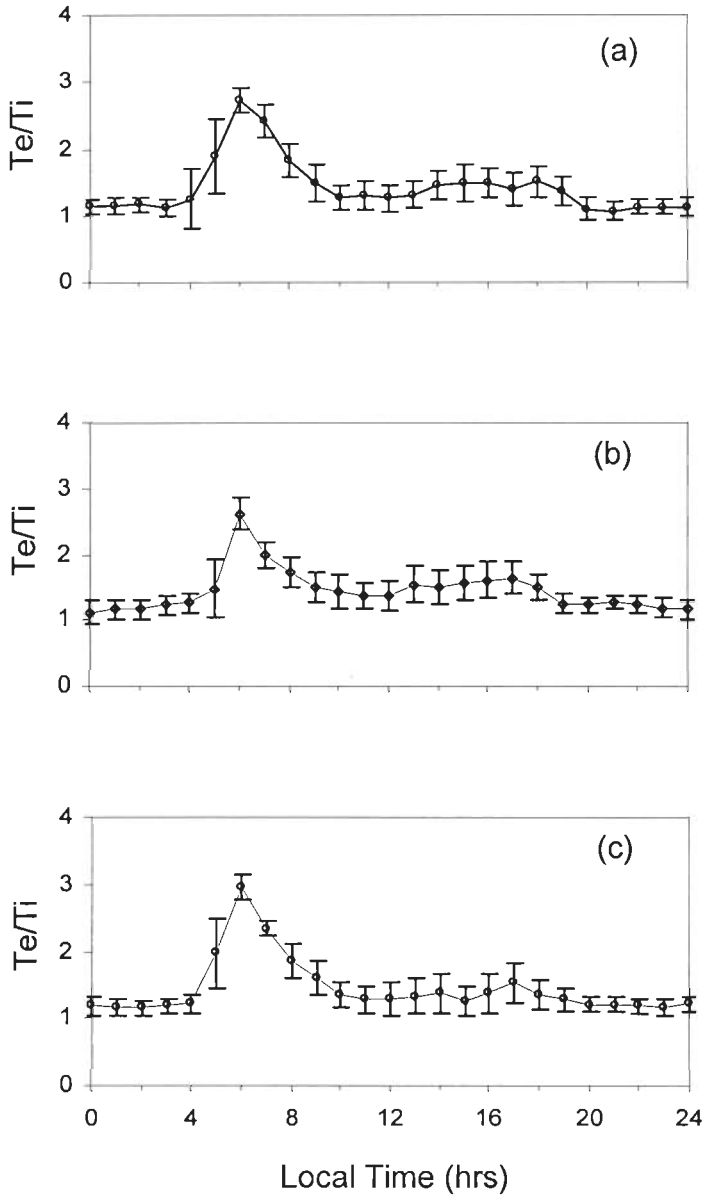

Figure 2.6: Diurnal variation of electron and ion temperatures ratio (Te/Ti) for different seasons: (a) summer, (b) winter and (c) equinoxes recorded by SROSS-C2 at ~500 km for the period 1998- 1999.

2.3 IONOSPHERIC TEMPERATURE ANOMALIES DUE TO EARTHQUAKE

After analyzing the normal average diurnal electron and ion temperature variations both individually and their ratio, our emphasis is shifted to study the response of ionosphere to the earthquake. For this study we have carefully selected earthquake events for which epicentral zone is covered in the SROSS-C2 satellite data. The ionospheric temperature data were carefully analyzed to avoid masking by other possible sources such as solar flare, thunderstorm, latitudinal, longitudinal, diurnal, altitude and magnetic storm variations.

2.3.1 Data Selection and Analysis

The data collected by SROSS-C2 satellite during the period from 1995 to 2000 were used to analyze the anomalous variations in the ionospheric electron and ion temperature due to earthquake events in the ionospheric F2 region. The details of earthquake (location and magnitude etc) events have been downloaded from United State Geological Survey (USGS) website (http://neic.usgs.gov). The seismic events with magnitude $M \geq 4.0$ occurred in the latitude range 0°- 35° N and longitude range 60°- 95° E are selected for the analysis. This is the zone of coverage in satellite data. The data of magnetic storm in terms of $\sum Kp$ have been downloaded from the website (http://swdcdb.kugi.kyoto-u.ac.jp). The $\sum Kp$ index related to magnetic activity has been used in analyzing the electron and ion temperature anomalies related to earthquakes.

In order to avoid the masking of ionospheric temperature perturbation due to solar flares, the solar flares data were obtained from National Geophysical Data Center (NGDC), Boulder, Colorado (USA). Only those earthquake events have been considered which are free from the solar flares. Similarly it has also been verified from the thunderstorms/lightning activity data obtained from India Meteorological Department (IMD) Pune, that the earthquake events are free from any effect due to the thunderstorms. Thus the possibility of ionospheric temperature anomaly due to solar flare and thunderstorm are negligible.

The $\sum Kp$ is the sum of Kp values between 0 and 9 for each day. The magnetic field amplitude may also be enhanced as a result of ULF signals

generated in the ionosphere during magnetic storms The ∑Kp index indicating the level of magnetic activity less than 30 indicating no severe magnetic storm. The magnetic storm is termed as isolated when ∑Kp exceeds 40 (Kushwah et al., 2005). Hayakawa et al. (2006) suggested that the geomagnetically the period is quiet if ∑Kp is 34. To examine the temperature anomalies relationship with magnetic activity, we have plotted ∑Kp for all earthquake events studied in the present thesis. Figure 3.7 show ∑Kp for all earthquake events used in the present work. The earthquake days are shown by inverted arrows. The magnitude of each earthquake event is indicated on the top of the arrow. The ∑Kp index for considered earthquake days fall below 40, indicating no isolated magnetic activity during the earthquake days. Therefore any temperature anomaly recorded during the earthquake days is free from magnetic activity.

It is a difficult task to study the ionospheric temperature using the satellite data associated with earthquake events because very rarely passes of satellite match with epicenter zone of earthquake events. The first task is to select the satellite data corresponding to the seismic event recorded during the period from 1995 to 2000. The recorded average electron temperature during earthquake has been compared with average normal day's electron temperature for the same time interval.

The ionospheric temperature data were analyzed in such a way that the perturbation due to diurnal, seasonal, latitudinal, longitudinal and altitude effects are negligible. One season data has been included for each event therefore, the possibility of seasonal effect has been ruled out. A 5° window in latitude and longitude around the epicenter zone has been selected to minimize the latitudinal and longitudinal effects. To calculate the temperature during normal days only event time duration data have been used to avoid any perturbation due to diurnal effect. All data recorded at an average altitude of 500 km, therefore the temperature anomalies due to altitude variation is negligible. All the temperature data recorded by the SROSS-C2 satellite are within the error limit of ±50 ^{0}K in the temperature range 500-5000 ^{0}K (Garg and Das, 1995; Sharma et al., 2004a). This error limit is applicable to all data presented in this study.

Non availability of the satellite data during all earthquake hours forces us to ignore the event. We could find only 14 earthquake events for electron temperature and 15 earthquake events for ion temperature which matched the satellite data recorded from the zones of coverage from January 1995 to December 2000. Literature on the similar studies (Pulinets et al., 1994; Pulinets, 1998a; Koshevaya et al., 1997; Molchanov and Hayakawa, 1998; Hayakawa, et al., 2000; Liu et al., 2000) suggest that 5 days (2 days pre, 2 days post and one earthquake day) can be defined as earthquake days, in which earthquake associated anomalies may be observed. In the present work we have also followed the same approach. For each event we have analyzed two months satellite data excluding 5 earthquakes days and the remaining pre and post earthquake days were considered as normal days for temperature anomalies due to earthquakes. The recorded average electron and ion temperature for earthquake duration has been compared with normal days and discussed separately in the following sections.

2.3.2 Effect of Seismic Activity on Electron Temperature

Following the procedure discussed above, electron temperature has been derived related to each event for earthquake and normal days. 14 earthquake events with magnitude greater than 4 on Richer scale, matched the corresponding available electron temperature data. Figure 2.8 shows the comparison of electron temperature recorded for the duration of earthquakes and associated normal days for all 14 events. The observed anomalies for a few selected events are discussed below.

On March 19, 1995; an earthquake with an epicenter location (9.88° N and 92.90° E) has been recorded. During this event the average electron temperature was enhanced by 1.2 times over the normal days average electron temperature as estimated from the data shown in Figure 2.8 (a). On May 24, 1995 and June 21, 1995 the earthquakes of magnitude 4.6 and 4.7 were recorded at (16.52° N, 79.68° E and 21.78° N, 85.33° E) respectively. The temperature anomalies during both these events were almost similar and the same are shown in Figures 2.8 (b, c). Three events were recorded in 1996; on January 18, September 25, and

October 8, with the magnitudes of 4.2, 5.0 and 4.2 respectively. Figures 2.8 (d, e, f) show the temperature recorded during the occurrence of events and normal days for these events. During the event of January 18, 1996 the average electron temperature was enhanced 1.5 times over the normal day's average electron temperature, as estimated from the data presented in Figures 2.8(d). On September 25, 1996 and October 8, 1996 the enhancement in average electron temperature were 1.4 and 1.3 times respectively, compared to the normal days average electron temperature as depicted in Figures 2.8 (e, f).

The analysis for two earthquake events recorded in 1997, three events recorded in 1998, two events in 1999 and one events in 2000 for the electron temperature respectively and the comparison of electron temperature during earthquake days along with the normal days for these events are shown in Figure 2.8 (g-o).

On March 19, 1997; an earthquake of magnitude 4.7 with an epicenter location (30.33° N, 67.96° E) has been recorded. Average electron temperature during the earthquake days was 791 ^{0}K and the corresponding normal days temperature was 660 ^{0}K. The enhancement in average electron temperature during earthquake days was found 1.2 times of the normal days as shown in Figure 2.8 (g). On December 29, 1997 the earthquake of magnitude 4.1 has been recorded with epicenter location (29.96° N and 69.32° E). The observed electron temperature during the earthquake and corresponding normal days is shown in Figure 2.8 (h). The average electron temperature during the earthquake days was 1467 ^{0}K whereas the same was 1874 ^{0}K for normal days. This shows the decrease in electron temperature during earthquake days in comparison to normal days. A similar analysis was performed for three earthquake events recorded in 1998, two events in 1999 and two events in 2000. The magnitude of these events varies from 4.1 to 5.4.

All these events show the enhancement in average electron temperature during earthquake days in comparison to the corresponding normal days. The enhancement in average electron temperature during the earthquake days varies between 1.1 to 1.5 times of the normal days. The magnitude, location of epicenter

and details of average electron temperature recorded during the earthquake days and corresponding normal days along with standard deviation are summarized in Table 2.1.

Encouraged with the observation of earthquake induced anomaly recorded in electron temperature, subsequently we have taken up a similar study for ion temperature.

2.3.3 Effect of Seismic Activity on Ion Temperature

To study the ion temperature anomalies associated with seismicity, 15 earthquake events fall in the zone of satellite data coverage. The magnitude of these events is above 4. Normal and earthquake days for each event are defined in the same fashion as used in case of electron temperature anomalies. Comparison of ion temperature during the earthquake days along with the normal days are shown in Figures 2.9 for the 15 events recorded during 1995-2000. On March 12, 1995; an earthquake of magnitude of 4.7 with an epicenter location (17.74° N and 73.77° E) has been recorded. Figure 2.9 (a) shows that the average ion temperature was enhanced by 1.2 times during the earthquake over the normal days average ion temperature. A similar enhancement in the ion temperature have been estimated from the Figures 2.9 (b, c) during the earthquake events on October 21, 1995 and December 09, 1995 with magnitude of 4.9 and 4.8 recorded at 31.43° N, 78.96° E and 15.44° N, 88.43° E respectively.

Three events were recorded in 1996; on February 12, September 25, and November 10, with the magnitude of 4.3, 5.0 and 4.1 respectively. These events show the average ion temperature enhancement of 1.2 times over the normal days average ion temperature in Figures 2.9 (d-f). The comparisons of ion temperature during earthquake days along with the normal days for the 9 events recorded in 1997-2000 are shown in Figures 2.9 (g-o). On September 05, 1997; an earthquake of magnitude 4.0 with an epicenter location (33.83° N, 72.82° E) shows an average ion temperature during the earthquake days, 1552 ^{0}K, and 1350 ^{0}K for normal days. Figure 2.9 (g) shows that the average ion temperature during the earthquake days was enhanced 1.2 times the normal days. However, contrary to

the general trend, December 29, 1997; earthquake of magnitude 4.1 with epicenter location (29.96° N, 69.32° E) shows the decrease in average ion temperature by 1.2 times of the earthquake days in comparison to normal days (Figure 2.9 h). For this event the average ion temperature during the earthquake days was 913 ^{0}K while the same was 1083 ^{0}K for the normal days.

Two earthquakes occurred in 1998, three in 1999 and two in 2000 for which ion temperatures were analyzed. The magnitude of these events varies from 4.1 to 5.2. All these events show the enhancement in ion temperature during earthquake days in comparison to the corresponding normal days. The enhancement in temperature during the earthquake days varies between 1.2 to 1.3 times of the normal days as shown in Figures 2.9 (i-o). The magnitude, location of epicenter and details of average ion temperature recorded during the earthquake days and corresponding normal days along with standard deviation are shown in Table 2.2.

The analysis of electron and ion temperature anomalies shows that there is a consistent enhancement of ionospheric temperature recorded during the earthquake days in majority of cases, except the event on December 29, 1997 which shows decrease in both electron and ion temperature during earthquake days over normal days. This indicates that in some cases the decrease in average electron and ion temperature is also possible. The electron temperature anomalies are higher than the ion temperature anomalies, indicating that the electrons are more sensitive in comparison to the ions. It is worth mentioning here that the ionospheric electron and ion temperature data were analyzed in such a way that the effect of diurnal, seasonal, latitudinal, longitudinal, altitudinal, solar flare, thunderstorm and magnetic storm variations are negligible. Therefore, we conclude that the temperature anomalies are related to earthquake events only.

2.3.4 Possible Physical Mechanism

Exact science for earthquake response to the ionospheric temperature has not yet fully established. Nevertheless, based on the literature and our own observations possible mechanism responsible for the earthquake response to the ionospheric electron and ion temperature can be discussed here. The sources of

atmosphere-ionosphere modification over the regions of preparing earthquakes is the emanation of radon, light gases and submicron aerosols with high metal content during seismic events (Alekseev and Alekseeva, 1992). A significant quantity of aerosols like Cu, Fe, Ni, Zn, Pb, Co, Cr and radon are enhanced into ground layer of atmosphere (Boyarchuk, 1997), the additional flux of metallic aerosols leads to anomalous field strength. Radon is the main source of alpha particles which produce intensive ionization of the near ground layer of the atmosphere. Aerosols in the atmosphere formed large electric fields up to several kV/m. These vertical fields penetrate into the ionosphere where, due to finite conductivity of ionosphere they transform into horizontal fields (Kim and Hegai, 1997). This field produces joule heating, electron temperature growth in the ionosphere and gravity wave generation. The emission and propagation of electromagnetic radiations in a wide frequency band, covering ULF to VLF from epicenter zone of earthquake region were also reported (Gokhberg et al., 1982; Parrot, 1995; Shalimov and Gokhberg, 1998; Hayakawa et al., 1996a, b, 2000: Gwal et al., 2006: Bhattacharya et al., 2009). The changes in F2 region of ionosphere may be caused by the electromagnetic radiation generated by seismic process and penetration into ionosphere, which leads to additional joule heating in the ionosphere. The seismogenic electric field within the ionosphere is modulated by daily variations of plasmaspheric electric fields that cause the daily variations of the sign of seismo-ionospheric variations (Pulinets et al., 1998c). The detailed theoretical calculations and further experimental observations strengthen the hypothesis of temperature enhancement due to earthquake over the epicenter zone of ionospheric region which may be developed in future as a short term precursor in future.

Possible electromagnetic emission by piezoelectric effect occurs due to electrostatic discharge produced by the deformation of piezoelectric minerals or charge separation on fractured surfaces in the earth. Fracture quartz crystals, tourmaline crystals and quartz bearing rocks emit electromagnetic waves in frequency range 1-10 MHz (Nitsan, 1977). Microfracture process of rocks inside earth is identified as possible mechanism for the generation of electromagnetic

waves (Molchanov and Hayakawa, 1995; Freund et al., 2006). Atomic bonds start to break when a rock is stressed under high pressure, take the form of crystalline structure, form charge distribution of opposite signs on opposite sides of microfracture, and consequently generates strong local electric field.

The emission and propagation of electromagnetic radiations in a wide frequency band, covering ULF, ELF and VLF from epicenter zone of earthquake were reported by several authors (Gokhberg et al., 1982; Koshevaya et al., 1997; Shalimov and Gokhberg, 1998; Hayakawa et al., 1996a, b, 2000; Parrot, 1995; Kushwah et al., 2005). These waves may create localized joule heating in the ionosphere. DC-ULF electromagnetic signals have a precursory time from few days to several weeks (Hayakawa et al., 2000), whereas much short time from few to several hours for VLF-VHF signals (Gokhberg et al., 1982; Eftaxias et al., 2001).

2.4 CONCLUSIONS

In this chapter, we have first studied the diurnal and seasonal variations of the ionospheric electron and ion temperatures and their ratio. Studies have been made using data from the SROSS-C2 satellite during the period from 1995 to 1999. The ionospheric electron temperature shows the 'morning overshoot' to about 3 to 5 times for average electron temperature and 1.5 to 2 times for ion temperature during the sunrise hours. The temperature ratio Te/Ti, was almost unity during the night time and show variations during the day time in all seasons. The change in ionospheric temperatures is related to the variation in the emission of solar radio flux from sun. The electron temperature is more sensitive to these changes in comparison to the ion temperature. The temperature ratio Te/Ti, increase with the increase in solar flux in winter and equinoxes. Whereas the ratio is slightly decreased in summer over Indian region.

We have analyzed 6 years (January 1995 to December 2000) data recorded by SROSS-C2 satellite for the present study. It is concluded the 13 events out of 14 show increase in average electron temperature during earthquake days by an amount approximately 1.1 to 1.5 times of the normal days while 14 events out of 15 show the increase in ion temperature during earthquake days by

amount 1.1 to 1.3 of the normal days. The higher electron temperature anomalies indicate that the electrons are more sensitive as compared to ions in the temperature perturbation due to earthquakes. The seismogenic vertical electric field and associated electromagnetic radiations reach up to ionospheric heights, induce joule heating and are responsible for the ionospheric temperature perturbations. A careful quantitative analysis of ionospheric temperature data recorded before and during the occurrence of earthquake shows, generally enhancement in the ionospheric electron and ion temperatures. These studies further broaden the scope of earthquake precursor studies using ionospheric temperature anomalies.

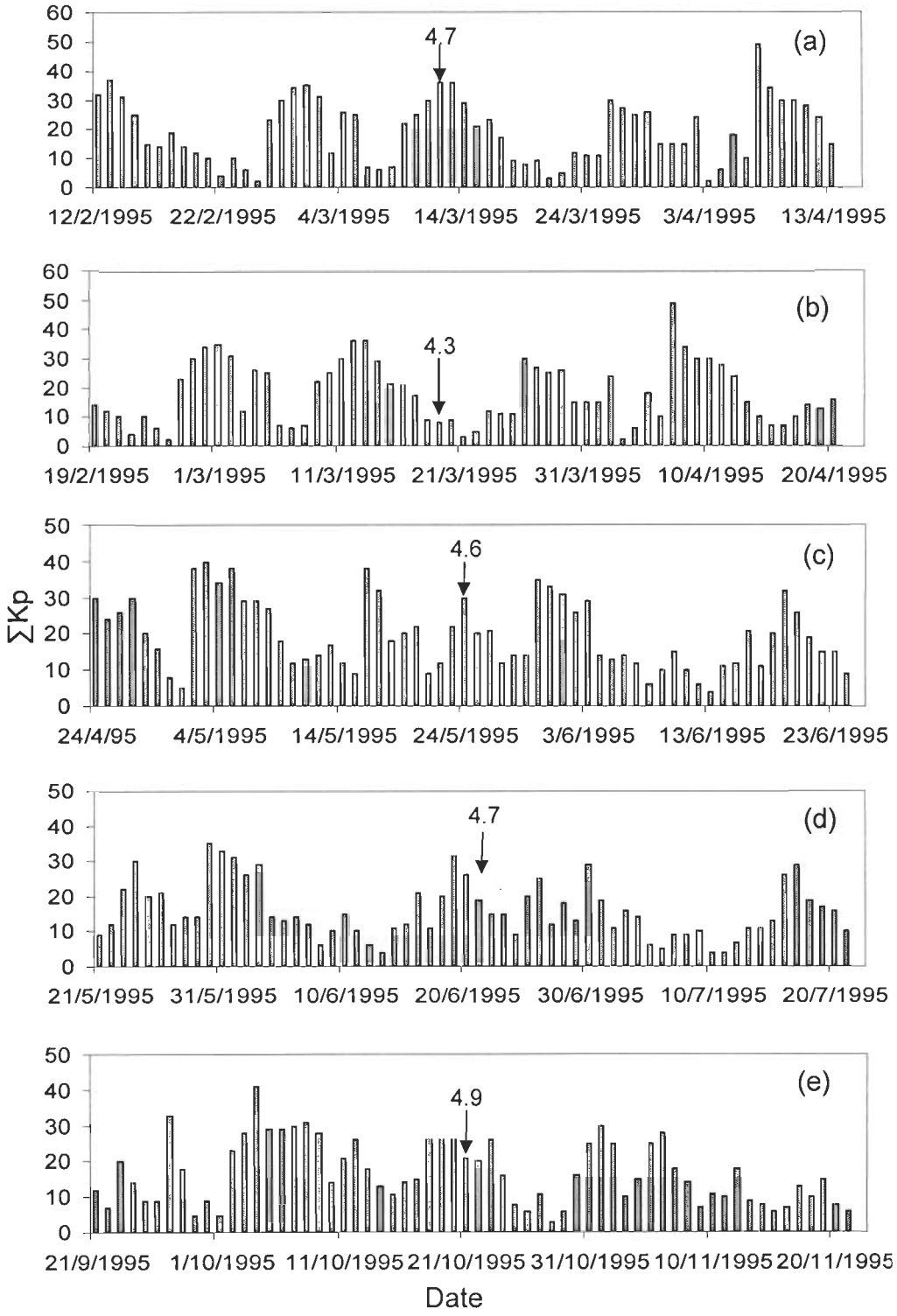

Figure 2.7 continues...

...Figure 2.7 continued

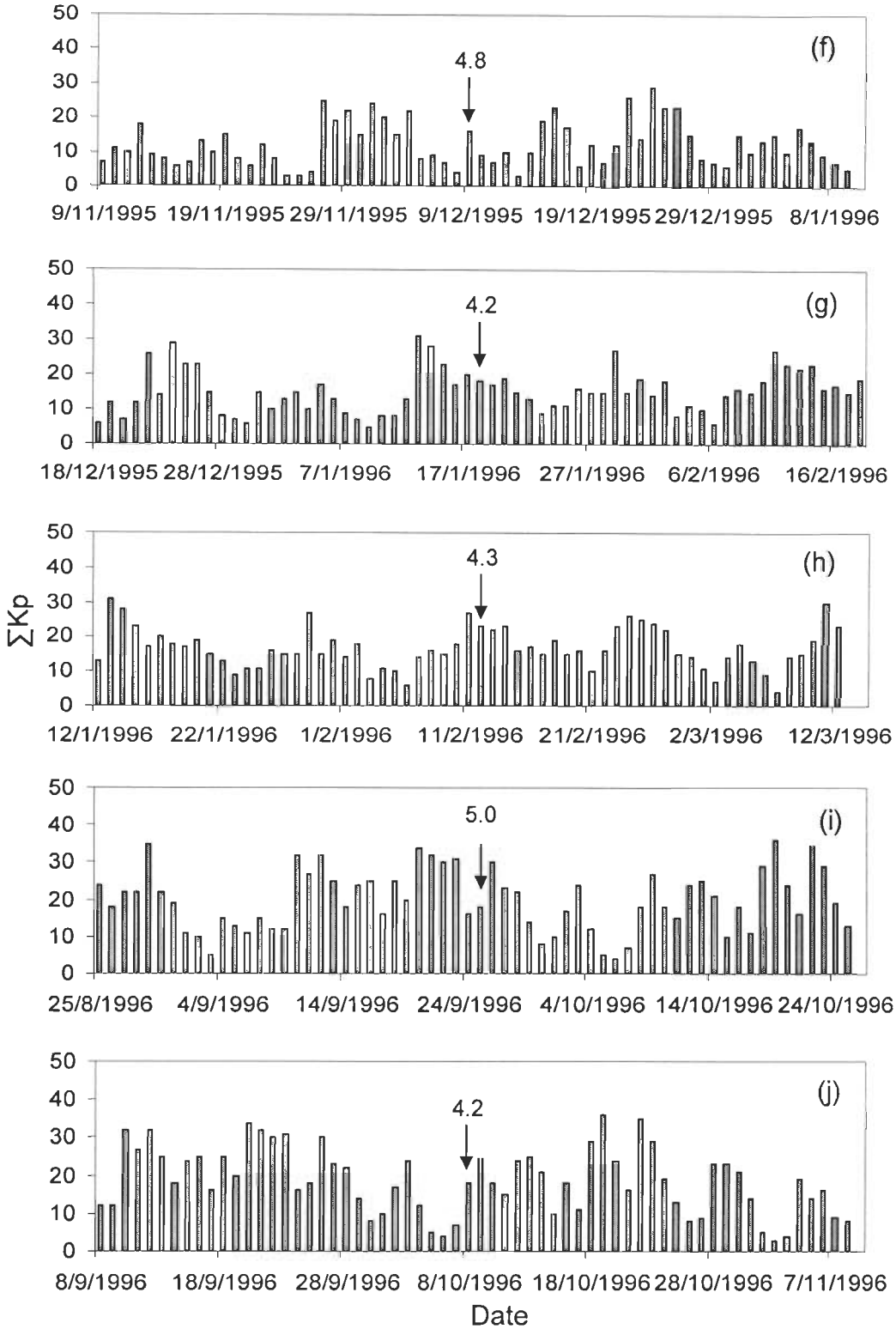

Figure 2.7 continues...

...Figure 2.7 continued

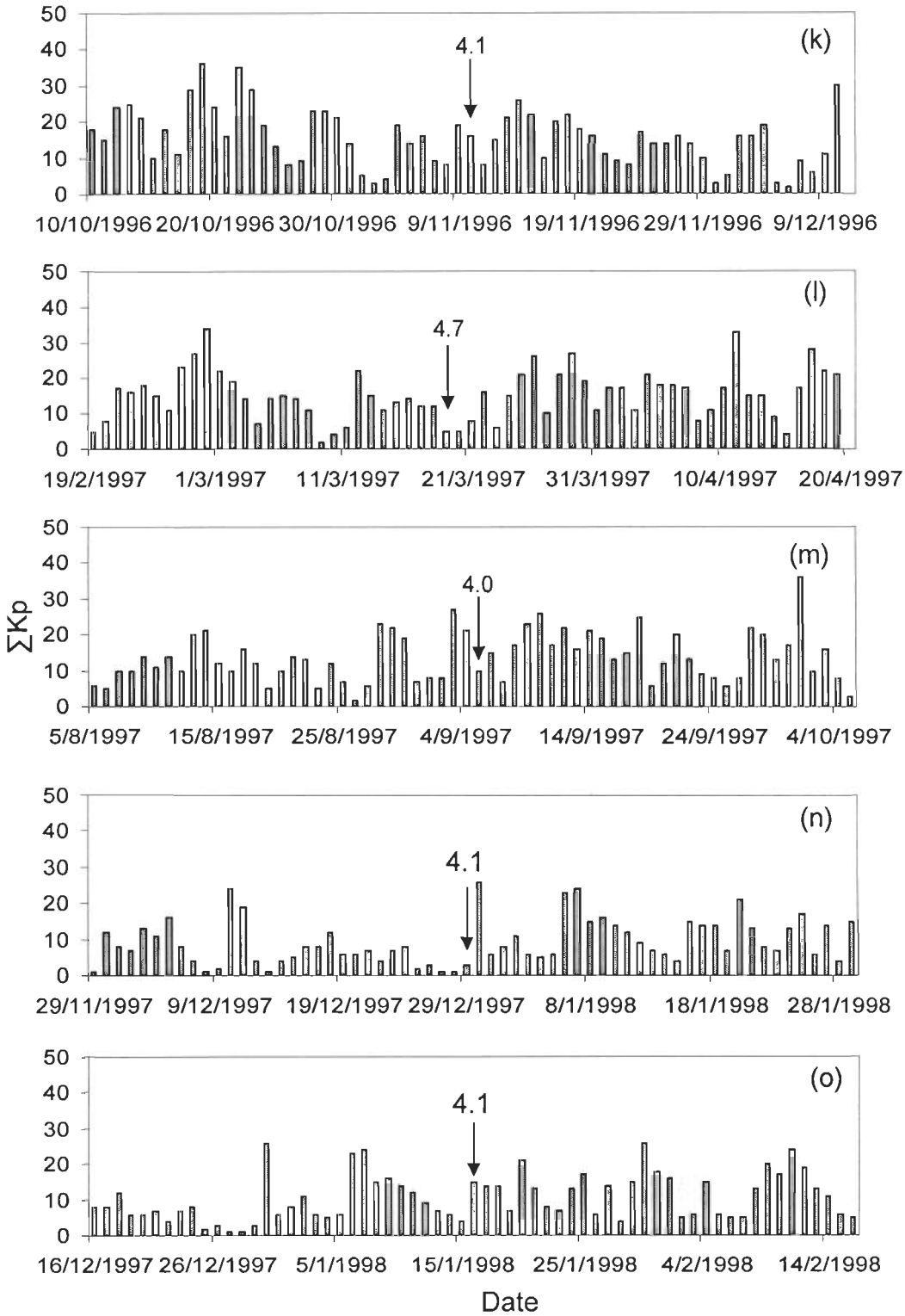

Figure 2.7 continues...

...Figure 2.7 continued

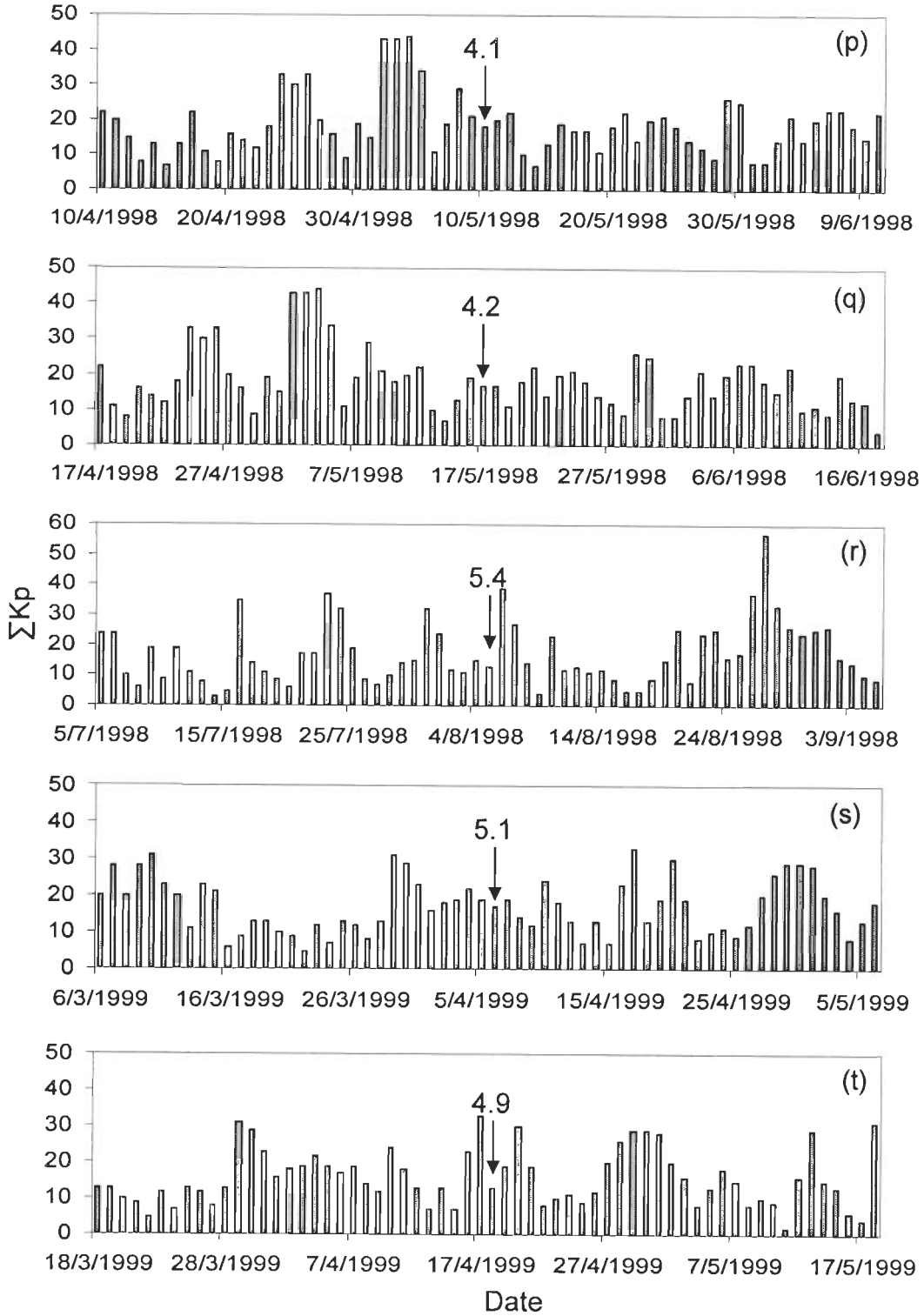

Figure 2.7 continues...

...Figure 2.7 continued

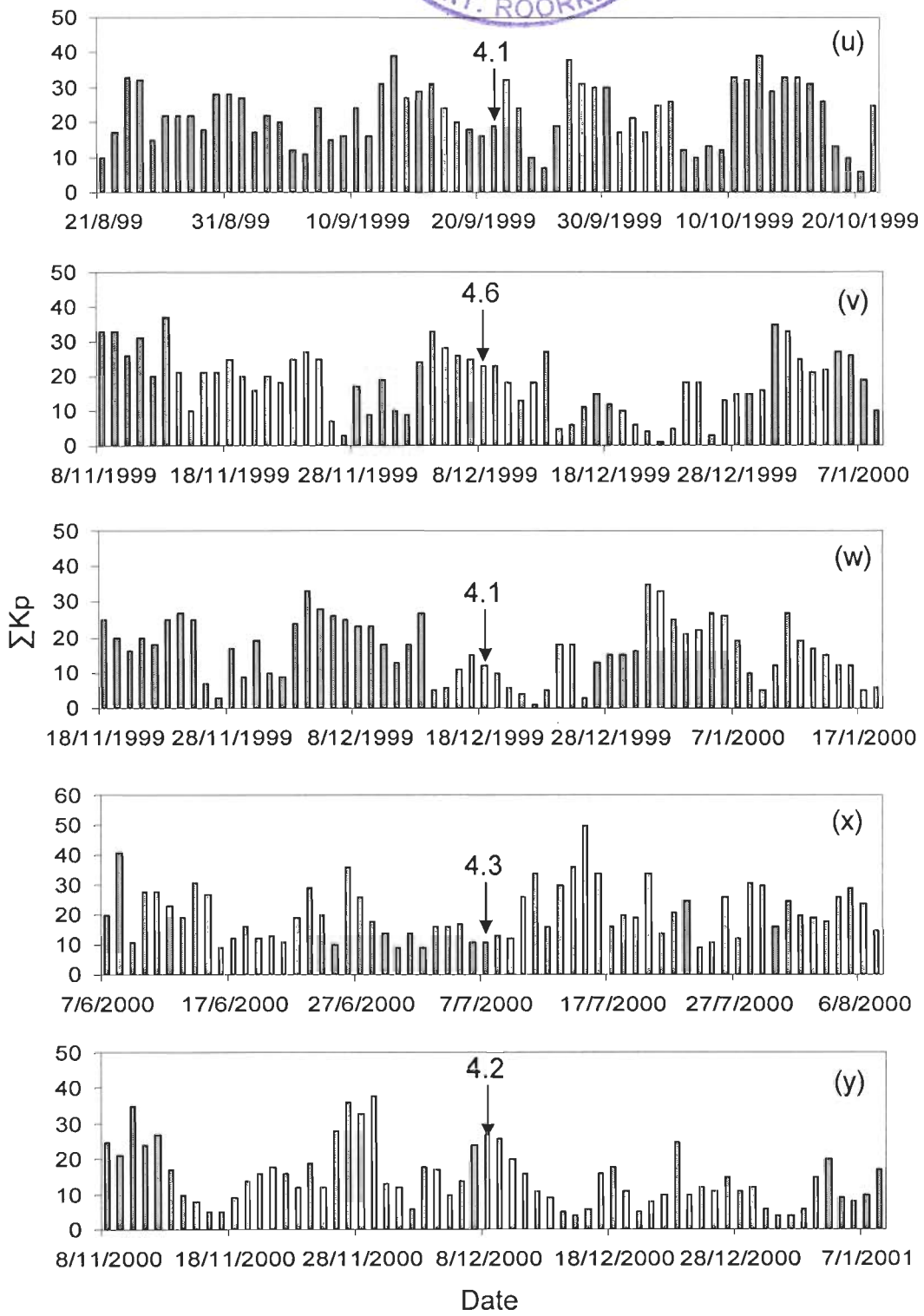

Figure 2.7 continues...

Figure 2.7: Variation of magnetic storm in terms of $\sum$Kp for the recorded events: (a) March 12, 1995, (b) March 19, 1995, (c) May 24, 1995, (d) June 21, 1995, (e) Oct 21, 1195, (f) Dec 9, 1995, (g) Jan 18, 1996, (h) Feb 12, 1996, (i) Sep 25, 1996, (j) Oct 8, 1996, (k) Nov 10, 1996 (l) Mar 19, 1997, (m) Sep 5, 1997, (n) December 29, 1997, (o) January 16, 1998, (p) May 10, 1998 (q) May 17, 1998 (r) August 05,1998 (s) April 06, 1999 (t) April 18, 1999 (u) September 21, 1999 (v) December 08, 1999, (w) December 18, 1999, (x) July 07, 2000, (y) December 08, 2000.

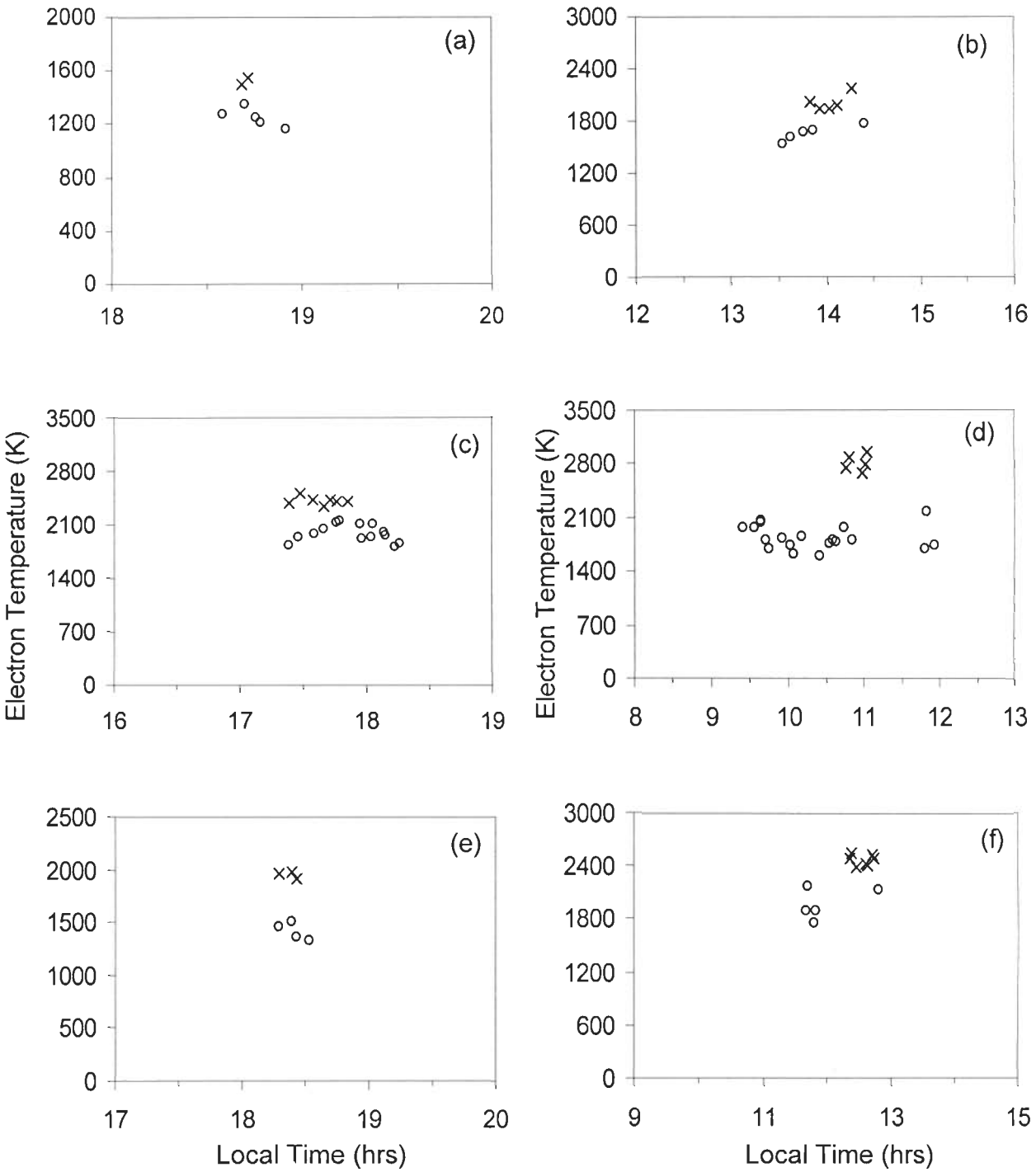

Figure 2.8 continues...

...Figure 2.8 continued

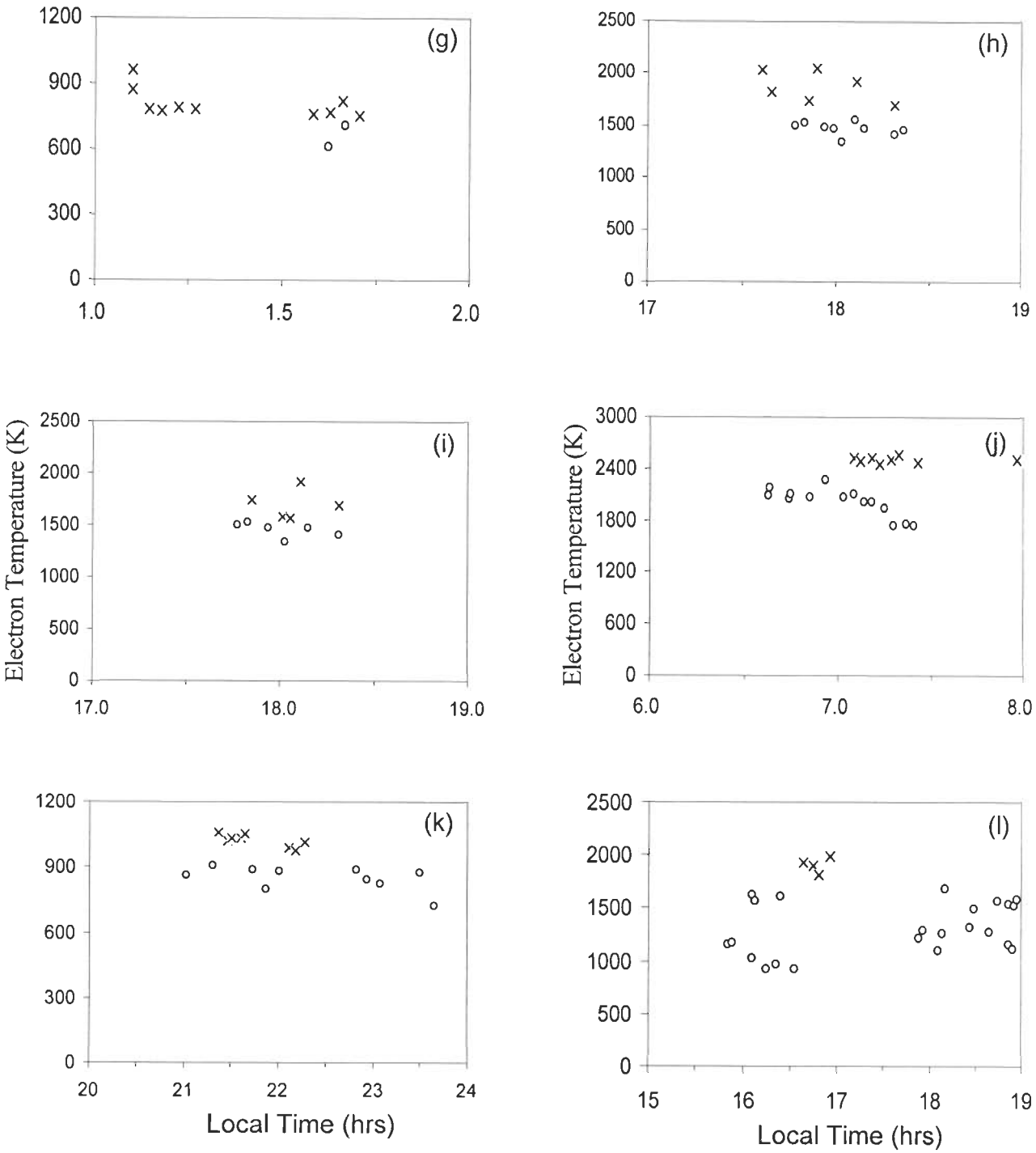

Figure 2.8 continues...

...Figure 2.8 continued

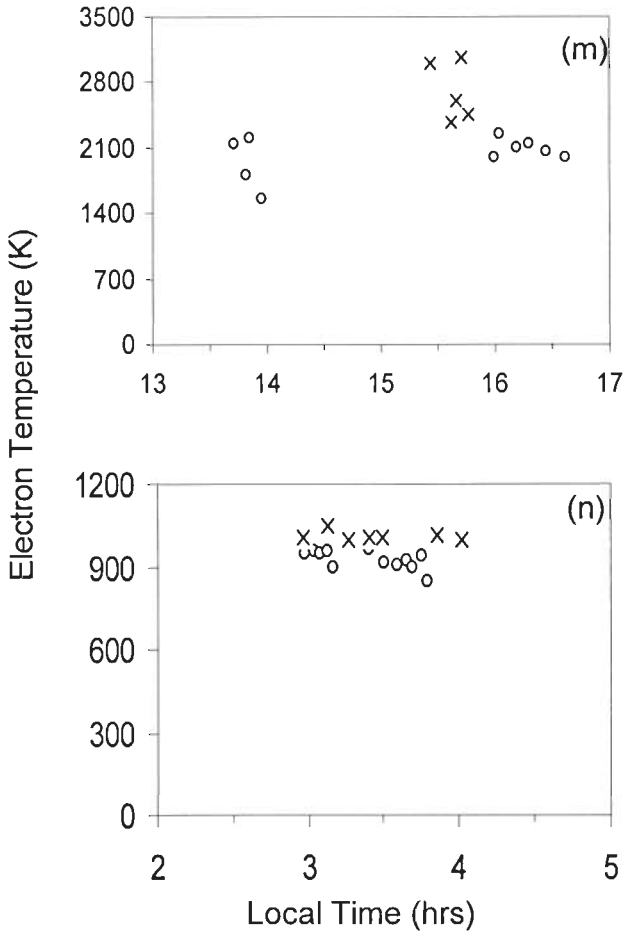

Figure 2.8: Comparison of electron temperature during earthquake days along with the normal days for the analysis events: (a) March 19, 1995 (b) May 24, 1995, (c) June 21, 1995, (d) January 18, 1996, (e) September 25, 1996 (f) October 08, 1996, (g) March 19, 1997, (h) December 29, 1997, (i) January 16, 1998, (j) May 17, 1998, (k) August 05,1998, (l) April 06, 1999, (m) December 08, 1999, (n) December 08, 2000. [Cross and circle sign represent temperatures of earthquake and normal days].

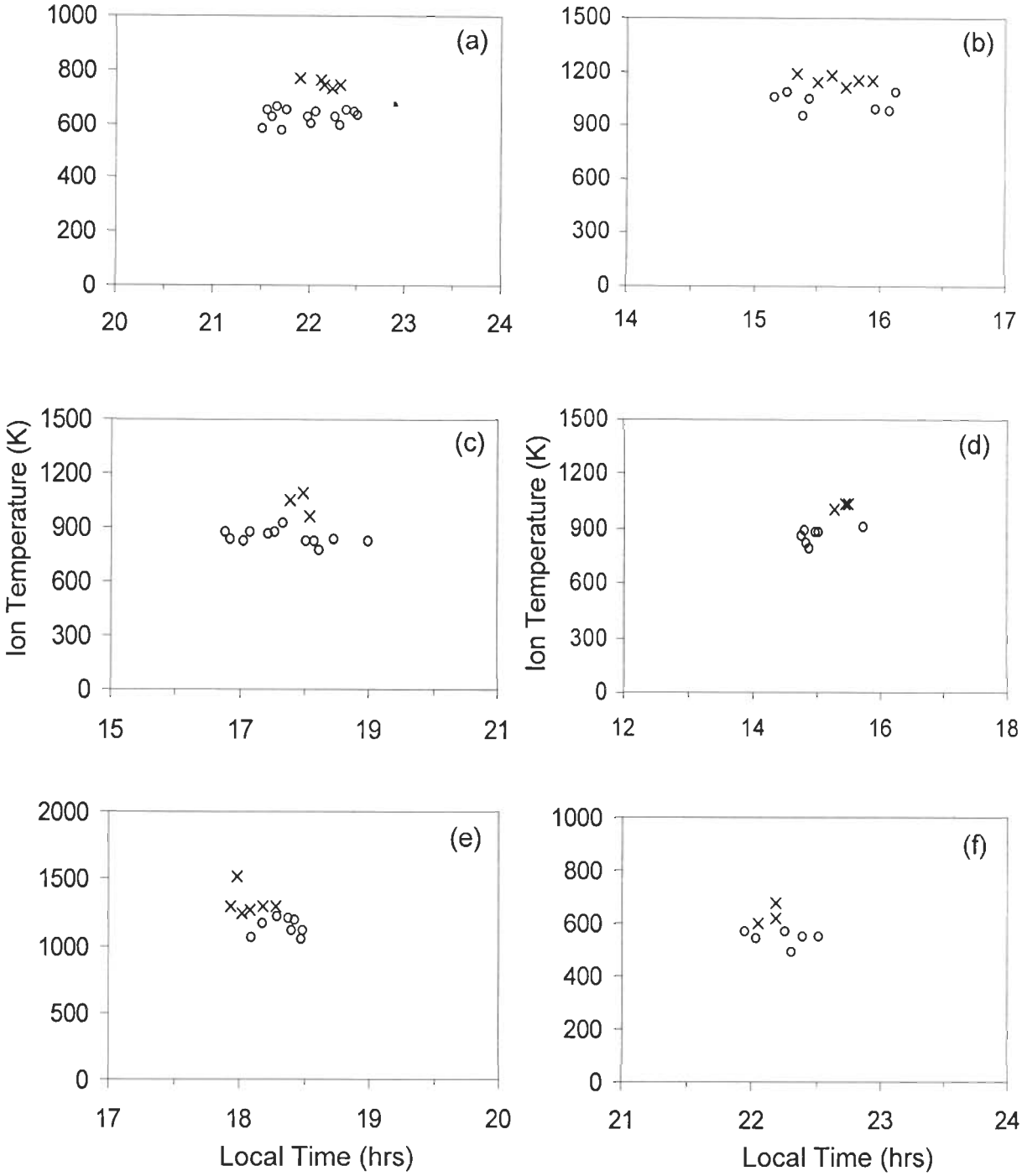

Figure 2.9 continues...

...Figure 2.9 continued

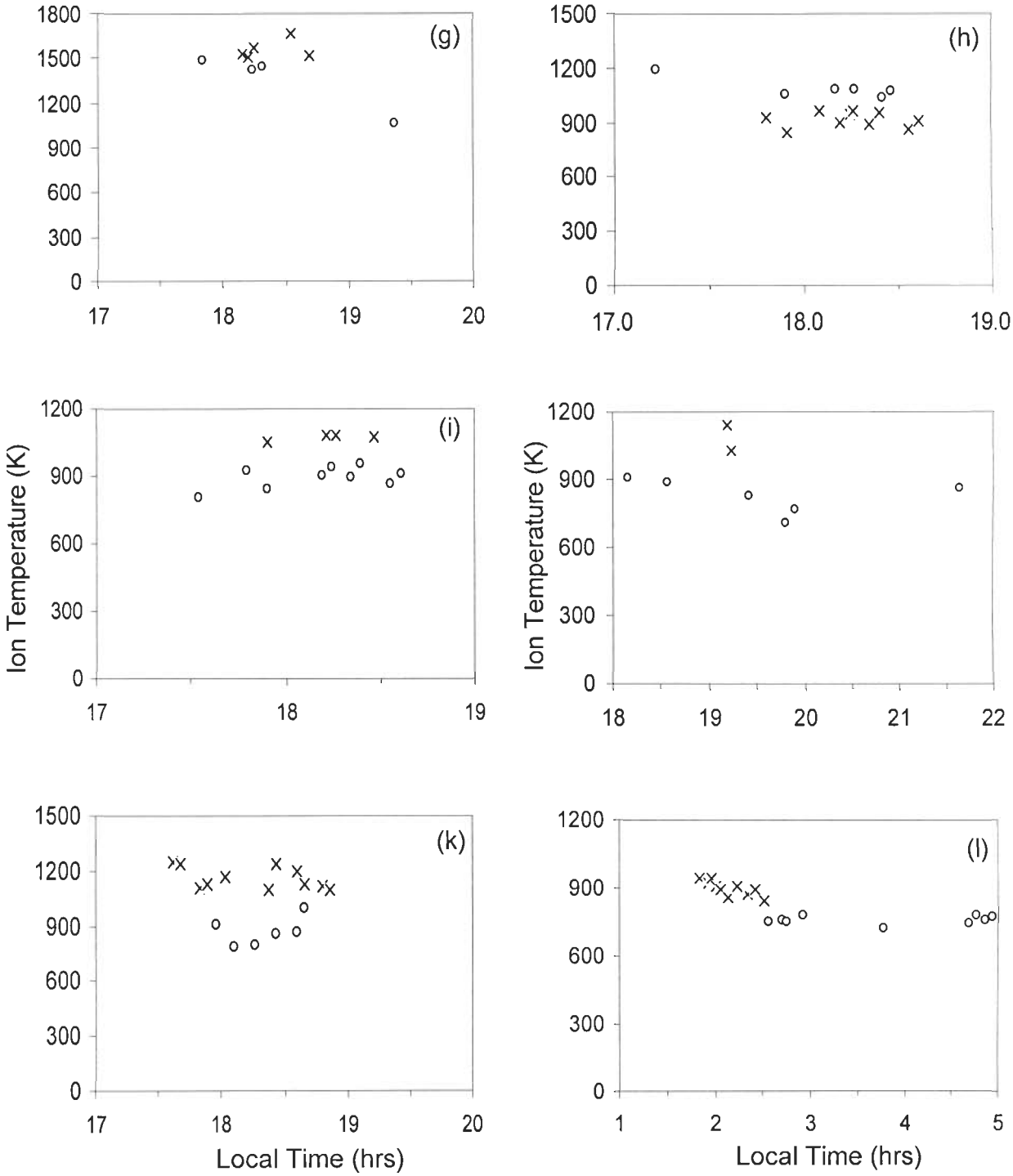

Figure 2.9 continues...

Figure 2.9 continued

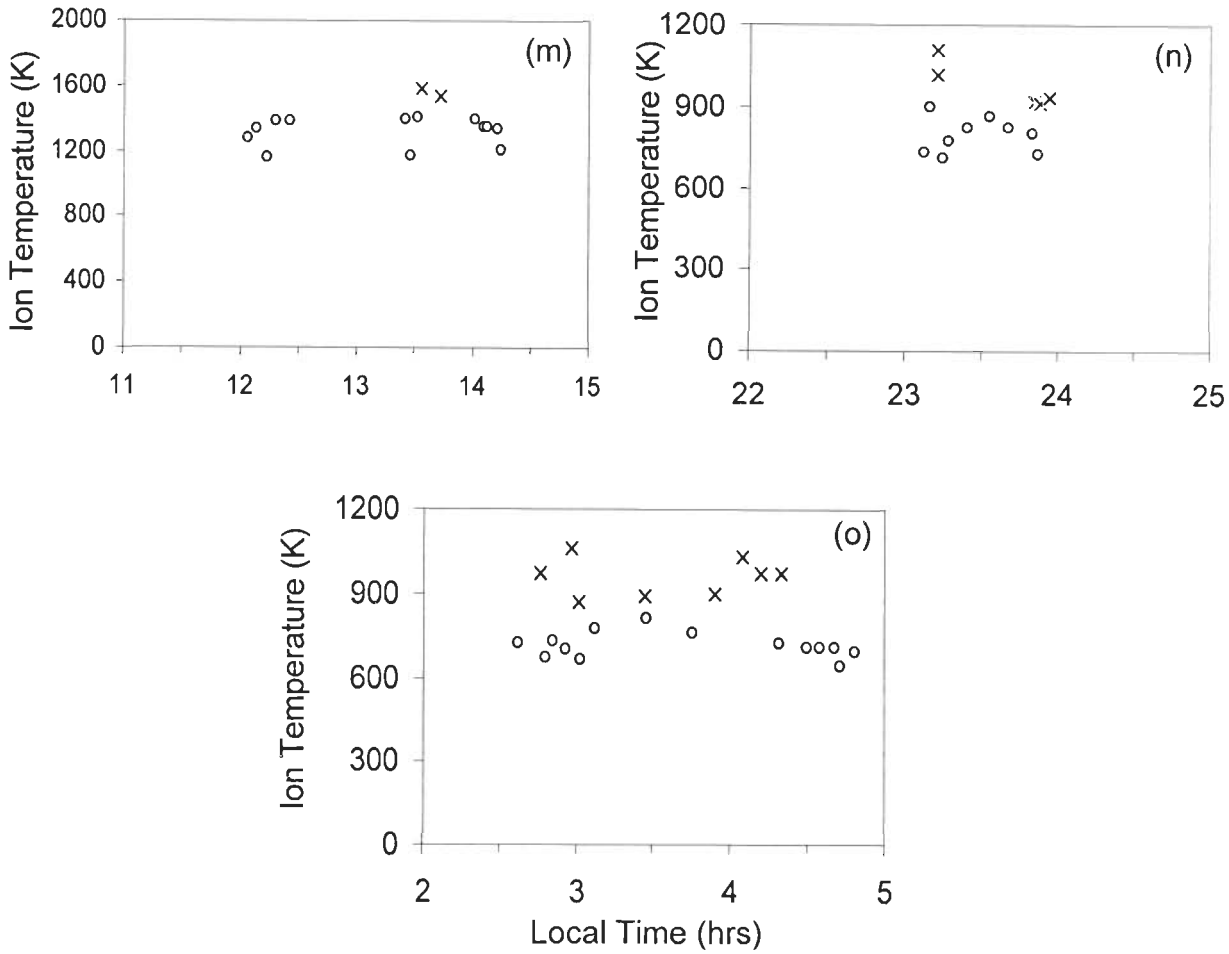

Figure 2.9: Comparison of ion temperature during earthquake days along with the normal days for the analysis events: (a) March 12, 1995, (b) October 21, 1995, (c) December 09, 1995, (d) February 12, 1996, (e) September 25, 1996, (f) November 10, 1996, (g) September 05, 1997, (h) December 29, 1997, (i) January 16, 1998, (j) May 10, 1998, (k) April 18, 1999, (l) September 21, 1999, (m) December 18, 1999, (n) July 07, 2000, (o) December 08, 2000. [Cross and circle sign represent temperatures of earthquake and normal days].

S. No.	Date of event	Origin time of seismic events (LT)	Location of epicenter	Magn-itude	Depth (km)	Electron temperature (K)		Ratio
						Average during earthquake days	Average during normal days	
1	Mar 19, 1995	16:44:48	09.88°N, 92.90° E	4.3	33	1519 ± 33	1240 ± 72	1.2
2	May 24, 1995	13:46:45	16.52°N, 79.68° E	4.6	33	2004 ± 93	1642 ± 85	1.2
3	June 21, 1995	18:35:41	21.78°N, 85.33° E	4.7	33	2407 ± 54	1977 ± 111	1.2
4	Jan 18, 1996	08:05:35	24.09°N, 82.62° E	4.2	33	2805 ± 107	1830 ± 152	1.5
5	Sept 25, 1996	17:41:17	27.43°N, 88.55° E	5.0	33	1952 ± 32	1411 ± 83	1.4
6	Oct 08, 1996	01:28:59	29.51°N, 61.06° E	4.2	33	2466 ± 60	1950 ± 161	1.3
7	Mar 19, 1997	11:15:50	30.33°N, 67.96° E	4.7	33	791 ± 61	660 ± 69	1.2
8	Dec 29, 1997	03:33:32	29.96°N, 69.32° E	4.1	33	1467 ± 65	1874 ± 146	1.3
9	Jan 16, 1998	21:14:51	29.70°N, 68.25° E	4.1	33	1700 ± 142	1454 ± 71	1.2
10	May 17, 1998	05:41:11	30.38°N, 67.95° E	4.2	33	2481 ± 80	2008 ± 160	1.2
11	Aug 05, 1998	03:16:38	29.33°N, 68.74° E	5.4	33	1024 ± 30	851 ± 56	1.2
12	Apr 06, 1999	19:37:24	30.41°N, 79.32° E	5.1	10	1906 ± 75	1301 ± 227	1.5
13	Dec 08, 1999	21:11:43	30.00°N, 68.20° E	4.6	33	2692 ± 315	2023 ± 204	1.3
14	Dec 08, 2000	13:23:07	17.04°N, 73.51° E	4.2	33	1011 ± 18	923 ± 34	1.1

Table 2.1: The magnitude, location of epicenter, depth and comparison of electron temperature during the earthquake days and normal days.

S. No.	Date of event	Origin time of seismic events (LT)	Location of epicenter	Magn-itude	Depth (km)	Ion temperature (K)		Ratio
						Average during earthquake days	Average during normal days	
1	Mar 12, 1995	08:22:54	17.64°N, 73.77°E	4.7	10	748 ± 16	623 ± 28	1.2
2	Oct 21, 1995	19:39:39	31.43°N, 78.96°E	4.9	33	1153 ± 29	1024 ± 51	1.1
3	Dec 09, 1995	10:04:44	15.44°N, 88.43°E	4.8	10	1033 ± 54	842 ± 38	1.2
4	Feb 12, 1996	20:39:54	22.62°N, 82.89°E	4.3	33	1030 ± 17	861 ± 42	1.2
5	Sept 25, 1996	17:41:17	27.43°N, 88.55°E	5.0	33	1320 ± 101	1136 ± 101	1.2
6	Nov 10, 1996	09:00:04	18.30°N, 76.69°E	4.1	33	633 ± 42	545 ± 30	1.2
7	Sep 05, 1997	15:41:51	33.83°N, 72.82°E	4.0	16	1552 ± 66	1350 ± 195	1.2
8	Dec 29,1997	03:33:32	29.96°N, 69.32°E	4.1	33	913 ± 41	1083 ± 56	1.2
9	Jan 16, 1998	21:14:51	29.70°N, 68.25°E	4.1	33	1070 ± 14	890 ± 49	1.2
10	May 10, 1998	14:56:22	29.41°N, 82.02°E	4.1	33	1085 ± 78	828 ± 76	1.3
11	Apr 18, 1999	17:16:36	30.24°N, 79.30°E	4.9	10	1163 ± 60	872 ± 77	1.3
12	Sep 21, 1999	07:48:00	09.37°N, 93.51°E	4.5	33	897 ± 33	757 ± 19	1.2
13	Dec18, 1999	00:50:34	07.14°N, 94.31°E	5.2	33	1560 ± 28	1322 ± 88	1.2
14	July 07, 2000	02:14:06	01.65°N, 66.70°E	4.3	10	985 ± 79	792 ± 65	1.2
15	Dec 08, 2000	13:23:07	17.04°N, 73.51°E	4.2	33	958 ± 67	714 ± 45	1.3

Table 2.2: The magnitude, location of epicenter, depth and comparison of ion temperature during the earthquake days and normal days.

CHAPTER 3

SEISMOGENIC DENSITY ANOMALIES IN THE IONOSPHERE

3.1 INTRODUCTION

Having observed consistent ionospheric electron and ion temperature anomalies induced by earthquakes, our emphasis is now shifted towards the study of ionospheric density response to the earthquakes. Keeping this in mind, we have ananlysed SROSS-C2 ion density data recorded during the period from 1995 to 2000. We have broadly used the same procedure as used in previous chapter, to study the ionospheric temperature anomalies associated with the earthquakes.

Initially we have reviewed the literature on the ionospheric density variation studies carried out using different data set. The ion density data recorded by SROSS-C2 satellite have been analysed to determine the ion density anomalies associated with the earthquakes. Various factors responsible for density variations have been discussed.

3.2 LITERATURE REVIEW

Ionospheric properties have been studied in literature generally either by using ground based ionosonde or by topside sounding from the satellite data. Variations in the critical frequencies of the ionospheric layers were generally observed by ground based ionospheric sounders, which may be subsequently translated into electron density. However, total electron content (TEC) is directly derived by satellite data (Evans, 1977). It has been reported that the temperature and density anomalies in ionospheric F region are inversely related to each other (Brace and Theis, 1978; Williams and Mcdonald, 1987). This means that the increase in electron density (Ne) is associated with the corresponding decrease in electron temperature (Te) and vice-versa. The inverse correlation between temperature and density anomalies has also been reported by Mahajan (1967, 1977). Changes were also observed in height scale, ion composition in ionospheric F region, electron density and temperature (Akmamedov, 1993).

The first publication dealing with the ionospheric parameter variation as seismic precursors was the study of the variations of f_0E parameter before the Tashkent earthquake in 1966 by Antselevich (1971). Local increase in the ionospheric electron density above the epicenter zone was revealed during above earthquake. The anomalous ionospheric electron density associated with the Tashkent earthquake was attributed to the redistribution of electric charge in the earth-atmosphere system. These effects are generally small in size and also masked by other ionospheric disturbances.

Chung-Li ionosonde data was used recently to determine the seismo-ionospheric signature prior to Taiwan earthquake by Liu et al. (2000). They found that the ionospheric electron density significantly decreases within 6 days before earthquakes. By analyzing the critical frequency of F2 layer (f_0F2), they have found that the peak electron density in F2 layer (NmF2) reduced about 51% from its normal value. Subsequently Liu et al. (2004) observed pre earthquake ionospheric anomalies in Taiwan area and found that the ionospheric total electron content (TEC) decreases a few days before earthquake. Pulinets (1998b) reported that the seismic activities provoke positive or negative variation in electron density, electron temperature, ion and neutral composition etc. Up to now, however, no regularity in sign changes has been found for seismo-ionospheric variations. Increases as well as decreases of the critical frequencies have been observed in the D, E, and F region before earthquake (Zaslavski et al., 1998).

Many satellite data were used to study the ionospheric response to the seismic event and earthquake precursor studies as Inter COSMOS-19, Inter COSMOS-24, OGO-6, Hinotori and SROSS-C2. French micro-satellite 'Detection of Electro-Magnetic Emissions Transmitted from Earthquake Regions' (DEMETER) is particularly dedicated to characterized ionospheric perturbations (ion composition, electron density and temperature, energetic particles) associated with the seismic activity.

Pulinets et al. (1994) have shown that the seismo-ionospheric instability emerge as an upward motion of the F2 layer using the results of topside sounding of the ionosphere from the Intercosmos-19 satellite. Electron density decreases at its maximum (down to 60%) and a small increase in electron density in the topside ionosphere has been recorded 2-3 days before the

earthquake. In some cases the seismic ionospheric variations have amplitude greater than 100% (Pulinets and Legenka, 2003).

Zakharenkova et al. (2007) presented the specific features of TEC response as probable precursor of Kythira earthquake using the data of GPS-IGS. Geomagnetic conditions were quiet well during the period of earthquake. They found day time increase in TEC up to 50% than the background condition, one day before the earthquake. The covering area of TEC enhancement had a size of about 4000 km in longitude and 1500 km in latitude. They have suggested that the ionospheric anomaly can be attributed to the seismogenic electric field, which penetrates into the ionosphere. Many other workers have studied the seismogenic anomalies in the ionosphere (Parrot, 1995; Molchanov and Hayakawa, 1998; Liu et al., 2000; Pulinets et al., 1994, 2003; Hayakawa et al., 1996, 2006; Sharma et al., 2006).

3.3 SEISMOGENIC DENSITY IRREGULARITIES OBSERVED IN THE IONOSPHERE

This study examines the variation in ion density in the ionosphere measured by satellite during the occurrence of earthquake. The ionospheric ion density data recorded by RPA payload aboard the Indian SROSS-C2 satellite during the period from January 1995 to December 2000 were used. Pre and post earthquake ionospheric ion density data were compared to the data recording during the normal days for the same duration. The favorable condition for these variations was the quiet geomagnetic situation during earthquake days.

3.3.1 Data Selection and Analysis

The ion density data (H^+, He^+, NO^+, $NO2^+$) recorded by RPA payload during the period from January 1995 to December 2000 were used for analyzing the ionospheric density variation in F2 region related to the seismic events. The sources of data collection (earthquake, thunderstorm, solar flare, geomagnetic storm) have been described in detail in AppendixA1. The data processing was done to remove the effects due to solar flare, thunderstorm, latitudinal, longitudinal, diurnal, altitude and magnetic storm variation such that

any observed density anomalies can be related as the ionospheric density response to the seismic events only.

Initially, two month's satellite data were selected corresponding to each seismic event. Only those earthquake events have been selected for analyses which were free from the solar flares and thunderstorms. To minimize the effect of high magnetic activity, magnetic storm parameter ∑Kp have been used. ∑Kp variation for the selected events March 12, 1995; May 24, 1995; June 21, 1995; September 05, 1997; December 29, 1997; January 16, 1998; December 18, 1999; December 08, 2000 have already been described in the previous chapter. ∑Kp variation for the remaining events April 26, 1996; July 27, 1996; August 4, 1996; and Ap ril 28, 1999 have been shown in Figure 3.1 (a-d) respectively. The inverted arrows shown in Figure 3.1 indicate the earthquake day and the magnitude of earthquakes are shown on the top of each arrow. The ∑Kp index for considered earthquake days fall below 40, indicating no isolated magnetic activity during the earthquake days. Thus any density anomaly recorded during the earthquake days is free from magnetic activity.

The effect of seasonal variation in the ion density is minimized by carefully selecting the recorded data for one season related to each seismic event. A 5° window in latitude and longitude around epicentral zone has been applied for the data selection corresponding to the event. This would eliminate anomalies due to longitudinal and latitudinal variations. Similarly diurnal effect has been removed by using the data of maximum four hours duration during the occurrence of earthquake. The satellite data has been recorded at an average altitude of ~ 500 km; therefore the ion density data are free from altitude variation. In view of the above constraint applied for events selection, only 12 earthquakes for different ion density components correspond to the satellite data, which are free from solar flare, thunderstorm, latitudinal, longitudinal, diurnal, altitude and magnetic storm variations. For these events any anomalous behavior in the ion density data can safely be interpreted as the ionospheric response to the seismic event only.

Many scientists observed anomalies in electron densities of the ionospheric F region few days before some earthquakes (Pulinets et al., 1994; Pulinets, 1994, 1998a; Gokhberg et al., 1988; Silina et al., 2001; Pulinets and Legenka, 2003; Liu et al., 2000, 2004; Rios et al., 2004). Therefore, we have

considered 5 days (2 days pre, 2 days post and one earthquake day) as earthquake days. This time interval is associated with the earthquake preparation and occurrence in which ionospheric anomalies related to the seismic events might be recorded. Two months satellite data have been analysed for each event in which 5 earthquakes days (as defined earlier) and the remaining days were considered as normal days for density anomalies.

The recorded average ion density during earthquake days has been compared with average ion density during normal days. The details of location, time of occurrence and magnitude of the 12 seismic events studied here is given in Table 3.1.

3.3.2 Results and Discussion on Density Irregularities

SROSS-C2 satellite has generally recorded H^+, He^+, NO^+, $NO2^+$ ion density data. However, all these ion densities were not available for all earthquake events. Types of ion density available for each earthquake are shown in Table 3.1. Ion type and density anomalies observed for each event are shown in Figure 3.2.

Three earthquake events each in 1995 and 1996, two in 1997, one in 1998, two in 1999 and one in 2000 were analyzed. The magnitude of these events varied from 4.0 to 5.2. An earthquake of magnitude 4.7 with the epicenter location (17.64° N, 73.77° E) has been recorded on March 12, 1995. Average H^+ ion density during earthquake days was 3.11×10^9 while the corresponding average H^+ ion density during normal days was 6.73×10^9. The decrease of average H^+ ion density during earthquake days was 54% over the average density during normal days is shown in Figure 3.2 (a), while for the same event the average NO^+ ion density during earthquake days was 7.09×10^9 and the average NO^+ ion density during normal days was 2.72×10^{10} as shown in Figure 3.2 (b). There is also decrease of average NO^+ ion density during earthquake days than the normal days. For the event on 24 May 1995 with epicenter location (16.52° N, 79.68° E), having magnitude 4.6, both H^+, NO^+ ion density shows the decrease in average density during earthquake days over the average density during normal days as shown in Figure 3.2 (c and d). The same analysis for remaining earthquake events (one on 21 June 1995, three in 1996, two in 1997, one in 1998, two in 1999 and one in 2000) for the ion

density was carried out. Except the event recorded in 1997; all the events show the decrease in ion density during earthquake days than corresponding normal days. The decrease in ion density during earthquake days varies from 21% to 95% over the average density during normal days. However, two events of 1997 show the increase in average ion density during earthquake days than the normal days from 43% to 90%. Results of ion density anomalies are summarized in Table 3.1. The average ion density during earthquake days decreases over the normal days in 11 events while one earthquake event shows the increase in average ion density during earthquake days than the normal days.

It may be mentioned here that the density data are free from diurnal, seasonal, latitudinal, longitudinal, altitude, solar flare, thunderstorm and magnetic storm activity. We therefore conclude that the ion density anomalies are related to earthquake events only.

The main sources of atmosphere-ionosphere modification over the regions of preparing earthquakes is the emanation of radon, light gases and submicron aerosols with high metal content during seismic events (Alekseev and Alekseeva, 1992). The gas concentration changes in durations from few hours to several months have been observed previous to many large earthquakes. The emanation of radioactive substances and charged aerosol in the atmosphere leads to a change of vertical electric current in the atmosphere so modify the electric field in the ionosphere. The additional flux of metallic aerosols leads to anomalous field strength. A large numbers of paper have been published on seismo-electromagnetic effects and disturbances of the neutral and ionized upper atmosphere and their possible mechanism (Pierce, 1976; Gokhberg et al., 1984; Pulinets, 1998a; Pulinets et al., 2000; Tsai and Liu, 2004; Hayakawa et al., 2006).

The coupling between the ground surface and the ionosphere is due to the anomalous electric field generated in the earthquake preparation area (Pulinets et al., 2000). Due to equipotentiality of geomagnetic field lines the electric field practically without any decay, penetrates at the higher levels of the ionosphere. In the area of maximal conductivity due to Joule heating acoustic gravity wave will be generated giving rise to the small scale density irregularities within the ionosphere (Hegai et al., 1997; Hegai et al., 2006). This

field produces joule heating, electron temperature growth in the ionosphere and gravity wave generation. The anomalous electric field penetrates into the ionosphere, causes the ion drift that results in the formation of electron densities irregularities (Kim and Hegai, 1997). It is well known that, at the exact time of a strong earthquake, or an underground explosion, acoustic waves induced by the ground motion in the epicentral region can generate disturbances in the ionosphere (Davies and Baker, 1965; Blanc, 1985). It is clear that during and after earthquake the generated acoustic-gravity waves perturb the ionosphere due to their intensity increasing with decreasing atmospheric density (Calais and Minister, 1995). Molchanov and Hayakawa (1998) reported ionospheric effect as transient oscillation pre and post for the duration of a few days and termed as long period gravity waves generation during earthquakes.

The emission and propagation of electromagnetic radiations in a wide frequency band, covering ULF to VLF from epicenter in earthquake region were also reported by several workers (Gokhberg et al., 1984; Parrot, 1995; Hayakawa et al., 1996a, b, 2000). Thus changes in F2 region of ionosphere may be caused by the electromagnetic radiation generated by seismic process and penetration into ionosphere, which leads to additional joule heating in the ionosphere.

We have analyzed the data on the variation of ion density for H^+, He^+, NO^+, $NO2^+$ ions in the ionospheric F2 region, recorded by RPA payload aboard SROSS-C2 satellite around the time of earthquake occurrence for six years. Twelve earthquake events were analysis for the ion density in ionospheric F2 region for which satellite data matches with the epicenter location. Out of 12 events, 10 events show decrease in ion density during earthquake days over normal days while only 2 event show increase during earthquake days than normal days. The observed density variation is consistent with the corresponding temperature anomalies discussed in previous chapter.

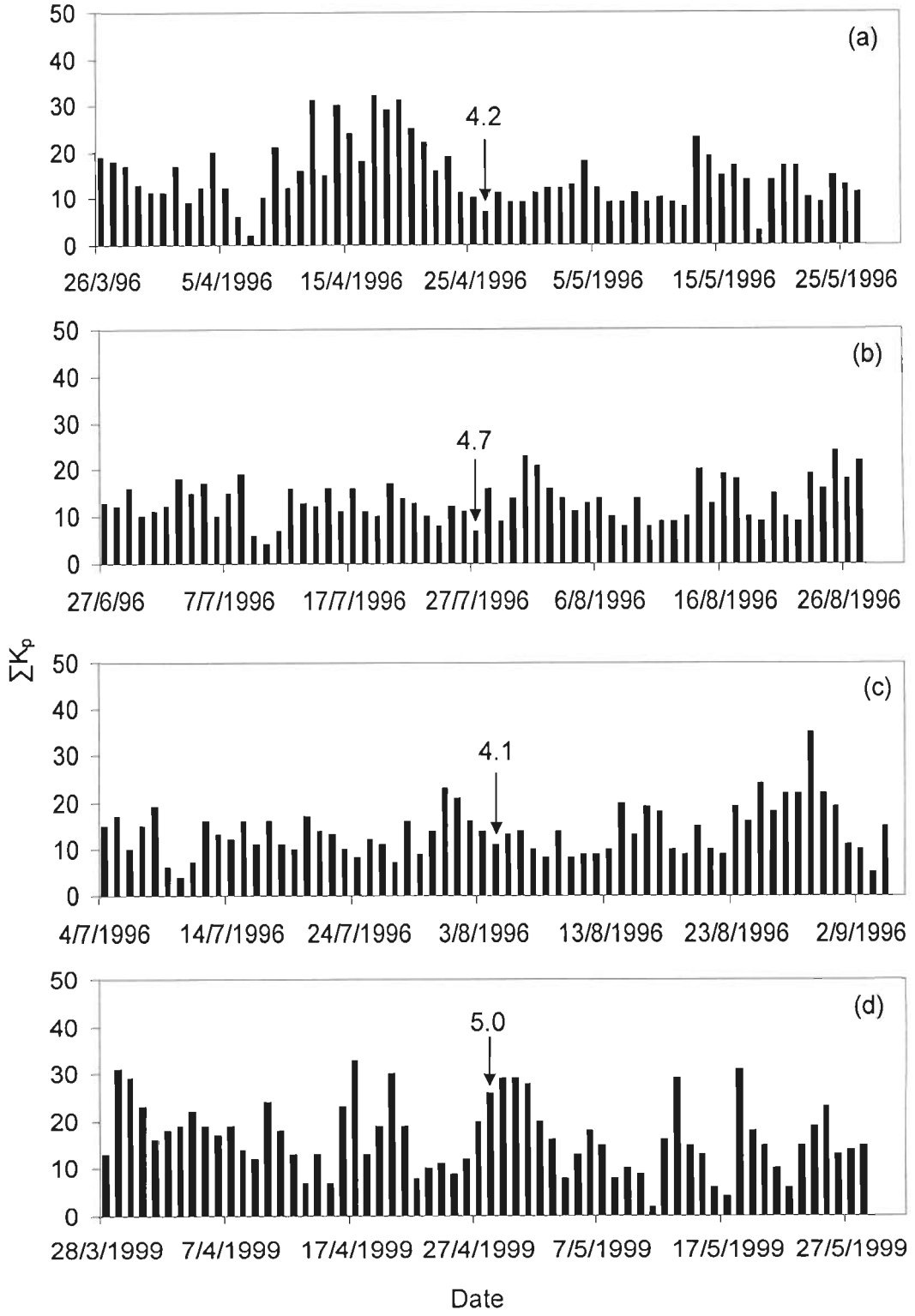

Figure 3.1: Variations of magnetic storm activity (Sum of Kp values) during analysis period for analysis events: (a) April 26, 1996 (b) July 27, 1996 (c) August 04, 1996 (d) April 28, 1999.

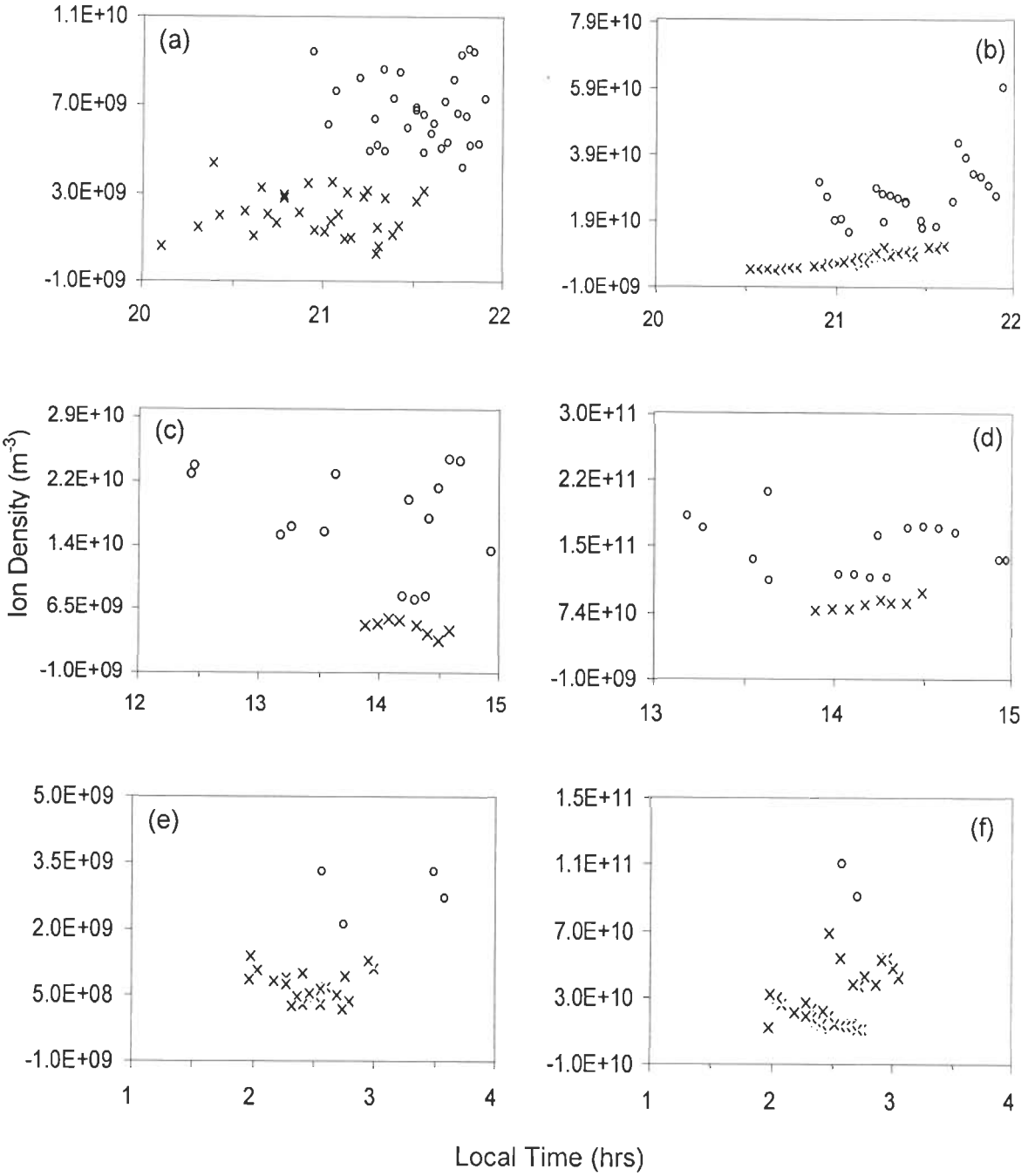

Figure 3.2 continues...

...Figure 3.2 continued

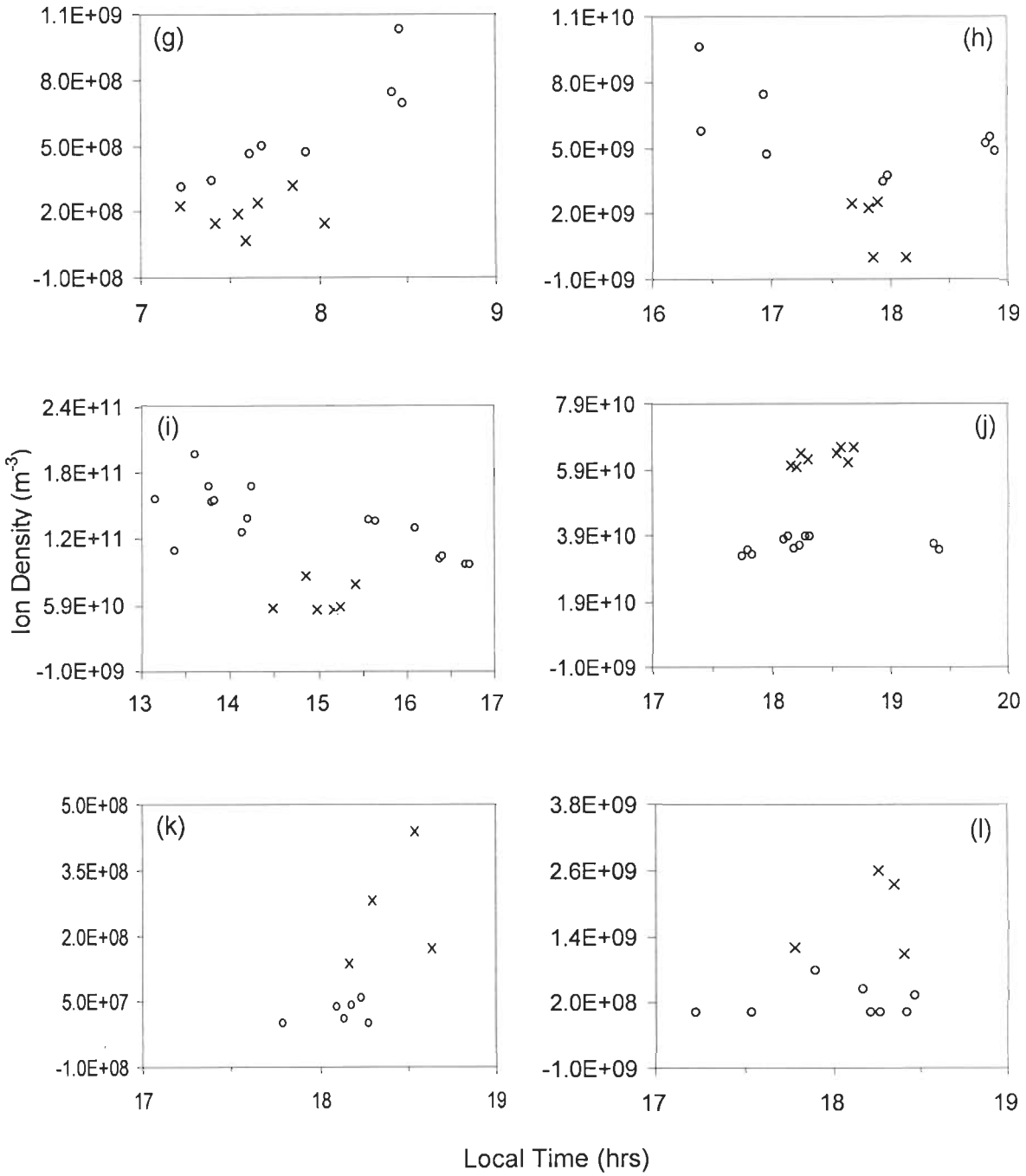

Figure 3.2 continues...

... Figure 3.2 continued

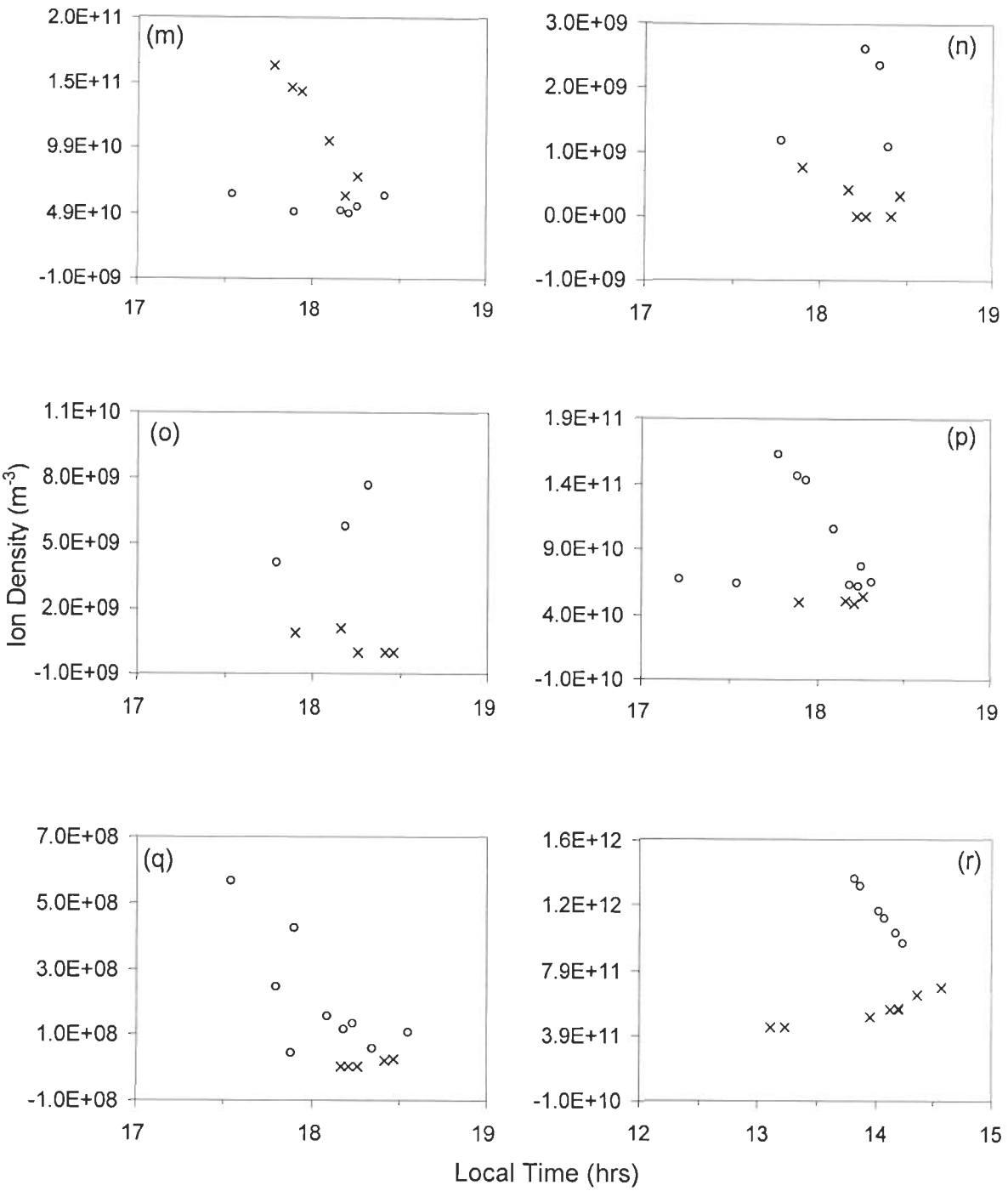

Figure 3.2 continues...

...Figure 3.2 continued

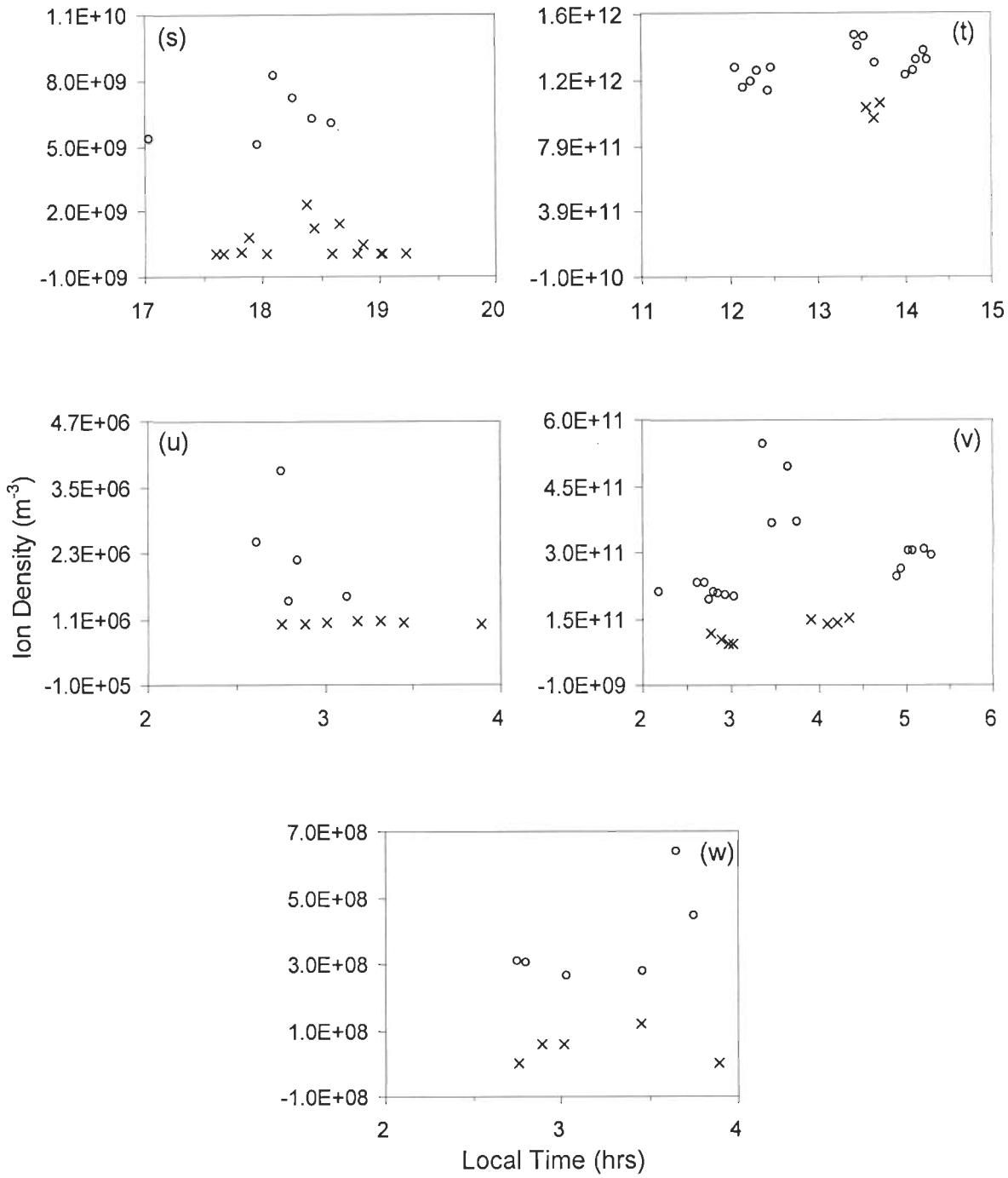

Figure 3.2 continues...

Figure 3.2: Comparison of ion density component during earthquake days along with the normal days for the analysis events: (a) March 12, 1995(H^+), (b) March 12, 1995(NO^+), (c) May 24, 1995 (H^+), (d) May 24, 1995 (NO^+), (e) June 21, 1995(H^+), (f) June 21, 1995 (NO^+), (g) April 26, 1996 ($NO2^+$), (h) July 27, 1996 (He^+), (i) August 04, 1996 (NO^+), (j) September 05, 1997 (NO^+), (k) September 05, 1997 ($NO2^+$), (l) December 29, 1997 (H^+), (m) December 29, 1997 (NO^+), (n) January 16, 1998 (H^+), (0) January 16, 1998 (He^+), (p) January 16, 1998 (NO^+), (q) January 16, 1998 ($NO2^+$), (r) April 28, 1999 (NO^+), (s) April 28, 1999 ($NO2^+$), (t) December 18, 1999 (NO^+), (u) December 08, 2000 (H^+), (v) December 08, 2000 (NO^+), (w) December 08, 2000 ($NO2^+$). [Cross and circle sign represent density of earthquake and normal days].

S. No.	Date of event	Origin time of seismic events (LT)	Location of epicenter	Magn-itude	Depth (km)	Average during earthquake days	Average during normal days	% change
1	12-03-1995, H+	08:22:54	17.64 N, 73.77 E	4.7	10	3.11E+09	6.73E+09	- 54
	12-03-1995, NO+	08:22:54	17.64 N, 73.77 E	4.7	10	7.09E+09	2.72E+10	- 74
2	24-05-1995, H+	13:46:45	16.52 N, 79.68 E	4.6	33	4.40E+09	1.71E+10	- 74
	24-05-1995, NO+	13:46:45	16.52 N, 79.68 E	4.6	33	8.30E+10	1.49E+11	- 44
3	21-06-1995, H+	18:35:41	21.78 N, 85.33 E	4.7	33	7.26E+08	2.8E+09	- 74
	21-06-1995, NO+	18:35:41	21.78 N, 85.33 E	4.7	33	2.73E+10	1.01E+11	- 73
4	26-04-1996, NO2+	12:19:33	17.16 N, 73.56 E	4.2	22	1.91E+08	9.41E+08	- 80
5	27-07-1996, He+	08:16:46	18.21 N, 87.43 E	4.7	33	1.43E+09	5.50E+09	- 74
6	04-08-1996, NO+	21:51:55	16.01 N, 79.85 E	4.1	10	6.42E+10	1.32E+11	- 51
7	05-09-1997, NO+	15:41:51	33.83 N, 72.82 E	4.0	16	6.27E+10	3.58E+10	+ 43
	05-09-1997, NO2+	15:41:51	33.83 N, 72.82 E	4.0	16	2.56E+08	2.45E+07	+ 90
8	29-12-1997, H+	03:33:32	29.96 N, 69.32 E	4.1	33	1.80E+09	1.87E+08	+ 90
	29-12-1997, NO+	03:33:32	29.96 N, 69.32 E	4.1	33	1.16E+11	5.46E+10	+ 53
9	16-01-1998, H+	21:14:51	29.70 N, 68.25 E	4.1	33	2.49E+08	1.80E+09	- 86
	16-01-1998, He+	21:14:51	29.70 N, 68.25 E	4.1	33	3.97E+08	5.83E+09	- 93
	16-01-1998, NO+	21:14:51	29.70 N, 68.25 E	4.1	33	5.05E+10	9.54E+10	- 47
	16-01-1998, NO2+	21:14:51	29.70 N, 68.25 E	4.1	33	1.06E+07	2.04E+08	- 95
10	28-04-1999, NO+	13:00:47	33.24 N, 73.22 E	5.0	19	5.50E+11	1.15E+12	- 52
	28-04-1999, NO2+	13:00:47	33.24 N, 73.22 E	5.0	19	4.41E+08	6.33E+09	- 93
11	18-12-1999, NO+	00:50:34	07.14 N, 94.31 E	5.2	33	1.01E+12	1.28E+12	- 21
12	08-12- 2000, H+	13:23:07	17.04 N, 73.51 E	4.2	33	1.01E+06	2.27E+06	- 56
	08-12-2000, NO+	13:23:07	17.04 N, 73.51 E	4.2	33	1.23E+11	2.87E+11	- 57
	08-12-2000, NO2+	13:23:07	17.04 N, 73.51 E	4.2	33	4.81E+07	3.74E+08	- 87

Table 3.1: The magnitude, location of epicenter, depth and comparison of different ion density component during the earthquake days and normal days.

CHAPTER 4

CHARACTERIZATION OF SCHUMANN RESONANCE IN HIMALAYAN REGION

4.1 INTRODUCTION

Natural electromagnetic waves field in the wide frequency range are generated by various processes associated with atmosphere and solar activities. The fields may either be associated by world-wide lightning/thunderstorm activity (>1 Hz) or the interaction of the solar wind with the earth's magnetosphere (<1 Hz) (Kaufman and Keller, 1981).

Lightning is defined as a discharge of electrical energy between positively and negatively charged regions. It may be classified as cloud-to-cloud, intracloud, cloud-to-air and cloud-to-ground. The lightning process, in case of the cloud-to-ground lightning, begins with electrical charge movement from cloud towards the ground along a path (channel). When this charged channel reaches near an object on the ground, a powerful surge of electrical current, from the ground moves upward towards the charged channel and produces the main lightning strike. The air near a lightning strike is heated to a very high temperature (~ 50,000 ^{0}F) (Rakov and Uman, 2006). The rapid heating and cooling of the air near the lightning causes a shock wave those results in thunder.

A very high current (~ 30 KA or more) in lightning channel flows for a very short duration (about 100 μs). The number of lightning flash is higher in tropics and oceanic region than temperate region. High density of lightning flash is also observed in mountainous regions. An average of about 100 lightning flashes strike each second on earth producing a very strong time varying electric and magnetic fields with Characteristic frequencies of >1 Hz (Kaufman and Keller, 1981). The field propagates to great distances in the waveguide mode between the earth and ionosphere. During the propagation, higher frequency components of electromagnetic field are attenuated while the lower frequency components are enhanced by waveguide propagation. The space between earth and ionosphere acts as resonant cavity for electromagnetic waves, generated by lightning

activities. Schumann resonances (SR) are observed in the power spectra of the electromagnetic field (Balsar and Wagner, 1960) around 8, 14, 20...Hz.

Electromagnetic wave with frequency <1 Hz are mainly generated by geomagnetic micro-pulsation activity, an interaction between magnetosphere and solar wind. Geomagnetic micro-pulsations are temporal variations in the earth's magnetic field that has a quasi-periodic structure in the frequency range from 10^{-4} - 1 Hz (Kaufman and Keller, 1981). The magnetosphere is the region around the Earth to which the earth magnetic field is confined by the solar wind. The solar wind consists of highly energetic ions (protons and electrons) ejected from the sun. These protons and electrons, deflected in opposite directions establish an electric field in the influence of earth magnetosphere (Figure 4.1). The complex interaction of solar wind and earth's magnetic field generates oscillations in the magnetosphere, which in turn result in geomagnetic pulsations and are popularly referred as micro-pulsations which propagate through the ionosphere and reach to the earth's surface (Mcpherron, 2005).

The geomagnetic pulsations are divided into two classes: continuous pulsations (Pc) and irregular pulsations (Pi). According to their frequency, the continuous pulsations (Pc) are further divided into five groups, the frequency range of each group are shown in Figure 4.2. Similarly, the irregular pulsations (Pi) are also divided into two groups (Jacobs et al., 1964). Due to unpredictable character of the geomagnetic pulsations, long time of recording is required to obtain rich spectrum of the signal in full frequency band width.

An example of the power spectrum of natural electromagnetic field is given by Simpson and Bahr (2005) and the same is shown in Figure 4.3. The natural electromagnetic fields were recorded in Himalayan region. The data is analyzed for SR studies in this chapter.

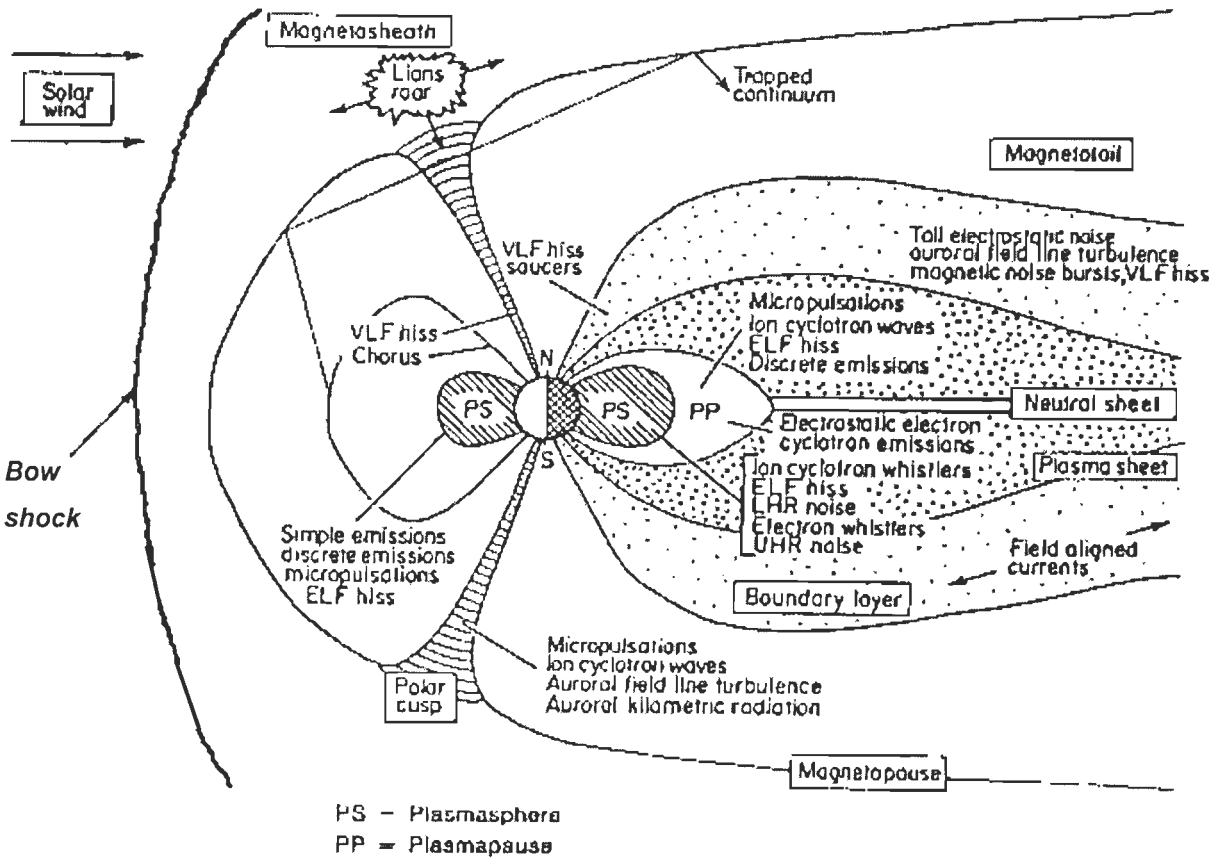

Figure 4.1: Earth's magnetosphere (www-istp.gsfc.nasa.gov).

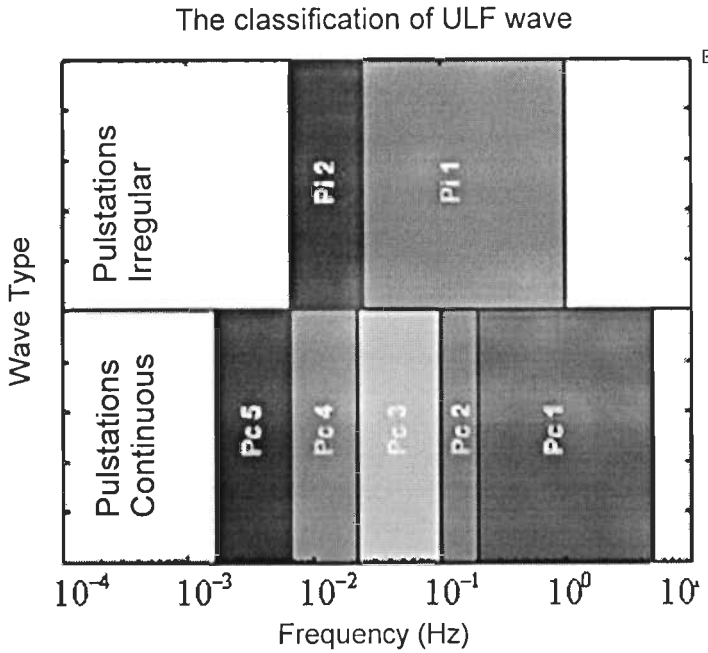

Irregular pulsations		
	Low edge	High edge
Class	Frequency (Hz)	Frequency (Hz)
Pi2	0.006	0.022
Pi1	0.022	1

Continuous pulsations		
	Low edge	High edge
Class	Frequency (Hz)	Frequency (Hz)
Pc5	0.0016	0.006
Pc4	0.006	0.022
Pc3	0.022	0.1
Pc2	0.1	0.2
Pc1	0.2	0.5

Figure 4.2: ULF Waves are classified into two types: continuous pulsation (Pc) and irregular pulsations (Pi): Each type is divided into frequency bands roughly corresponding to distinct phenomena (Jacobs et al., 1964).

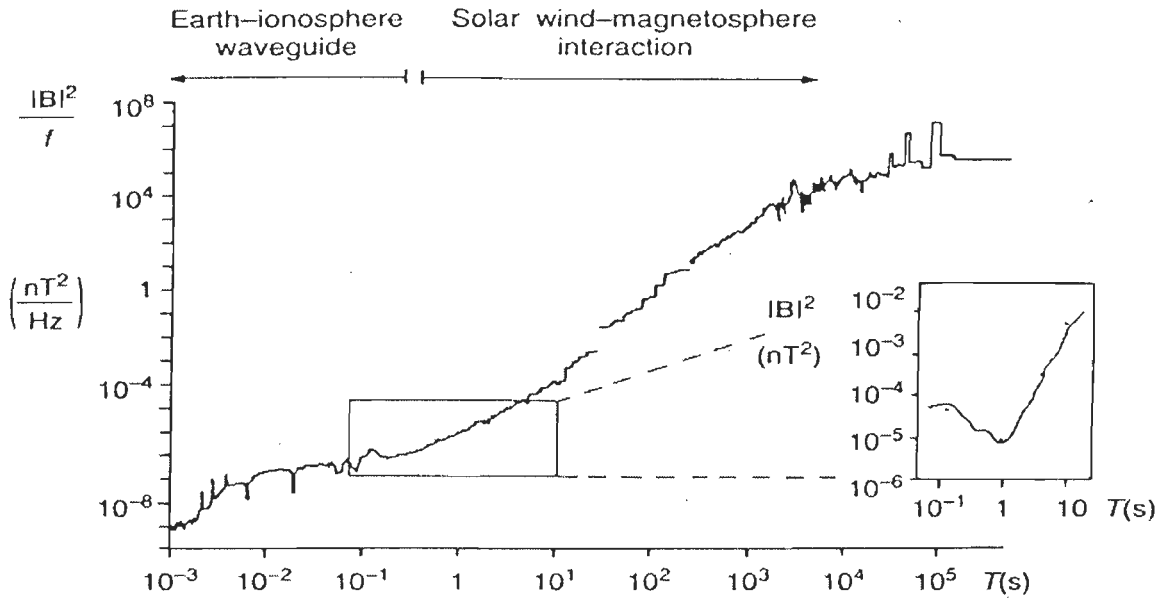

Figure 4.3: Power spectrum of natural magnetic variation (Simpson and Bahr, 2005).

4.2 SITES SELECTION AND EQUIPMENT USED

Natural electromagnetic fields were recorded at 23 sites spread in a corridor along Roorkee-Gangotri and in Pipal Koti (Chamoli) region of Himalaya. Locations of the recording sites (latitude, longitude, altitude and recording time) are given in Table 4.1. Appropriate sites selection is necessary for meaningful data recording in the field.

4.2.1 Site Selection

A careful site selection is important for acquiring good quality data which is least affected by man made electrical noise (cultural noise). To avoid any cultural noise, the recording sites should be few hundred meters away from ordinary electrical line and 2 to 5 km away from high voltage power lines. It is evident, from grounding resistance measured at various sites, that the Himalayan terrain is resistive in general, which support the propagation of electrical signal to a very far distance without much attenuation. In the Himalayan region, power lines and vehicular noise were the dominant sources of man made electrical noise.

The Himalaya terrain is very tough and generally not accessible and as a result a lot of time was spent on site selection in finding open areas in the forest and in avoiding roads and power lines. Animals can also be dangerous to data acquisition system as they may disturb cables and system during recording. An optimal compromise has been done to select an appropriate recording site in Himalayan region.

Site No.	Location	Latitude	Longitude	Elevation (m)	Start date and time	Stop date and time	Total recor ding time (hours)
1	Kirgani	30:24:2.79	78:22:58.25	1293	21.02.06 & 12:15 pm	23.02.06 & 9:00 am	45
2	Bore Jolangi (Reservior	30:24:37.41	78:25:32.82	1354	22.02.06 & 11:50 am	25.02.06 & 9:00 am	68
3	Alara	30:26:53.45	78:23:32.15	1216	23.02.06 & 2:55 pm	26.02.06 & 10:00 am	67
4	Kamand (Enchoni)	30:26:23.52	78:21:36.88	1037	25.02.06 & 4:20 pm	27.02.06 & 2:00 pm	45
5	Patha	30:45:2.30	78:26:26.00	1493	10.03.06 & 2:19 pm	13.03.06 & 9:00 am	67
6	Henna (Nelata)	30:44:16.65	78:29:53.58	1228	11.03.06 & 2:26 pm.	14.03.06 & 4:30 pm.	74
7	Matali (Rethal)	30:49:9.62	78:36:37.13	1895	14.03.06 & 11:36 am	17.03.06 & 10:00 am	70
8	Pala (Barsu)	30:50:30.7	78:36:57.91	2015	16.03.06 & 2:16 pm	19.03.06 & 12:30 pm	70
9	Lata	30:46:22.27	78:36:9.22	1404	18.03.06 & 1:25 pm	20.03.06 & 4:00 pm	50
10	Sukkhi	30:59:57.42	78:42:21.61	2389	12.05.06 & 3:30 pm	15.05.06 & 10.00 am	66
11	Gangnani	30:54:10.84	78:40:55.20	2038	13.05.06 & 3:07 pm	16.05.06 & 10.00 am	66

Table 4.1 continues...

...Table 4.1 continued

12	Jhala	31:00:53.41	78:42:52.80	2444	16.05.06 & 4:33 pm	20.05.06 & 11.00 am	85
13	Dharli	31:02:22.42	78:47:56.37	2591	17.05.06 & 8:15 pm	20.05.06 & 11.00 am	62
14	Lanka	31:02:14.82	78:51:21.31	2747	20.05.06 & 3:18 pm	23.05.06 & 10.00 am	66
15	Power House	30:25:02.96	79:24:50.47	1091	11.02.07 & 04:45 pm	16.02.07 & 10.00 am	104
16	Mayapur 1	30:25:2.04	79:24:58.71	1133	12.02.07 & 01:55 pm	14.02.07 & 10.00 am	44
17	Mayapur 2	30:25:14.59	79:24:56.32	1067	14.02.07 & 02:30 pm	18.02.07 & 10.00 am	92
18	Hat 1	30:25:33.92	79:25:17.60	1101	16.02.07 & 02:47 pm	18.02.07 & 10.00 am	42
19	Hat 2	30:25:21.99	79:25:51.89	1092	18.02.07 & 01:35 pm	20.02.07 & 04.00 pm	45
20	Hat 3	30:25:29.28	79:25:04.74	1146	18.02.07 & 04:55 pm	20.02.07 & 10:00 am	40
21	GulabKoti	30:30:31.58	79:29:15.54	1268	07.06.07 & 01:15 pm	13.06.07 & 10:00 am	128
22	Helang 1	30:31:28.82	79:30:00.88	1293	08.06.07 & 01:48 pm	10.06.07 & 05:00 pm	50
23	Helang 2	30:31:46.00	79:30:0.00	1588	11.06.07 & 12:50 pm	13.06.07 & 04:00 pm	50

Table 4.1: The GPS location of 23 stations, data was recorded from Garhwal Himalaya along with the duration of record, at each station.

4.2.2 Description of Magnetotelluric Equipment and Sensors

Magnetotelluric equipment measures the time varying orthogonal electric and magnetic field components. Metronix MT system was used for this purpose. The horizontal orthogonal electric field components (Ex and Ey) were derived by measuring the voltage drop between pairs of non-polarisable electrodes deployed in the ground. These pairs of electrodes were configured orthogonal to each other, with one pair of electrodes oriented in the magnetic north-south (N-S), measure Ex component, and the other in the magnetic east-west (E-W) direction, measure Ey component. The typical separation between the electrodes was kept between 60 to 90 m. Non-polarisable lead/lead-chloride electrodes (EFP06) were used to avoid distortion in the recorded signal. In order to have an optimum common mode rejection ratio of disturbing radio transmitters, the data logger (ADU06), control and storage unit, was located in the center of the electric field dipoles. Figure 4.4 show a typical field recording layout.

Induction coil magnetometer (MFS06) was used to measure the horizontal orthogonal time varying magnetic field components (Bx and By). The induction coil magnetometer consists of a loop of copper wire wound into a high-permeability core and sealed within a shock-resistant casing. The output voltage of an induction coil is proportional to the number of loops in the coil and their cross-sectional area. The response of the induction coil is governed by the rate of change of magnetic flux within the coil (Kaufmann and Keller, 1981). The voltage response recorded by the induction coil is transformed into the magnetic field units using transfer function of the coil. Separate coil was deployed for each horizontal component with a separation of 6-8 m between them in order to avoid any cross-talk. Figure 4.5 shows deployment of induction coil (MFS06) for data recording in field.

The ADU06 is the central core unit of the Metronix MT system. It contains the complete circuitry for analog signal conditioning, the 24 Bit A/D converter, the data storage as well as a very precise GPS controlled time base.

Magnetotelluric data were recorded in the 5 bands: HF, LF1, Free, LF2 and LF3, each band is characterized by different sampling rate. All these bands together constitute complete time series data to cover frequency range from

0.001-1000 Hz. In the Schumann resonance study, we require the ELF band data for the frequency interval of 1-30 Hz, which is covered in LF2 band recorded at 64 Hz sampling rate.

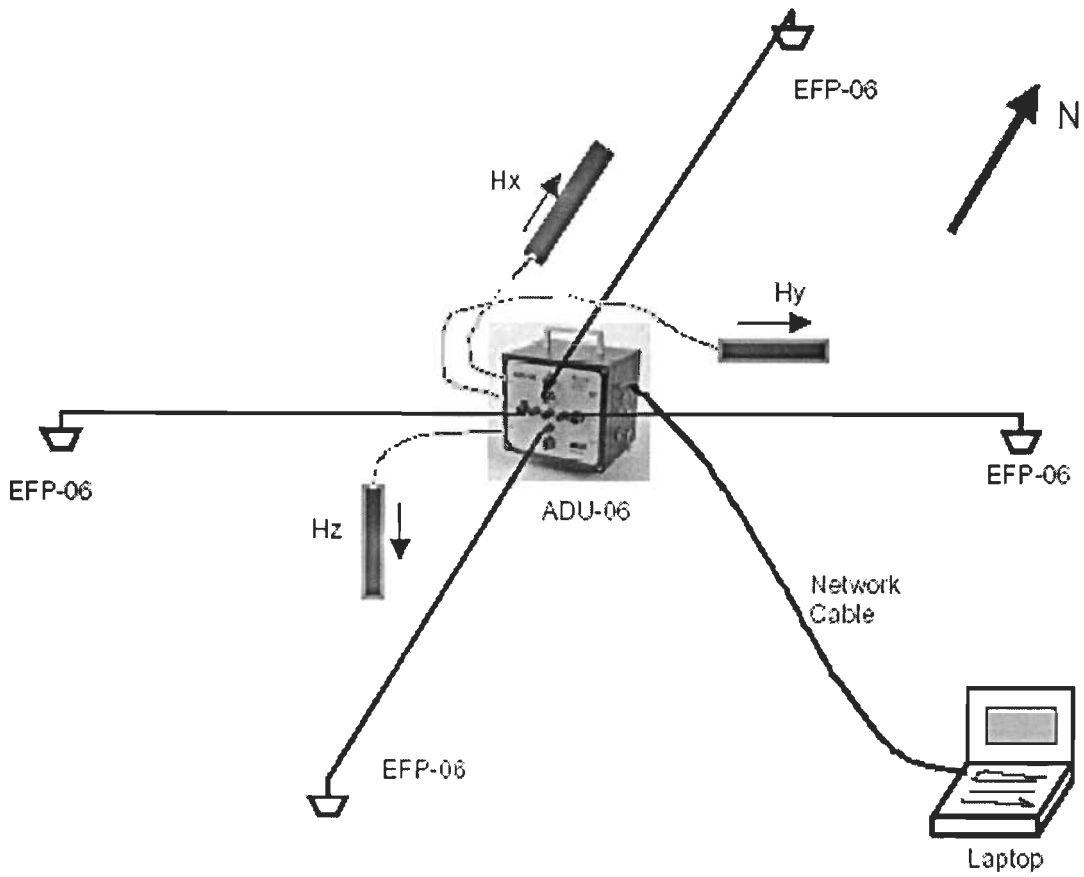

Figure 4.4: Typical 5-channel magnetotelluric field setup (Friedrichs, 2003).

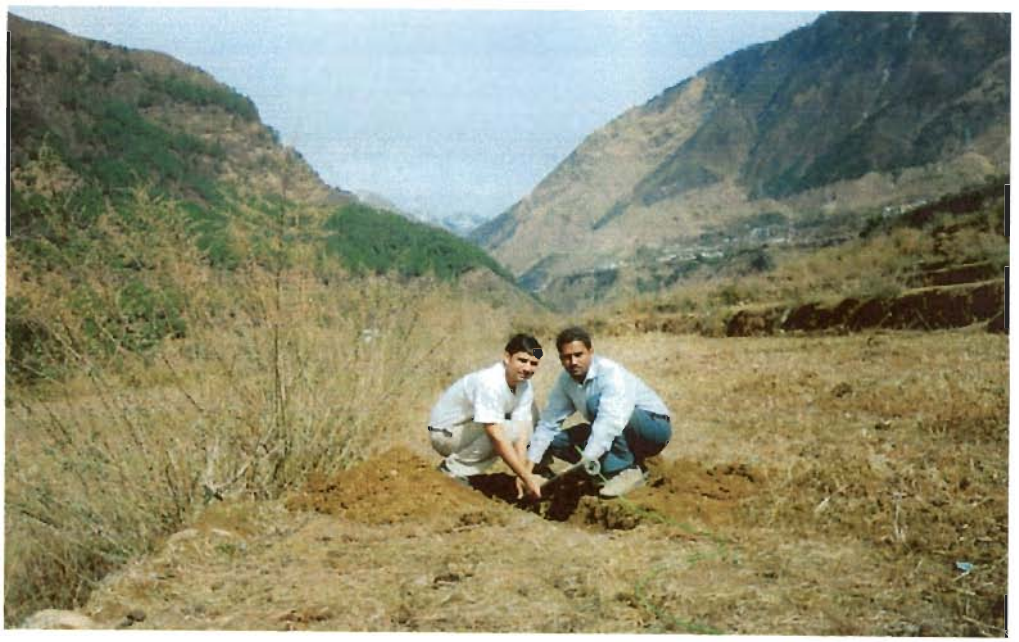

Figure 4.5: Deployment of magnetic field sensors in field at site (Pala).

4.3 GENERAL CHARACTERISTICS OF ELF SIGNALS

Extremely low frequency (ELF) falls in the frequency band between 3 Hz-3 kHz of electromagnetic spectrum. In addition to this, the data were also recorded in ULF and VLF bands. The electromagnetic field in the different band are originated by different sources associated with natural and man made activities. Complex interaction of magnetospheric and solar wind generates electromagnetic field <1 Hz whereas worldwide lightning/thunderstorm activity >1 Hz. Schumann resonance phenomena is significant in the field generated by lightning activity. Approximate 1/f decrease in field amplitude in overall ULF/ELF range is generally observed. The source changes the 1/f characteristics to approximate $1/f^{1.25}$ characteristics in 0.1-2 Hz region (Dea, et al., 1993). As there is no significant energy generated in 2-5 Hz range, a typical frequency spectrum shows low amplitude in the 2-5 Hz region (Figure 4.3). We have recorded electromagnetic field in Himalayan region in ULF and ELF bands; however, Schumann resonance frequencies are covered in ELF band and therefore in the present chapter electromagnetic field recorded in ELF band is analyzed. Descriptions of three major classes of ELF signals recorded in Himalayan region are gi ven in the following.

4.3.1 ELF Continuous Background

ELF continuous signal is always present and is the response of the earth-ionosphere cavity to the worldwide lightning activity. It is a stable intensity signal from a few minutes to an hour recorded in LF2 band and its variance remains constant over time intervals of the order of 10-100 minutes. The background signal recorded at Tangni (lat 30:28:50.16; long 79:27:46.58) at an elevation of 1334 m above mean sea level (amsl) in Himalayan region, India, on April 22, 2007 is shown in Figure 4.6.

4.3.2 ELF Flash

ELF flashes are huge transient event, which exceeds the regular background by substantial factor and have different wave form and duration

(Bilokh et al., 1980). These events originate from near lightning activity (Nickolaenko and Hayakawa, 2002) and can saturate output wave form. Figure 4.7 shows an example of such event recorded at Tangni in Himalayan region.

4.3.3 Quiet Burst

Quiet burst (Q-burst) signal is originated by distant powerful lightning stroke and has large magnitude in comparison to the background signal. The electromagnetic field of distant powerful lightning stroke is used as source in magnetotelluric method for investigating conductivity structure of crust. An example of a typical signal contains radiation as well as inductive component (Bliokh et al., 1980) is shown in Figure 4.8 from Pipalkoti area in Himalayan region on April 22, 2007.

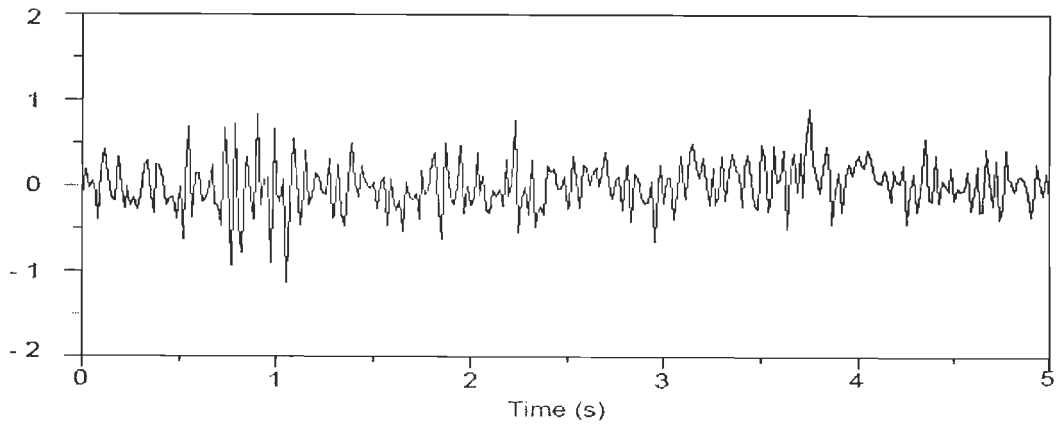

Figure 4.6: Continuous background signal recorded in Ex channel on April 22, 2007 at Tangni site (lat 30:28:50.17; long 79:27:46.59).

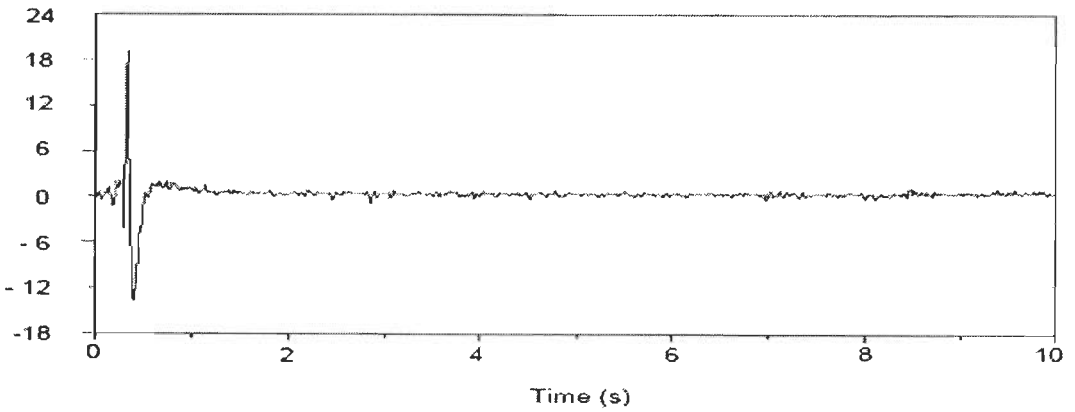

Figure 4.7: ELF flash signal recorded in Ex channel on April 22, 2007 at Tangni site (lat 30:28:50.17; long 79:27:46.59).

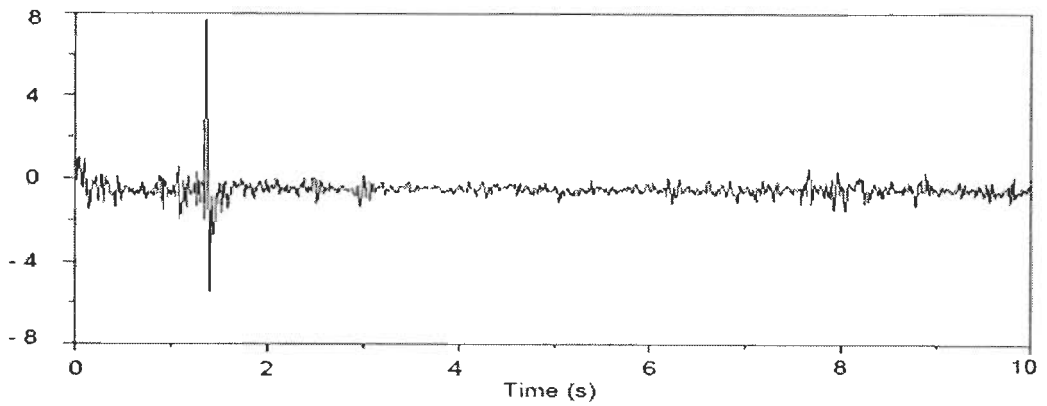

Figure 4.8: ELF burst signal recorded in Ex channel on April 22, 2007 at Tangni site (lat 30:28:50.17; long 79:27:46.59).

4.4 AMPLITUDE AND FREQUENCY CHARACTERISTICS OF SCHUMANN RESONANCE

Schumann (1952) has predicted an ELF resonance in the earth-ionosphere cavity. The resonance occurs between the electromagnetic wave generated by lightning and thunderstorm, traveling along ground surface and returning to the starting point with phase difference of 2πn (n = integer number). Assuming the perfectly conducting earth and ionospheric boundaries, different modes of resonance frequencies can be derived from the following relation (Schumann, 1952),

$$f_n \equiv \frac{\omega_n}{2\pi} \approx \frac{c}{2\pi R_E}\sqrt{n(n+1)} = 10.6\sqrt{\frac{n(n+1)}{2}} \text{ Hz} \qquad (4.1)$$

Where n is an integer, c is the velocity of light and R_E is the radius of earth. According to equation (4.1) the first five resonance frequencies are 10.6, 18.4, 26.0, 35.5 and 41.1 Hz. In reality the ionosphere is not perfectly conducting medium and energy losses due to its finite conductivity, reduce the resonance frequencies to 7.8, 14.1, 20.3, 26.3 and 32.5 Hz (Madden and Thomson, 1965). Characteristics of Schumann resonance frequencies depend on the characteristics of their source, location of o bservation point with respect to the source, and ionospheric electron density/conductivity behavior. Thus for a local region assuming the average constant source distribution, Schumann resonance frequency variations can be used to determine average conductivity profile of the ionosphere (Tran and Polk, 1979a, b). Different attenuation characteristics and frequency shift were observed in N-S (Bx) and E-W (By) magnetic field components (Sentman, 1987, 1989). It has been well established that the resonance frequencies contain information about space time distribution of lightning strokes around the globe. Diurnal variation in SR frequencies depends on the point of observation, which may also vary in different field components (Bliokh et al., 1980; Nickolaenko, 1997; Roldugin et al., 2004a).

Theoretically, SR frequencies can be estimated as eigenvalues, by solving wave equation using spherically symmetric ionosphere. Steady state model for fixed ionospheric conductivity generate constant resonance frequency for each

mode. By incorporating different realistic ionospheric electrical conductivity models, characteristics of resonance frequencies can be estimated (Tran and Polk, 1979a, b; Sentman, 1983).

The vertical electric field and horizontal magnetic field components show the diurnal variation in SR intensities (Sentman and Fraser, 1991; Märcz et al., 1997). The intensities of SR reflect global thunderstorm activity, which excite transverse magnetic normal modes of earth-ionosphere cavity (Balser and Wagner, 1962; Pierce, 1963; Sentman, 1996; Nickolaenko and Hayakawa, 2002). Penetration of electric and magnetic field components of the Schumann resonances into the ionosphere was numerically investigated by Grimalsky et al. (2005) for possible day time and night time variation of conductivity in the ionospheric D- and E- layers. It was shown that the penetration height for magnetic field components is 2-3 times greater than the electric field components. SR intensity and global thunderstorm activity have a night time or early dawn minimum and a maximum in the afternoon hours (Märcz et al., 1997).

Sao et al. (1973) concluded experimentally that the day-to-day variation of the resonance frequency coincides with the variation of the lower ionospheric conductivity. The amplitude of SR shows daily variability due to the polarization of the electromagnetic field radiated by lightning strokes (Füllekrug, 1995). The changes in SR frequencies are sensitive to increase/decrease of conductivity within outer layer (Sátori et al., 2005). It has been found experimentally that the variations in the N-S and E-W magnetic field components occur in anti phase for the first Schumann resonance frequency (Roldugin et al., 2004a). Sátori (1996) studied that the average daily frequency patterns are different for three modes. The frequencies in different magnetic and electric field components for particular resonance mode are not the same. Schumann resonance frequencies determined separately for N-S and E-W magnetic field component differ by 0.5-1.8 Hz (Sentman, 1987, 1989). The variation in first and second mode SR frequency occurred during the intense solar X-ray burst by ~0.2 Hz and 0.3 Hz respectively (Roldugin et al., 2004b). Hayakawa et al. (2008a) showed the short term spectral modification, associated with the Moshiri (Japan) earthquake, in the SR frequency

band of 2.5-40 Hz. For SR amplitude and frequency characterization in the present work, the time series data recoded in LF2 band, with a sampling frequency of 64 Hz have been used.

4.4.1 Amplitude Variation of Schumann Resonances

Time series data in LF2 band was recorded continuously for 24 hours or more. Spectral analysis of time domain records was performed using Fast Fourier Transform (FFT). According to the sampling theory, Fourier transformation of 2048 sample points recorded at 64 Hz sampling frequency (LF2 band), generates a frequency spectrum between 0.03-32 Hz with frequency resolution of 0.03 Hz. The frequency band thus obtained includes first three SR modes. Figure 4.9, shows an example of the hourly amplitude spectrum of two magnetic field components recorded in the form of time series, in LF2 band, from Himalayan region at Dharali (lat 31:02:22.42; long 78:47:56.37) on may 18, 2006. Figure 4.9 shows that generally first three modes resonance frequencies are successfully recovered from the data.

Time domain record of electromagnetic field describes the temporal response of earth-ionospheric cavity. The data are transformed to the frequency domain using FFT algorithms by selected 2048 points (32s) in each window length. Individual spectra, obtained from a segment of 2048 samples points, are averaged over N segments to improve the signal no noise ratio. This stabilization of the spectrum for varying N is displayed in Figure 4.10. The horizontal axis shows the frequency and vertical axis is shifted vertically for each N value, to represent spectra amplitude in arbitrary scale. It is observed that the SR modes are not clearly visible in using only one segment (N=1). When the number, N, of segments increases, the SR modes become visible. The spectrum is stabilized and first three SR modes frequencies clearly visible in spectra of magnetic field (Bx) component for N=32 (Figure 4.10). The objective was to find out the minimum value of *N* desired, for the clear visibility of SR modes frequencies. Figure 4.11 shows the amplitude spectral variation with frequency during the night, sunrise, noon and solar terminator (sunset) in horizontal electric and magnetic field

components. It is clear from the Figure 4.11 that the amplitude spectral variation shows its maximum value during noon time and minimum value during night time. The analysis has been done for one hour local time (LT) data: night (00:00-01:00 h), sunrise (06:00-07:00 h), noon (13:00-14:00 h) and sunset (18:00-19:00 h), averaged and the frequency spectrum was obtained for each of the above time intervals.

4.4.2 Frequency Variation of Schumann Resonances

Diurnal variations of SR frequencies for first three modes have been studied in electric and magnetic field components. Figure 4.12 (a-f) shows the observed diurnal frequency variation for two polarizations. It has been observed that the pair of field components belong to the same polarization (e.g. Ex & Hy, or Ey & Hx) shows the similar frequency variation in all three modes. Therefore it is concluded that the information contain in the two field components (Ex & Hy, or Ey & Hx) corresponding to the same polarization are same. However, frequency variation in the two field components belongs to the different polarization show opposite phase. For example morning sunrise time Ex component shows the decrease in frequency Figure (4.13 a), whereas in Hx it is increased (Figure 4.13 b), hence the frequency variation in Ex & Hx components are opposite in phase (Figure 4.13). This may be mentioned here that the features discussed above are valid in majority of data set analyzed. However, in Figure 4.12 and Figure 4.13 we have presented the different days data in which the feature are prominent. To improve the statistics, average diurnal frequency variation in first three SR modes, in the data recorded from March 10 to May 23, 2006, in magnetic field components along with standard deviation are shown in Figure 4.14. Generally, periodic frequency variations are observed in all field components. For example Hx component shows maximum frequency during LT sunrise (06:00 h) and sunset (18:00 h) in first mode, similarly, Hy component shows minimum frequency during LT sun rise and sun set (Figure 4.14). It may also be mentioned here that in some components, the periodicity is not so clearly visible. The frequency variation in different components varies from 1.9 to 4.2%, 1.5 to 3.1% and 1.8 to 3.4% in first, second and third SR modes respectively.

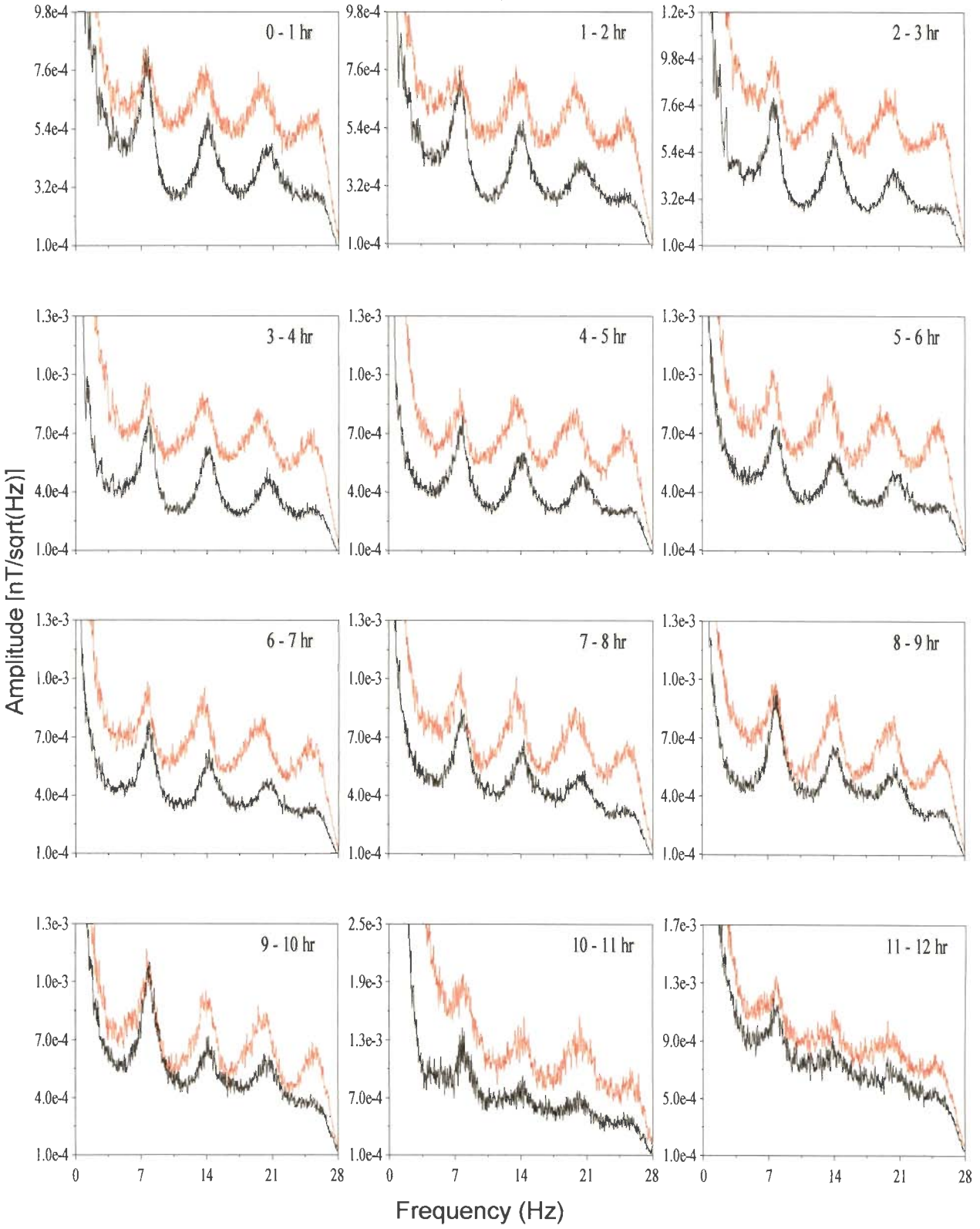

Figure 4.9 continues...

....Figure 4.9 continued

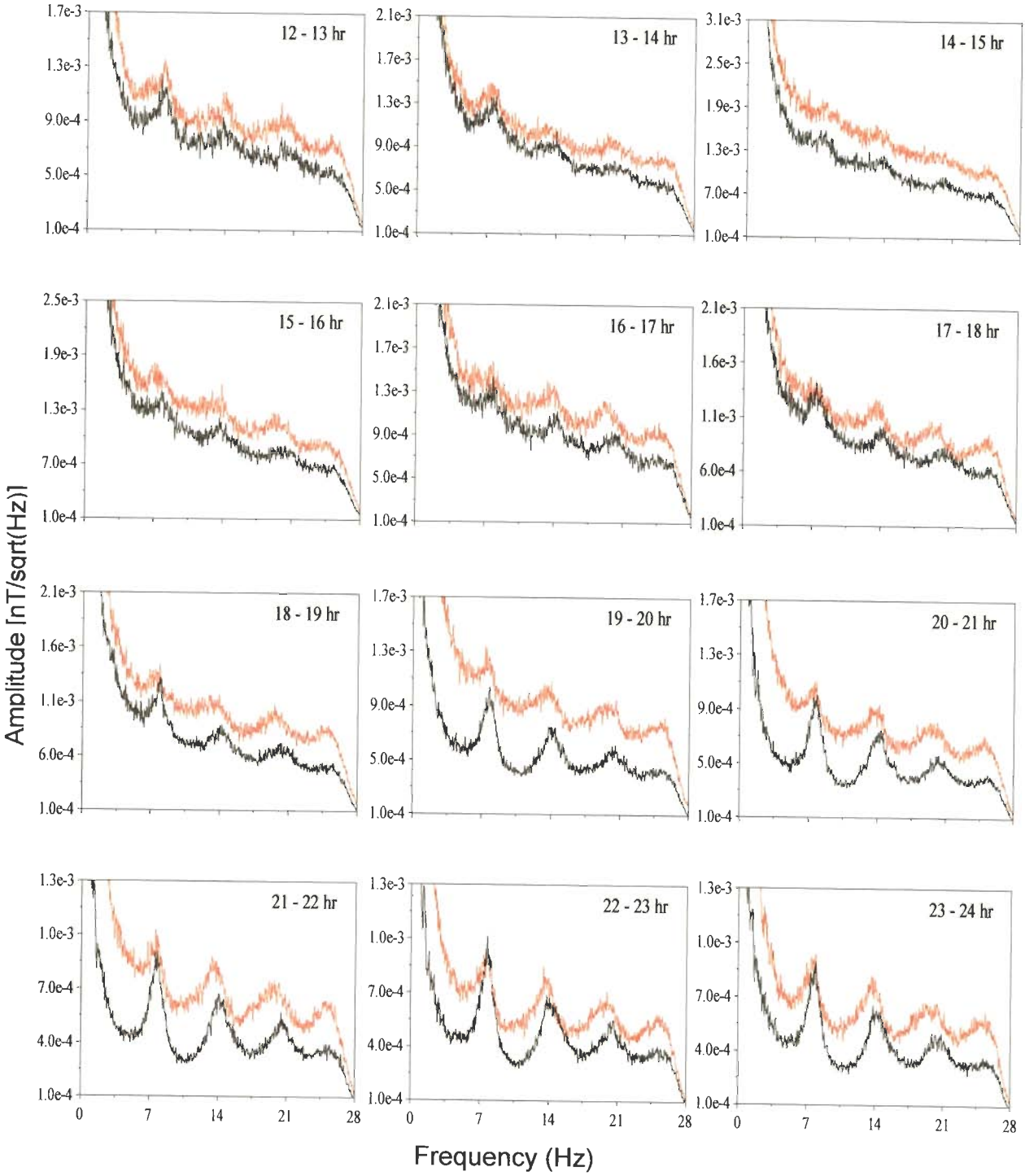

Figure 4.9: The hourly variation in amplitude-frequency spectrum of two magnetic field components (Hx and Hy), from Garhwal Himalayan region recorded at Dharali (lat 31:02:22.42; long 78:47:56.37) on may 18, 2006. Hx and Hy components are shown by black and red colour respectively.

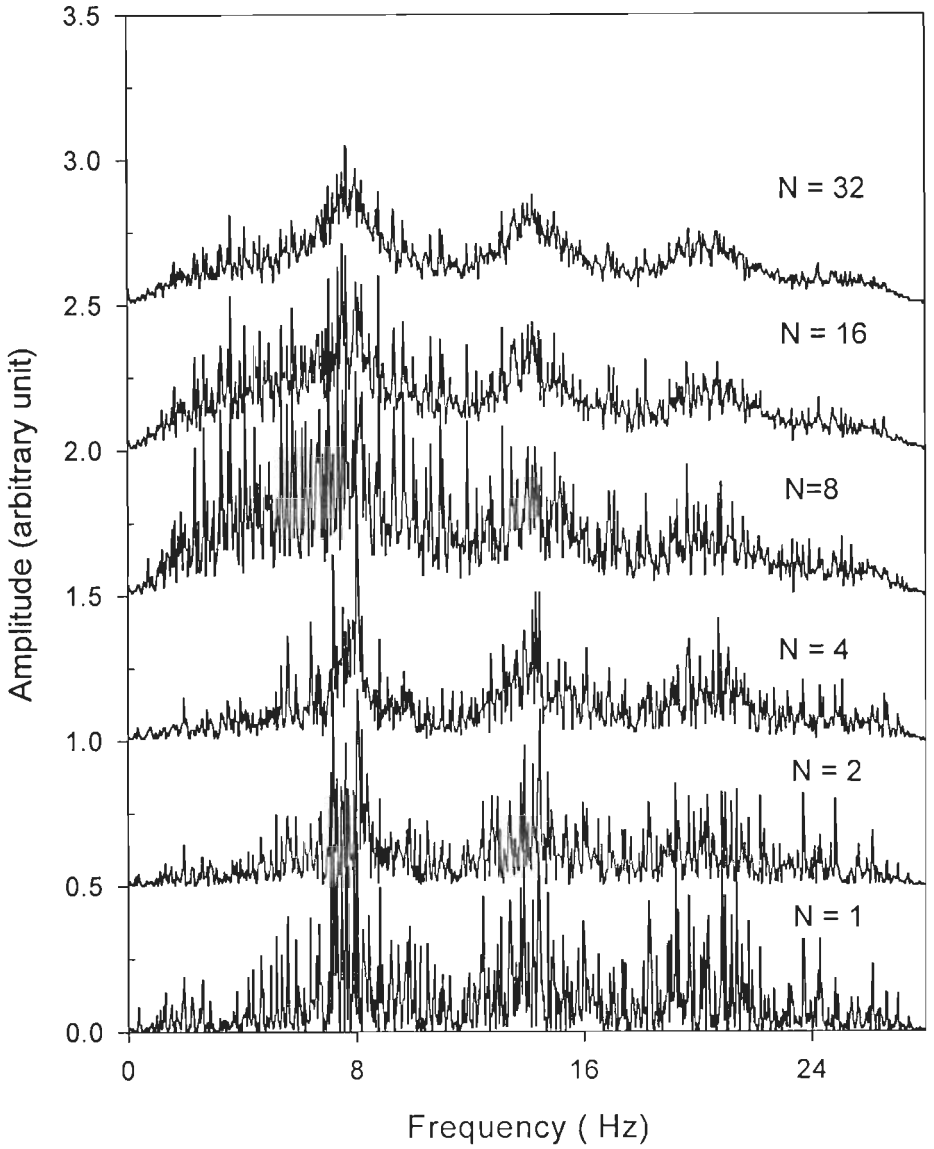

Figure 4.10: Natural stabilization of stacked spectral estimate at first three Schumann resonance (SR) modes for magnetic field (Hx) component in Garhwal Himalayan region. Horizontal axis represents the frequency and vertical axis, the amplitude in shifted arbitrary scale for different number of stacked segment (N).

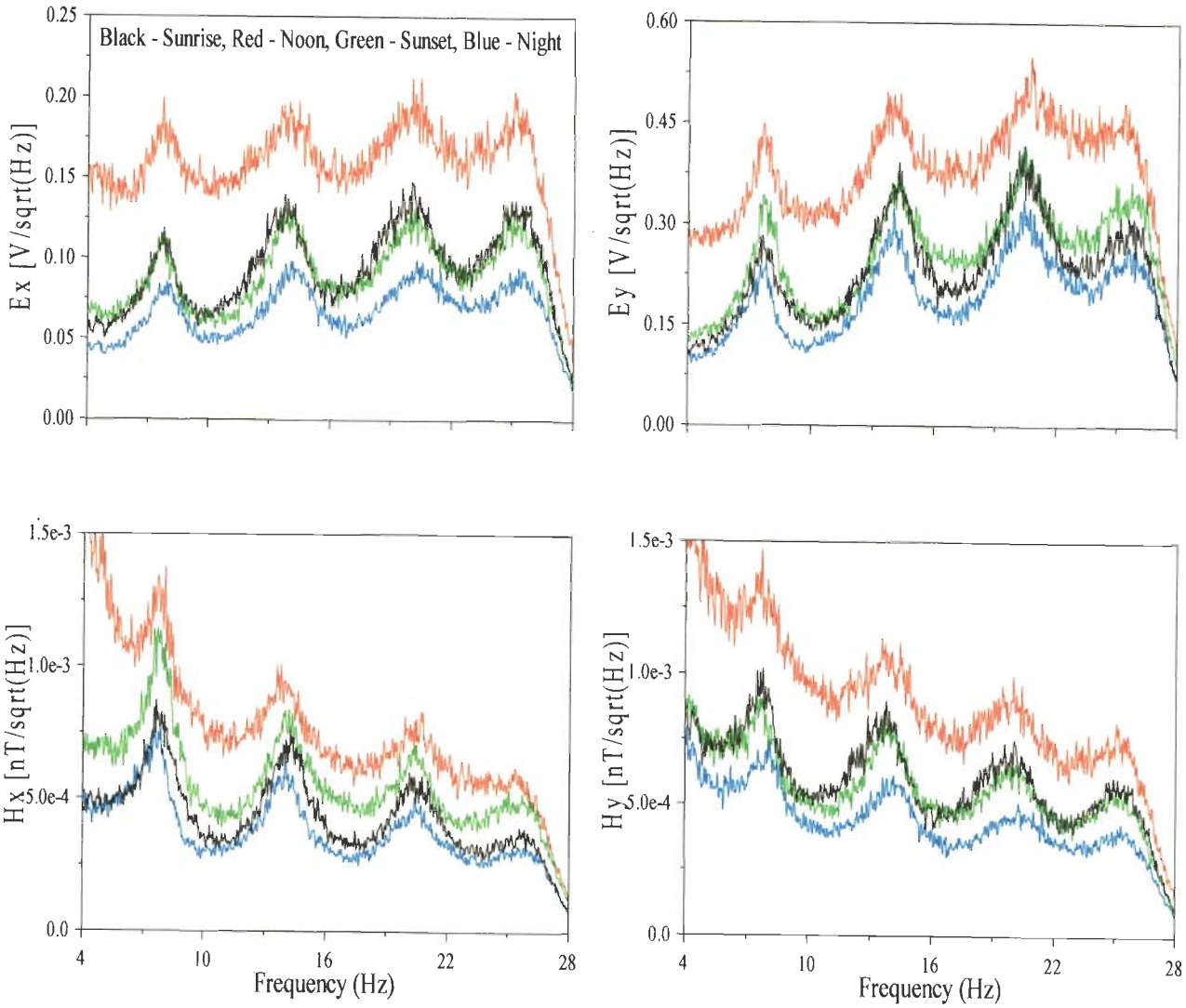

Figure 4.11: Amplitude spectral variation in the frequency during the night, sunrise, noon and sunset time for electric and magnetic field components recorded on 21 May, 2006 at Lanka site (lat 31:02:14.82; long 78:51:21.31). [Black - sunrise, Red - noon, Green -sunset, Blue - night time].

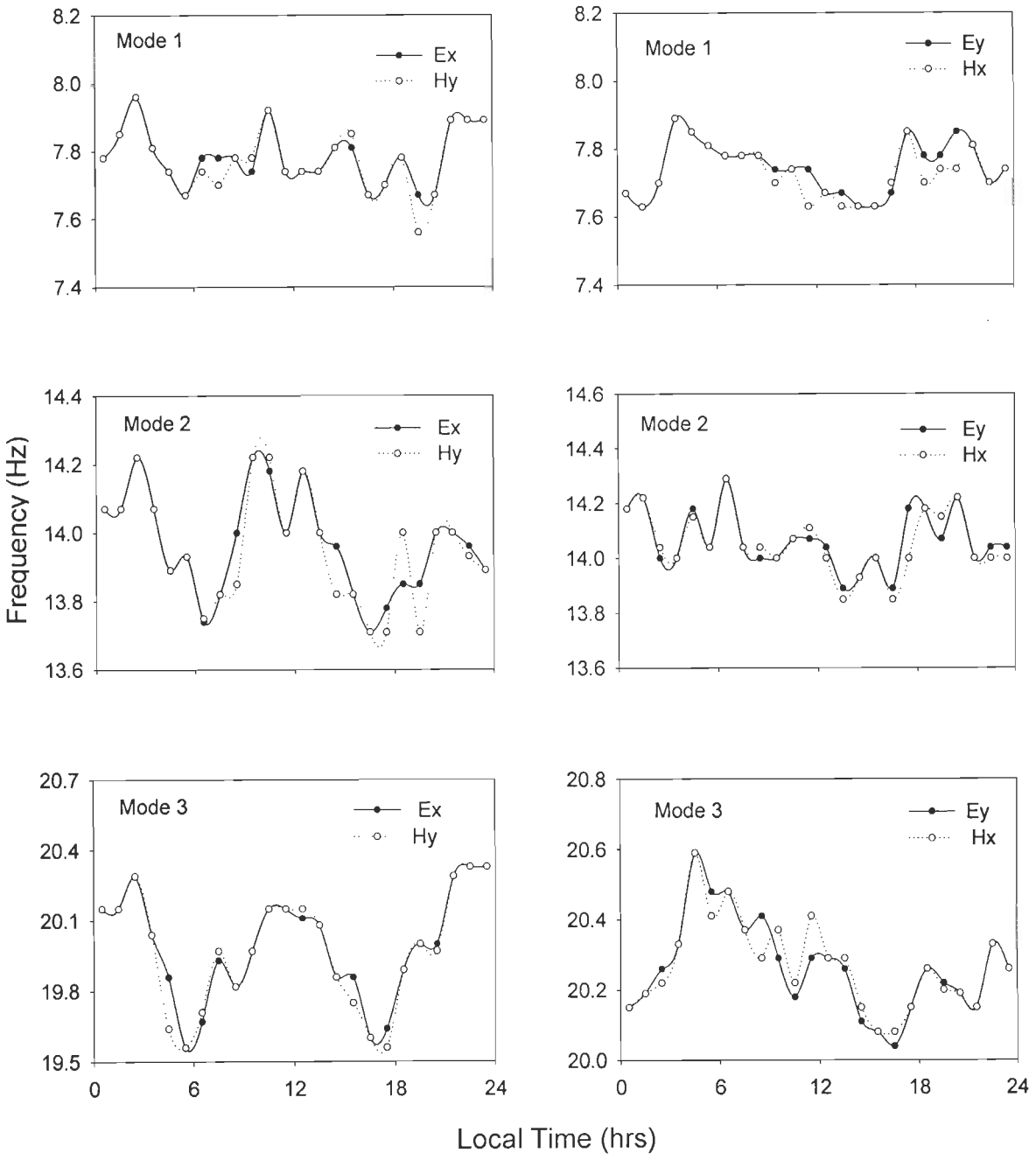

Figure 4.12: The diurnal variations of first three Schumann resonance modes, showing the frequency variation in different components in the same polarization depicting the similar behavior.

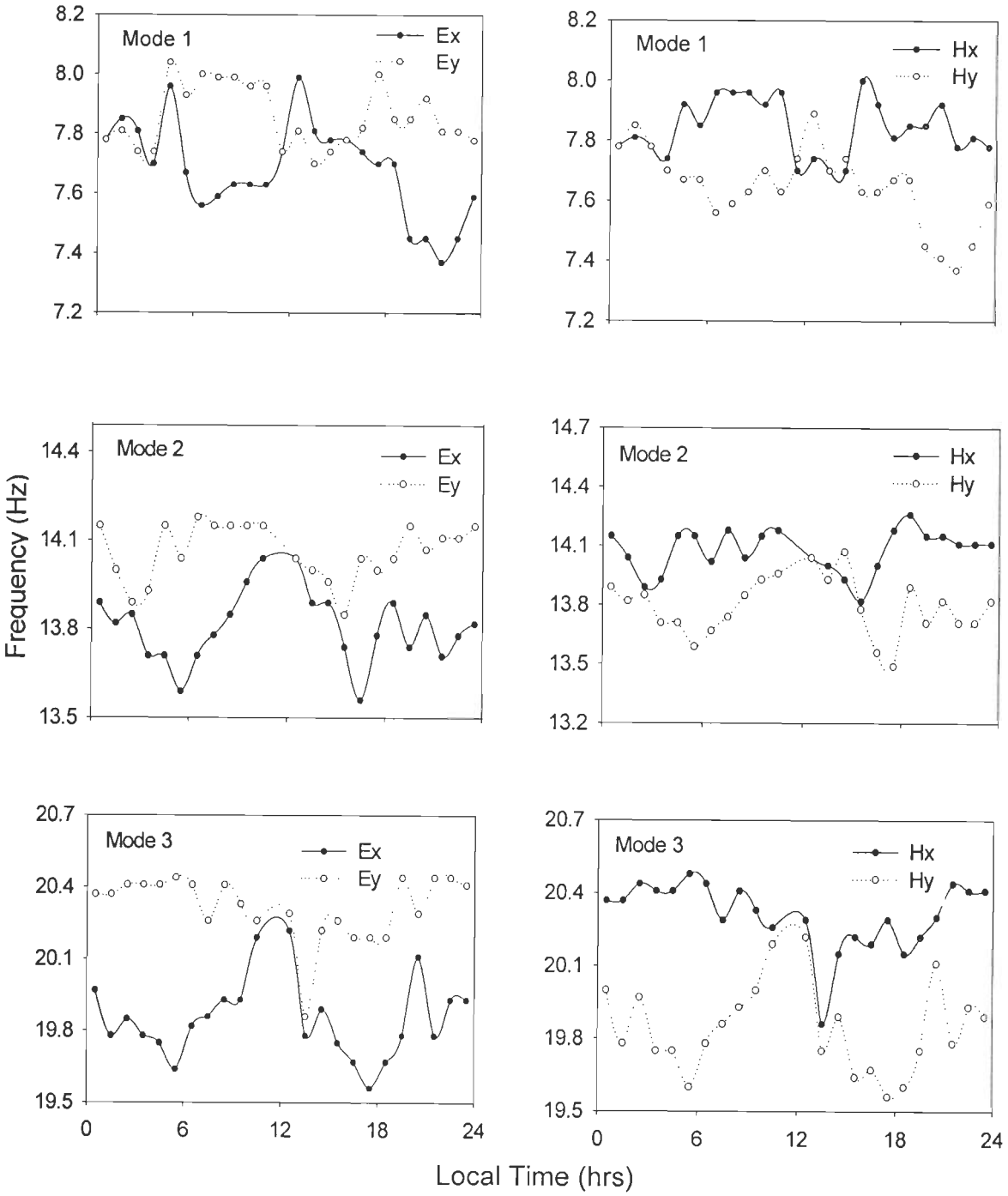

Figure 4.13: The diurnal variations of the first three Schumann resonance modes, showing the frequency variation is in opposite phase in different components.

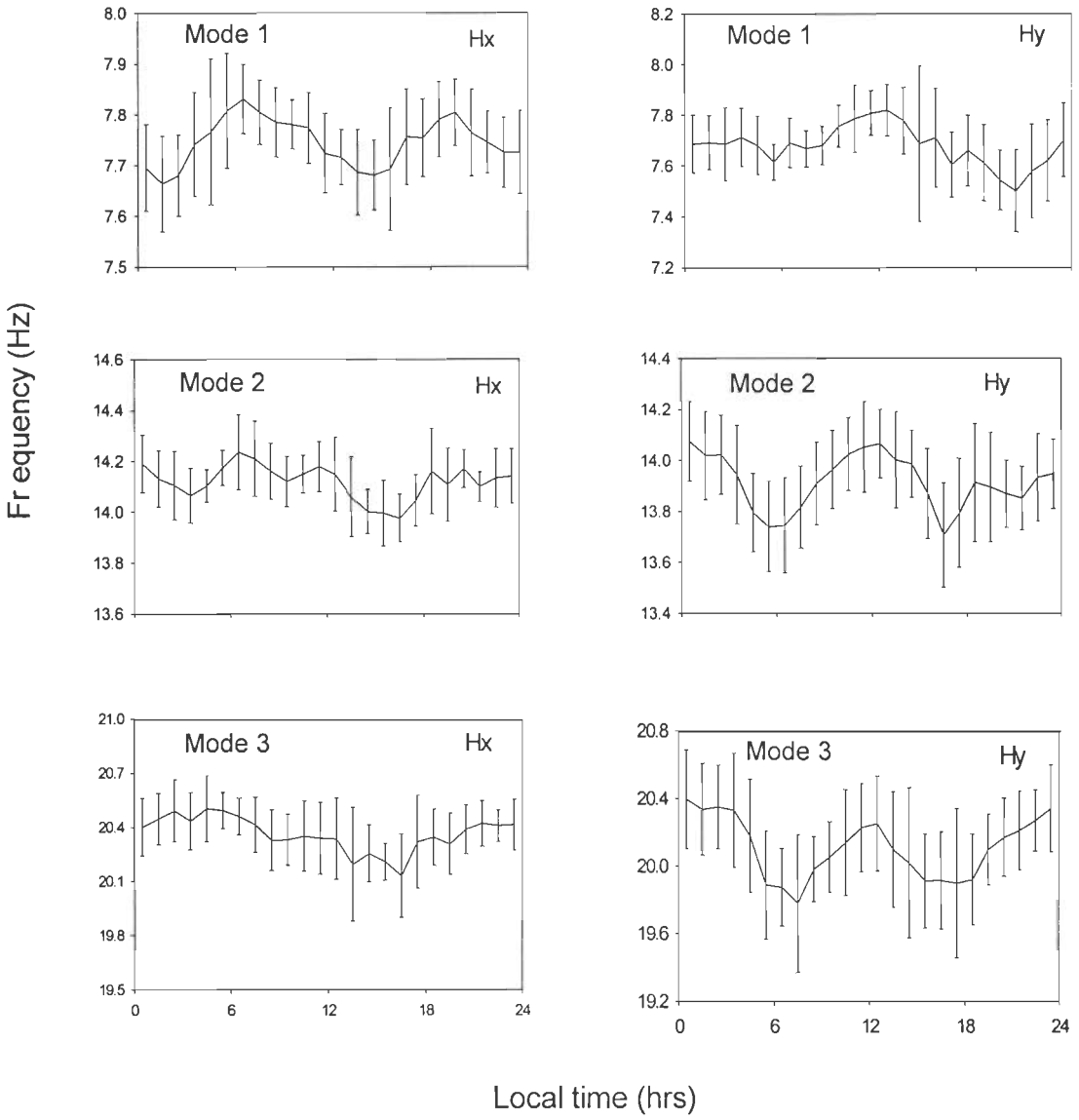

Figure 4.14: The average diurnal frequency variation observed in first three SR modes of magnetic field components during, March 10 to May 23, 2006. Error bar indicates standard deviation.

4.5 ELECTRON DENSITY ESTIMATION IN LOWER IONOSPHERE

Electromagnetic resonance frequencies mainly excited by lightning discharge in the cavity formed by the earth and the ionosphere, were estimated by Schumann (1952); using simplest vacuum model confined with two concentric perfectly conducting spheres. Subsequently, it was investigated that SR frequency depends on the dielectric permeability of ionospheric D-region and the focus was shifted to use more realistic dielectric permeability models of D-region to explain the observed SR frequencies (Balser and Wagner, 1962; Bliokh et al., 1980). Greifinger and Greifinger, 1978; Sentman, 1983, 90; considered, ionospheric model, in which dielectric permeability increases exponentially with altitude, which has generated resonance frequencies, in good agreement with the observations. Sentman and Fraser (1991) showed the dependence of the observed resonance power on the effective height of the ionospheric D-region at the observation point. Ionospheric dielectric permeability is mainly determined by the electron density and the collision frequency between neutral particles and electrons within the lower ionosphere (D-layer). The electron density changes regularly with the position of the sun, during geomagnetic storm and solar flares etc. Any change in the electrons density in lower ionosphere will modify its dielectric permeability, which play an important role in modifying the SR frequency. Rodulgin et al. (1999) showed that the SR frequency depends both on the electron density in the ionospheric D-region and on the base height of this region.

For the interpretation of our data we now consider in some detail the simple model of Rodulgin et al. (2003), for which the authors establish a quantitative relation between SR frequencies and ionospheric parameters, using a two-layer model, where the discontinuous relative electrical permittivity assumes the values [taking z from the Earth's surface positive and assuming a time factor *exp(iωt)*]

$$\varepsilon(z) = \begin{cases} 1, 0 \le z < a, \\ \dfrac{\omega_{02}^2}{i\omega\nu_{e2}} \exp[(z-a)/h] = \dfrac{\sigma_2}{i\omega\varepsilon_0} \exp[(z-a)/h], z > a. \end{cases} \quad (4.2)$$

The first layer is the non-conducting air layer and the second layer models the D-region with its base at z = a. It is characterized either by the plasma

frequency ω_{02} and electron collision frequency ν_{e2} at z = *a* or by the electrical conductivity σ_2 at that level. These parameters can be defined as (Nickolaenko and Hayakawa 2002, Bliokh et al., 1980)

$$\omega_{02}^2 = \frac{N_2 e^2}{m_e \varepsilon_0}, \quad \sigma_2 = \frac{N_2 e^2}{m_e \nu_{e2}} = \frac{\omega_{02}^2 \varepsilon_0}{\nu_{e2}} \tag{4.3}$$

where N_2 is the electron density at z = *a*, *e* the electric unit charge, m_e the electron mass and ε_0 the vacuum permittivity. The model in equation (4.2) assumes that in the D-layer the ratio $N_e(z)/\nu_e(z)$ or equivalently the electrical conductivity $\sigma(z)$ increases exponentially with the scale height *h*. The ionospheric model defined by equation (4.2) is a low-frequency approximation based on the valid relations $\omega << \nu_{e2}$ and $\omega << \omega_{02}^2/\nu_{e2}$. The latter condition means that at the base of the ionosphere, the conduction current is much greater than the displacement current.

From this model of the lower ionosphere, Rodulgin et al. (2003) determine the SR frequencies in terms of the ionospheric parameters. In the following we have worked out Rodulgin et al. (2003) formulation for theoretical calculation SR frequencies and proposed minor correction in their corresponding formula. Rodulgin et al. (2003) have solved following equation for azimuthal magnetic field component (B_Φ)

$$\frac{\partial}{\partial z}\frac{1}{\varepsilon}\frac{\partial B_\phi}{\partial z} = \left(\frac{k_s^2}{\varepsilon} - k^2\right) B_\phi \tag{4.4}$$

Equation 4.4 is first transformed into standard Bessel equation by using following substitution

$$B_\phi = \sqrt{\varepsilon}\, y \tag{4.5}$$

$$x = 2kh\sqrt{\varepsilon} \tag{4.6}$$

$$\nu^2 = 1 + 4k_s^2 h^2 \tag{4.7}$$

$$k_s = \frac{c\sqrt{n(n+1)}}{R_E} \tag{4.8}$$

Using transformation 4.5, 4.6, 4.7 and 4.8, equation (4.4) can be written as

$$\frac{d^2y}{dx^2}+\frac{1}{x}\frac{dy}{dx}+\left(1-\frac{\nu^2}{x^2}\right)y=0 \tag{4.9}$$

Solution of equation (4.9) can be written as in the form of Bessel function as

$$y = AH_\nu^1(x)+BH_\nu^2(x) \tag{4.10}$$

Where $H_\nu^1 = J_\nu(x)+iy_\nu(x)$

$$H_\nu^2 = j_\nu(x)-iy_\nu(x)$$

The values of unknown coefficients A & B in equation (4.10) are obtained by using following boundary condition

$$\frac{\partial B_\phi}{\partial z}\Big|_{z=0}=0, \tag{4.11}$$

$$B_\phi\Big|_{z=a-0}=B_\phi\Big|_{z=a+0}, \tag{4.12}$$

$$\frac{1}{\varepsilon}\frac{\partial B_\phi}{\partial z}\Big|_{z=a-0}=\frac{1}{\varepsilon}\frac{\partial B_\phi}{\partial z}\Big|_{z=a+0}, \tag{4.13}$$

$$B_\phi\Big|_{z\to\infty}\to 0. \tag{4.14}$$

On using boundary conditions, we have found that Rodulgin's corresponding formula is incorrect and the slightly modified expression for the SR frequency is given by

$$\omega = \frac{c\sqrt{n(n+1)}}{R_E}\cdot\frac{1}{\sqrt{1-\frac{2h}{a}\left[\gamma+\ln\left(\frac{\omega_{02}h}{c}\sqrt{\frac{i\omega}{\nu_{e2}}}\right)\right]}}, \tag{4.15}$$

n = 1, 2,..., where γ = 0.577 is Euler's constant. Our formula given by equation (4.15) differs from the corresponding formula of Rodulgin et al. (2003) in two important details

a) The sign in front of γ has been changed from - to +. With this correction, the electron density N_2 as estimated from Re(ω) (with a, h and ν_{e2} given), is reduced by a factor of $\exp(4\gamma)\approx 10$.

b) Also the sign in front of the imaginary unit i has been changed from - to +. This change is required when considering the more complete small argument expansion of the Hankel function as,

$$H_0^{(2)}(\chi) = 1 - \frac{2i}{\pi}[\gamma + \ln(\chi/2)] + O(\chi^2), \qquad (4.16)$$

with $\chi = 2kh\sqrt{\varepsilon_2}$,

where the first term is missing in equation (21) of Rodulgin et al. (2003). The correction changes the sign of the imaginary part of ω and renders Im(ω) positive. This positivity is required in order that the time factor exp(iωt) describes a decaying dissipative signal. On the other hand, the negative imaginary parts of the Schumann resonances produced by the Rodulgin et al. (2003) are incompatible with this time factor.

After inserting reasonable ionospheric parameters into equation (4.15), we also arrive at a reasonable set of SR frequencies. Assuming for example

$$a = 55 \text{ km}, h = 7 \text{ km}, N2 = 4 \times 10^7 \text{ m}^{-3}, \nu_{e2} = 1 \times 10^7 \text{ s}^{-1},$$

the first three SR resonances are:

$f_1 = (7.71 + 0.43i)$ Hz, $f_2 = (13.62 + 0.78i)$ Hz, $f_3 = (19.51 + 1.15i)$ Hz. (4.17)

Since ω occurs also on the right-hand side of equation 4.15, a few iterations are required to get the final values. Apart from the sign, the imaginary parts of the SR frequencies equation (4.17) are about a factor two greater than those predicted by Rodulgin et al. (2003), equations (25) and (27), and are thus closer to the experimentally determined values displayed in their Figure 5.

Equation (4.15) is now used to determine the daily variation of electron density (N_2) from the experimental values of Re (f_n), given *a, h* and ν_{e2}. From equations (4.2) and (4.3) or equations (4.3) and (4.15) it is inferred that only the ratio N_2/ν_{e2} can be resolved. With the parameters a = 61.00 km, h = variable, ν_{e2} = $1x10^7$ (Thrane and Piggott, 1966) the estimated electron density N_2 obtained from equation (4.15) for n = 2 are displayed in Figure 4.15. Then the results are compared with the values derived from the International Reference Ionosphere (IRI) model. It has been observed that for h = 6.5 km, electron density N_2 is closely matching with the values derived from IRI model. The method discussed by Ishisaka et al. (2005) to determine electron density in lower ionosphere, has been used to obtained electron density from IRI model in lower ionosphere. It may also

be mentioned, that the IRI values are shown only in day time as the model is not applicable in night time for lower ionosphere.

Finally, Figure 4.16 shows corresponding display the value Q = $Re(f_n)/[$ $2Im(f_n)$], for scale height (h) = 6.5 km, which gives the number of periods, after which the energy is decreased by a factor of 1/e = 0.37).

The spectral analysis of magnetotelluric data recorded from Himalayan region, India has been done to study the Schumann resonance frequency variation. Orthogonal horizontal (N-S and E-W) time varying electric and magnetic field components data recorded in Himalayan region, at 23 stations during March 10 to May 23, 2006 were used. FFT algorithm has been used to obtain a frequency spectrum with a resolution of 0.03 Hz. Same polarization components, shows a similar variation in SR frequencies. Different frequency variations were obtained for the north-south (N-S) and east-west (E-W) magnetic field components in the SR modes resonance frequency. Spectral analysis shows an average periodic variation in SR frequencies, however, the variation in the two magnetic field components (Hx and Hy) are not in the same phase. The frequency variation is related with the effective size of the thunderstorm and associated ionospheric conductivity. The frequency variation in different components varies from 1.9 to 4.2%, 1.5 to 3.1% and 1.8 to 3.4% in first, second and third SR modes respectively. Further, electron density variation and corresponding attenuation factor in lower ionosphere were estimated from SR frequency observed in Indian region assuming a constant lightning source distribution.

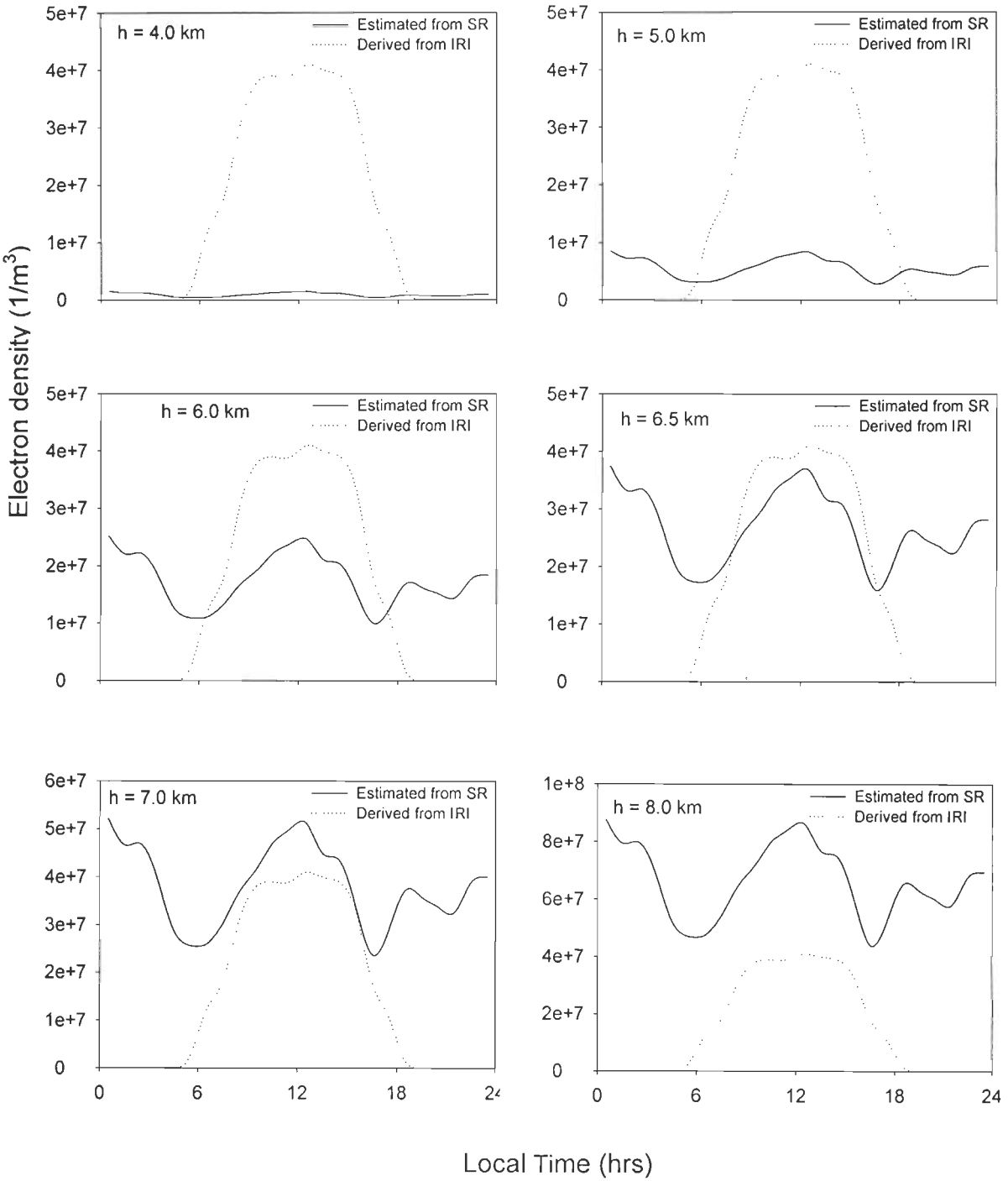

Figure 4.15: Electron number density estimation from Schumann resonance frequency along with values derived from IRI model in lower ionospheric layer (D-layer).

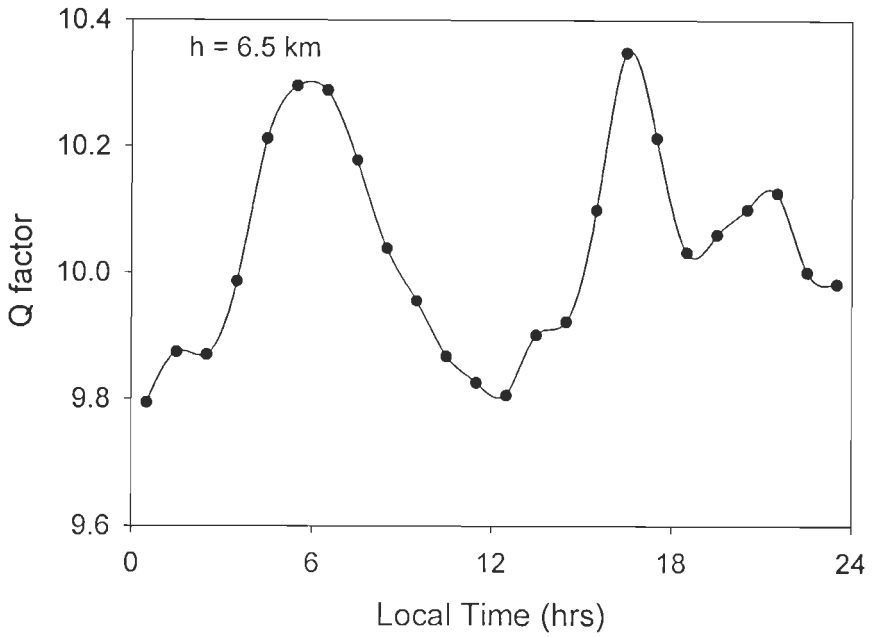

Figure 4.16: The quality factor Q [= $Re(f_n)/[\ 2Im(f_n)]$], which gives the number of periods, after which the energy of electromagnetic wave is decreased by a factor 1/e.

CHAPTER 5

SUMMARY AND CONCLUSIONS

5.1 SUMMARY

Present thesis is devoted to study the ionospheric response to the earthquakes and Schumann resonances. Various chapters of the thesis discussed the ionospheric diurnal and seasonal electron and ion temperature variations. Subsequently, temperature and density anomaly associated with the seismological events in Indian region has been presented.

Amplitude and frequency variations of Schumann resonance modes have been studied in the magnetotelluric (MT) data recorded in the Himalayan region, India. Observed Schumann resonance frequencies have also been used to determine electron density profile in lower ionosphere. Acquired MT data were also used to delineate electrical structure of earth crust along a selected profile in Himalayan region which is not directly related to the topic of the thesis, and therefore added as an appendix in the thesis.

Electron and ion temperature data recorded by SROSS-C2 satellite in ionospheric F2 region during the period from 1995 to 2000 is used for this purpose. In addition to this thunderstorm data for the Indian region were obtained from Indian meteorological department, solar flare data taken from NGDC, USA, seismological data were downloaded from USGS website.

For Schumann resonance study, MT data recorded during February, 2006 to June, 2007 in Himalayan region was used. Observed resonance frequencies were used to define electron density in the lower ionospheric region using a simple two layer model.

Diurnal variation in electron temperature shows the 'morning overshoot' to about 3 to 5 times of average electron temperature and 1.5 to 2 times of average ion temperature during the sunrise hours. It was found that the electron and ion temperature ratio (Te/Ti), was almost unity during the night time and shows variations during the day time in all seasons.

The ionospheric electron temperature response to earthquakes has been studied for 14 earthquake events and found that 13 events out of 14 show increase in average electron temperature during earthquake days by an amount approximately 1.1 to 1.5 times of the normal days. Whereas, 15 events were studied for ion temperature out of which 14 events show the increase in ion temperature during earthquake days by an amount 1.1 to 1.3 of the normal days. Electron and ion temperature data were analyzed in such a way that the diurnal, seasonal, latitudinal, longitudinal, altitudinal, solar flare, thunderstorm and magnetic storm variations are not masked with the earthquake anomalies. The seismogenic vertical electric field and associated electromagnetic radiation from epicentral zones reaches up to ionospheric height, induces joule heating and might be responsible for the ionospheric temperature perturbation.

Ion density response to the 12 earthquake events were analyzed in ionospheric F2 region for which satellite data matches with the epicenter location. Out of these, 10 events show decrease in ion density during earthquake days over normal days while only 2 events show increase during earthquake days than normal days. The observed density variation is generally consistent with the corresponding temperature anomalies. We therefore conclude that in majority of events the ion density anomalies are related to earthquakes.

Schumann resonance (SR) frequency variation using MT data recorded in one of the world toughest and generally inaccessible Himalayan terrain. Spectral analysis of MT time series data at frequency resolution of 0.03 Hz has been performed using Fast Fourier Transform (FFT) algorithm. It has been observed that pair of same polarization components, shows a similar variation in SR frequencies. However, different frequency variations were observed for different polarizations: north-south (N-S) and east-west (E-W) magnetic field components.

SR frequency variation obtained in the recorded data was used to estimate electron density in lower ionosphere. For this purpose we have reformulated Roldugin et al. (2003) analytic expression for SR frequencies in a two-layer wave guide model. We believe, however, their corresponding formula is incorrect and proposed the slightly modified alternative expression relating SR frequency with

the electron density in the lower ionosphere. We have then estimated the electron density in lower ionosphere from SR frequencies. The estimated electron density has been compared with the values derived from the International Reference Ionosphere (IRI) model.

Magnetotelluric data recorded in Himalayan region were also used to determine electrical structure of the upper crust to a depth of about 6 km along the selected profile. Based on the regional geology, possible geological interpretation of the Geoelectrical model is presented. The MT studies have been kept in the appendix of the present thesis.

5.2 CONCLUSIONS

Concept of seismo-ionospheric coupling has been used to study the ionospheric temperature and density anomalies associated with the seismic events in Indian region. The main data used for this purpose were recorded by the SROSS-C2 satellite using Retarded Potential Analyzer (RPA) pay load. The data selection and analysis were challenging in the sense that one has to first match the satellite recorded data with epicentral zone of the earth quake. This process has left with a very limited data matching with the earthquake events. In majority of the events studied in the present thesis shows a consistent increase in the temperature as a response to the earthquake. For the density anomalies the response is negative which is in general consistent with the corresponding density anomalies.

In the present work it has also been demonstrated that magnetotelluric data can be used to study the Schumann resonance frequency variation. It is now possible to carry out SR studies as an integral part of MT studies. Apart from the amplitude and frequency characterization of first three SR modes frequencies, the study was also extended for the estimation of electron density in the lower ionosphere. For this study we have now considered in some detail the simple model of Rodulgin et al. (2003), for which the authors establish a quantitative relation between SR frequencies and ionospheric parameters. A two-layer model, where the discontinuous relative electrical permittivity assumes the exponential

variation with height was used for theoretical computations. The first layer is the non-conducting air layer and the second layer models the D-region with its base at z = a. It is characterized either by the plasma frequency ω_{02} and electron collision frequency ν_{e2} at z = *a* or by the electrical conductivity σ_2 at that level. Our formulation differs from the corresponding formula of Rodulgin et al. (2003) in two important details:

(a) The sign in front of γ has been changed from - to +. With this correction, the electron density N_2 as estimated from Re*(ω)* (with *a, h* and ν_{e2} given), is reduced by a factor of $\exp(4\gamma) \approx 10$.

(b) Also the sign in front of the imaginary unit *i* has been changed from - to +. This change is required when considering the more complete small argument expansion of the Hankel function as,

$$H_0^{(2)}(\chi) = 1 - \frac{2i}{\pi}[\gamma + \ln(\chi/2)] + O(\chi^2),$$

with $\chi = 2kh\sqrt{\varepsilon_2}$,

where the first term is missing in equation(21) of Rodulgin et al. (2003). The correction changes the sign of the imaginary part of ω and renders Im(ω) positive. This positivity is required in order that the time factor exp(iωt) describes a decaying dissipative signal. On the other hand, the negative imaginary parts of the SR resonances produced by the Rodulgin et al. (2003) are incompatible with this time factor. Apart from the sign, the imaginary parts of the SR frequencies are about a factor two greater than those predicted by Rodulgin et al. (2003), and are thus closer to the experimentally determined values. It has been observed that for *h* = 6.50 km, electron density N_2 is closely matching with the values derived from IRI model.

5.3 SCOPE OF FUTURE WORK

1. The science of the earthquake response to the ionosphere is not exact and also not very well defined. Most of the work is based on the observational data which are associated with its own limitations in terms of quantity and

quality. Results presented in this thesis are also based on the finite data set. These results would be more meaningful if supported by some theoretical conceptual model. Due to paucity of time this could not be attempted here and could be undertaken in future.

2. In the present work it has been established that Schumann resonance studies is possible by the data set collected for magnetotelluric investigation. Therefore Schumann resonance studies could form an integral part of MT studies and no separate data set is required for Schumann resonance studies. More data could be recorded in future to study the seasonal variation in SR frequency modes.
3. In the present study electron density in the lower ionosphere has been estimated using a simple two layer model. This approach could be further extended to determine earth's outer layer conductivity globally.
4. More realistic layered model for the ionosphere may be used to determine electrical characteristic of ionosphere and earth using Schumann resonance frequency variations.

APPENDIX A1

THE RPA PAYLOAD AND THE IONOSPHERIC MEASUREMENTS

During last four decades the ionosphere has been studied widely by many researchers on using experimental measurements of ionospheric parameters as well as theoretical models. Many instruments like satellites, rockets, balloons, coherent and incoherent scatter radar, magnetometers and some ground-based system have been used to study the ionospheric characteristics (Farley et al., 1967; Evans, 1973; Oyama and Hirao, 1975; Brace and Theis, 1978; Oyama et al., 1985; Su et al., 1995; Watanabe et al., 1995; Bhuyan and Kakoty, 2000; Pulinets et al., 2003; Parrot et al., 2006 and others). Some global models were also developed for the ionospheric studies (Geisler and Bowhill, 1965; Banks and Nagy, 1970; Bailey et al., 1975; Schunk and Sojka, 1982; Tiwari et al., 1985; Tiwari and Yadav, 1987; Tiwari and Verma, 1991; Tiwari and Goyal, 1997; Das and Kumar, 2006; Kumar et al., 2007 and others). It is now well known that ionospheric properties changes with latitude, longitude, altitude, universal time, season, solar cycle, geomagnetic disturbance, seismic activity. These changes occur due to solar UV radiation, energetic particle precipitation, solar flares, sunrise effect, thunderstorms, lightning and sprites, seismic activity, etc. Gravity waves and tides propagating up from the lower atmosphere can appreciably affect the ionosphere. These processes affect the composition, density, and temperatures of electron, ion, and neutral constituents in the ionosphere. At mid-latitudes, the distribution of average electron density tends to be uniform, with a gradual transition from day side high densities to night side low densities. The equatorial electron density also tends to be uniform on the dayside (Schunk and Sojka, 1996).

The composition and temperature of the ionosphere may also vary appreciably from hour to hour, day to day and season to season. The weather disturbances in the ionosphere can affect over-the-horizon radars, High frequency communication surveying and navigation systems that use global positioning

system (GPS), satellite lifetime, satellite tracking, power grids and magnetotelluric sources on the earth (Chamberlin and Hunten, 1987; Kleusberg, 1992; Shapka, 1992 and others).

After some decades of extensive research we have reached to results that specific forecasting are feasible concerning ionospheric behavior. There are several agencies to study the ionospheric system and their effects on other natural atmospheric processes and many man-made activities. Some of these agencies are National Oceanic and Atmospheric Administration (NOAA), National Aeronautics and Space Administration (NASA), European Space Agency (ESA) and Indian Space Research Organization (ISRO), etc.

In this appendix the description of the Retarding Potential Analyzer (RPA) payload of Stretched Rohini Series Satellite (SROSS-C2) launched by ISRO which was used to study the ionospheric density and temperature anomalies, has been presented.

A1.1 SOME IONOSPHERIC PROBES

Since a few decades various instrumental techniques have been used for the ionospheric studies. Generally the data obtained by ground-based ionosonde and by top side vertical sounding from satellite are used for finding the ionospheric anomalies. Studies on the ionospheric response to the seismic events and earthquake precursors were made using Inter COSMOS-19, Inter COSMOS-24, inter COSMOS-1809, OGO-6, Nimbus, GEOS2, DEMETER and SROSS-C2 satellites. Some ionospheric probes are described below through which the characteristics of ionosphere can be studied.

Global Positioning System (GPS) - The dual frequency beacons from the GPS satellites are measured by either a ground based or space based GPS receiver. The relative phase shift of the signal from the two frequencies provides a measurement of the integrated total electron content (TEC) between the GPS satellite and the receiver. The advantage of Low Frequency Array (LOFAR) over GPS is the accuracy as well as resolution both spatially and temporally. The major

benefit of the GPS measurements is that they can be made at any place with comparatively low-cost dual frequency GPS receiver. Gaussiran et al. (2004) used LOFAR as an ionospheric probe to provide regional maps of the TEC and phase distortion.

Sounder - Ground based radio transmitters sweep a frequency band typically from 1 to 20 MHz. The relative time delay of the reflected signal is associated with the electron density directly above the sounder. Sounders are the superb device for determining bottom-side ionospheric characteristics together with the profile and peak densities.

In situ spacecraft instruments - The measurements of the electron density can be made at a point in space with the help of *in situ* spacecraft instruments. These measurements are considered more accurate because these are actually direct local measurements rather than remote measurements, but lack the spatial diversity of a remote sensing technique.

Incoherent Scatter Radar - The radar measures numerous ionospheric parameters from the backscattered power along the beam path. ISR makes excellent measurements of electron density and can steer the beam to cover a large area. ISR data is both spatially and temporally limited due to high construction and operating costs.

A1.2 SROSS-C2 SATELLITE

For the present study RPA payload aboard SROSS-C2 satellite was used. On May 4, 1994 the SROSS-C2 satellite was launched with the help of Augmented Satellite Launch Vehicle (ASLV-D4) rocket in the orbit of about 930 km x 425 km. The apogee of satellite was brought down to about 625 km after two months of its operation in high altitude orbit. The satellite returned to earth on July 12, 2001 after successful operation for seven years continuously. SROSS-C2 was the fourth satellite of the Stretched Rohini Series Satellite Programme of ISRO and it was designed, developed, fabricated and tested at ISRO Satellite Center (ISAC),

Bangalore. The weight of the satellite was 114 kg, carrying 6 kg hydrazine fuel and was designed to generate 50 watt onboard power (Garg and Das, 1995). Figure A 1.1 shows the configuration of satellite with its main parts.

The SROSS-C2 satellite had an orbit having 46° inclination with the equatorial plane. This was a spin-stabilized satellite with spin rate of 5 revolutions per minute keeping the spin axis perpendicular to the orbital plane. Figure A1.2 shows the orbital motion of the satellite. Retarding Potential Analyzer (RPA) sensors face the velocity vector once in each spin cycle of satellite in such orbital motion. The angle θ between the sensor normal and satellite velocity vector keeps on changing from 0 to 360° at the rate of 30°/sec. The RPA measurements are taken when the sensor normal faces the satellite velocity vector but this situation remains for a fraction of a second in a spin stabilized satellite. The RPA sensors collect data within ±30° (for ions) and within ±90° (for electrons) of the satellite velocity vector once in each spin period. The velocity of satellite was 7.8 km/sec.

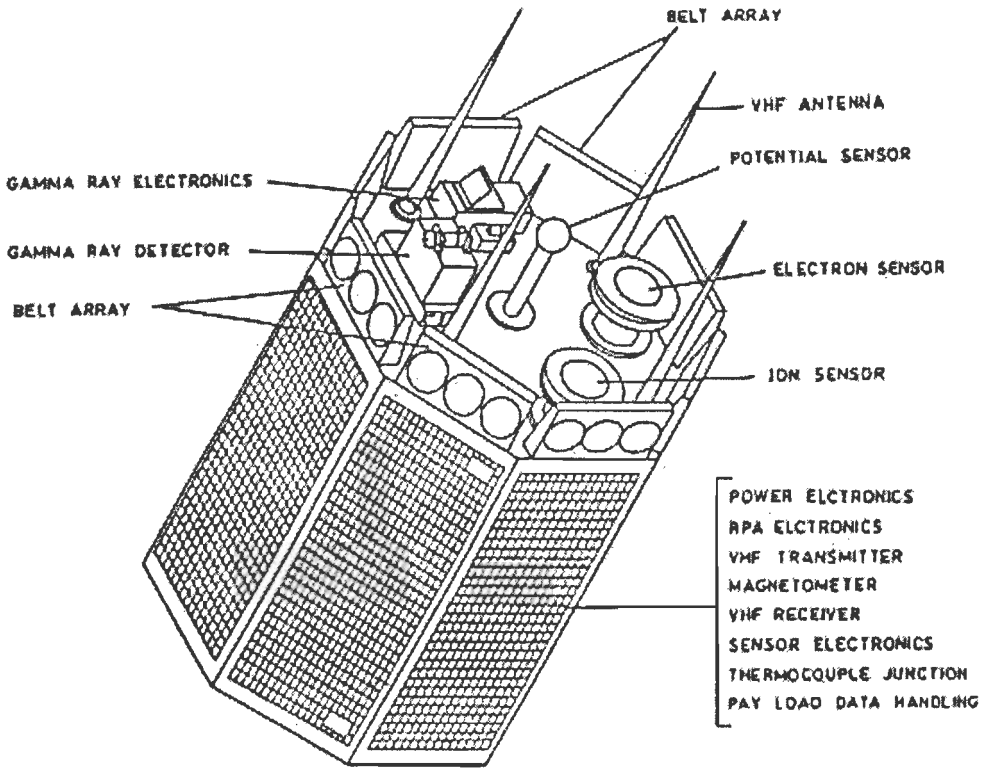

Figure A1.1: Orbital configuration of SROSS-C2 satellite (Garg et al., 1996)

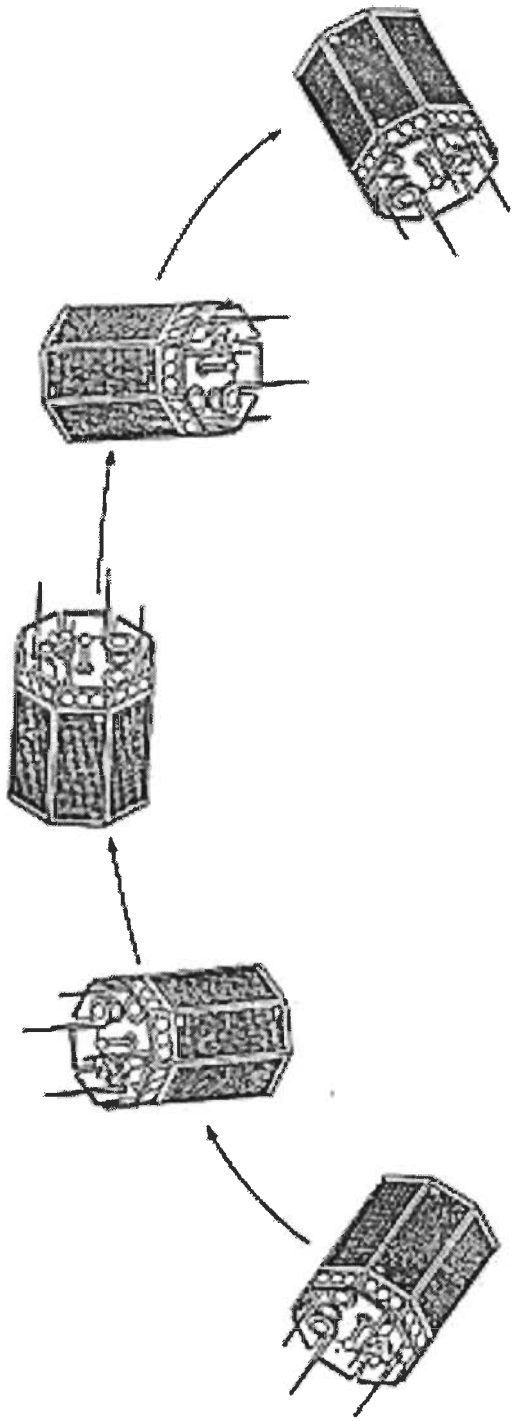

Figure A1.2: Motion of SROSS-C2 satellite in orbit (Garg et al., 1996)

A1.3 RPA PAYLOAD

The Retarding Potential Analyzer (RPA) payload measured the following ionospheric parameters (Garg et al., 1992)

(a) Electron temperature T_e

(b) Ion temperature T_i

(c) Total ion density N_i

(d) Ion composition O^+, O_2^+, NO^+, H^+, He^+

(e) Suprathermal electron flux (STEF) (upto 30 eV)

(f) Irregu larities in the electron and ion densities

(g) Satellite potential with respect to plasma

The accuracy of measurements were:

Parameter	Accuracy
N_i and N_e	± 5%
T_i and T_e	± 50 K
STEF	±10%

The RPA payload was switched on in orbit first time on May 21, 1992 using SROSS-C satellite through ground commands issued from ISRO Satellite Tracking Center (ISTRAC), Bangalore. Again on May 4, 1994 the RPA payload placed in orbit by SROSS-C2 mission. The design and development of RPA for SROSS series of satellite was taken up by NPL under SROSS Aeronomy Satellite Project (SASP), in the year 1985-86. The instrument was designed for minimum power consumption, size and weight to have maximum possible reliability and flexibility for its operation in space through ground commands.

The RPA payload consists of electron and ion sensors and a potential probe for making simultaneous measurements of ionospheric electron and ion plasma parameters. The structure of the electron and ion RPA sensors is identical but has different grid voltages suitable for the collection of electrons and ions, respectively. The different grids in the sensor are known as the entrance grid, the retarding grid, the suppressor grid and the screen grid. These grids are made of gold-plated tungsten wire. Retarding grid acts as an energy filter for ions or electrons entering the sensors. The charged particles whose energies are greater

than the applied voltage on the retarding grid pass through various grids and finally reach the collector electrode to cause the sensor current. Electrometer measures the current collected by the RPA sensors.

The RPA sensor is analogous to vacuum tube pentode where ionospheric plasma serves as the cathode. The ions and electrons enter the sensor through its open aperture and pass through the region, which is electrically segmented by a series of very fine gold plated tungsten wire electrodes and then reach the collector electrode. The current thus collected over the collector plate varies from tens of micro amperes down to the fraction of pico amperes. By changing the bias voltage on the retarding grid, different energy electrons/ions reach the collector plate to cause the collector current. This gives the measurement of flux in different energy ranges. Characteristic curves (Figure A1.3) of the collector current (I) versus retarding grid bias (V) are generated separately for electrons and ions. These characteristic curves are used for deriving different ionospheric parameters of interest.

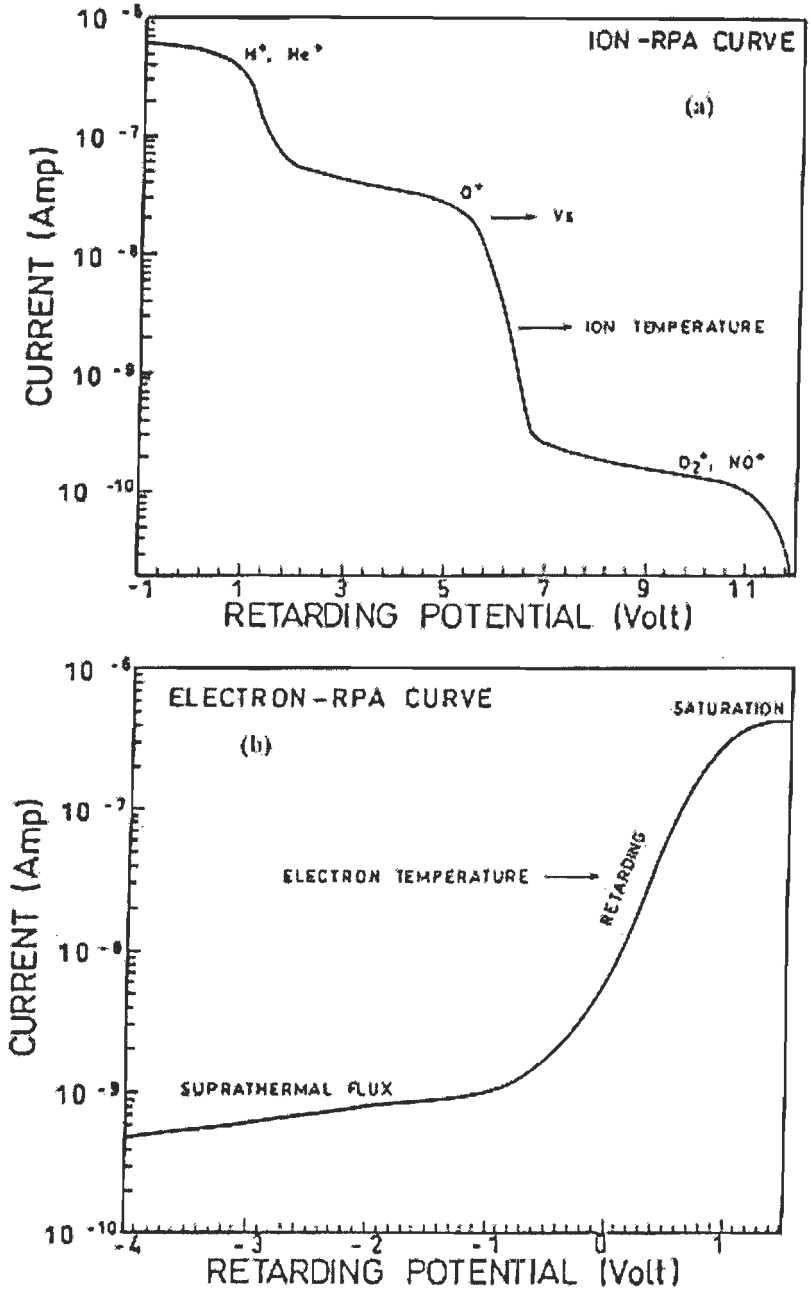

Figure A1.3: Characteristics curves of ion and electron RPA (Garg and Das, 1995)

A1.3.1 Recording of Data

The RPA payload did not possess any onboard memory for storing data therefore the data was recorded at the ground stations. The longitude and latitude coverage of data was restricted to certain limited range. The data was collected at ISRO, Bangalore (12.5° N, 77.3° E) and Lucknow (26.8° N, 80.8° E) ground stations and also from foreign ground station located in Mauritius (20° S, 56° E). After recording the data, it was processed at ISTRAC, Bangalore to generate altitude and orbital parameters of the satellite. The raw data have been obtained in the form of LOTUS file. These files are divided into months and marked the data corresponding to satellite orbit number from separately dated files.

A1.3.2 Temperature and Density of Ions

Ionosphere, the multi-constituent plasma comprises of different ion species. O^+, O_2^+, NO^+, H^+ and He^+ are the most common ion species of our interest in the altitude range 425-625 km. These ions get retarded at different voltages due to their masses; result in the decrease of ion current at different voltages corresponding to the ion masses giving rise to a composite I-V curve as shown in Figure 2.3 (a). The ion current reaching the sensor in response to the retarding voltages is governed by the equation (Garg et al., 1996).

$$I = AeU_S\eta\cos\theta\sum_{i=0}^{n}N_i\left\{\frac{1}{2}+\frac{1}{2}erf(x)+C_i\frac{\exp(-x^2)}{2\sqrt{\pi}U_S\cos\theta}\right\} \qquad \text{(A1.1)}$$

where, θ = angle between the velocity vector and probe normal

N_i = density of i^{th} ion (m^{-3})

$x = U_s\cos\theta - [\{e(V+V_s)\}^{1/2}/kT_i]$,

V_s = the satellite potential w.r.t. plasma,

V = probe potential w.r.t. satellite,

k = Boltzmann constant $=1.38\times10^{-23}$ JK^{-1}

$C_i = (2kT_i/m_i)^{1/2}$, most probable velocity of the ion constituent

T_i = ion temperature (K), m_i = mass of ion (kg)

On acquiring the I-V curve, the main task is to recover the ion density and temperature using the above equation. Ion density gives the total ion concentration as well as information on the composition of the major ion constituents. Satellite potential is also one of the unknown parameters. The U_s and θ, are available from the measurements. Equation (A1.1) is a non-linear equation and therefore unknown parameters are obtained by computerized curve fitting (Ga rg et al., 1996). In this approach, computer program first constructs a model I-V curve with the help of the above equation by using typical values of the unknown variables N_i, T_i, V_s, which are selected as reasonable approximations for the anticipated ambient ionospheric conditions. Estimation procedure involves adjusting these parameters in the computer generated curve applying least square method of minimizing standard errors. By iteration we update the model curve step by step using the variables. The standard error is calculated every time and iterations are continued until the best least square fit to the measured curve is obtained. When the two curves match, the fitted variables yield the needed plasma parameters corresponding to the experimental curve.

The saturation current around zero volt retarding voltage gives the total ion density as all the ions reach the sensor and collected by probe without any retardation. Equation (A1.1) reduces to

$$I_{i,o} = N_i e \eta A U_s \cos\theta \qquad \text{(A1.2)}$$

where, $I_{i,0}$ = Saturation current for the i^{th} ion at zero retarding voltage

Therefore total ion density can be calculated first by knowing U_s and θ without having any information of T_i and V_s.

To find the temperature from I-V curve from RPA data, the limit of theta ±40° is considered for ion temperature analysis. For generating I-V curve 64 sets of data are taken in one complete sweep. Each data set is collected after every 22 msec; duration of each sweep becomes 1.408 sec. During this period retarding grid voltage is swept from 0 to 22 V in up and down sweeps and theta changes by 45° at 5 rpm spin rate (Garg and Das, 1995). For each sweep of ion RPA one set file is created. The T_i values and different ion compositions so derived are put in a file in a specified format. The file is finally processed in MS Excel program.

A1.3.3 Electron Temperature

The I-V curve obtained from the electron RPA curve is shown in Figure A1.3 (b). Here the log of electron current measured by the probe is plotted along with the retarding grid voltage. Three different regions are identified in this curve. When the probe voltage is positive relative to plasma, electrons are accelerated towards the probe and a fairly flat saturation portion of the probe characteristics obtained. When the probe voltage is made negative with respect to plasma, the incoming electrons experience a retarding field and the probe current decreases exponentially resulting in retarding region of characteristic. The region is linear on a semi log scale. As the probe is made more negative, the low energy thermal electrons repelled away. But probe still collects a small current, due to higher energy suprathermal electrons. The lower flat portion of the curve denotes the suprathermal region. During day time this flux is more and also gets contaminated by the plate electrons if its probe is sunlit. The retarding region of I-V curve is related to the distribution of electron energies and hence can be used to obtain electron temperature (T_e).

The relationship between the collector current (I) and retarding grid voltage (V) can be given by

$$I_e = I_o \exp\left[\frac{-e(V+V_S)}{kT_e}\right] \qquad \text{(A1.3)}$$

where, $I_o = \frac{1}{4}\eta e A N_e U_e$ = random current when probe is at plasma potential i.e. for $V+V_s = 0$

η = efficiency of the probe, A = area of the probe = 20 cm^2

N_e = electron density (m^{-3}), e = electron charge = 1.6×10^{-19} C

U_e = mean thermal velocity of the electron = $\sqrt{\frac{8kT_e}{\pi m_e}}$

m_e = mass of electron = 9.1×10^{-31} kg

T_e = electron temperature (K), V = retarding grid voltage w.r.t satellite

V_s= satellite potential w.r.t. plasma

Equation (A1.3) may be written as

$$\ln I_e = \ln I_o - \frac{e(V + V_S)}{kT_e} \qquad \text{(A1.4)}$$

During a single I-V curve the satellite potential can be assumed to remain constant. Therefore I_o and V_s may be taken as constant. The above equation represents a linear relationship in $\ln I_e$ and V with slope (e/kT_e), the temperature can be determined from the slope of the semi logarithmic plot of the I-V curve. Therefore above equation now becomes

$$\frac{d}{dV}(\ln I_e) = -\frac{e}{kT_e} \qquad \text{(A1.5)}$$

The electron temperature can be obtained easily from equation (2.5) using the values of e and k. The slope of the linear region of the I-V curve gives the electron temperature. The approach that has been adopted for evaluating the slope is the linear curve fitting, in which least square technique is applied to fit a straight line to the measured data in the retarding region. The data within ±60° of the angle of θ limits has been considered for electron temperature analysis.

A1.4 SUPPLEMENTARY DATA USED FOR IONOSPHERIC STUDIES

For removing the effect of other events on the ionosphere, following data have been used. Care has been taken to choose the seismic events during which other events which may cause ionospheric changes are absent.

A1.4.1 Geomagnetic Data

The magnetic field of the earth varies diurnally, seasonally, and with solar activity. The net variation at the earth's surface is the sum of two parts: (1) caused by external currents and (2) produced by induced earth currents. Quiet days (Q) are those days on which magnetic field vary smoothly; other days are the disturbed or D days (Matsushita, 1967). The degree of magnetic disturbance is indicated by a variety of indices (Rostoker, 1972; Parkinson, 1983). These indices include the K and A indices and the auroral activity indices AE. The planetary Kp index is derived by calculating a weighted average of K-indices from geomagnetic observatories.

The geomagnetic indices: Bartels introduced *K* index as a magnetic index in 1949 and has been derived since then at the Institut für Geophysik at Göttingen University, Germany. Both K and Kp were officially adopted by the International Association for Terrestrial Magnetism and Electricity (IATME, which later became the International Association for Geomagnetism and Aeronomy, IAGA) in 1951. Kp and its related indices (*ap*, *Ap*, *Cp*) have been widely used in ionospheric and magnetospheric studies and are generally recognized as indices measuring worldwide geomagnetic activity. The Kp index are 3 hours range designed to measure the irregular variations associated with magnetic field disturbances. Geomagnetic disturbances can be monitored by ground-based magnetic observatories recording the three magnetic field components. Each observatory assigns an integer from 0 to 9 to each of eight 3 hours UT intervals. A permanent scale is adopted for a given observatory but the scale differs from observatory to observatory. The selection of the quietest days (Q-days) and most disturbed days (D-days) of each month is deduced from the Kp values on the basis of three criteria for each day:

(1)The sum of the eight Kp values.

(2)The sum of squares of the eight Kp values.

(3)The maximum of the eight Kp values.

The data of magnetic storms in terms of ∑Kp have been downloaded from the website (http://swdcdb.kugi.kyoto-u.ac.jp). The ∑Kp indices related to magnetic storms during the occurrence of the earthquake and also during pre - and post- occurrences days have been used in analyzing the electron and ion temperature anomalies related to earthquakes.

A1.4.2 Seismic Data

Ionospheric response to the seismic events has been studied by analyzing the variation in electron and ion temperature during the occurrence of earthquake. For this purpose the details of earthquake events are obtained from USGS earthquake data information website. The USGS makes accessible most of the raw and processed data from the various monitoring networks including

earthquake catalogs, earthquake hazard data, waveform data, ground shaking data, crustal data and fault information. The mission of the National Earthquake Information Center (NEIC) is to determine the location and size of all destructive earthquakes worldwide and to immediately disseminate this information to concerned national and international agencies, scientists, and the general public. We have obtained the information regarding original time, location, depth as well as magnitude of the seismic events.

A1.4.3 Solar Flares Data

Ionospheric parameters in *F2* region may be changed due to many agencies which play the important role in the modification of ionosphere. Solar flare is one of them, which directly affects the ionosphere and radio communication on earth and also releases energetic particles into the space. These energetic particles accelerated in space are risky to astronauts and interfere with the electronic systems in satellite and spacecrafts. The effect of solar flare on the earth's ionosphere has become a significant study in the present time. The data on solar flare has been obtained from National Geophysical Data Center (NGDC), Boulder, Colorado (USA) in the present study.

A1.4.4 IRI model

The International Reference Ionosphere (IRI) is an international project sponsored by the International Union on Radio Science (URSI) and the Committee on Space Research (COSPAR). The Task Group was established to develop and improve a standard model of the ionospheric plasma parameters in the late sixties. The model is primarily based on experimental evidences using all available space and ground data sources. The prime interest of COSPAR is for the evaluation of environmental effects on spacecraft and experiments in space and the prime interest of URSI is in the electron density part of IRI for radiowave propagation studies and applications. The model uses the data from the main sources of worldwide network of ionosondes, incoherent scatter radars, the ISIS and Alouette topside sounders, and in situ instruments on several rockets and satellites. IRI model provides electron temperature, ion temperature, neutral temperature,

electron density and ion composition, density of peaks corresponding to different layers, total Electron Content etc. in the altitude range 60-2000 km for given location, time, date, sunspot number and ionospheric index. The IRI-2007 model is used for downloaded density data from the Internet for the present study.

A1.4.5 Thunderstorms Data

Thunderstorm is the main source of lightning/sprites, which influence the ionospheric temperatures. The data on thunderstorms have been obtained from India Meteorological Department (IMD), Pune for the same period for excluding the thunderstorm effects on the ionospheric electron and ion temperatures and densities.

APPENDIX A2

MAGNETOTELLURIC INVESTIGATIONS FOR ELECTRICAL STRUCTURE OF EARTH CRUSTAL IN HIMALAYAN REGION

The magnetotelluric (MT) method is used to study the electrical structure of earth crust in the desired depth range. For this purpose, natural time varying orthogonal horizontal electric and magnetic field components are measured. These electric and magnetic field components are linearly related through appropriate transfer function (Tikhonov, 1950 and Cagniard, 1953). The depth of penetration of electromagnetic wave depends upon its frequency and the conductivity structure of earth's interior in which field permeates. The behavior of MT field is governed by the basic induction laws and the derived mathematical equations. MT method is used by several workers Adam,1997; Adam et al., 2005; Harinarayna et al., 2004, 2006; Tezkan, 1994; Tezkan et al., 1996. T his appendix of the thesis discusses the theory of magnetotelluric investigations and detailed procedure to determine the electrical structure of the earth from the measured field components. In the end an electrical model of the earth crust, delineated from the measured magnetotelluric data in Himalayan region along with its geological significance has been presented.

A2.1 THEORY OF MAGNETOTELLURIC METHOD

Electromagnetic field behavior in source free region (earth interior) can be described by Maxwell's equations, which can be written in differential form as

$$\vec{\nabla} \times \vec{E} = -\frac{\partial \vec{B}}{\partial t}, \qquad \text{Faraday's law} \qquad \text{(A2.1)}$$

$$\vec{\nabla} \times \vec{H} = \vec{J} + \frac{\partial \vec{D}}{\partial t}, \qquad \text{modified Ampere's law} \qquad \text{(A2.2)}$$

$$\vec{\nabla}.\vec{D} = \rho_v, \qquad \text{Gauss's law} \qquad \text{(A2.3)}$$

$$\vec{\nabla}.\vec{B} = 0, \qquad \text{Gauss's law for magnetism} \qquad \text{(A2.4)}$$

Where $\vec{E}$ (V/m) and $\vec{H}$ (A/m) are the electric and magnetic field intensity vectors, $\vec{B}$ (T) is the magnetic induction vector, $\vec{J}$ (A/m^2) is the current density vector, $\vec{D}$ (C/m^2) is the electric displacement vector and ρ_v (C/m^3) is the free electric charge density.

Maxwell's equations are statements of the mathematical relationships between five vector field variables, ($\vec{E}$ and $\vec{B}$ are primary variables while $\vec{H}$, $\vec{J}$ and $\vec{D}$ are secondary variables). The electrical properties of the medium (earth) can be incorporated in the Maxwell's equations by using the following constitutive relationships:

$$\vec{J} = \sigma\vec{E}, \tag{A2.5}$$

$$\vec{D} = \varepsilon\vec{E}, \tag{A2.6}$$

$$\vec{B} = \mu\vec{H}, \tag{A2.7}$$

where $\sigma(S/m)$ is the electrical conductivity, ε (F/m) is the dielectric permittivity and μ (H/m) is the magnetic permeability. These are intrinsic properties of the earth crust through which the electromagnetic field propagates. In magnetotelluric investigations, only variation in electrical conductivity is important for the crust structure delineation. Therefore, dielectric permittivity and magnetic permeability are used as constant for the crustal material.

Classifications of the electrical properties of rocks and minerals have been widely discussed in literature (Grant and West, 1965; Keller and Frischknecht, 1966; Ward and Fraser, 1967).

At the interface separating the two media, 1 and 2, with different electrical conductivities, the electromagnetic fields and current density satisfy the following boundary conditions:

$$\hat{n}\times(\vec{E}_2 - \vec{E}_1) = 0, \tag{A2.8}$$

$$\hat{n}\times(\vec{H}_2 - \vec{H}_1) = \vec{J}_S, \tag{A2.9}$$

$$\hat{n}\cdot(\vec{D}_2 - \vec{D}_1) = \rho_S, \tag{A2.10}$$

$$\hat{n}\cdot(\vec{B}_2 - \vec{B}_1) = 0, \tag{A2.11}$$

$$\hat{n}\cdot(\vec{J}_2-\vec{J}_1)=0\,, \tag{A2.12}$$

where $\hat{n}$ is the unit vector normal to the interface. In the absence of surface currents, the tangential component of electric field $\vec{E}$ and the normal component of current density $\vec{J}$ are continuous, while the tangential component of $\vec{B}$ is discontinuous and normal component of magnetic field $\vec{B}$ is continuous across the discontinuity. Substituting equations A2.5, A2.6 and A2.7 in equations A2.1 and A2.2, the Maxwell's equations reduce to the following form

$$\nabla\times\vec{E}=-\mu\frac{\partial\vec{H}}{\partial t}, \tag{A2.13}$$

$$\nabla\times\vec{H}=\sigma\vec{E}+\varepsilon\frac{\partial\vec{E}}{\partial t}. \tag{A2.14}$$

To obtain separate equations for vectors $\vec{E}$ and $\vec{H}$, we eliminate either $\vec{H}$ or $\vec{E}$ from equations A2.13 and A2.14 and use the following vector identity,

$$\nabla\times\nabla\times A=\nabla(\nabla.A)-\nabla^2A, \tag{A2.15}$$

where ∇^2 is the Laplacian operator,

$$\nabla^2=\frac{\partial^2}{\partial x^2}+\frac{\partial^2}{\partial y^2}+\frac{\partial^2}{\partial z^2}.$$

The resulting equation for the $\vec{E}$ and $\vec{H}$ field vectors are given below,

$$\nabla^2\vec{E}=\sigma\mu\frac{\partial\vec{E}}{\partial t}+\mu\varepsilon\frac{\partial^2\vec{E}}{\partial t^2}, \tag{A2.16}$$

$$\nabla^2\vec{H}=\sigma\mu\frac{\partial\vec{H}}{\partial t}+\mu\varepsilon\frac{\partial^2\vec{H}}{\partial t^2}. \tag{A2.17}$$

Considering the linear, isotropic medium and harmonic temporal variation of field ($e^{-i\omega t}$), the damped wave equations become

$$\nabla^2\vec{E}(r,\omega)=-i\sigma\mu\omega\vec{E}(r,\omega)-\mu\varepsilon\omega^2\vec{E}(r,\omega), \tag{A2.18}$$

$$\nabla^2\vec{H}(r,\omega)=-i\sigma\mu\omega\vec{H}(r,\omega)-\mu\varepsilon\omega^2\vec{H}(r,\omega). \tag{A2.19}$$

The values of electric permittivity (ε) and magnetic permeability (μ) for the earth's crust are (i.e. $\varepsilon=\varepsilon_0=8.85\times10^{-12}$ (F/m) and $\mu=\mu_0=4\pi\times10^{-7}$ (H/m)).

Magnetotelluric fields propagate only by the diffusion process ($\omega\varepsilon << \sigma$), which is dealt with the following equations,

$$\nabla^2 \vec{E}(r,\omega) = -i\sigma\mu\omega\vec{E}(r,\omega), \tag{A2.20}$$

$$\nabla^2 \vec{H}(r,\omega) = -i\sigma\mu\omega\vec{H}(r,\omega). \tag{A2.21}$$

The penetration depth or the skin depth or the diffusion depth in a homogenous earth is given by,

$$\delta(\omega) = \sqrt{\frac{2}{\omega\mu\sigma}} = \sqrt{\frac{\rho T}{\pi\mu}}, \tag{A2.22}$$

where $\delta(\omega)$ is the electromagnetic skin depth in meters for a given angular frequency ω, ρ is the resistivity of the medium, μ is magnetic permeability and T is the period. At a depth, $\delta(\omega)$, electromagnetic fields are attenuated to $1/e$ of its amplitudes at the surface. Figure A2.1 shows the general behavior of electromagnetic wave of different frequency penetrating to different depth, Which demonstrate that the low frequency wave penetrate to deeper depth.

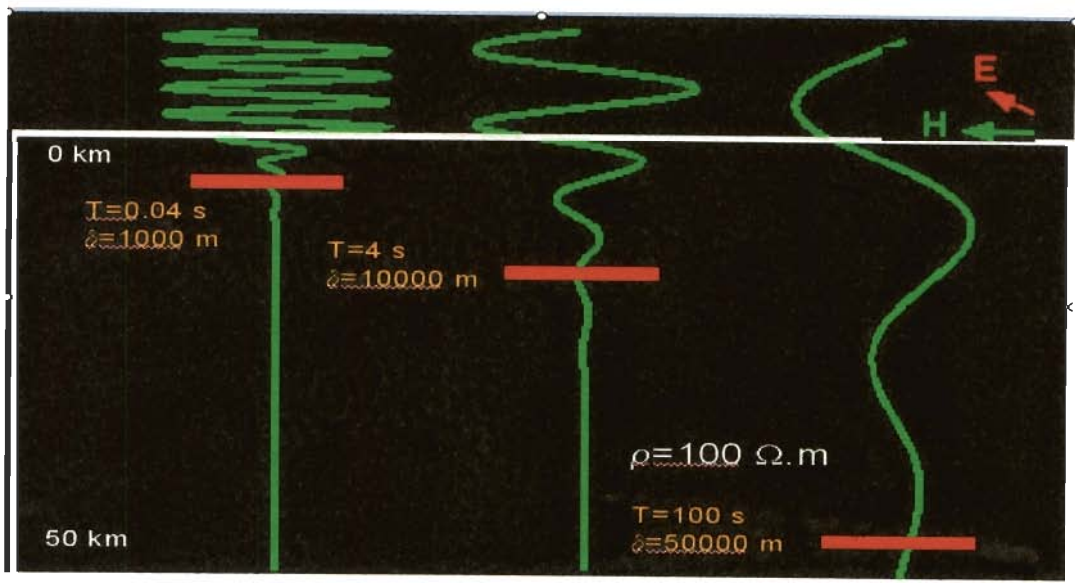

Figure A2.1: The EM waves of different frequency penetrate into the Earth (www.en.wikipedia.org).

A2.1.1 TE- and TM- Polarization Modes

If the electromagnetic field is propagating in the earth crust, represented by two-dimensional (2D) resistivity structure, the Maxwell's equations can be written in terms of the two modes of polarization: transverse electric or TE-mode and transverse magnetic or TM- mode. TE- mode is corresponding to the electric field component being transverse to the z-direction (vertical) and parallel to the strike while, transverse magnetic or TM-mode of polarization is one in which magnetic field component is transverse to z-direction and parallel to the strike. For these modes of polarization, Maxwell's equations are given by:

Transverse Electric (TE) polarization (E_x, H_y, H_z)

$$\frac{\partial E_x}{\partial y} = -i\omega\mu H_z , \tag{A2.23}$$

$$\frac{\partial E_x}{\partial z} = i\omega\mu H_y , \tag{A2.24}$$

$$\frac{\partial H_z}{\partial y} - \frac{\partial H_y}{\partial z} = \sigma E_x . \tag{A2.25}$$

Transverse Magnetic(TM) polarization (H_x, E_y, E_z)

$$\frac{\partial H_x}{\partial y} = -\sigma E_z , \tag{A2.26}$$

$$\frac{\partial H_x}{\partial z} = \sigma E_y , \tag{A2.27}$$

$$\frac{\partial E_z}{\partial y} - \frac{\partial E_y}{\partial z} = i\omega\mu H_x . \tag{A2.28}$$

For the two dimensional earth crust, the Helmholtz's equations for TE- and TM- modes are written as (Weaver, 1994),

$$\left(\frac{\partial^2}{\partial y^2} + \frac{\partial^2}{\partial z^2} + k^2\right) E_x = 0 , \tag{A2.29}$$

$$\left(\frac{\partial^2}{\partial y^2} + \frac{\partial^2}{\partial z^2} - \frac{1}{\sigma}\frac{\partial \sigma}{\partial y}\frac{\partial}{\partial y} - \frac{1}{\sigma}\frac{\partial \sigma}{\partial z}\frac{\partial}{\partial z} + k^2\right) H_x = 0 . \tag{A2.30}$$

An example of the typical two dimensional earth crust is shown in Figure A2.2, in which electrical resistivity varies only in one horizontal (x) and vertical direction (z). There is no variation of electrical resistivity in y- direction.

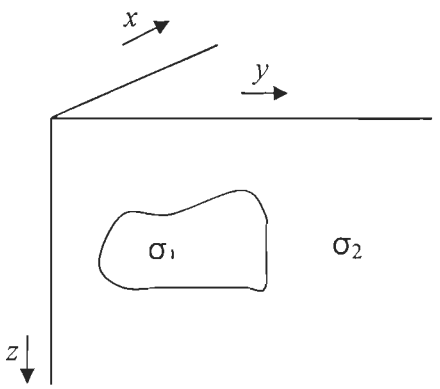

Figure A2.2: Typical 2D Earth model in coordinate system. σ_1 and σ_2 are the conductivity of host medium and anomalous body.

A2.1.2 Magnetotelluric Impedance Tensor and its Properties

The measured electric and magnetic field components may be used to define impedances, which are the function of electrical properties of the medium, direction of field measurement and direction of the arrival of primary field. Definition of scalar impedance for layered medium was given by Cagniard (1953). Subsequently, the concept of impedance tensor was introduced (Swift, 1967; Berdichevsky, 1998; Sims et al., 1971). The linear relationship between the horizontal components of the field at the surface of the earth can be written in terms of the impedance tensor as,

$$E_x = Z_{xx}H_x + Z_{xy}H_y, \qquad \text{(A2.31)}$$

$$E_y = Z_{yx}H_x + Z_{yy}H_y . \qquad \text{(A2.32)}$$

Similarly, the magnetic transfer function can be written as,

$$H_z = T_{zx}H_x + T_{zy}H_y. \qquad \text{(A2.33)}$$

The complex quantities $Z_{xx}, Z_{xy}, Z_{yx}, Z_{yy}$ and T_{zx}, T_{zy} are the components of the impedance tensor and the tipper vector respectively and these are functions of

frequency, electrical properties of medium, orientation of measurement axes and location of the observation site.

The complex impedance (transfer function) Z is usually represented by its amplitude and phase. The electrical resistivity, ρ, (inverse of conductivity, σ) as a function of depth can be inferred from the EM field of the corresponding penetration depth. Resistivity obtained from the ratio of the measured electric and magnetic fields is called "apparent" resistivity, which is frequency dependent. The apparent resistivity ρ_{axy} $[\Omega m]$ is defined in terms of the impedance tensor elements as:

$$\rho_{axy}(\omega) = \frac{1}{\mu_0 \omega} \left| Z_{xy}(\omega) \right|^2 . \qquad \text{(A2.34)}$$

In case of a homogenous earth, the apparent resistivity reflects the true value of the earth's resistivity. The phase of the transfer function element describes the phase shift between the electric and magnetic field components.

$$\varphi_{xy} = \tan^{-1}\left(\frac{\mathrm{Im}(Z_{xy})}{\mathrm{Re}(Z_{xy})}\right). \qquad \text{(A2.35)}$$

In a homogenous earth the impedance phase is $\pi/4\,(45^0)$. In a 1D-layered earth, the phase increases over 45^0 when the EM response penetrates into higher conductivity media. By the same convention, phase decay below 45^0 for the EM response penetrating into a less conducting media. This means that by the diffusive process the phase shift between the orthogonal electric and magnetic field components attenuates when the field penetrates into less conductive media.

The equations A2.31 and A2.32 can be written in matrix form as,

$$\begin{bmatrix} E_x \\ E_y \end{bmatrix} = \begin{bmatrix} Z_{xx} & Z_{xy} \\ Z_{yx} & Z_{yy} \end{bmatrix} \begin{bmatrix} H_x \\ H_y \end{bmatrix}. \qquad \text{(A2.36)}$$

The error free impedance tensor exhibits following dimensionality properties

(i) If the earth is represented by a 1D structure (layered model), the amplitude of off diagonal elements of impedance tensor are equal and diagonal elements are zero. The impedance tensor reduces to a scalar impedance:

$$Z_{xy} = -Z_{yx} = |Z| \quad and \quad Z_{xx} = Z_{yy} = 0 . \tag{A2.37}$$

In case of tipper, since there is no net vertical component of magnetic field, H_Z, both components of tipper T_{zx} and T_{zy} are zero.

(ii) For a 2D earth, if the electric field is measured parallel and perpendicular to the strike direction, the diagonal elements vanish and the off diagonal elements are different,

$$Z_{xx} = Z_{yy} = 0, \quad Z_{xy} \neq Z_{yx} . \tag{A2.38}$$

In 2D case, the tipper is not zero, and it is related to the horizontal component of the magnetic field, H_y, (i.e. $T_{zx} = 0$). Both real and imaginary induction arrows are oriented perpendicular to the strike direction and point to the zone of more conductivity (Parkinson, 1959). Tippers are used to infer the presence or absence of lateral variations in conductivity (Simpson and Bahr, 2005).

Normally field components are recorded in geographical coordinate system. The estimated impedance tensor can be rotated, to any desired direction (strike direction), using rotation matrix R as,

$$Z_{obs} = R Z R^T , \tag{A2.39}$$

where

$$R = \begin{bmatrix} \cos\theta & \sin\theta \\ -\sin\theta & \cos\theta \end{bmatrix}. \tag{A2.40}$$

The impedance tensor elements are referred to as transverse electric (TE-mode) when rotated so that the electric field is defined in the strike direction. If the magnetic field is in the strike direction, the impedance element is referred as transverse magnetic or TM-mode. Therefore, if x-axis is the strike direction, then Z_{xy} and Z_{yx} are referred as TE- and TM-mode impedances respectively. Once rotated optimally, the tensor may be written as,

$$Z_{obs} = \begin{bmatrix} 0 & Z_{TE} \\ Z_{TM} & 0 \end{bmatrix}. \tag{A2.41}$$

The impedance elements in measured and rotated coordinate system are shown in Figure A2.3.

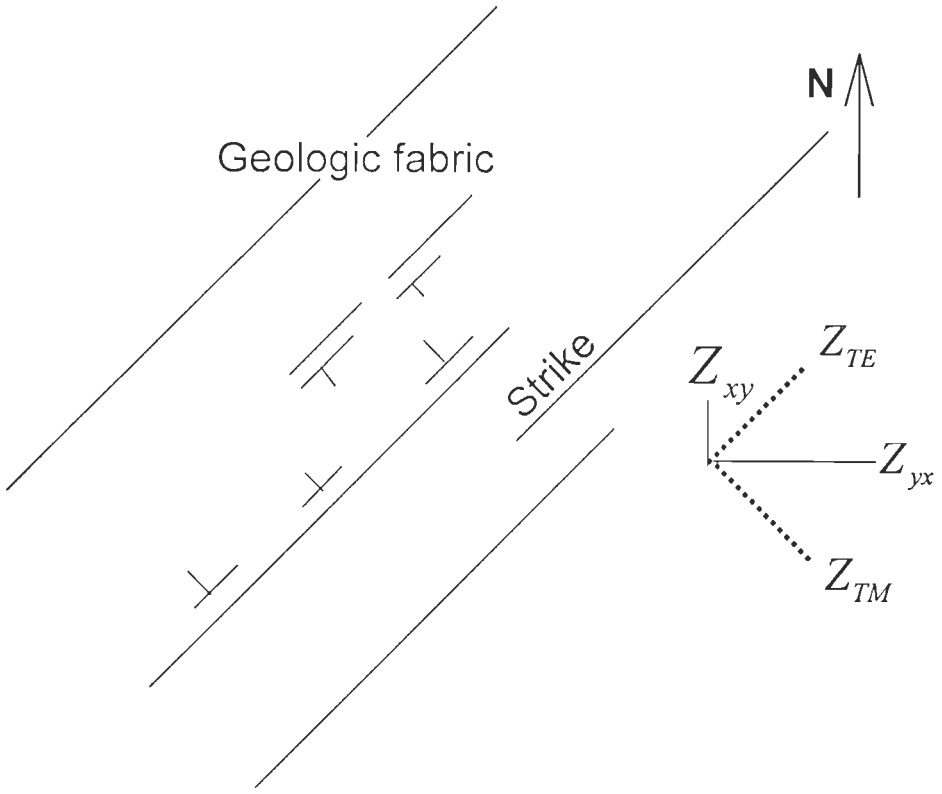

Figure A2.3: Planar view, off diagonal tensor elements become unequal when geology has a preferred direction. On rotating the tensor to the strike, diagonal elements get minimized (Lezaeta, 2001).

A2.1.3 Inversion of Magnetotelluric Data

Modeling and inversion constitute an integral part of the process of deriving conductivity distribution in the subsurface from the measured field components at the earth's surface. Modeling mainly concerns the techniques used for the computation of response for the assumed conductivity models. Analytical solutions of forward problems are only available for simple geometries like homogenous and layered media. For most of the complex geometries, only approximate numerical solutions are feasible. Popular numerical methods are Finite Element Method (FEM), Finite Difference Method (FDM) and Integral Equation Method (IEM).

One-dimensional (1D) inversion is used to determine layered model from the measured response. For this purpose, problem is linearized and solved using some kind of weighted least square solution (Marquardt, 1963). However, in some cases when the problem is over parameterized, a weighted minimum norm solution is adopted (Constable et al., 1987; Gupta et al., 1996; Israil et al., 2004). We have carried out 1D inversion of MT data using least square inversion and Occam's techniques to have feeling of approximate resistivity structure and to design and initial model for 2D inversion.

For two dimensional (2D) inversion, RLM2DI code (Mackie et al., 1997), uses Tikhonov regularization and it computes forward responses through FDM. REBOCC code developed by Siripunvaraporn and Egbert (2000) is a variant of the Occam's algorithm (Constable et al., 1987) that allows inversion of any resistivity and phase of TE- and TM- modes and real and imaginary part of tipper. Rodi and Mackie (2001) gave 2D inversion scheme based on non-linear conjugate gradient method. A linearized algorithm to invert noisy 2D MT data for subsurface conductivity structures represented by smooth boundaries defining sharp boundary contrasts was developed by deGroot-Hedlin and Constable (2004). Pedersen and Engels (2005) solved the 2D inversion problem using the determinant of impedance tensor as a variant of REBOCC code. This code is known as DetREBOCC and it can resolve both conductive as well as resistive structure. For the present data set, the RLM2DI code (Mackie et al., 1997 and Rodi and Mackie, 2001) available in Geosystem's WinGLink software was used for 2D inversion.

A2.2 TRANSFER FUNCTION ESTIMATION FROM MEASURED FIELD COMPONENTS

In the frequency domain, the relationship between the electric and magnetic fields, at the surface of the earth can be written as (Swift, 1967)

$$E_x(f) = Z_{xx}(f)H_x(f) + Z_{xy}(f)H_y(f), \qquad \text{(A2.42)}$$

$$E_y(f) = Z_{yx}(f)H_x(f) + Z_{yy}(f)H_y(f), \qquad \text{(A2.43)}$$

or, in short

$$\vec{E} = \tilde{Z}\vec{H}\,, \tag{A2.44}$$

where $\vec{E}$ and $\vec{H}$ are the horizontal electric and magnetic field vectors and $\tilde{Z}$ is the second rank impedance tensor. In addition, the relationship between the vertical (H_z) and horizontal (H_x, H_y) magnetic field components can be expressed as,

$$H_z(f) = T_x(f)\,H_x(f) + T_y(f)\,H_y(f)\,. \tag{A2.45}$$

where T_x and T_y are called tipper (Vozoff, 1991).

The observed signal components of electric and magnetic fields are associated with noise or error in the measured magnetotelluric time series. So, the equation A2.44 can be written as,

$$\vec{E} = \tilde{Z}\vec{H} + \vec{e}\,, \tag{A2.46}$$

where the last term $\vec{e}$ in equation (A2.46) is the residual (error) parameter.

The impedance tensor $\tilde{Z}$ is determined in the classical way by the least square technique (Swift, 1967; Sims et al., 1971), where the square of the residual power in equation A2.46 is minimized to yield the impedance $\tilde{Z}$. For the determination of $\tilde{Z}$, we assume that M data segments are available and that E_{xi}, E_{yi}, H_{xi} *and* H_{yi} are the band–averaged Fourier amplitudes of segment i. Writing one component of equation (A2.46) as,

$$E_{xi} = Z_{xx}H_{xi} + Z_{xy}H_{yi} + e_i\,. \tag{A2.47}$$

We have to minimize

$$e^2 = \sum_{i=1}^{M} e_i e_i^* = \sum_{i=1}^{M} \left(E_{xi} - Z_{xx}H_{xi} - Z_{xy}H_{yi}\right)\left(E_{xi}^* - Z_{xx}^* H_{xi}^* - Z_{xy}^* H_{yi}^*\right). \tag{A2.48}$$

After differentiation with respect to Z_{xx}^* and Z_{xy}^*, we obtain the two equations,

$$\sum_{i=1}^{M}\left(E_{xi} - Z_{xx}H_{xi} - Z_{xy}H_{yi}\right)H_{xi}^* = 0\,,$$

$$\sum_{i=1}^{M}\left(E_{xi} - Z_{xx}H_{xi} - Z_{xy}H_{yi}\right)H_{yi}^* = 0\,. \tag{A2.49}$$

Or more comprehensively,

$$< H_x H_x^* > Z_{xx} + < H_y H_x^* > Z_{xy} = < E_x H_x^* >,$$

$$< H_x H_y^* > Z_{xx} + < H_y H_y^* > Z_{xy} = < E_x H_y^* >, \qquad \text{(A2.50)}$$

where $< A\ B >= \sum_{i=1}^{M} A_i\ B_i$

The solution of system A2.50 is,

$$Z_{xx} = \left(< E_x H_x^* > < H_y H_y^* > - < E_x H_y^* > < H_y H_x^* >\right) / Det,$$

$$Z_{xy} = \left(< E_x H_y^* > < H_x H_x^* > - < E_x H_x^* > < H_x H_y^* >\right) / Det, \qquad \text{(A2.51)}$$

with $Det = < H_x H_x^* > < H_y H_y^* > - < H_x H_y^* > < H_y H_x^* >$.

The two other impedance tensor elements are obtained similarly from E_{yi}.

In equation (A2.47), it is assumed that all observation errors are due to E_x, while H_x and H_y are assumed to be free of errors. This, of course, does not depict the real situation.

In the following discussion we assume, for simplicity the 1D case

$$E_{xi} = Z_{xy} H_{yi} + e_i, \qquad \text{(A2.52)}$$

with the solution

$$Z_{xy} = \frac{< E_x H_y^* >}{< H_y H_y^* >}. \qquad \text{(A2.53)}$$

Since, in reality H_{yi} also has an error, say δH_{yi},

$$H_{yi} = \overline{H}_{yi} + \delta H_{yi},$$

where $\overline{H}_{yi}$ is the true value. The denominator of equation (A2.53) can be written as,

$$< H_y H_y^* > = < \overline{H}_y \overline{H}_y^* > + < \delta H_y \delta H_y^* > + 2\,\mathrm{Re} < \overline{H}_y \delta H_y^* >. \qquad \text{(A2.54)}$$

Assuming that $< \overline{H}_y \delta H_y^* >$ is very small for a sufficiently large number M of segments, equation (A2.54) reduces to

$$< H_y H_y^* > = < \overline{H}_y \overline{H}_y^* > + < \delta H_y \delta H_y^* > \geq < \overline{H}_y\ \overline{H}_y^* >. \qquad \text{(A2.55)}$$

As a consequence, the impedance estimate (A2.53) is systematically down weighted by the errors in H_y.

Above procedure has been implemented in MARROS (Friedrichs, 2003) code, which has been used to obtain impedance tensor components from the measured field in time domain at 13 sites from Garhwal Himalaya.

A2.2.1 Determination of Apparent Resistivity and Phase

From the estimated impedance tensor, $Z(f)$, apparent resistivity ρ_a and phase ψ are determined from the off-diagonal elements Z_{xy} and Z_{yx} using following relations,

$$\rho_{axy} = \frac{1}{2\pi f\mu}\left|Z_{xy}\right|^2, \qquad \tan(\psi_{xy}) = \frac{\mathrm{Im}(Z_{xy})}{\mathrm{Re}(Z_{xy})},$$

$$\rho_{ayx} = \frac{1}{2\pi f\mu}\left|Z_{yx}\right|^2, \qquad \tan(\psi_{yx}) = \frac{\mathrm{Im}(Z_{yx})}{\mathrm{Re}(Z_{yx})}. \tag{A2.56}$$

The error terms are estimated as

$$\Delta\rho_{axy} = 2\rho_{axy}\frac{\Delta Z_{xy}}{\left|Z_{xy}\right|}, \qquad \Delta\psi_{xy} = \frac{\Delta Z_{xy}}{\left|Z_{xy}\right|},$$

$$\Delta\rho_{ayx} = 2\rho_{ayx}\frac{\Delta Z_{yx}}{\left|Z_{yx}\right|}, \qquad \Delta\psi_{yx} = \frac{\Delta Z_{yx}}{\left|Z_{yx}\right|}, \tag{A2.57}$$

where ΔZ_{xy} and ΔZ_{yx} are the estimated errors in impedance.

The locations of MT stations are shown in Figure A2.4. Table A2.1, shows the GPS locations of 13 sites, along a pro file in Himalayan, as recorded by the system. Due to limited accessibility in the tough terrain it was not possible to record good quality noise free data at all sites in the study area. A complete elimination of the noise sources was not possible in the study area. After processing it was found that out of 13 sites data recorded from the field along the PipalKoti profile, 4 sites data were highly noisy and have not been used for further analysis and interpretation. Remaining 9 sites data were given site code VP1 to VP6, as shown in Table A2.1 and the same are numbered from 1 to 9 in Figure A2.4.

S. No.	Site code	Latitude	Longitude	Elevation (m)
1	VP1	30:25:02.9600	79:24:50.4700	1091
2	Noisy not used	30:25:02.4000	79:24:58.7000	1133
3	VP2	30:25:14.5900	79:24:56.3200	1067
4	VP3	30:25:33.9200	79:25:17.6000	1101
5	Noisy not used	30:25:21.9900	79:25:51.8900	1092
6	Noisy not used	30:25:29.2800	79:25:04.7400	1146
7	Noisy not used	30:26:32.7100	79:25:31.8900	1163
8	VP4	30:26:59.3000	79:25:22.3700	1275
9	VP5	30:28:07.4000	79:26:21.6000	1221
10	VP6	30:28:50.1600	79:27:46.5800	1334
11	VP7	30:30:31.5800	79:29:15.5400	1268
12	VP8	30:31:28.8200	79:30:00.8800	1293
13	VP9	30:31:48.0000	79:30:0.0000	1588

Table A2.1: GPS locations: Latitude, Longitude and Elevation of 13 sites in Pipalkoti area.

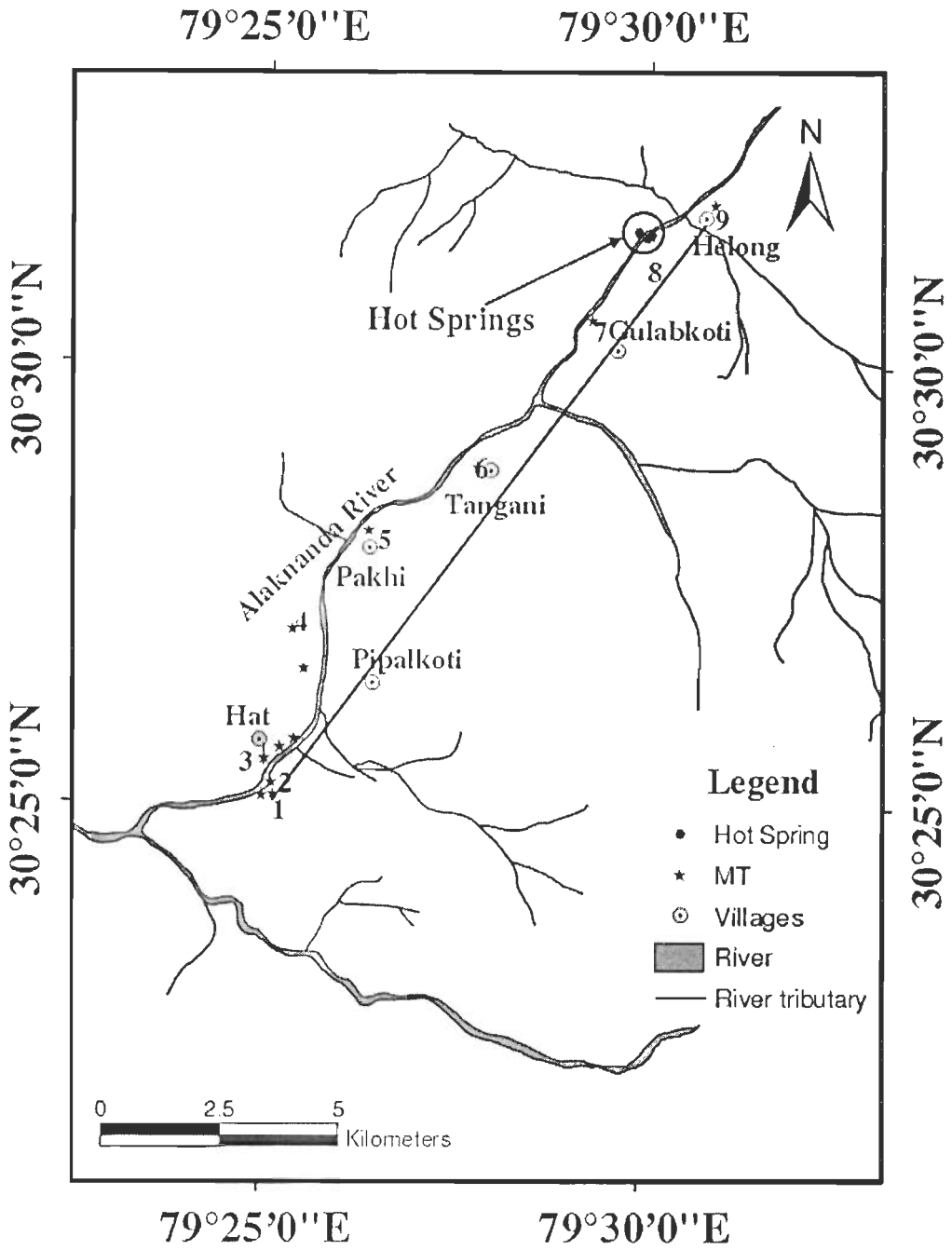

Figure A2.4: Locations of Magnetotelluric site in project area.

A2.3 ESTIMATION OF GEOELECTRIC STRIKE

Accurate interpretation of magnetotelluric data requires an understanding of the directionality and dimensionality inherent in the data and is obtained through impedance tensor decomposition discussed earlier in section A2.1.2. Groom and Bailey (1989) decomposition as implemented in 'strike' code of McNeice and Jones (2001) have been used to determine distortion parameters (twist and shear) and the regional geoelectric strike from the measured response.

To determine geoelectric strike direction and estimate the usefulness of 2D inversion Impedance decomposition have been performed for the data set. Twist and shear give the amount of distortions due to small scale 3D inhomogeneities and usefulness of 2D inversion. Geoelectric strike has been determined using 'strike' code in three different modes: (i) single-site, single frequency, (ii) single-site, multi-frequency and (iii) multi-site, multi-frequency mode. The Multi-site, Multi-frequency tensor decomposition is also used to estimate the regional strike angle from the measured data. The average geoelectric strike estimated from the data is $N77^{0}W$. The responses were rotated to obtained TE and TM modes data for inversion.

A2.4 1D INVERSION OF MAGNETOTELLURIC DATA

1D inversion of magnetotelluric response curve has been performed to derive subsurface resistivity structure at each site from the observed data. This has been done for both modes (TE and TM) responses in dependently using Marquardt's (Marquardt, 1963) and occam's (Constable et al., 1987) inversion techniques as implemented in WingLink inversion code. Resistivity-depth profile at each site has been derived using 1D inversion. Resistivity depth profile generated from the two modes (TE and TM) responses at a particular site will be similar if the underlying resistivity structure is 1D. In the presence of 2D resistivity structure, 1D models derived from two modes responses are different. In such cases, 1D model derived from TE-mode response is more closure to the true resistivity depth profile as TE-mode curve is not distorted due to the presence of

lateral inhomogeneities. 1D inversion model has been used to obtain first initial resistivity-depth model at each site.

1D inversion results of TE and TM modes responses for a representative 7 sites from the study area are shown in Figure A2.5 (a-g) and A2.6 (a-g) respectively. Station code for the site is mentioned in top left corner. Left side of each figure show the observed and calculated apparent resistivity and phase responses and the corresponding resistivity-depth model with resistivity (ohm-m) and depth (km) are shown in right site of the figures. Figures A2.5 (a-g) and A2.6 (a-g) show that Occam's inversion models are smooth and produce large number of constant thickness layers indicating smooth resistivity variation with depth. The particular mode data used for the inversion is highlighted in each figure. This gives nearly continuous variation of resistivity with depth. On the other hand Marquardt method is based on the least number of subsurface layers. Electrically these two models derived from occam's and Marquadt's inversion are equivalent and capable to fit the observed responses. It has also been experienced that 1D inversion of TE-mode apparent resistivity curve is less affected by lateral inhomogeneities. In addition the TM-mode apparent resistivity curve changes shape in the presence of lateral discontinuity (Berdichevsky et al., 1998). Therefore, the resistivity-depth model obtained from TE-mode data give an approximate picture of resistivity variation with depth in the study area and is also used to generate initial model for 2D inversion along the profile line.

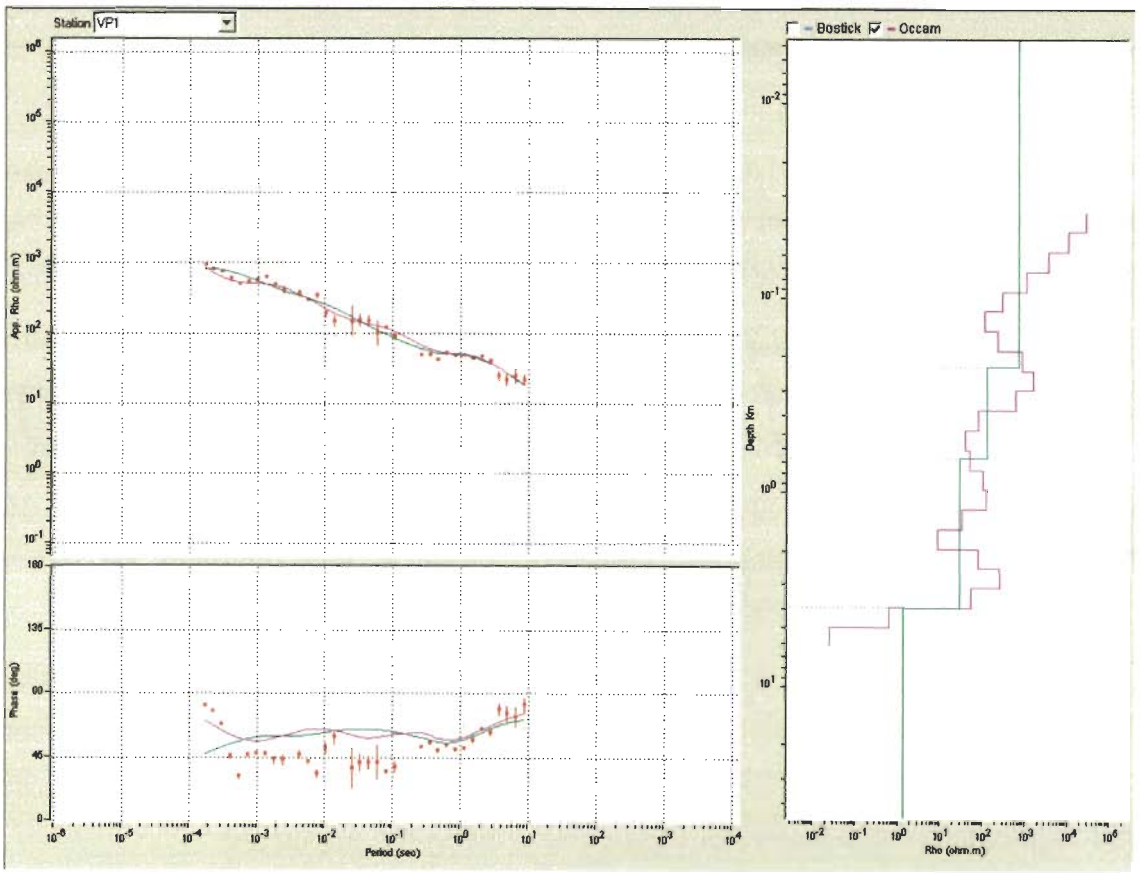

Figure A2.5a: **1D inversion of TE mode MT response at site 1 (VP1). Observed and calculated responses are shown in the left. Inverted models showing resistivity variation with depth obtained after inversion using occam's and Marquardt's techniques are shown in the right.**

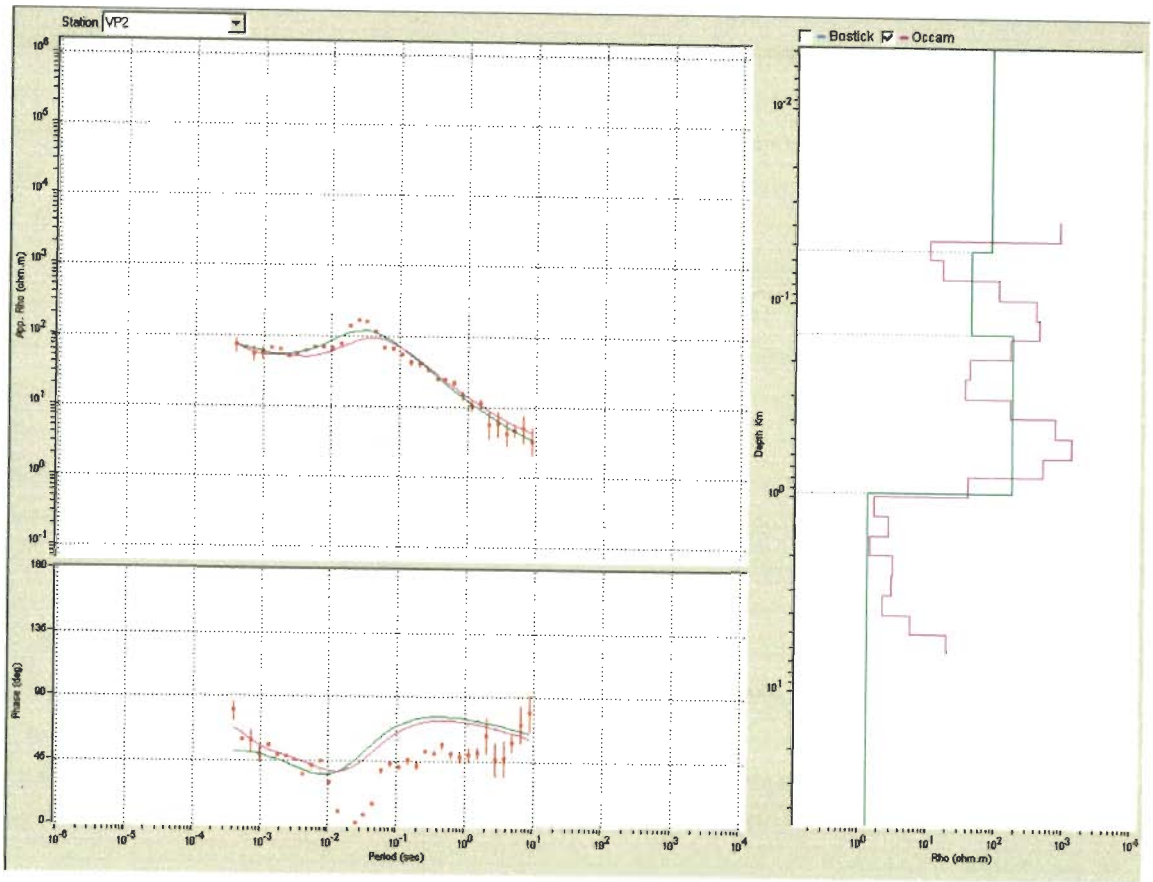

Figure A2.5b: **1D inversion of TE mode MT response at site 2 (VP2). Observed and calculated responses are shown in the left. Inverted models showing resistivity variation with depth obtained after inversion using occam's and Marquardt's techniques are shown in the right.**

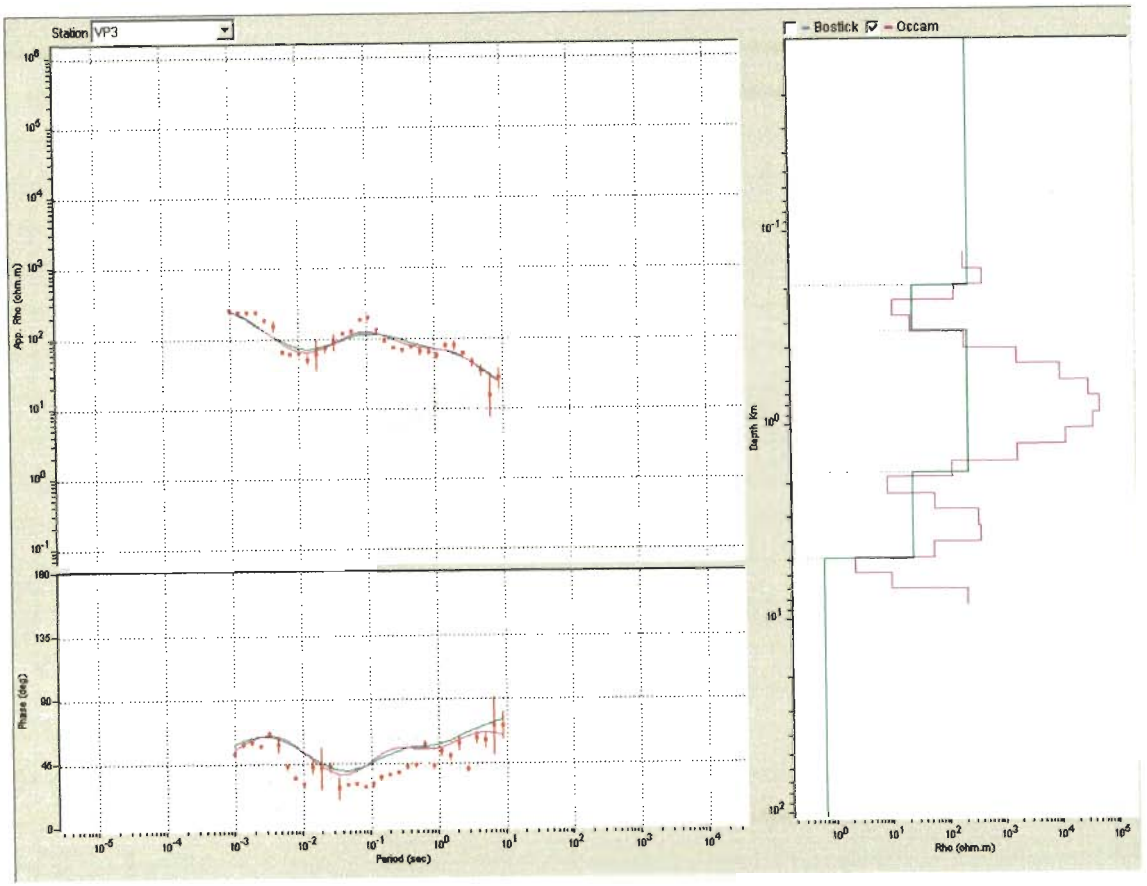

Figure A2.5c: **1D inversion of TE mode MT response at site 3 (VP3). Observed and calculated responses are shown in the left. Inverted models showing resistivity variation with depth obtained after inversion using occam's and Marquardt's techniques are shown in the right.**

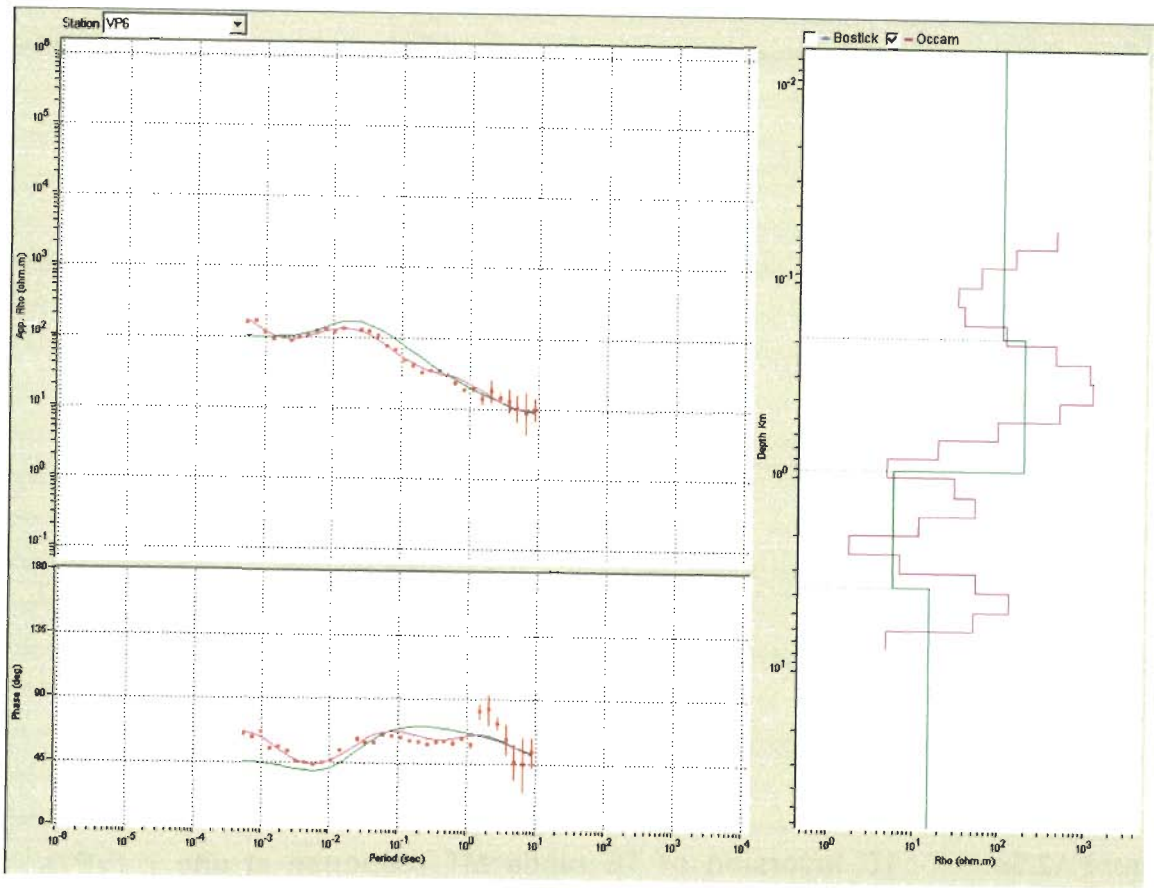

Figure A2.5d: **1D inversion of TE mode MT response at site 6 (VP6). Observed and calculated responses are shown in the left. Inverted models showing resistivity variation with depth obtained after inversion using occam's and Marquardt's techniques are shown in the right.**

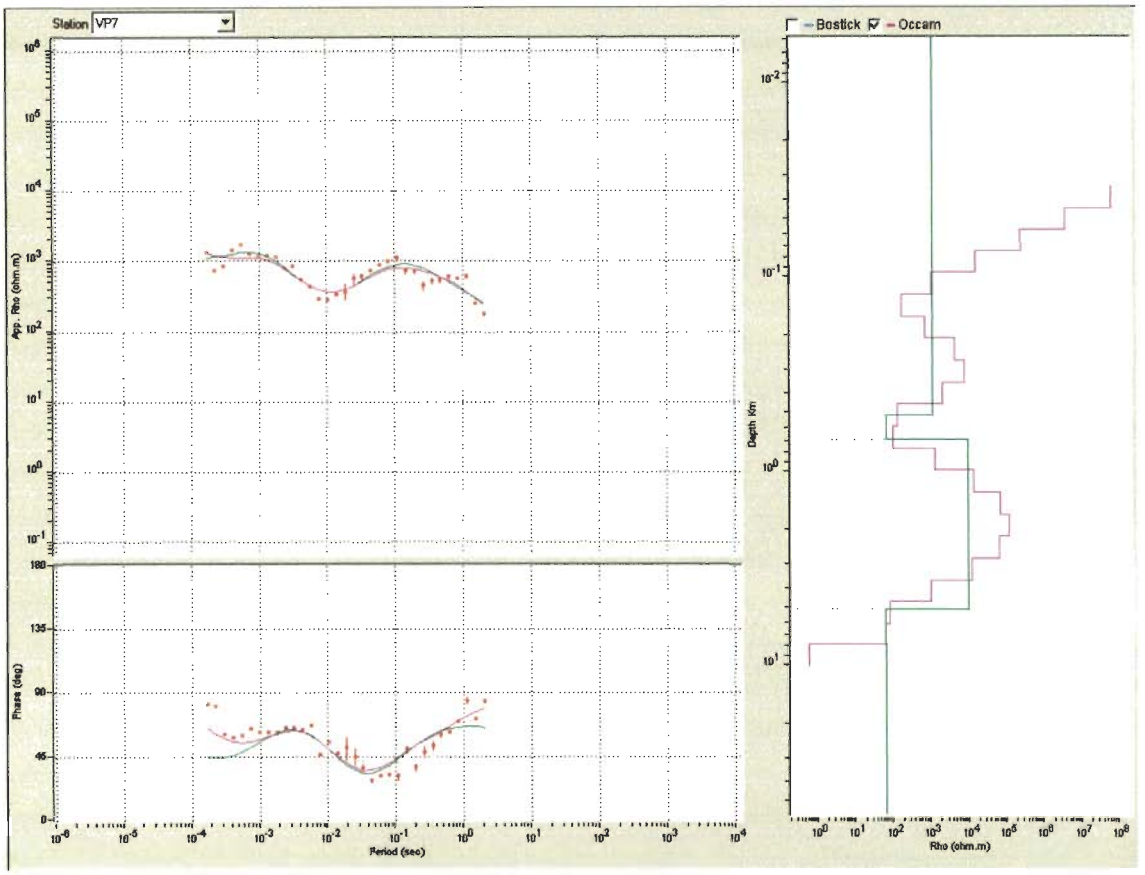

Figure A2.5e: **1D inversion of TE mode MT response at site 7 (VP7). Observed and calculated responses are shown in the left. Inverted models showing resistivity variation with depth obtained after inversion using occam's and Marquardt's techniques are shown in the right.**

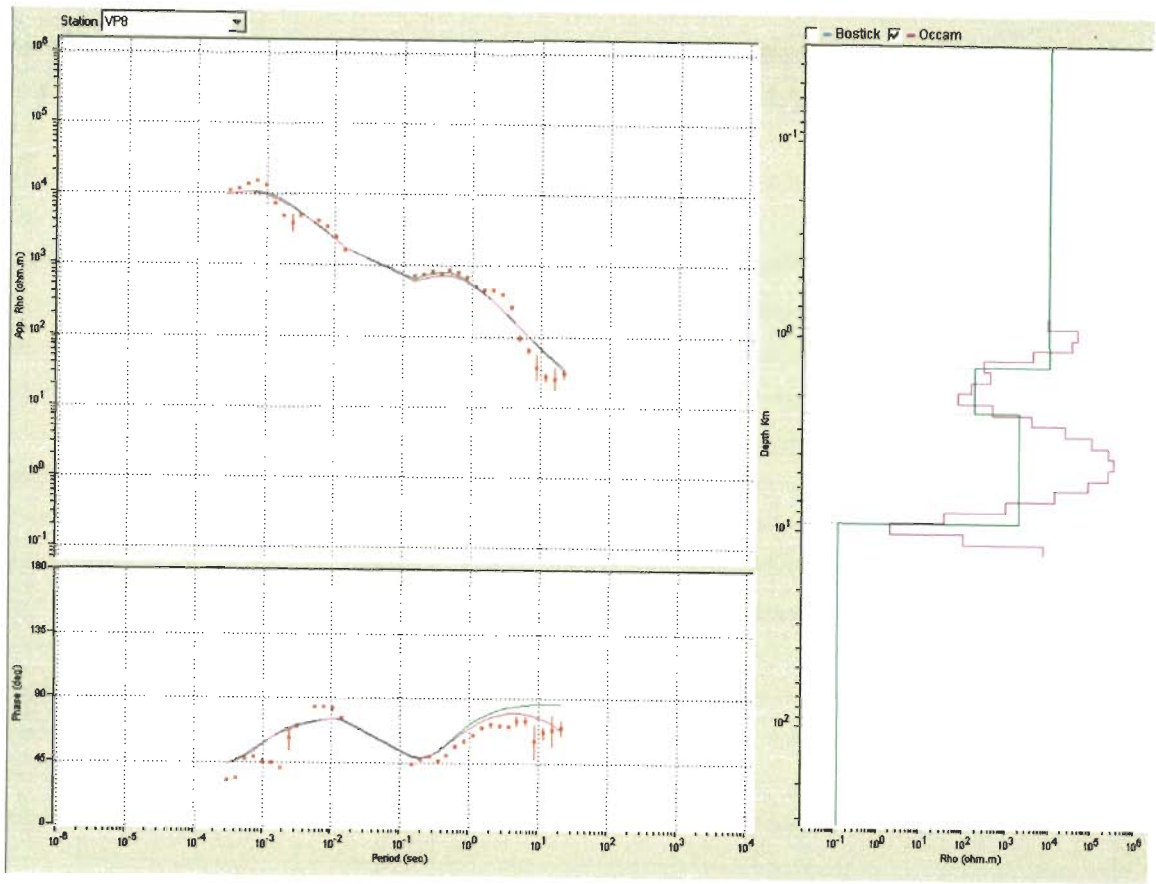

Figure A2.5f: **1D inversion of TE mode MT response at site 8 (VP8). Observed and calculated responses are shown in the left. Inverted models showing resistivity variation with depth obtained after inversion using occam's and Marquardt's techniques are shown in the right.**

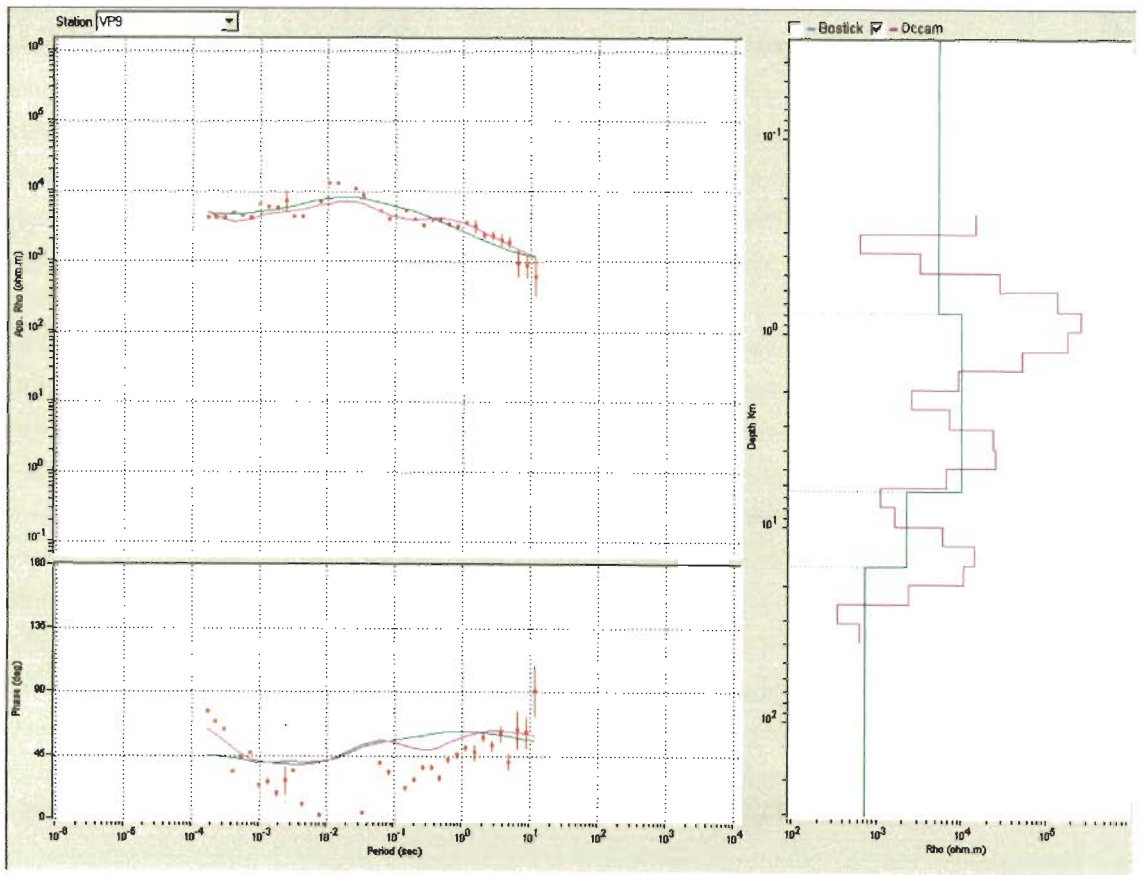

Figure A2.5g: **1D inversion of TE mode MT response at site 9 (VP9). Observed and calculated responses are shown in the left. Inverted models showing resistivity variation with depth obtained after inversion using occam's and Marquardt's techniques are shown in the right.**

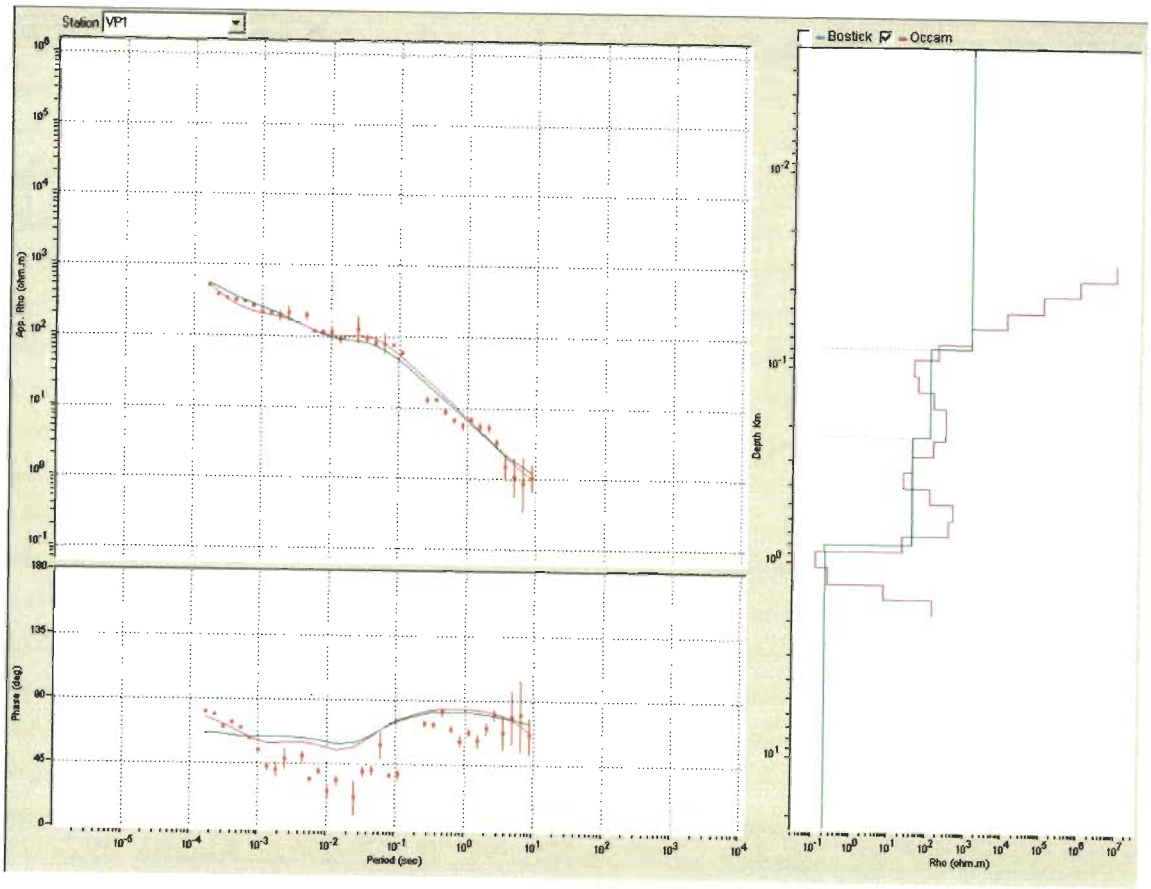

Figure A2.6a: **1D inversion of TM mode MT response at site 1 (VP1). Observed and calculated responses are shown in the left. Inverted models showing resistivity variation with depth obtained after inversion using occam's and Marquardt's techniques are shown in the right.**

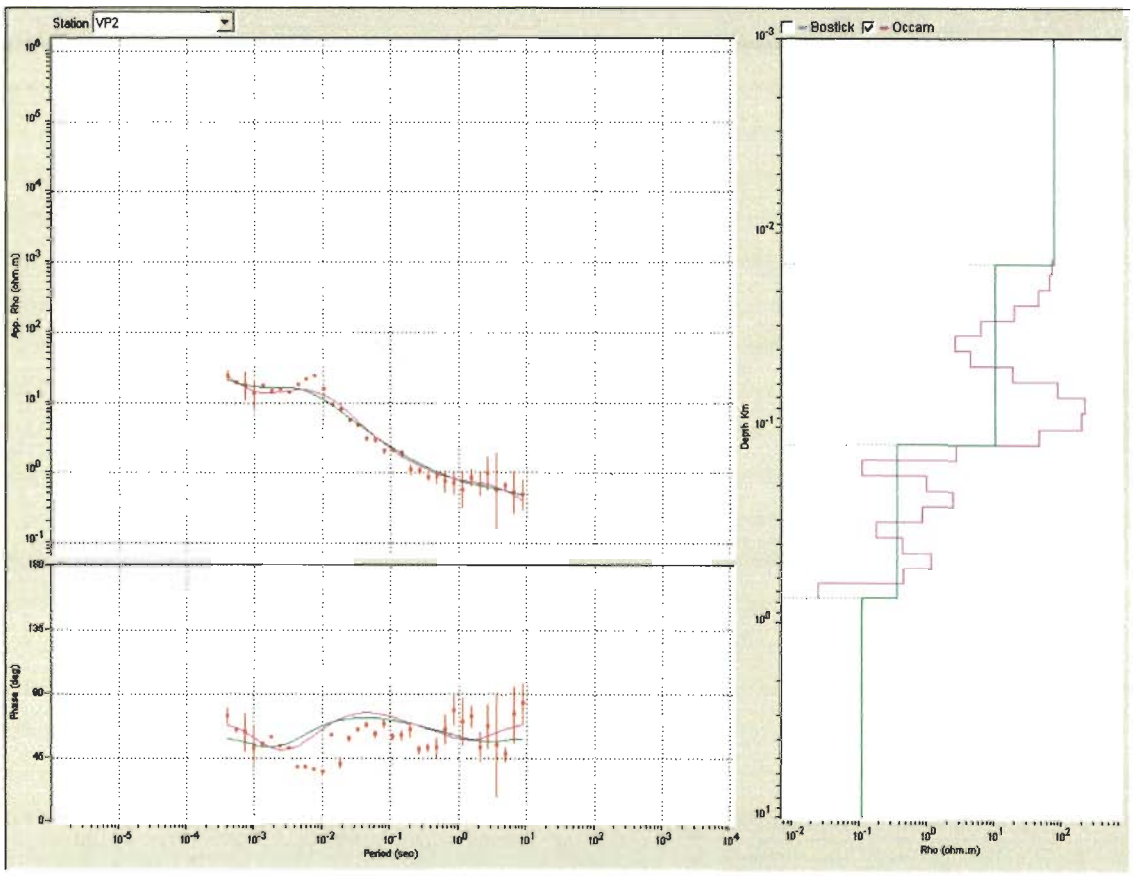

Figure A2.6b: **1D inversion of TM mode MT response at site 2 (VP2). Observed and calculated responses are shown in the left. Inverted models showing resistivity variation with depth obtained after inversion using occam's and Marquardt's techniques are shown in the right.**

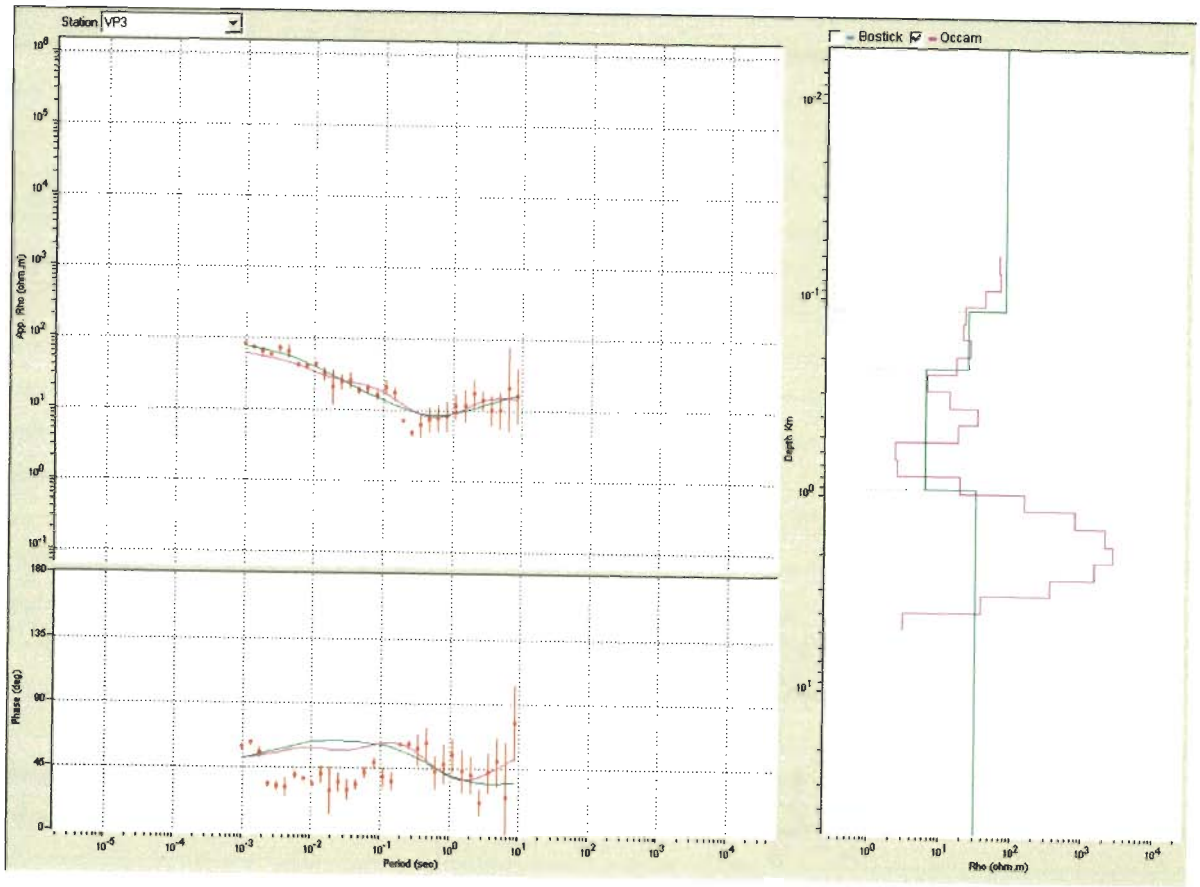

Figure A2.6c: **1D inversion of TM mode MT response at site 3 (VP3). Observed and calculated responses are shown in the left. Inverted models showing resistivity variation with depth obtained after inversion using occam's and Marquardt's techniques are shown in the right.**

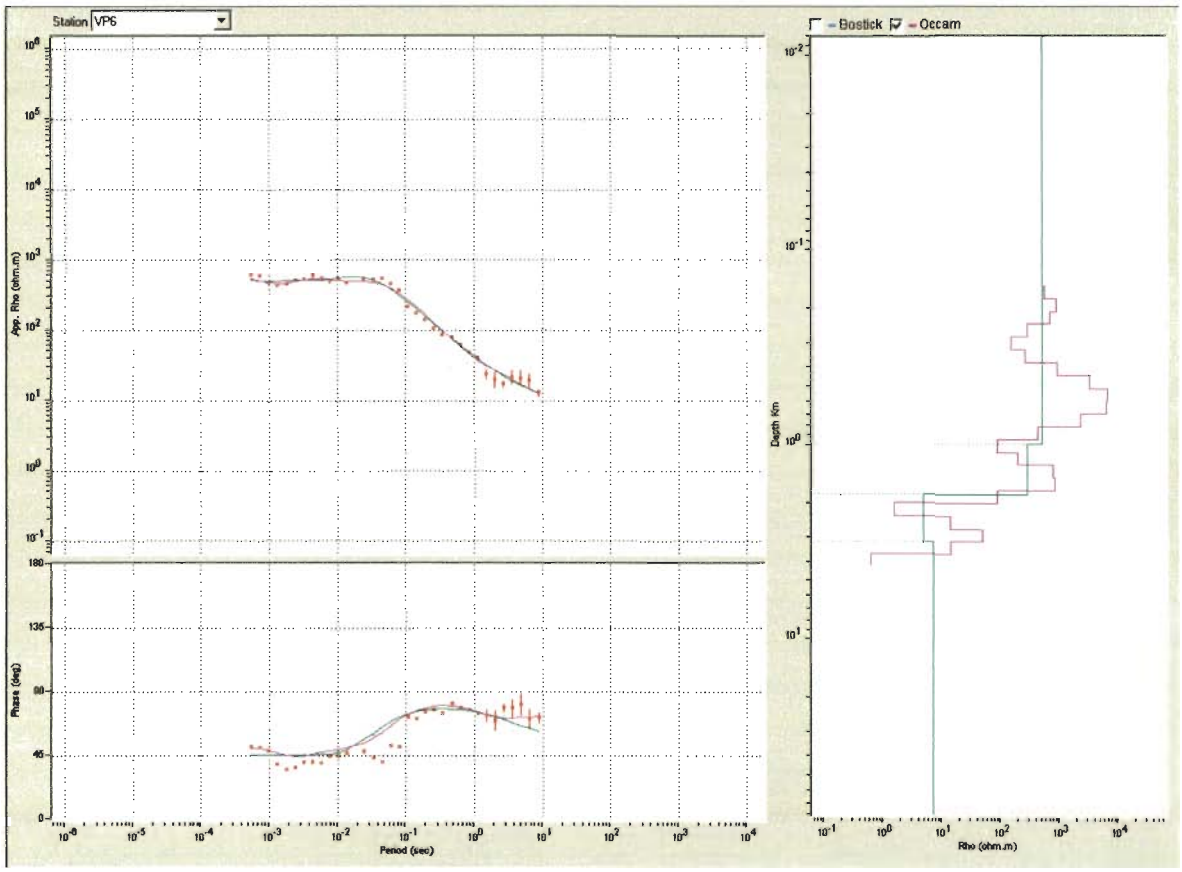

Figure A2.6d: **1D inversion of TM mode MT response at site 6 (VP6). Observed and calculated responses are shown in the left. Inverted models showing resistivity variation with depth obtained after inversion using occam's and Marquardt's techniques are shown in the right.**

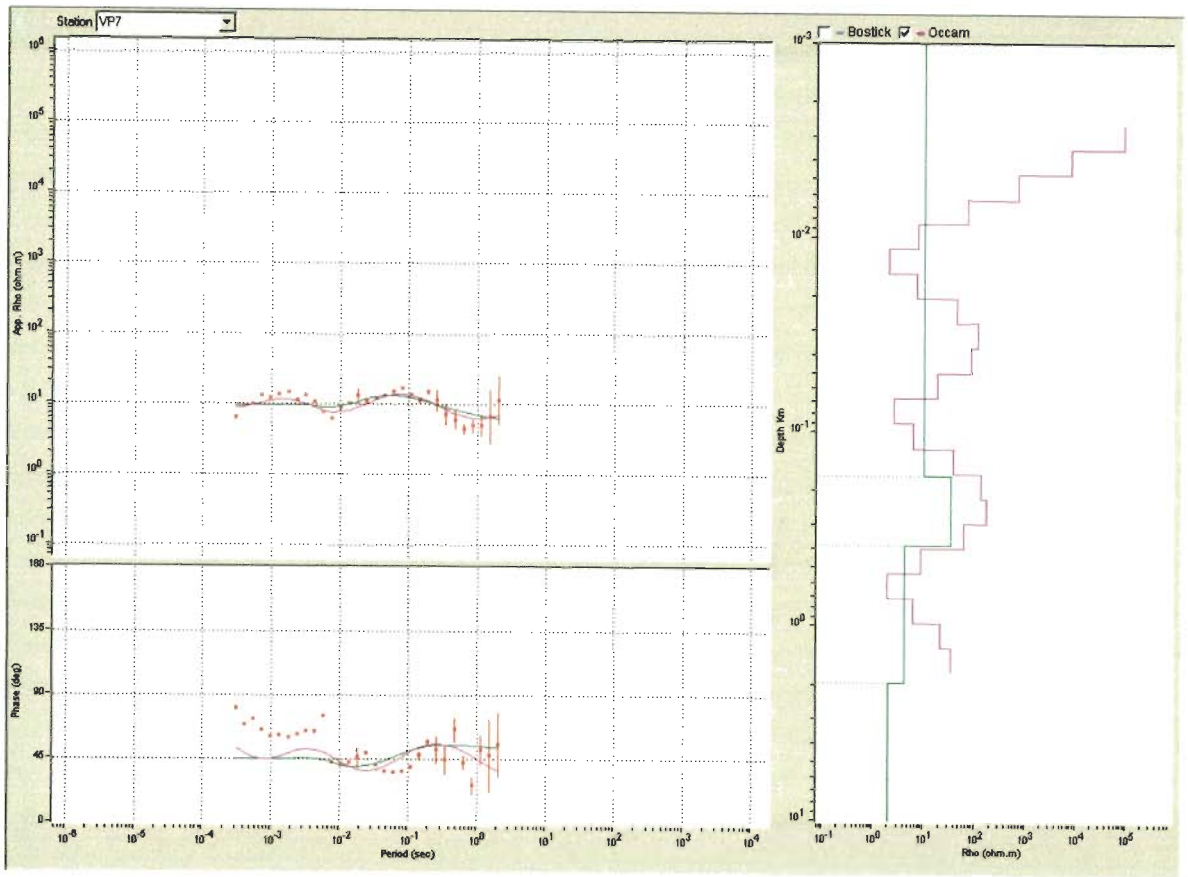

Figure A2.6e: **1D inversion of TM mode MT response at site 7 (VP7). Observed and calculated responses are shown in the left. Inverted models showing resistivity variation with depth obtained after inversion using occam's and Marquardt's techniques are shown in the right.**

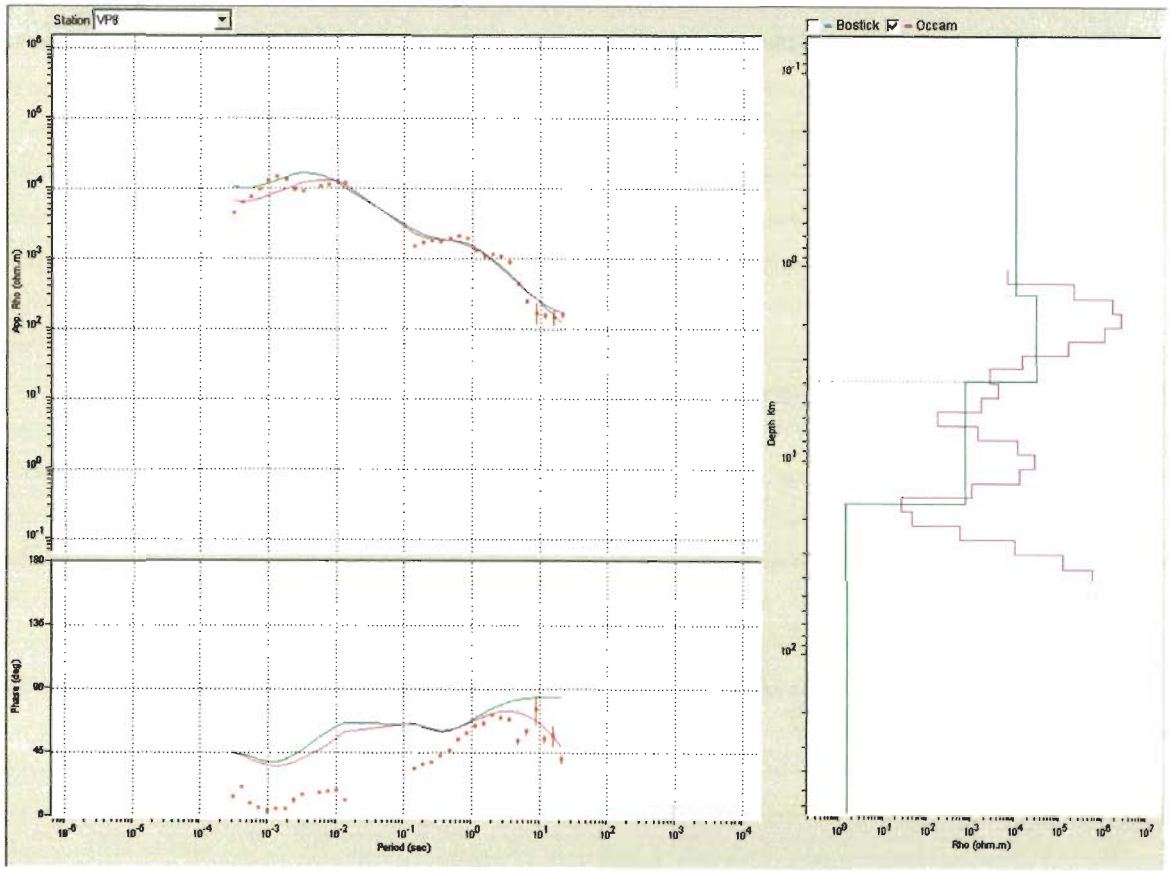

Figure A2.6f: **1D inversion of TM mode MT response at site 8 (VP8). Observed and calculated responses are shown in the left. Inverted models showing resistivity variation with depth obtained after inversion using occam's and Marquardt's techniques are shown in the right.**

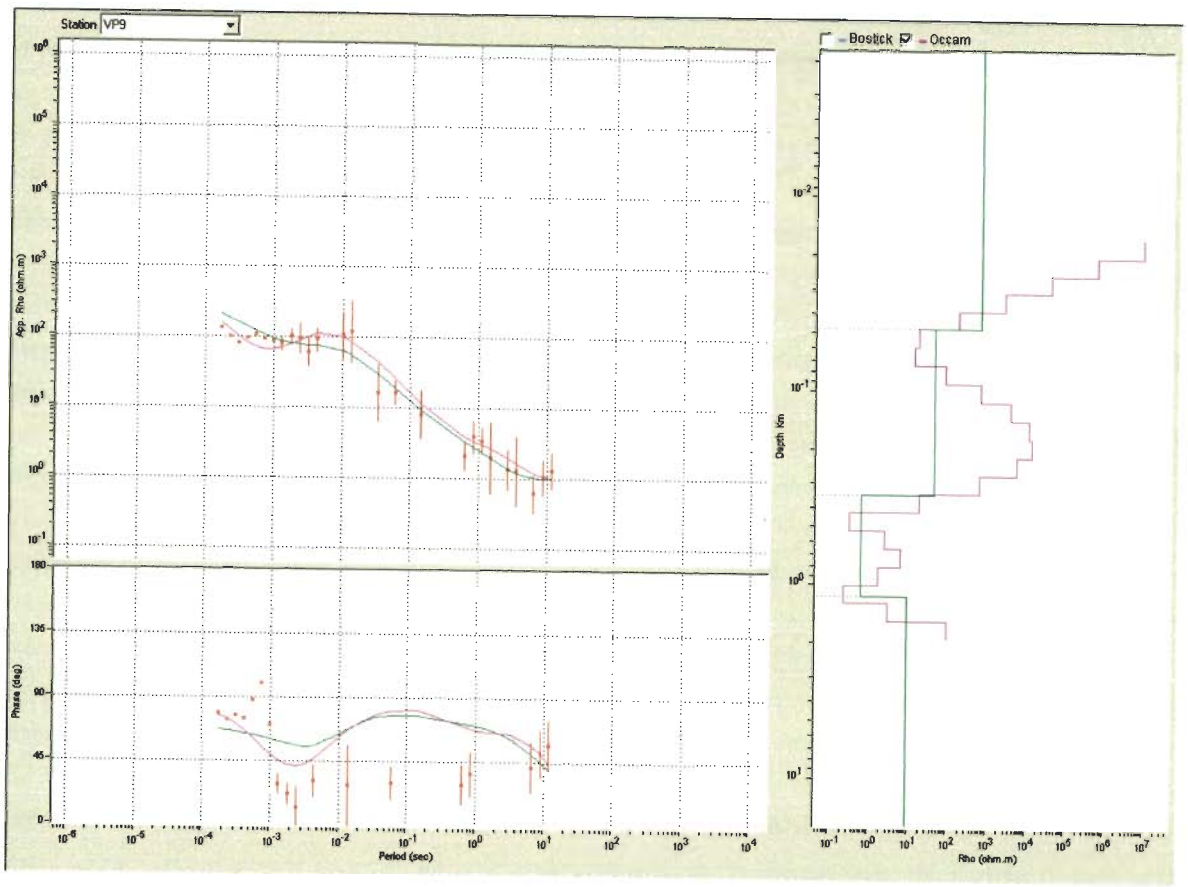

Figure A2.6g: **1D inversion of TM mode MT response at site 9 (VP9). Observed and calculated responses are shown in the left. Inverted models showing resistivity variation with depth obtained after inversion using occam's and Marquardt's techniques are shown in the right.**

A2.5 2D INVERSION OF MAGNETOTELLURIC DATA

After 1D inversion it is clear that TE and TM responses and respective inverted models are not consistent. In such case 1D model obtained from TE mode data may be considered as approximate resistivity-depth model and 2D inversion is essential for the MT responses. 2D smooth inversion (deGroot-Hedlin and Constable, 1990) has been used to derive reliable resistivity-depth model along the profile. Smooth inversion finds the smoothest model whose response fits the observed data. The misfit between the observed apparent resistivity (ρ^o) and phase (φ^o) and the corresponding computed apparent resistivity (ρ^c) and phase (φ^c) is given by the estimated root mean square (*rms*) error, ε, defined as (Xiao, 2004),

$$\varepsilon = \sqrt{\frac{1}{2NM}\sum_{j=1}^{M}\sum_{i=1}^{N}\left[\left(\frac{\rho_{ij}^{o}-\rho_{ij}^{c}}{e_{\rho ij}}\right)^2+\left(\frac{\psi_{ij}^{o}-\psi_{ij}^{c}}{e_{\psi ij}}\right)^2\right]}. \qquad \text{(A2.58)}$$

Here suffices i and j specify the i^{th} site j^{th} frequency, superscripts o and c imply observed and corresponding computed response. N is the number of sites, M is the number of frequencies at each site, e_ρ and e_ψ are the standard errors associated with the apparent resistivity and phase at each data point, respectively.

Instead of using variable individual data point errors, we have used error floors in apparent resistivity, ρ, and in phase, ψ, which provide a more uniform fit to the observed data. The error floor for a data set is defined as the average error level in the observed response.

Inversion has been done without correcting the data for static shift. Any static shift in the data will appear as an additional error in the apparent resistivity. As the phase is not affected by static shift, error floor in phase is kept lower than the error floor in apparent resistivity. To accommodate any static shift, error floor of magnitude 20% in apparent resistivity and 10% in phase is used. Root mean square (*rms*) misfit is significantly larger than unity indicates that the inversion is incapable of fitting the MT data. It either implies that the noise in the data is larger

than the defined error floor or that a three-dimensional effect is present in the data. A misfit significantly less than unity indicates either the errors are too small or that the data is being over fitted. In the latter case, the resistivity model usually is very rough.

The inverse problem defined here is solved in the sense of Tikhonov and Arsenin (1977), where an objective function, ϕ, defined below, is minimized,

$$\phi(m) = (d - F[m])^T V^{-1}(d - F[m]) + \tau m^T L^T L m . \qquad \text{(A2.59)}$$

Here *d* is the observed data vector, *F* is the forward modeling operator, *m* is the unknown model vector, V is the positive definite covariance matrix of the data errors, τ is regularization parameter and L is linear regularization operator. In equation (A2.59), the first term measures the data misfit and the second term, the model smoothness. The trade-off between data misfit and model smoothness is controlled by the regularization parameter τ. We have used 2D inversion code as implemented in WinGlink software package for 2D smooth inversion (deGroot-Hedlin and Constable, 1990) of our MT data. The parameter τ is not automatically determined, but found through several inversions with different values of τ. With increasing τ both data misfit and smoothness increase. An optimum smoothness parameter, τ, is obtained by the trade-off between the smoothness of the model and *rms* misfit. Large values cause a smoother model at the expanse of a worse data fit. The smoothness (τ), 10, is obtained from the L- curve plotted between model roughness and *rms* error for the present data set. We have used Laplacian operator as smoothing operator, L, which is defined as

$$L = \alpha \partial^2 / \partial y^2 + \beta \partial^2 / \partial z^2 , \qquad \text{(A2.60)}$$

where α and β are the weights for horizontal and vertical smoothness.

An increase of the weight α, increases the horizontal smoothness and an increase of β, increases the vertical smoothness of the model. By systematic trials, an optimal value for the weighting function α and β is estimated as 8 and 3 respectively.

Keeping in view of the different sensitivities of TE and TM mode responses to the geoelectrical structure, we have carried out inversion in three stages

sequentially to arrive a consistent geoelectrical model. The final model incorporates the important features of both TE and TM responses. For consistency or non-uniqueness checks, the inversion experiments were repeated with different half-space initial models. Further, initial guess model based on the experience of 1D inversion, were also used for 2D inversion. The broad features of these models match except for small degree of variations in resistivity values.

Inverted model is given in Figure A2.7 which presents (i) 2D smooth geoelectric model obtained from the joint inversion of TE and TM responses (ii) locations of 9 MT sites indicated by vertical bar with station code VP. The inversion parameters: smoothness, data type, frequency range and regularization parameters used, are shown in Table A2.2. Fitting of observed and calculated responses for TE and TM modes are shown in Figures A2.8. The geoelectrical model is in general consistent with the tectonic model. The characters A, B, C, and D in Figure A2.7 indicate the major electrical features of the model. The electrical characteristics, its importance and possible geological inference of the area are discussed in the following in terms of these features.

Input data	Apparent resistivity and phase data for TE- and TM-modes. Frequency 1000 Hz to 0.01 Hz is used.
Parameter for smooth inversion	Solve for smoothest model Regularization Laplacian: Standard grid Laplacian operator Regularization order: Minimize integral of $\|\text{Laplacian}\|^2$
Error floor	20% for apparent resistivity, 15% for phase for both modes
τ, regularization parameter	τ = 10
Weighting function	α = 8, β = 3

Table A2.2: Definition of parameters used in 2D inversion

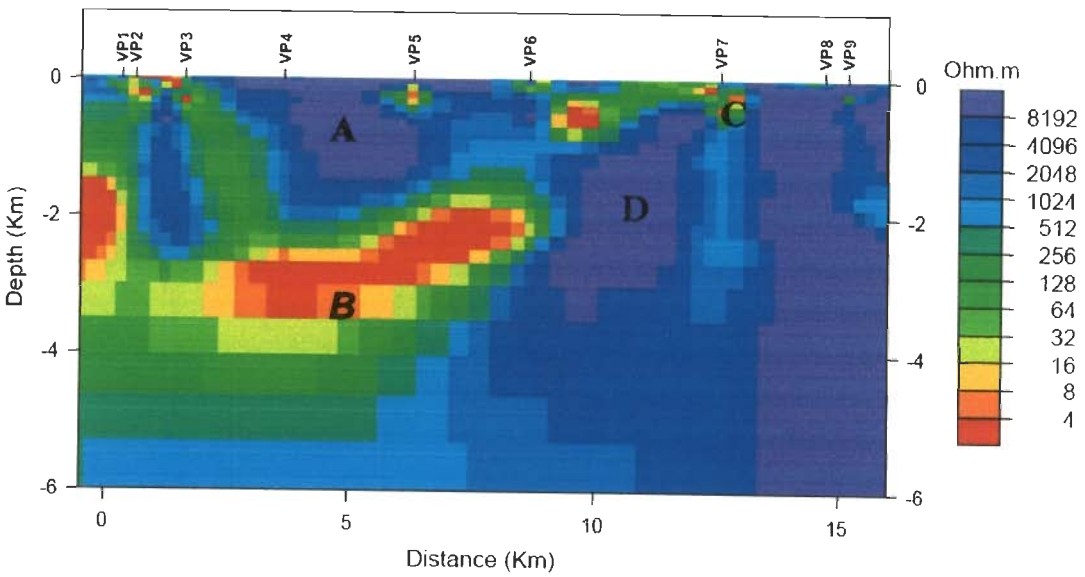

Figure A2.7: 2D model showing (i) 2D smooth geoelectric model obtained from the joint inversion of TE and TM responses (ii) locations of 9 MT sites indicated by vertical bar with station code VP.

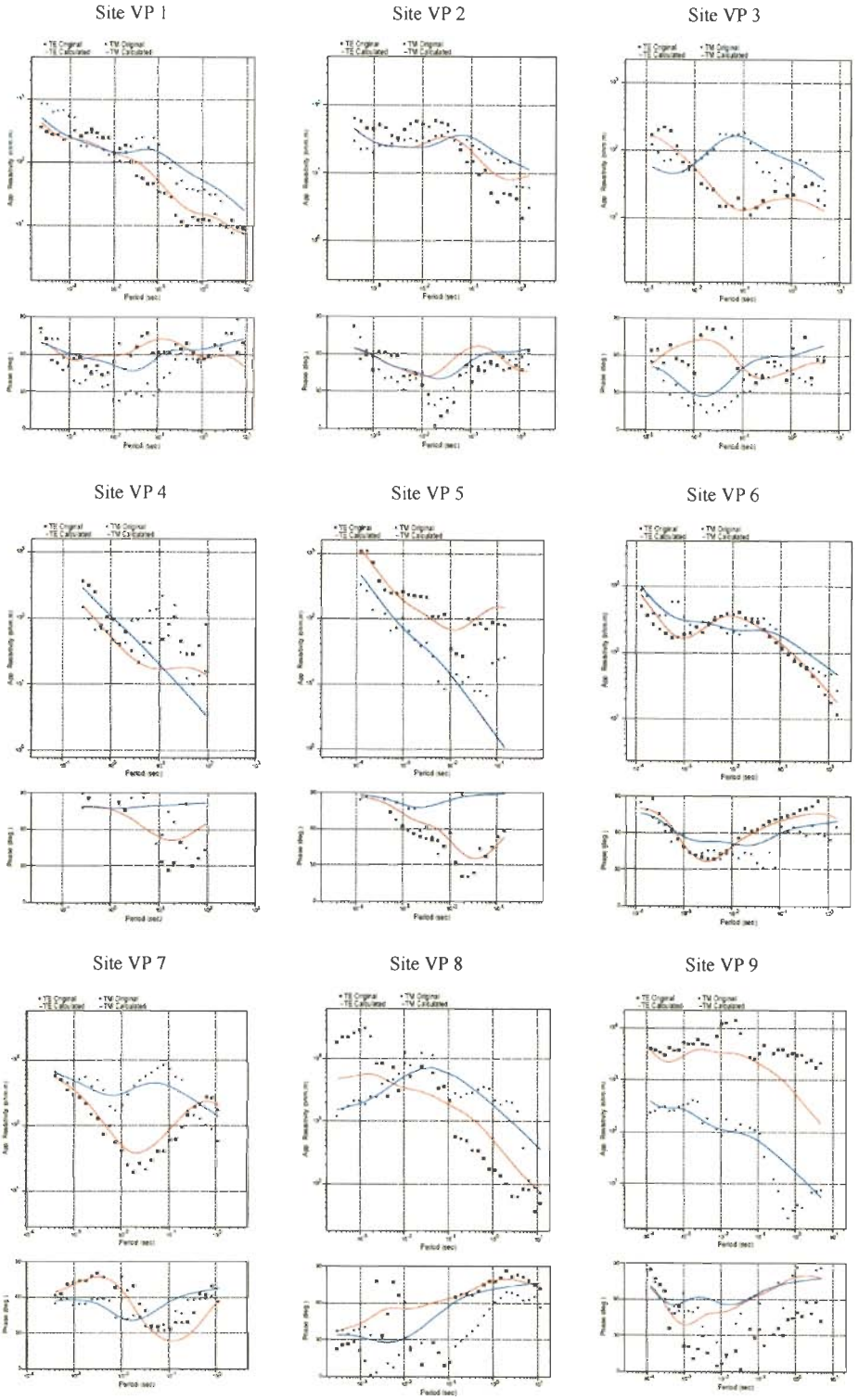

Figure A2.8: Fitting of MT data observed and calculated responses for TE and TM modes, from the project area.

Feature A

This is a highly resistive structure (>1000 Ω-m) mainly related to the hard rock formation extending from the surface to a depth of about 2.0 km confined in the southern zone (from VP4 and VP5) with minor fractured zone underneath VP5 and VP6 sites. Thickness of resistive formation is about 2 km underneath the VP4, which reduces northward. From VP6 to VP8, the formations are fractured and jointed which exhibit a relatively low resistivity formation. Some of these fractures are reaching to a deeper depth.

Feature B

This is a very low resistivity (< 5 Ω-m) formation at depth varying from 2.0 to 3.5 km. In southern part of the area depth is maximum (3.5 km) and towards the north it becomes shallower (2.0 km) underneath VP5 and VP6 sites. The low resistivity zone is overlain and underlain by resistive formations. The low resistivity (< 5 Ω-m) zone below Main Central Thrust (MCT) is a typical example of low resistivity zone in Himalayan region. The zone is extended laterally from VP4 to VP6 with an average thickness of about 800 m, mainly around MCT zone. Main Central Thrust zone falls in high heat flow area, majority of hot springs are concentrated around this zone. GSI (1991) reported high heat flow (130 ± 30 mW/m^2) and high temperature gradient (60^0 ± 20^0 C/km) in the MCT zone, whereas the foothill Himalayan belts shows low heat flow (41 ± 10 mW/m^2) and low temperature gradient (17^0 ± 5^0 C/km). On the basis of annual mean surface temperature of 15 ^{0}C in this area and average temperature gradient, 60^0 ± 20 ^{0}C/ km (GSI, 1991) in the MCT zone, which is close by, the approximate average temperature at 2 km depth is estimated to be about 135 ^{0}C. This suggests that the subsurface temperature is elevated in the MCT zone. Hot springs observed in the area and elevated temperature in the rock appears to be related with this zone.

Feature C

This is a low resistivity zone extending vertically underneath VP7, between the two high resistivity zones. This is an example of deeper fracture and joint in the

rock mass. Near surface local very low resistivity zone might be related to the water channels.

Feature D

This is a highly resistive feature underlying rock mass between VP6 and VP7 sites. The depth of the top of this zone is about 0.5 km, which extends to a depth of 6.0 km.

The electrical features discussed above are generally observed in all inverted geoelectrical models generated with various experiments with different initial guess models. However, these features do show small degree of variations in different experiments. Some of the features are artifacts of the numerical modeling, and are not related to the geological structure. For example the conducting zone in the southern end of the profile at about 2 km depth is generated by numerical fitting of the response and has no data control (Figure A2.7). High heat flow may also be related to the frictional heat generated due to large-scale faulting or fracturing in the MCT zone.

A2.6 GEOLOGICAL INTERPRETATION OF GEOELECTRICAL MODEL

The outcome of 2D smooth inversion was a resistivity-depth image showing electrical structure up to about 6.0 km depth. The magnetotelluric model generated from 2D inversion of MT responses recorded from the study area indicates electrical configuration both of the near surface shallow and deeper geological scenario.

Based on the analysis of these data, an electrical model of subsurface scene is postulated. A major electrical feature of the model is existence of deep (> 2.0 km) conductor extending from the southern zone near VP3 to the northern zone of the profile near VP6. The depth to the top of conductor varies from 2.0 to 3.5 km. It has maximum depth 3.5 km in the southern part of the zone, underneath VP3 whereas towards the northern zone of the profile it is shallower (2.0 km). This water saturated fractured zone, which is almost 800 m thick is the most likely the source of heat in the area, from which hot water springs such as the one reported near VP6 emerge. Resistive formation above the low resistivity zone is acting, in

general as cap rock in the entire region. Hence, except through fractures, there appears no direct hydraulic connection between the low resistivity hot water zones, with near surface formations. It seems that the meteoric water reach this zone through some of the deep fracture and gets accumulated under pressure. Some other fractures allow this water to ooze out under pressure in the form of spring. The average geothermal gradient in the MCT zone is about $60^0 \pm 20^0$C/ km (GSI, 1991) with an average surface temperature of about 15^0C in the Dam area, which is close to the MCT. On the basis of these data, the temperature is worked out as about 135^0C at 2 km depth. The relatively low electrical resistivity (< 5 Ω-m)/conductive zone in an otherwise resistive rocks below the depth of 2.0 to 3.5 km is attributed to existence of water in the secondary pore space created by intersection of a number of deep fractures.

REFERENCES

Adam, A., 1997. Magnetotelluric phase anisotropy above extensional structures of the Neogene Pannonian basin. J. Geomagn. Geoelectr., **49**, 1549-1557.

Adam, A., Novak, K., and Szarka, L., 2005. Tectonic weak zones determined by magnetotellurics along the CEL-7 deep seismics profile. Acta Geod. Geoph. Hung., **40**, 413-430.

Afraimovich, E. L., Altynsev, A. T., Grechnev, V. V., and Leonovich, L. A., 2002. The response of the ionosphere to faint and bright solar flares as deduced from global GPS network data. Ann. Geophys., **45**, 31-39.

Agarwal, R. R., Rai, J., and Varshneya, N. C., 1995. Effect of ionization and particulate pollutants on GEC parameters over the Indian subcontinent. Ind. J. Radio Space Phys., **24**, 159-165.

Akmamedov, Kh., 1993. Interferometric temperature measurements in the F2 ionospheric layer during the June 20, 1990 earthquake in Iran. Geomagn. Aeron., **33**, 163-166.

Alekseev, V. A., and Alekseeva, N. G., 1992. Investigation of metal transfer in the biosphere during gaseous emission in zones of tectonic activity using methods of nuclear-physics. Nucl. Geophys., **6**, 99-110.

Anastasiadis, A., 1999. Electron acceleration in solar flares by spatially random DC electric fields. Phys. Chem. Earth (C), **24**, 269-274.

Anderson, D. N., 1973. A theoretical study of the ionospheric F-region equatorial anomaly. Planet. Space Sci., **21**, 409-420.

Antsilevich, M. G., 1971. The influence of Tashkent earthquake on the Earth's magnetic field and the ionosphere. Tashkent earthquake 26 April 1966, Tashkent FAN, 187-188.

Baba, Y., and Rakov, V. A., 2008. Influence of strike object grounding on close lightning electric fields. J. Geophys. Res., **113**, D 12109.

Bailey, G. J., Moffett, R. J., and Swartz, W. E., 1975. Effects of photoelectron heating and interhemisphere transport on day-time plasma temperatures at low latitudes. Planet. Space Sci., **23**, 599-610.

Balan, N., Oyama, K. I., Bailey, G. J., Fukao, S., Watanabe, S., and Abdu, M. A., 1997. A plasma temperature anomaly in the equatorial topside ionosphere. J. Geophys. Res., **102**, 7485-7492.

Balser, M., and Wagner, C. A., 1960. Observations of earth-ionosphere cavity resonance. Nature, **188**, 638-641.

Balser, M., and Wagner, C. A, 1962. Diurnal power variations of the Earth-Ionosphere cavity modes and their relationship to world-wide thunderstorm activity. J. Geophys. Res., **67**, 619-625.

Banks, P. M., and Nagy, A. F., 1970. Concerning the influence of elastic scattering upon photoelectron transport and escape. J. Geophys. Res., **75**, 1902-1910.

Banks, P. M., and Kockarts, G., 1973. Vertical temperature distribution in the earth's atmosphere with emphasis on thermosphere. Academic Press, New York, USA, Part-A, pp 3.

Banks, P. M., Schunk, R. W., and Raitt, W. J., 1974. NO^+ and O^+ in the high latitude F region. Geophys. Res. Lett., **1**, 239-242.

Barr, R., 1987. The diffraction of VLF radio waves by the Antarctic ice cap. J. Atmos. Terr. Phys., **49**, 1-5.

Beamish, D., and Tzanis, A., 1986. High resolution spectral characteristics of the Earth-ionosphere cavity resonances. J. Atmos. Terr. Phys., **48**, 187-203.

Bell, T. F., Pasko, V. P., and Inan, U. S., 1995. Runaway electrons as a source of Red Sprites in the mesosphere. Geophys. Res. Lett., **22**, 2127-2130.

Berdichevsky, M. N., Dmitriev, V. I., and Pozdnjakova, E. E., 1998. On two-dimensional interpretation of magnetotelluric soundings. Geophys. J. Int., **133**, 585-606.

Bhattacharya, S., Sarkar, S., Gwal, A. K., and Parrot, M., 2009. Electric and magnetic field perturbations recorded by DEMETER satellite before seismic

events of the 17th July 2006 M 7.7 earthquake in Indonesia. J. Asian Earth Sci., **34**, 634-644.

Bhuyan, P. K., and Kakoty, P. K., 2000. Comparison of electron and ion temperature measurements at ± 10° magnetic latitudes from SROSS-C2 with the IRI, Abstract book on NSSS-2K, Puri, India, pp 99.

Bhuyan, P. K., and Kakoty, P. K., 2002. Theoretical simulation of O^+ and H^+ concentrations obtained by the Indian SROSS-C2 satellite in the topside F-region and comparison with the IRI. Adv. Space Res., **29**, 859-864.

Bhuyan, P. K., Chamua, M., Bhuyan, K., Subrahmanyam, P., and Garg, S. C., 2003. Diurnal, seasonal and latitudinal variation of electron density in the topside F-region of the Indian zone ionosphere at solar minimum and comparison with the IRI. J. Atmos. Solar-Terr. Phys., **65**, 359-368.

Blanc, E., 1985. Observations in the upper atmosphere of infrasonic waves from natural or artificial sources: a summary. Ann. Geophys., **3**, 673-688.

Bliokh, P. V., Nickolaenko, A. P., and Filippov, Yu. F., 1980. Schumann resonances in the Earth-ionosphere cavity. Peter Peregrinus, London, New York.

Boyarchuk, K. A., 1997. Kinetics of elementary ions in the lower atmosphere acted upon by ionizing radiation, Proceed. of Russ. Acad. Sci., Atmos. Ocean. Phys., **33**, pp 236.

Boyarchuk, K. A., Lomonosov, A. M., and Pulinets, S. A., 1997. Electrode effect-earthquakes precursor, BRAS Physics / Supplement Physics of Vibrations, **61**, pp 84.

Boys, C. V., 1929. Progressive lightning. Nature, **124**, 54-55.

Brace, L. H., and Theis, R. F., 1978. An empirical model of the interrelationship of electron temperature and density in the daytime thermosphere at solar minimum. Geophys. Res. Lett., **5**, 275–279.

Cagniard, L., 1953. Basic theory of the magnetotelluric method of geophysical prospecting. Geophys., **18**, 605-635.

Calais, E., and Minster, J. B., 1995. GPS detection of ionospheric perturbations following the January 17, 1994, Northridge earthquake. Geophys. Res. Lett., **22**, 1045-1048.

Carpenter, D. L., Stone, K., Siren, J. C., and Crystal, T. L., 1972. Magnetospheric electric fields deduced from drifting whistler paths. J. Geophys. Res., **77**, 2819-2834.

Carrington, R. C., 1860. Description of a singular appearance seen in the sun on September 1, 1859. Monthly Notices of the Royal Astronomical Society, **20**, 13-15.

Chamberlain, J. W., and Hunten, D. M., 1987. Theory of planetary atmospheres. International Geophysics Series, 36, Academic Press, New York, USA.

Chao, C. K., Su, S. Y., and Yeh, H. C., 2003. Presunrise ion temperature enhancement observed at 600 km low- and mid-latitude ionosphere. Geophys. Res. Lett., **30**, 1187-1190.

Chmyrev, V. M., Isaev, N. V., Bilichenko, S. V., and Stanev, G., 1989. Observation by space-borne detectors of electric fields and hydromagnetic waves in the ionosphere over an earthquake centre. Phys. Earth Planet. Int., **57**, 110-114.

Clarke, J., Gamble, T. D., Goubau, W. M., Koch, R. H., and Miracky, R. F., 1983. Remote-reference magnetotellurics: equipment and procedures. Geophys. Prospect., **31**, 149-170.

Cobb, W. E., 1967. Evidence of a solar influence on the atmospheric electric elements at Mauna Loa observatory. Monthly Weather Rev., **95**, 905-911.

Constable, S. C., Parker, R. L., and Constable C. G., 1987. Occam's inversion: A practical algorithm for generating smooth models from electromagnetic sounding data. Geophys., **52**, 289-300.

Cooray, V., 1992. Horizontal fields generated by return strokes. Radio Sci., **27**, 529-537.

Dalgarno, A., McElroy, M. B., and Moffett, R. J., 1963. Electron temperatures in the ionosphere. Planet Space Sci., **11**, 463-484.

Das, I. M. L., and Kumar, P., 2006. Retrieval of the vertical temperature profile of atmosphere from MST radar backscattered signal. Ind. J. Radio Space Phys., **35**, 280-285.

Davies, K., and Baker, D. M., 1965. Ionospheric effects observed around the time of the Alaskan earthquake of March 28, 1964. J. Geophys. Res., **70**, 2251-2253.

Davies, K., 1990. Ionospheric radio. Peter Peregrinus, London.

Davis, M. J., and Rosa, A. V., 1969. Traveling ionospheric disturbances originating in the auroral oval during polar substorms. J. Geophys. Res., **74**, 5721-5735.

Dea, J. Y., Hansen, P. M., and Boerner, W. M., 1993. Long-term ELF background noise measurements, the existence of window regions, and applications to earthquake precursor emission studies. Phys. Earth. Planet. Int., **77**, 109-125.

deGroot-Hedlin, C., and Constable, S., 1990. Occam's inversion to generate smooth, two-dimensional models from magnetotelluric data. Geophys., **55**, 1613-1624.

deGroot-Hedlin, C., and Constable, S., 2004. Inversion of magnetotelluric data for 2D structure with sharp resistivity contrasts. Geophys., **69**, 78-86.

Dennis, A. S., and Pierce, E. T., 1964. The return stroke of the lightning flash to earth as a source of VLF atmospherics. Radio Sci., **68**, 777-794.

Depuev, V., and Zelenova, T., 1996. Electron density profile changes in a pre-earthquake period. Adv. Space Res., **18**, 115-118.

Divya, and Rai, J., 1985. Parallel and perpendicular electric field components of a lightning discharge. Geoexploration, **23**, 227-237.

Divya, and Rai, J., 1986. Calculation of electric fields from lightning above finitely conducting ground. Ind. J. Radio Space Phys., **15**, 96.

Eack, K. B., Suszcynsky, D. M., Beasley, W. H., Roussel-Dupre, R., and Symbalisity, E., 2000. Gamma-ray emissions observed in a thunderstorm anvil. Geophys. Res. Lett., **27**, 185-188.

Eftaxias, K., Kapiris, P., Polygiannakis, J., Bogris, N., Kopanas, J., Antonopoulos, G., Peratzakis, A., and Hadjicontis, V., 2001. Signatures of pending earthquake from electromagnetic anomalies. Geophys. Res. Lett., **28**, 3321-3324.

Evans, J. V., 1973. Seasonal and sunspot cycle variations of F region electron temperatures and protonospheric heat fluxes. J. Geophys. Res., **78**, 2344-2349.

Evans, J. V., 1977. Satellite beacon contributions to studies of the structure of the ionosphere. Rev. Geophys. Space Phys., **15**, 325-350.

Farley, D. T., McClure, J. P., Sterling, D. L., and Green, J. L., 1967. Temperature and composition of the equatorial ionosphere. J. Geophys. Res., **72**, 5837-5851.

Fishman, G. J., Bhat, P. N., Mallozzi, R., Horack, J. M., Koshut, T., Kouveliotou, C., Pendleton, G. N., Meegan, C. A., Wilson, R. B., Paciesas, W. S., Goodman, S. J., and Christian, H. J., 1994. Discovery of intense gamma-ray flashes of atmospheric origin. Science, **264**, 1313-1316.

Fleagle, R. G., and Businger, J. A., 1963. An introduction to atmospheric physics. Academic press, New York, pp 235.

Freund, F. T., Takeuchi, A., and Lau, B. W. S., 2006. Electric currents streaming out of stressed igneous rocks -A step towards understanding pre-earthquake low frequency EM emissions. Phys. Chem. Earth, **31**, 389-396.

Friedrichs, B., 2003. MAPROS: magnetotelluric data processing software. Metronix GmbH, Braunschweig, Germany.

Fujinawa, Y., and Takahashi, K., 1998. Electromagnetic radiations associated with major earthquakes. Phys. Earth Planet. Int., **105**, 249-259.

Füllekrug, M., 1995. Schumann resonances in magnetic field components. J. Atmos. Terr. Phys., **57**, 479-484.

Füllekrug, M., and Fraser-Smith, A. C., 1997. Global lightning and climate variability inferred from ELF magnetic field variations. Geophys. Res. Lett., **24**, 2411-2414.

Garg, S. C., Bahl, M., Maini, H. K., Chopra, P., Jhon, T., Singh, V., and Singh, D., 1992. NPL's aeronomy experiment in space. NPL Technical Bulletin, New Delhi, India.

Garg, S. C., and Das, U. N., 1995. Aeronomy experiment on SROSS-C2. J. Spacecraft Technology, **5**, 11-15.

Garg, S. C., Bahl, M., Maini, H. K., Chopra, P., Jhon, T., Singh, V., and Singh, D., 1996. RPA payload data processing and analysis, Document prepared for RPA data analysis and utilization training program, ISRO, Bangalore, India.

Gaussiran, T. L., Bust, G. S., and Garner, T. W., 2004. LOFAR as an ionospheric probe. Planet Space Sci., **52**, 1375-1380.

Geisler, J. E., and Bowhill, S. A., 1965. Exchange of energy between the ionosphere and the protonosphere. J. Atmos. Terr. Phys., **27**, 1119-1146.

Glover, P. W. J., and Adam, A., 2008. Correlation between crustal high conductivity zones and seismic activity and the role of carbon during shear deformation. J. Geophys. Res., **113**, B12210.

Gokhberg, M. B., Morgounov, V. A., Yoshino, T., and Tomizawa, I., 1982. Experimental measurement of electromagnetic emissions possibly related to earthquakes in Japan. J. Geophys. Res., **87**, 7824-7828.

Gokhberg, M. B., Gershenzon, N. I., Gufel'd, I. L., Kustov, A. V., Lipervosky, V. A., and Husameddinov, S. S., 1984. Possible effects of the action of electric fields of seismic origin on the ionosphere. Geomag. Aeron., **24**, 183-186.

Gokhberg, M. B., Kustov, A. V., Liperovsky, V. A., Liperovskaya, R. Kh., Kharin, E. P., and Shalimov, S. L., 1988. About disturbances in F-region of ionosphere before strong earthquakes. Izvestiya Acad. Sci. USSR, Ser. Phys., Earth **4**, 12-20.

Gokhberg, M. B., Nekrasov, A. K., and Shalimov, S. L., 1994. A new approach to the problem of the lithosphere-ionosphere coupling before the earthquakes, in: Electromagnetic phenomena related to earthquake prediction, edited by: Hayakawa, M., Fujinawa, Y., Tokyo, TERRAPUB, 619-625.

Gokhberg, M. B., Morgounov, V. A., and Pokhotelov, O. A., 1995. Earthquake prediction; Seismo-Electromagnetic phenomena. Gordon and Breach publishers, Amesterdam, Netherland.

Gomes, C., Cooray, V., Fernando, M., Montano, R., and Sonnadara, U., 2004. Characteristics of chaotic pulse trains generated by lightning flashes. J. Atmos. solar Terr. Phys., **66**, 1733-1743.

Grant, F. S., and West, G. F., 1965. Interpretation theory in applied geophysics. McGraw-Hill Book Company, New York, pp. 584.

Greifinger, C., and Greifinger, P., 1978. Approximate method for determining ELF eigenvalues in the earth-ionosphere waveguide. Radio Sci., **13**, 831-837.

Grimalsky, V., Koshevaya, S., Kotsarenko, A., and Enriquez, R. P., 2005. Penetration of the electric and magnetic field components of Schumann resonances into the ionosphere. Ann. Geophys., **23**, 2559-2564.

Groom, R. W., and Bailey, R. C., 1989. Decomposition of Magnetotelluric impedance tensors in the presence of local three-dimensional galvanic distortion. J. Geophys. Res., **94**, 1913-1925.

Guo, C., and Krider, E. P., 1982. The optical and radiation field signatures produced by lightning return strokes. J. Geophys. Res., **87**, 8913-8922.

Gupta, P. K., Niwas, S., and Gaur, V. K., 1996. Straightforward inversion scheme (SIS) for one-dimensional magnetotelluric data. Earth Planets Sci., **105**, 413-429.

Gwal, A. K., Shrivastava, A., and Malhotra, K., 2006. Observation of seismogenic ultra low frequency electric field fluctuations detected as a burst in the ionosphere during tsunamis over the Andaman and Nicobar Islands. Current Sci., **91**, 229-234.

Harinarayana, T., Abdul Azeez, K. K., Naganjaneyulu, K., Manoj, C., Veeraswamy, K., Murthy, D. N., and Rao, S. P., 2004. Magnetotelluric studies in Puga valley geothermal field, NW Himalaya, Jammu and Kashmir, India. J. Volcan. Geoth. Res., **138**, 405-424.

Harinarayana, T., Abdul Azeez, K. K., Murthy, D. N., Veeraswamy, K., Rao, S. P., Manoj, C., and Naganjaneyulu, K., 2006. Exploration of geothermal

structure in puga geothermal field, Ladakh Himalayas, India by magnetotelluric studies. J. Appl. Geophys., **58**, 280-295.

Hayakawa, M., and Ohtsu, J., 1973. Ducted propagation of low-latitude whistlers deduced from simultaneous observations at multi-station. J. Atmos. Terr. Phys., **35**, 1685-1697.

Hayakawa, M., Okada, T., and Iwai, A., 1981. Direction findings of medium-latitude whistlers and their propagation characteristics. J. Geophys. Res., **86**, 6939-6946.

Hayakawa, M., Kawate, R., Molchanov, O. A., and Yumoto, K., 1996a. Results of ultra-low-frequency magnetic field measurements during the Guam earthquake of 8 August 1993. Geophys. Res. Lett., **23**, 241-244.

Hayakawa, M., Molchanov, O. A., Ondoh, T., and Kawai, E., 1996b. The precursory signature effect of the Kobe earthquake on VLF subionospheric signals. J. Comm. Res. Lab., Tokyo, **43**, 169-180.

Hayakawa, M., Itoh, T., Hattori, K., and Yumoto, K., 2000. ULF electromagnetic precursors for an earthquake at Biak, Indonesia on February 17, 1996. Geophys. Res. Lett., **27**, 1531-1534.

Hayakawa, M., 2004. Electromagnetic phenomena associated with earthquakes; A frontier in terrestrial electromagnetic noise environment. Recent Res., Develop. Geophys., **6**, 81-112.

Hayakawa, M., Pulinets, S. A., Parrot, M., and Molchanov, O. A., (Eds) 2006. Recent progress in Seismo Electromagnetics and related phenomena. Phys. Chem. Earth, **31**, 129-131.

Hayakawa, M., Nickolaenko, A. P., Sekiguchi, M., Yamashita, K., Ida, Y., and Yano, M., 2008a. Anomalous ELF phenomena in the Schumann resonance band as observed at Moshiri (Japan) in possible association with an earthquake in Taiwan. Nat. Hazards Earth Syst. Sci., **8**, 1309-1316.

Hayakawa, M., Iudin, D. I., and Trakhtengerts, V. Y., 2008b. Modeling of thundercloud VHF/UHF radiation on the lightning preliminary breakdown stage. J. Atmos. solar Terr. Phys., **70**, 1660-1668.

Hays, P. B., and Roble, R. G., 1979. A quasi-static model of global atmospheric electricity 1. The lower atmosphere. J. Geophys. Res., **84**, 3291-3305.

Hazarika, S., Kumar, K., Agarwal, S. S., and Rai, J., 1987. Measurement of vertically and horizontally polarized components of whistling atmospherics: Instrumentation and analysis. J. Inst. Soc. India, **17**, 143-150.

Hegai, V. V., Kim, V. P., and Nikiforova, L. I., 1997. A possible generation mechanism of acoustic- gravity waves in the ionosphere before strong earthquakes. J. Earthquake Predict. Res., **6**, 584-589.

Hegai, V. V., Kim, V. P., and Liu, J. Y., 2006. The ionospheric effect of atmospheric gravity waves excited prior to strong earthquake. Adv. Space Res., **37**, 653-659.

Herman, J. R., and Goldberg, R. A., 1978. Sun, Weather and Climate. NASA-SP 426, Washington D. C., USA.

Hill, R. D., 1979. A survey of lightning energy estimates. Rev. Geophys. Space Phys., **17**, 155-164.

Holzworth, R. H., and Mozer, F. S., 1979. Direct evidence of solar flare modification of stratospheric electric fields. J. Geophys. Res., **84**, 363-367.

Hoppel, W. A., 1967. Theory of Electrode effect. J. Atmos. Terr. Phys., **29**, 709-721.

Idone, V. P., and Orville, R. E., 1982. Lightning return stroke velocities in the thunderstorm research international program (TRIP). J. Geophys. Res., **87**, 4903-4915.

Inan, U. S., Bell, T. F., and Rodriguez, J. V., 1991. Heating and ionization of the lower ionosphere by lightning. Geophys. Res. Lett., **18**, 705-708.

Inan, U. S., Reising, S. C., Fishman, G. J., and Horack, J. M., 1996. On the association of terrestrial gamma ray bursts with lightning and implications for sprites. Geophys. Res. Lett., **23**, 1017-1020.

Ishisaka, K., Okada, T., Hawkins, J., Murakami, S., Miyake, T., Murayama, Y., Nagano, I., and Matsumoto, H., 2005. Investigation of electron density profile in the lower ionosphere by SRP-4 rocket experiment. Earth Planets Space, **57**, 879-884.

Israil, M., Gupta, P. K., and Tyagi, D. K., 2004. Determining sharp layer boundaries from straightforward inversion of resistivity sounding data. The J. Ind. Geophys. Union, **8**, 125-134.

Israil, M., Tyagi, D. K., Gupta, P. K., and Niwas, S., 2008. Magnetotelluric investigations for imaging electrical structure of Garhwal Himalayan corridor, Uttarakhand, India. J. Earth Syst. Sci., **117**, 189-200.

Jacob, J. A., Kato, Y., Matsushita, S., and Troitskaya, V. A., 1964. Classification of geomagnetic micropulsations. J. Geophys. Res., **69**, 180-181.

Jacobson, A. R., Cummins, K. L., Carter, M., Klingner, P., Roussel-Dupre, D., and Knox, S. O., 2000. FORTE radio-frequency observations of lightning strokes detected by the National Lightning Detection Network. J. Geophys. Res., **105**, 15653-15662.

Kalscheuer, T., Commer, M., Helwig, S. L., Hordt, A., and Tezkan, B., 2007. Electromagnetic evidence for an ancient avalanche caldera rim on the south flank of Mount Merapi Indonesia. J. Volcan. Geoth. Res., **162**, 81-97.

Karmann, R., 1977. Search coil magnetometers with optimum signal-to-noise ratio. in Vozoff, K. (ed) magnetotelluric methods: SEG geophysics reprint series, **5**, 215-218.

Kaufman, A. A., and Keller, G. V., 1981. The magnetotelluric sounding method. Elsevier Scientific Publishing Company, Amsterdam.

Kazimirovsky, E., Herraiz, M., and De La Morena, B. A., 2003. Effects on the ionosphere due to phenomena occurring below it. Surv. Geophys., **24**, 139-184.

Keller, G. V., and Frischknecht, F. C., 1966. Electrical method of geophysical prospecting. Pergamon Press, New York, pp. 519.

Khastgir, S. R., and Saha, S. K., 1972. On Intra-cloud discharges and their accompanying electric field changes. J. Atmos. Terr. Phys., **34**, 115-126.

Kleusberg, A., 1992. The global positioning system and ionospheric conditions. Solar Terr. Predict., **IV**, 142-146.

Kim, V. P., Hegai, V. V., and Illich-Svitych, P. V., 1994. On the possible precursor of earthquakes. Fizika zemli, **3**, 37-40.

Kim, V. P., and Hegai, V. V., 1997. On possible changes in the midlatitude upper ionosphere before strong earthquakes. J. Earthq. Predict. Res., **6**, 275-280.

King, C. Y., 1986. Gas geochemistry applied to earthquake prediction: An overview. J. Geophys. Res., **91**, 12269- 12281.

Kosarev, E. L., Zatsepin, V. G., and Mitrofanov, A. V., 1970. Ultra high frequency radiation from lightnings. J. Geophys. Res., **75**, 7524-7530.

Koshevaya, S. V., Perez-Enriquez, R., and Kotsarenko N. Ya., 1997. The detection of electromagnetic processes in the ionosphere caused by seismic activity. Geofis. Int., **36**, 47-52.

Krehbiel, P. R., Brook, M., and McCrory, R. A., 1979. An Analysis of the charge structure of lightning discharges to ground. J. Geophys. Res., **84**, 2432-2456.

Kudryashev, G. S., and Avakyan, S. V., 2000. Ionization and excitation of the upper atmosphere during solar flares. Phys. Chem. Earth (C), **25**, 511-514.

Kumar, R., 1995. Lightning and its interaction with troposphere. Ph.D. thesis, University of Roorkee (India).

Kumar, R., Das, I. M. L., Gairola, R. M., Sarkar, A., and Agarwal, V. K., 2007. Rainfall retrieval from TRMM radiometric channels using artificial neutral networks. Indian J. Radio Space Phys., **36**, 114-127.

Kushwah, V., Singh, V., Singh, B., and Hayakawa, M., 2005. Ultralow frequency (ULF) magnetic field anomalies observed at Agra and their relation to moderate seismic activities in Indian region. J. Atmos. Solar-Terr. Phys., **67**, 992-1001.

Lastovicka, J., 1996. Effects of geomagnetic storms in the lower ionosphere, middle atmosphere and troposphere. J. Atmos. Solar-Terr. Phys., **58**, 831-843.

Lastovicka, J., 1997. Effects of geomagnetic storms-different morphology and origin in the upper middle atmosphere and the troposphere. Stud. Geophys. Geod., **41**, 73-81.

Lezaeta, P., 2001. Distortion analysis and 3-D modeling of magnetotelluric data in the southern central Andes. Ph. D. Thesis, Free University of Berlin, Germany.

Ligda, M. H., 1956. The radar observations of lightning. J. Atmos. Terr. Phys., **9**, 329-346.

Liu, X., and Krehbiel, P. R., 1985. The initial streamer of Intracloud lightning flashes. J. Geophys. Res., **90**, 6211-6218.

Liu, J. Y., Chen, Y. I., Pulinets, S. A., Tsai, Y. B., and Chuo, Y. J., 2000. Seismo-ionospheric signatures prior to $M \geq 6.0$ Taiwan earthquakes. Geophys. Res. Lett., **27**, 3113-3116.

Liu, J. Y., Chen, Y. I., Chuo, Y. J., and Tsai, H. F., 2001. Variations of ionospheric total electron content during the Chi-Chi earthquake. Geophys. Res. Lett., **28**, 1383-1386.

Liu, J. Y., Chuo, Y. J., Shan, S. J., Tsai, Y. B., Chen, Y. I., Pulinets, S. A., and Yu, S. B., 2004. Pre-earthquake ionospheric anomalies registered by continuous GPS TEC measurements. Ann. Geophys., **22**, 1585-1593.

Lyons, W. A., 1994. Characteristics of luminous structures in the stratosphere above thunderstorms as imaged by low-light level video. Geophys. Res. Lett., **21**, 875-878.

Mackerras, D., 1968. A Comparison of discharge processes in cloud and ground lightning flashes. J. Geophys. Res., **73**, 1175-1183.

Mackie, R. L., Rieven, S., and Rodi, W., 1997. User's manual and software documentation for two-dimensional inversion of magnetotelluric data. San Francisco: GSY-USA Inc.

Madden, T., and Thompson, W., 1965. Low frequency electromagnetic oscillations of the Earth-ionosphere cavity. Rev. Geophys., **3**, 211-254.

Mahajan, K. K., 1967. Extent of thermal non-equilibrium in the ionosphere. J. Atmos. Terr. Phys., **29**, 1137-1151.

Mahajan, K. K., 1977. Models of electron temperature in the ionospheric F-region using electron density height profiles. J. Atmos. Terr. Phys., **39**, 637-639.

Märcz, F., Sátori, G., and Zieger, B., 1997. Variations in Schumann resonances and their relation to atmospheric electric parameters at Nagycenk station. Ann. Geophys., **15**, 1604-1614.

Marquardt, D. W., 1963. An algorithm for least-squares estimation of non-linear parameters. J. Soc. Ind. Appl. Math., **11**, 431-441.

Matsushita, S., 1967. Solar quiet and lunar daily variation fields, in Matsushita, S., and Campbell, W. H., (Eds.): Physics of geomagnetic phenomena, Academic press, New York, pp 302.

McCarthy, M., a nd Parks, G. K., 1985. Further observations of X-rays inside thunderstorms. Geophys. Res. Lett., **12**, 393-396.

McNeice, G. W., and Jones, A. G., 2001. Multisite, multifrequency tensor decomposition of magnetotelluric data. Geophys., **66**, 158-173.

Melnikov, A., Price, C., Sátori, G., and Füllekrug, M., 2004. Influence of solar terminator passages on Schumann resonance parameters. J. Atmos. Solar-Terr. Phys., **66**, 1187-1194.

Mitra, S. K., 1992. The upper atmosphere. The Asiatic Society, Monograph Series, V, Calcutta, India.

Molchanov, O. A., and Hayakawa, M., 1995. Generation of ULF electromagnetic emissions by microfracturing. Geophys. Res. Lett., **22**, 3091-3094.

Molchanov, O. A., Hayakawa, M., and Rafalsky, V. A., 1995. Penetration characteristics of electromagnetic emissions from an underground seismic source into the atmosphere, ionosphere and magnetosphere. J. Geophys. Res., **100**, 1691-1712.

Molchanov, O. A., and Hayakawa, M., 1998. On the generation mechanism of ULF seismogenic electromagnetic emissions. Phys. Earth Planet. Int., **105**, 201-210.

Molchanov, O. A., Hayakawa, M., Oudoh, T., and Kawai, E., 1998. Precursory effects in the subionospheric VLF signals for the Kobe earthquake. Phys. Earth Planet. Int., **105**, 239-248.

Mukherjee, G. K., 1999. Airglow, ionospheric signatures associated with earthquakes. Bull IAPT, 303-305.

Munro, R. H., and Withbroe, G. L., 1972. Properties of a coronal hole derived from extreme-ultraviolet observations. Astrophys. J., **176**, 511-520.

Muto, F., Yoshida, M., Horie, T., Hayakawa, M., Parrot, M., and Molchanov, O. A., 2008. Detection of ionospheric perturbations associated with Japanese earthquakes on the basis of reception of LF transmitter signals on the satellite DEMETER. Nat. Hazards Earth Syst. Sci., **8**, 135-141.

Nag, A., and Rakov, V. A., 2008. Pulse trains characteristics of preliminary breakdown in cloud-to-ground lightning that are not followed by return stroke pulses. J. Geophys. Res., **113**, D01102.

Nakono, M., 1979. The cloud discharge in winter thunderstorms of the Hokuriku coast. J. Meteor. Soc. Japan, **57**, 444-451.

Nickolaenko, A. P., 1997. Modern aspects of Schumann resonance studies. J. Atmos. Solar-Terr. Phys., **59**, 805-816.

Nickolaenko, A. P., and Hayakawa, M., 2002. Resonances in the Earth-Ionosphere cavity. Kluwer Academic Publisher, Dordrecht, Netherland.

Nitsan, U., 1977. Electromagnetic emission accompanying fracture of quartz-bearing rocks. Geophys. Res. Lett., **4**, 333-336.

Ogawa, T., and Brook, M., 1964. The mechanism of the intracloud lightning discharge. J. Geophys. Res., **69**, 5141-5150.

Ogawa, T., 1982. The lightning current. In Handbook of Atmospherics, 1, ed., H. Voland, Boca Raton, Florida: CRC press. pp 23-63.

Ondoh, T., 1998. Ionospheric disturbances associated with great earthquake of Hokkaido southwest coast, Japan of July 12, 1993. Phys. Earth Planet. Int., **105**, 261-269.

Ondoh, T., 2000. Seismo-ionospheric phenomena. Adv. Space Res., **26**, 1267-1272.

Orville, R. E., Lala, G. G., and Idone, V. P., 1978. Daylight time-resolved photographs of lightning. Science, **201**, 59-61.

Otsuyana, T., Hobara, Y., and Hayakawa, M., 1999. EM radiation associated with sprites. Proc. 11th International conference on Atmospheric Electricity. Guntersville., AL, 96-98.

Oyama, K. I., and Hirao, K., 1975. Electron temperature probe experiments on the satellite 'TAIYO'. J. Geomagn. Geoelectr., **27**, 321-330.

Oyama, K. I., Hirao, K., and Yasuhara, F., 1985. Electron temperature probe on board Japan's 9th scientific satellite 'OHZORA'. J. Geomagn. Geoelectr., **37**, 413-430.

Oyama, K. I., Balan, N., Watanabe, S., Takahashi, T., Isoda, F., Bailey, G. J., and Oya, H., 1996a. Morning overshoot of Te enhanced by downward plasma drift in the equatorial topside ionosphere. J. Geomagn. Geoelectr., **48**, 959-966.

Oyama, K. I., Watanabe, S., Su, Y., Takahashi, T., and Hirao, K., 1996b. Season, local time, and longitude variations of electron temperature at the height of ~ 600 km in the low latitude region. Adv. Space Res., **18**, 269-278.

Pappert, R. A., and Bickel, J. E., 1970. Vertical and horizontal VLF fields excited by dipoles of arbitrary orientation and elevation. Radio Sci., **5**, 1445-1452.

Park, C. G., 1976. Solar magnetic sector effects on the vertical atmospheric electric field at Vostok, Antarctica. Geophys. Res. Lett., **3**, 475-478.

Parkinson, W. D., 1959. Directions of rapid geomagnetic fluctuations. Geophys. J. R. Astr. Soc., **2**, 1-14.

Parkinson, W. D., 1983. Introduction to geomagnetism. Scottish Academic Press Ltd., Edinburgh.

Parks, G. K., Mauk, B. H., Spiger, R., and Chin, J., 1981. X-ray enhancements detected during thunderstorm and lightning activity. Geophys. Res. Lett., **8**, 1176-1179.

Parrot, M., 1994. Statistical study of ELF/VLF emissions recorded by a low-altitude satellite during seismic events. J. Geophys. Res., **99**, 23339-23347.

Parrot, M., 1995. Use of satellites to detect seismo–electromagnetic effects. Adv. Space Res., **15**, 27-35.

Parrot, M., Berthelier, J. J., Lebreton, J. P., Sauvaud, J. A., Santolík, O., and Blecki, J., 2006. Examples of unusual ionospheric observations made by the DEMETER satellite over seismic regions. Phys. Chem. Earth, **31**, 486-495.

Pathak, P. P., Rai, J., and Varshneya, N. C., 1980. Electrochemical charge separation in clouds. Ann. Geophys., **36**, 613-621.

Pedersen, L. B., and Engels, M., 2005. Routine 2D inversion of magnetotelluric data using the determinant of the impedance tensor. Geophys., **70**, G33-G41.

Pierce, E. T., 1963. Excitation of Erath-ionosphere resonances by lightning flashes. J. Geophys. Res., **68**, 4125.

Pierce, E. T., 1976. Atmospheric electricity and earthquake prediction. Geophys. Res. Lett., **3**, 185-188.

Priest, E. R., 1992. Basic magnetic configuration and energy supply processes for an interacting flux model of eruptive solar flares, edited by Svestka Z., Jackson, B. and Machado, M., Lecture Notes in Physics, 399, 15.

Pulinets, S. A., Legen'ka, A. D., and Alekseev, V. A., 1994. "Pre-earthquake ionospheric effects and their possible mechanisms" Dusty and Dirty Plasmas, Noise, and Chaos in Space and in the Laboratory, Ed. by Kikuchi, H., Plenum Pub., New York, pp 545-557.

Pulinets, S. A., 1998a. Strong earthquake prediction possibility with the help of topside sounding from satellites. Adv. Space Res., **21**, 455-458.

Pulinets, S. A., 1998b. Seismic activity as a source of the ionospheric variability. Adv. Space Res., **22**, 903-906.

Pulinets, S. A., Khegai, V. V., Boyarchuk, K. A., and Lomonosov, A. M, 1998c. The atmospheric electric field as a source of variability in the ionosphere. Physics-Uspekhi, **41**, 515-522.

Pulinets, S. A., Boyarchuk, K. A., Hegai, V. V., Kim, V. P., and Lomonosov, A. M., 2000. Quasielectrostatic model of Atmosphere-Thermosphere-Ionosphere coupling. Adv. Space Res., **26**, 1209-1218.

Pulinets, S. A., and Legen'ka, A. D., 2003. Spatial-Temporal characteristics of large scale disturbances of electron density observed in the ionospheric F-region before strong earthquakes. Cosmic Res., **41**, 221-229.

Pulinets, S. A., Legen'ka, A. D., Gaivoronskaya, T. V., and Depuev, V. Kh., 2003. Main phenomenological features of ionospheric precursors of strong earthquakes. J. Atmos. Solar-Terr. Phys., **65**, 1337-1347.

Pulinets, S. A., and Boyarchuk, K. A., 2004. Ionospheric precursors of earthquakes. Springer Berlin Heidelberg New York.

Pulinets, S. A., 2004. Ionospheric precursors of earthquakes; Recent advances in theory and practical applications. Terr. Atmos. Oceanic Sci., **15**, 413-435.

Pulinets, S. A., and Liu, J. Y., 2004. Ionospheric variability unrelated to solar and geomagnetic activity. Adv. Space Res., **34**, 1926-1933.

Rai, J., Rao, M., and Tantry, B. A. P., 1972. Bremsstrahlung as a possible source of UHF emissions from lightning. Nature (Physical Science), **238**, 59-60.

Rai, J., 1974. Some studies of lightning discharge and radio atmospherics, Ph.D. thesis, Banaras Hindu University, Banaras (India).

Rai, J., Gupta, S. P., and Bhattacharya, P. K., 1974. Electromagnetic field of multiple return stroke lightning. Int. J. Electron., **36**, 649-654.

Rai, J., 1978. On the origin of UHF atmospherics. J. Atmos. Terr. Phys., **40**, 475-478.

Rai, J., and Varshneya, N. C., 1982. Return strokes and K-field changes in tropical thunderstorms. J. Atmos. Terr. Phys., **44**, 291-299.

Rakov, V. A., and Uman, M. A., 1990. Some properties of negative cloud-to-ground lightning flashes versus stroke order. J. Geophys. Res., **95**, 5447-5453.

Rakov, V. A., and Uman, M. A., 2006. Lightning: Physics and effects. Encyclopedia of lightning. URL~http://plaza.ufl.edu/rakov/LPE/LPE.html.

Rao, M., 1967. Corona currents after the return stroke and the emission of ELF waves in a lightning flash to earth. Radio Sci., **2**, 241-244.

Reid, G. C., and Collins, C., 1959. Observations of abnormal VHF radiowave absorption at medium and high latitudes. J. Atmos. Terr. Phys., **14**, 63-81.

Reiter, R., 1972. Case study concerning the impact of solar activity upon potential gradient and air-earth current in the lower troposphere. Pure Appl. Geophys., **94**, 218-225.

Reiter, R., 1977. The electric potential of the ionosphere as controlled by the solar magnetic sector structure; reults of a study over the period of a solar cycle. J. Atmos. Terrs. Phys., **39**, 95-99.

Rinnert, K., Lanzerotti, L. J., Dehmel, G., Gliem, F. O., Krider, E. P., and Uman, M. A., 1985. Measurements of the RF characteristics of earth lightning with the Galileo probe lightning experiment. J. Geophys. Res., **90**, 6239-6244.

Rios, V. H., Kim, V. P., and Hegai, V. V., 2004. Abnormal perturbations in the F2 region ionosphere observed prior to the great San Juan earthquake of 23 November 1977. Adv. Space Res., **33**, 323-327.

Rishbeth, H., 2006. F-region links with the lower atmosphere? J. Atmos. Solar-Terr. Phys., **68**, 469-478.

Roble, R. G., and Hays, P. B., 1979. A quasi-static model of global atmospheric electricity 2. Electrical coupling between the upper and lower atmosphere. J. Geophys. Res., **84**, 7247-7256.

Rodi, W. L., and Mackie, R. L., 2001. Nonlinear conjugate gradients algorithm for 2-D magnetotelluric inversion. Geophys., **66**, 174-187.

Roldugin, V. C., Maltsev, Y. P., Vasiljev, A. N., and Vashenyuk, E. V., 1999. Changes of the first Schumann resonance frequency during relativistic solar proton precipitation in the 6 November 1997 event. Ann. Geophys., **17**, 1293-1297.

Roldugin, V. C., Maltsev, Y. P., Petrova, G. A., and Vasiljev, A. N., 2001. Decrease of first Schumann resonance frequency during solar proton events. J. Geophys. Res., **106**, 18555-18562.

Roldugin, V. C., Maltsev, Y. P., Vasiljev, A. N., Shvets, A. V., and Nikolaenko, A. P., 2003. Changes of Schumann resonance parameters during the solar proton event of July 14, 2000. J. Geophys. Res., **108** (A3), 1103, 2-7.

Roldugin, V. C., Maltsev, Y. P., Vasiljev, A. N., Schokotov, A. Y., and Belyajev, G. G., 2004a. Diurnal variations of Schumann resonance frequency in NS and EW magnetic components. J. Geophys. Res., **109**, A08304.

Roldugin, V. C., Maltsev, Y. P., Vasiljev, A. N., Schokotov, A. Y., and Belyajev, G. G., 2004b. Schumann resonance frequency increase during solar X-ray bursts. J. Geophys. Res., **109**, A01216.

Rosenberg, T. J., and Ianzerotti, L. J., 1979. Direct energy inputs to the middle atmosphere, Middle Atmosphere Electrodynamics, edited by N. C. Maynard, NASA CP-2090, USA, pp 43-70.

Rostoker, G., 1972. Polar magnetic substorms. Rev. Geophys. Space phys., **10**, 157-211.

Sao, K., Yamashita, M., Tanahashi, S., Jindoh, H., and Ohta, K., 1973. Experimental investigations of Schumann resonance frequencies. J. Atmos. Terr. Phys., **35**, 2047-2053.

Sarkar, S., Gwal, A. K., and Parrot, M., 2007. Ionospheric variations observed by the DEMETER satellite in the mid-latitude region during strong earthquakes. J. Atmos. Solar-Terr. Phys., **69**, 1524-1540.

Saroso, S., Hattori, K., Ishikawa, H., Ida, Y., Shirogane, R., Hayakawa, M., Yumoto, K., Shiokawa, K., and Nishihashi, M., 2009. ULF geomagnetic anomalous changes possibly associated with 2004-2005 Sumatra earthquakes. Phys. Chem. Earth, **34**, 343-349.

Sátori, G., 1996. Monitoring Schumann resonances-II. Daily and seasonal frequency variations. J. Atmos. Terr. Phys., **58**, 1483-1488.

Sátori, G., Williams, E., and Mushtak, V., 2005. Response of the Earth-ionosphere cavity resonator to the 11-year solar cycle in X-radiation. J. Atmos. Solar-Terr. Phys., **67**, 553-562.

Schumann, W. O.,1952. Über die stralungslosen Eigenschwingungen einer leitenden Kugel die von Luftschicht und einer Ionospharenhulle umgeben ist. Z. Naturforsch., **7a**, 149-154.

Schunk, R. W., and Sojka, J. J., 1982. Ion-temperature variations in the daytime high-latitude F region. J. Geophys. Res., **87**, 5169-5183.

Schunk, R. W., and Sojka, J. J., 1996. Ionosphere-thermosphere space weather issues. J. Atmos. Terr. Phys., **58**, 1527-1574.

Sentman, D. D., 1983. Schumann resonance effects of electrical conductivity perturbations in an exponential atmospheric/ionospheric profile. J. Atmos. Solar-Terr. Phys., **45**, 55-66.

Sentman, D. D., 1987. Magnetic elliptical polarization of Schumann resonances. Radio Sci., **22**, 595-606.

Sentman, D. D., 1989. Detection of elliptical polarization and mode splitting in discrete Schumann resonance excitations. J. Atmos. Terr. Phys., **51**, 507-519.

Sentman, D. D., 1990. Approximate Schumann resonance parameters for a two-scale height ionosphere. J. Atmos. Terr. Phys., **52**, 35-46.

Sentman, D. D., and Fraser, B. J., 1991. Simultaneous observations of Schumann resonances in California and Australia: evidence for intensity modulation by the local height of the D region. J. Geophys. Res., **96**, 15973-15984.

Sentman, D. D., and Wescott, E. M., 1993. Observations of upper atmospheric optical flashes recorded from an aircraft. Geophys. Res. Lett., **20**, 2857-2860.

Sentman, D. D., 1996. Schumann resonance spectra in a two-scale-height Earth-ionosphere cavity. J. Geophys. Res., **101**, 9479-9487.

Shalimov, S., and Gokhberg, M., 1998. Lithosphere-ionosphere coupling mechanism and its application to the earthquake in Iran on June 20, 1990. A review of ionospheric measurements and basic assumptions. Phys. Earth Planet. Int., **105**, 211-218.

Shapka, R., 1992. Geomagnetic effects on modern pipeline system. Solar-Terrestrial Predictions, **IV**, 163-170.

Sharma, D. K., Rai, J., Israil, M., Subrahmanyam, P., Chopra, P., and Garg, S. C., 2004a. Enhancement in ionospheric temperatures during thunderstorms. J. Atmos. Solar-Terr. Phys., **66**, 51-56.

Sharma, D. K., Rai, J., Israil, M., Subrahmanyam, P., Chopra, P., and Garg, S. C., 2004b. Enhancement in electron and ion temperatures due to solar flares as measured by SROSS-C2 satellite. Ann. Geophys., **22**, 2047-2052.

Sharma, D. K., Rai, J., Israil, M., and Subrahmanyam, P., 2005. Diurnal, seasonal and latitudinal variations of ionospheric temperatures of the topside F region over the Indian region during solar minimum (1995-1996). J. Atmos. Solar-Terr. Phys., **67**, 269-274.

Sharma, D. K., Israil, M., Chand, R., Rai, J., Subrahmanyam, P., and Garg, S. C., 2006. Signature of seismic activities in the F2 region ionospheric electron temperature. J. Atmos. Solar-Terr. Phys., **68**, 691-696.

Silina, A. S., Liperovskaya, E. V., Liperovsky, V. A., and Meister, C. V., 2001. Ionospheric phenomena before strong earthquakes. Nat. Hazards Earth Syst. Sci., **1**, 113-118.

Simpson, G. C., and Scrase, F. J., 1937. The distribution of electricity in thunderclouds. Proc. Roy. Soc. London, A161, 309-352.

Simpson, F., and Bahr, K., 2005. Practical Magnetotellurics. Cambridge University Press, U. K., pp 246.

Sims, W. E., Bostick, F. X., and Smith, H. W., 1971. The estimation of magnetotelluric impedance tensor elements from measured data. Geophys., **36**, 938-942.

Singh, R. P., and Patel, R. P., 2001. Lightning generated ELF, VLF, Optical waves and their diagnostic features. Proceedings of the National Workshop on Recent Developments in Atmospheric and Space Sciences, IIT Roorkee, India, 9-32.

Singh, B., Kushwah, V., Singh, O. P., Lakshmi, D. R., and Reddy, B. M., 2004. Ionospheric perturbations caused by some major earthquakes in India. Phys. Chem. Earth, **29**, 537-550.

Siripunvaraporn, W., and Egbert, G., 2000. An efficient data-subspace inversion method for 2-D magnetotelluric data. Geophys., **65**, 791-803.

Smith, L. G., 1957. Intracloud lightning discharges. Quart. J. Roy. Meteor. Soc., **83**, 103-111.

Soriano, L. R., Pablo, F. D., and Tomas, C., 2005. Ten-year study of cloud-to-ground lightning activity in the Iberian Peninsula. J. Atmos. Solar-Terr. Phys., **67**, 1632-1639.

Sorokin, V. M., Chmyrev, V. M., and Yaschenko, A. K., 2001. Electrodynamic model of the lower atmosphere and the ionosphere coupling. J. Atmos. Solar-Terr. Phys., **63**, 1681-1691.

Su, Y. Z., Oyama, K. I., Bailey, G. J., Takahashi, T., and Watanabe, S., 1995. Comparison of satellite electron density and temperature measurements at low latitudes with a plasmasphere-ionosphere model. J. Geophys. Res., **100**, 14591-14604.

Su, Y. Z., Oyama, K. I., Bailey, G. J., Fukao, S., Takahashi, T., and Oya, H., 1996. Longitudinal variations of the topside ionosphere at low latitudes: satellite measurements and mathematical modelings. J. Geophys. Res., **101**, 17191-17205.

Swift, C. M. J., 1967. A magnetotelluric investigation of an electrical conductivity anomaly in the southwestern United State. Ph. D. Dissertation, Geophysics Laboratory, M.I.T., Cambridge.

Taranenko, Y. N., Inan, U. S., and Bell, T. F., 1993. Interaction with the lower ionosphere of electromagnetic pulses from lightning - heating, attachment, and ionization. Geophys. Res. Lett., **20**, 1539-1542.

Taylor, W. L., and Jean, A. G., 1959. Very low frequency radiation spectra of lightning discharges. J. Res. NBS, **63 D**, 199-204.

Tezkan, B., 1994. On the detectability of a highly conductive layer in the upper mantle beneath the Black Forest crystalline using magnetotelluric methods. Geophys. J. Int., **118**, 185-200.

Tezkan, B., Goldman, M., Greinwald, G., Hordt, A., Muller, I., Neubauer, F. M., and Zacher, G., 1996. A joint application of radiomagnetotellurics and transient electromagnetics to the investigation of a waste deposit in Cologne (Germany). J. Appl. Geophys., **34**, 199-212.

Tezkan, B., 1999. A review of environmental applications of quasi-stationary electromagnetic techniques. Surveys in Geophys., **20**, 279-308.

Thome, G. D., and Wagner, L. S., 1971. Electron density enhancement in the E and F regions of the ionosphere during solar flares. J. Geophys. Res., **76**, 6883-6895.

Thomson, R. J., and Dowden, R. L., 1977. Simultaneous ground and satellite reception of whistlers -2. PL whistlers. J. Atmos. Terr. Phys., **39**, 879-890.

Thrane, E. V., and Piggott, W. R., 1966. The collision frequency in the E- and D-regions of the ionosphere. J. Atmos. Terr. Phys., **28**, 721-737.

Tikhonov, A. N., and Arsenin, V. Y., 1977. Solutions of ill-posed problems. V. H. Winston and Sons, Washington, D. C.

Tiwari, G. N., and Goyal, R. K., 1997. Thermal modeling of a greenhouse: A pollution free controlled environment for crop productions. Proc. Int. Symp. Asian Monsoon and Pollution over the Monsoon Environment, IIT Delhi, pp 179.

Tiwari, M. S., Pandey, R. P., and Misra, K. D., 1985. Particle aspect analysis of drift instability in the presence of inhomogeneous magnetic field. J. Plasma Phys., **34**, 163-175.

Tiwari, G. N., and Yadav, Y. P., 1987. Comparative designs and long term performance of various designs of solar distiller. Energy conservion and management, **27**, 327-333.

Tiwari, M. S., and Varma, P., 1991. Drift instability in the presence of a parallel electric field and an inhomogeneous magnetic field-Particle aspect analysis. J. Plasma Phys., **46**, 49-62.

Tran, A., and Polk, C., 1979a. Schumann resonances and electrical conductivity of the atmosphere and lower ionosphere-I. Effects of conductivity at various altitudes on resonance frequencies and attenuation. J. Atmos. Terr. Phys., **41**, 1241-1248.

Tran, A., and Polk, C., 1979b. Schumann resonances and electrical conductivity of the atmosphere and lower ionosphere-II. Evaluation of conductivity profiles from experimental Schumann resonance data. J. Atmos. Terr. Phys., **41**, 1249-1261.

Tsai, Y. B., and Liu, J. Y., 2004. Special issue on Earthquake Precursors of Terrestrial, Atmospheric and Oceanic Sciences, **15**, 33-45.

Tulunay, Y., Altuntas, E., Tulunay, E., Price, C., Ciloglu, T., Bahadirlar, Y., and Senalp, E. T., 2008. A case study on the ELF characterization of the Earth-

ionosphere cavity: Forecasting the Schumann resonances intensities. J. Atmos. Solar-Terr. Phys., **70**, 669-674.

Uman, M. A., and Orville, R. E., 1965. The opacity of lightning. J. Geophys. Res., **70**, 5491-5497.

Uman, M. A., 1969. Lightning, McGraw-Hill Book Company, New York.

Uman, M. A., 1985. Lightning return stroke electric and magnetic fields. J. Geophys. Res., **90**, 6121-6130.

Velinov, P. I. Y., and Tonev, P. T., 2008. Electric currents from thunderstorms to the ionosphere during a solar cycle: Quasi-static modeling of the coupling mechanism. Adv. Space Res., **42**, 1569-1575.

Vozoff, K., 1991. The magnetotelluric method in electromagnetic methods in applied geophysics. Ed by M. N. Nabighian, Society of Exploration Geophysics, Tulsa, USA.

Wait, J. R., 1970. Electromagnetic waves in stratified media, Pergamon Press, Oxford.

Wang, C. P., 1963. Lightning discharges in the tropics: 2. Component ground-strokes and cloud dart streamer discharges. J. Geophys. Res., **68**, 1951-1958.

Ward, S. H., and Fraser, D. C., 1967. Electromagnetic theory for geophysical application. In: Mining Geophysics, **Vol. II**, Chap II, Part B, Society of Exploration Geophysics, Tulsa, Oklahoma.

Watanabe, S., Oyama, K. I., and Abdu, M. A., 1995. Computer simulation of electron and ion densities and temperatures in the equatorial F region and comparison with Hinotori results. J. Geophys. Res., **100**, 14581-14590.

Weidman, C. D., and Krider, E. P., 1980. Submicrosecond risetimes in lightning return-stroke fields. Geophys. Res. Lett., **7**, 955-958.

Weidman, C. D., Krider, E. P., and Uman, M. A., 1981. Lightning amplitude spectra in the interval from 100 kHz to 20 MHz. Geophys. Res. Lett., **8**, 931-934.

Wescott, E. M., Sentman, D. D., Osborne, D. L, Hampton, D. L., and Heavner, M. J., 1995. Preliminary results from the Sprites 94 aircraft campaign: Blue jets. Geophys. Res. Lett., **22**, 1209-1212.

Wescott, E. M., Sentman, D. D., Heavner, M. J., Hampton, D. L., Osborne, D. L., and Vaughan, O. H., 1996. Blue Starters: Brief upward discharges from an intense Arkansas thunderstorm. Geophys. Res. Lett., **23**, 2153-2156.

Whitten, R. C., and Poppoff, I. G., 1971. Fundamentals of Aeronomy. John Wiley and Sons, New York.

Williams, P. J. S., and McDonald, J. N., 1987. Electron temperature and electron density in the F-region of the ionosphere. II. The role of atomic oxygen and molecular nitrogen. J. Atmos. Solar-Terr. Phys., **49**, 873-887.

Yamada, I., Masuda, K., and Mizutani, H., 1989. Electromagnetic and acoustic emission associated with rock fracture. Phys. Earth Planet. Int., **57**, 157-168.

Yan, M., and Zhang, Y., 1992. Solar activities and atmospheric electric processes. Proc. 9th Int. Conf. Atmos. Elect., St. Petersburg, Russia, pp 480-483.

Yiyan, Z., Yun, W., Xuejun, Q., and Xunxie, Z., 2009. Ionospheric anomalies detected by ground-based GPS before the Mw7.9 Wenchuan earthquake of May 12, 2008, China. J. Atmos. Solar-Terr. Phys., **71**, 959-966.

Zakharenkova, I. E., Shagimuratov, I. I., and Krankowski, A., 2007. Features of the ionosphere behavior before the Kythira 2006 earthquake. Acta Geophys., **55**, 524-534.

Zaslavski, Y., Parrot, M., and Blanc, E., 1998. Analysis of TEC measurements above active seismic regions. Phys. Earth Planet. Int., **105**, 219-228.

Site References

The electromagnetic waves of different frequency penetrate into the earth (www.en.wikipedia.org.).

Earth's magnetosphere (www-istp.gsfc.nasa.gov).

The details of earthquake events have been used from United State Geological Survey (USGS) website (http://neic.usgs.gov).

The data of magnetic storm have been used from the website (http://swdcdb.kugi.kyoto-u.ac.jp).